

DESIGN, STRUCTURE, AND ACTION OF AN
ARTIFICIAL PHOTOSYNTHETIC REACTION CENTER

Nathan Ennist

A DISSERTATION

in

Biochemistry and Molecular Biophysics

Presented to the Faculties of the University of Pennsylvania

in

Partial Fulfillment of the Requirements for the

Degree of Doctor of Philosophy

2017

Supervisor of Dissertation

P. Leslie Dutton, Ph.D., FRS

Eldridge Reeves Johnson Professor of Biochemistry and Biophysics and Director of the Johnson Foundation for Molecular Biophysics

Graduate Group Chairperson

Kim A. Sharp, Ph.D.

Associate Professor of Biochemistry and Biophysics

Dissertation Committee

Kim A. Sharp, Ph.D., Associate Professor of Biochemistry and Biophysics

Sergei Vinogradov, Ph.D., Associate Professor of Biochemistry and Biophysics

Fevzi Daldal, Ph.D., Professor of Biology

Mitchell Lewis, Ph.D., John Morgan Professor of Biochemistry and Biophysics

Kurt Warncke, Ph.D., Professor of Physics

ACKNOWLEDGMENTS

I'm happy to have the opportunity to recognize the many people who supported me and collaborated with me over the years, and thereby made this thesis possible.

First and foremost, I want to thank my advisor, Les Dutton. Les always gave me the benefit of the doubt when my experiments weren't going as planned. My work in his lab began with about a year of designing and characterizing a handful of proteins that didn't produce the desired results. Despite my dismal track record, Les gave me the latitude to try a different approach. He kept an eye on me, but gave me the space to make my own mistakes, and in the end, I learned from them, and managed to design and characterize a protein that met our goals. Les encouraged me to be innovative when I otherwise would have been worried about wasting the lab's money on a far-fetched idea. I often felt as though he had more trust in my abilities than I did, and that confidence helped me to grow as a scientist.

Chris Moser's wealth of background knowledge and technical expertise in the lab has provided invaluable guidance during the development of my thesis. He is sharp, thoughtful, and patient, and always willing to walk me through something I don't understand. He has a way of jumping up from his chair to help as soon as I mention a problem with the laser or some other instrument in the lab. If my persistent questions ever started to irritate him, he never let on.

When I first started in the lab as a rotation student, Lee Solomon took me under his wing. In training me, I think it's safe to say that Lee put in more work than he got out, but he never complained. When I joined the lab in my third year, Goutham Kodali was an excellent mentor. He spent a lot of time getting me up to speed on basically everything and discussing questions and ideas I had about my project.

The atmosphere in the Dutton lab has always been congenial and collaborative. Bohdana Discher is a constant positive influence. Geetha Goparaju, Tammer Farid, Bruce Lichtenstein, Molly Sheehan, Bryan Fry, Chris Bialas, Zhenyu Zhao, Josh Mancini, Dirk Auman, and Martin Iwanicki have all been more than happy to discuss results or ideas with me. I'm grateful to have been able to work in a lab where everyone gets along and people help each other out.

I would be remiss not to mention Steve Stayrook, who runs the crystallography lab, for all the work he has put into helping me solve crystal structures. Steve once drove me in his car all the way to Long Island to pull an all-nighter collecting data at the NSLS synchrotron. That experiment became a foundational piece of my thesis, and I'm not sure how any of the crystallography would have been accomplished without Steve.

Huiguang Li in the lab of Greg van Duyne helped me get started on crystallography and using the mosquito robot, and the van Duyne lab generously allowed me to use their incubators and microscopes for my protein crystallization experiments. Tanya Esipova in the lab of Sergei Vinogradov synthesized a number of zinc porphyrins for us that were indispensable for my crystallography and transient absorption experiments that make up the bulk of my thesis.

My thesis committee members, Sergei Vinogradov, Kim Sharp, Fevzi Daldal, and Mitch Lewis, offered valuable suggestions and criticisms throughout my PhD to help steer me in the right direction. I'm especially thankful to Kurt Warncke for getting me started as an undergraduate in his biophysics lab and for coming all the way up from Emory for my thesis defense.

Last but not least, I'm lucky to have a wonderful family. My mom and dad support me in everything I do, and my sister Claire is a true friend. Their faith in me helps sustain my self-confidence when experiments aren't working, and I'm always grateful for their support.

ABSTRACT

DESIGN, STRUCTURE, AND ACTION OF AN ARTIFICIAL PHOTOSYNTHETIC REACTION CENTER

Nathan Ennist

P. Leslie Dutton

At the heart of photosystem II is the reaction center, where solar energy is used to separate charge. Set within a large and highly complex protein system, the handful of redox cofactors that make up the reaction center form an electron transport chain that converts the energy of a central, light-activated pigment into a reductant at one end and an oxidant at the other. The central aim of this thesis is to reproduce the charge separating function of photosystem II in a comparatively simple *de novo* designed protein maquette. The maquette effectively eliminates the complexity contributed by parts of photosystem II that are not directly involved in charge separation and facilitates a streamlined investigation of fundamental factors essential to this function. Previous work has produced light-activatable maquettes that are competent for electron transfer between tetrapyrroles but are unable to trap a charge separated state that is necessary for fuel generation.

This thesis details the design, structure, and action of MZH3, a multi-cofactor maquette that stabilizes a long-lived charge separated state. X-ray crystallographic structures of MZH3 are solved in complex with heme B, a synthetic zinc porphyrin, and metal ion cofactors. Despite sharing low sequence identity with natural proteins, MZH3 exhibits significant structural similarity to cytochrome b at the heme site and bacterioferritin at the metal site. Transient

absorption spectroscopy shows that the reduced state of heme B is stabilized in the presence of a tyrosine residue for 150 ms after light absorption at pH 9.5. The binding of ferrous iron extends the charge separated state lifetime to 300 ms at pH 7.5. Providing the tyrosine with a hydrogen bond to histidine increases the yield of the charge separated state but decreases its lifetime. Mutation of a heme-ligating histidine to alanine gives rise to an unexpected oxygen binding function with an oxyferrous lifetime of 38 hours, comparable to natural oxygen transport proteins. These results show that MZH3 is a uniquely structured, functional reaction center maquette that is readily adapted to new functions. Continuing development will be directed toward multinuclear metal cluster assembly and *in vivo* generation of solar fuel from water.

TABLE OF CONTENTS

ACKNOWLEDGMENTS	II
ABSTRACT	V
TABLE OF CONTENTS	VII
LIST OF TABLES	XI
LIST OF FIGURES	XII
CHAPTER 1: THESIS STATEMENT AND INTRODUCTION	1
1.1 Photosynthesis, natural and artificial	2
1.1.1 Structure and function of photosystem II and its reaction center	3
1.1.2 Photosynthetic reactions and the potential for improvement	7
1.1.3 The oxygen evolving complex (OEC) of photosystem II	9
1.1.4 Photoassembly of the oxygen evolving complex (OEC)	10
1.1.5 Redox active tyrosines of photosystem II: Y _D and Y _Z	11
1.1.6 Functions of Y _D and Y _Z	15
1.1.7 Tyrosine Z model systems	17
1.1.8 Hydrogen evolution in artificial photosynthesis	19
1.1.9 Reengineering natural proteins for artificial photosynthesis	20
1.2 Four-helix bundle design	22
1.2.1 Introduction to protein maquettes	24
1.2.2 Coiled coils	26
1.2.3 Layers of hydrophobic amino acids in the core	27
1.2.4 Heme binding in natural four-helix bundles	31
1.2.5 The role of the apo-state in heme binding	34
1.2.6 Due Ferro series of maquettes.....	35
1.2.7 Negative design.....	37
1.2.8 Inter-helical loops	40
1.2.9 Four-helix bundle length	41
1.2.10 Caps at helical termini.....	42
1.2.11 Summary	43
1.3 References	44
CHAPTER 2: DESIGN AND CHARACTERIZATION OF A REACTION CENTER MAQUETTE	59
2.1 Crystallization trials with BT6, a multifunctional heme-binding maquette	59
2.1.1 Efforts to crystallize BT6.....	61

2.1.2 Improved crystal growth in a modified BT6, BT6_2sl	63
2.1.3 Promising results from BT6_3sl crystallography	65
2.2 Design of the reaction center maquette MZH3	67
2.2.1 Use of the Due Ferro maquette sequences in MZH3	69
2.2.2 Tetrapyrrole binding section of MZH3	70
2.2.3 Helix-helix interfaces in MZH3	73
2.2.4 Inter-helical loops in MZH3	75
2.2.5 Inter-helical charge pairing interactions	76
2.3 Routine characterization of MZH3	79
2.3.1 Size exclusion chromatography	79
2.3.2 Ultraviolet/visible spectroscopy	81
2.3.3 UV/vis spectroscopy: Acceptor site	83
2.3.4 UV/vis spectroscopy: Pigment site.....	87
2.3.5 UV/vis spectroscopy: Donor site	94
2.3.6 Ferroxidase activity	95
2.3.7 Circular dichroism to assay secondary structure	96
2.3.8 Circular dichroism in Soret region to assay exciton coupling	100
2.3.9 Heme B Redox titration.....	102
2.4 DDH2: A truncated version of MZH3 that binds two hemes	103
2.4.1 Size exclusion chromatography	105
2.4.2 Ultraviolet/visible spectroscopy of DDH2 with heme B.....	106
2.4.3 Circular dichroism of DDH2 with heme B.....	107
2.4.4 Significance of DDH2.....	110
2.5 References	110
CHAPTER 3: STRUCTURE OF A REACTION CENTER MAQUETTE.....	116
3.1 Crystallographic structure determination of MZH3	116
3.2 Overall structure of MZH3	119
3.2.1 MZH3 is a coiled coil	120
3.2.2 Layers in the hydrophobic core.....	121
3.2.3 Inter-helical charge patterning interactions	123
3.2.4 Inter-helical loops	123
3.3 Electron acceptor site	124
3.3.1 Heme B binding site agrees with design	124
3.3.2 Multiple heme conformations in the acceptor site	126
3.3.3 Influence of arginine and tryptophan residues on heme binding in MZH3	128
3.3.4 Structural similarity between heme sites of MZH3 and cytochrome b	129
3.3.5 Apo-state of the acceptor site	130
3.4 Pigment site	132
3.4.1 Apo-state of the pigment site	132
3.4.2 Holo-state of the pigment site	134
3.4.3 ZnPCP can bind to an unexpected site in MZH3	137

3.5 Metal-binding site	142
3.5.1 Di-metal site structure consistent with design	142
3.5.2 Di-metal site structure with metal in unintended position	144
3.6 Leu71His mutation and His-Tyr hydrogen bond.....	146
3.7 Summary.....	148
3.8 References	150
CHAPTER 4: LIGHT-DRIVEN ELECTRON TRANSFER IN A REACTION CENTER MAQUETTE	153
4.1 Electron transfer background	154
4.1.1 A kinetic model of electron transfer in MZH3.....	154
4.1.2 Parameters that govern electron transfer rates	156
4.2 Transient absorption	160
4.2.1 Transient absorption experimental approach	160
4.2.2 Monad and Dyad in MZH3	163
4.2.3 Triad with tyrosine in MZH3.....	165
4.2.4 Triad with iron in MZH3	173
4.2.5 MZH3 reverts to dyad behavior in the presence of Zn, Cd, or Mn	177
4.2.6 Photo-reduction of cobalt protoporphyrin IX	181
4.3 Summary of electron transfer in MZH3	184
4.3.1 ZnPCP binding to metal cavity is not consistent with transient absorption results.....	184
4.3.2 Analysis of transient absorption results.....	185
4.3.3 Conclusion and future directions	187
4.4 References	188
CHAPTER 5: OXYGEN BINDING AND ALTERNATIVE HEME LIGATIONS.....	192
5.1 MZH3 mutants bind heme B with ligands other than histidine	193
5.2 Heme B midpoint potentials in MZH3 mutants.....	195
5.3 Oxygen binding in MZH3-His110Ala	199
5.3.1 Introduction to oxygen transport proteins	200
5.3.2 Oxygen binding results in MZH3-His110Ala.....	201
5.3.3 Oxygen binding conclusions and future directions	207
5.4 References	210
CHAPTER 6: CONCLUSION	213
6.1 Four-helix bundle protein design strategy	213

6.2 Light-driven electron transfer	216
6.3 Oxygen binding	218
6.4 Summary	219
6.5 References	219
CHAPTER 7: APPENDIX	222
7.1 Protein expression and purification.....	222
7.2 Ultraviolet/visible spectroscopy.....	223
7.3 Circular dichroism.....	224
7.4 Redox titration	225
7.5 Crystallography methods and crystal structure statistics.....	225
7.6 Transient absorption	229
7.7 Singular value decomposition (SVD)	230
7.8 Spectroelectrochemistry	231
7.9 References	232

LIST OF TABLES

Table 2.1: Amino acid sequence of MZH3	68
Table 2.2: Comparison of the Due Ferro section of MZH3 to DF2t and DF3 sequences	70
Table 2.3: Summary of properties of tetrapyrroles tested for binding to MZH3 acceptor site	87
Table 2.4: Zinc tetrapyrroles that bind to MZH3/Heme with high affinity	91
Table 2.5: Zinc tetrapyrroles that do not bind to MZH3/Heme with high affinity	92
Table 2.6: MZH3 circular dichroism measurements	97
Table 2.7: Amino acid sequence of DDH2 compared to MZH3	105
Table 3.1: Crystallization conditions used to grow MZH3 crystals	118
Table 3.2: List of MZH3 crystal structures	119
Table 4.1: Rates of change of each state of the MZH3 triad system	155
Table 4.2: Summary of parameters that determine electron transfer rates in MZH3	159
Table 4.3: Transient absorption results in MZH3 with heme B and ZnPCP	172
Table 5.1: Summary of heme B properties in different MZH3 mutants	199
Table 7.1: Crystallization conditions used to obtain MZH3 crystal structures	227
Table 7.2: Multiwavelength anomalous dispersion (MAD) statistics for crystal structure CS-A.	228
Table 7.3: Data collection and refinement statistics	229

LIST OF FIGURES

Figure 1.1: Photosystem II crystal structure	5
Figure 1.2: Energy diagram of photosystem II	8
Figure 1.3: Photoactivation of the oxygen evolving complex.....	11
Figure 1.4: Redox active tyrosines of photosystem II	13
Figure 1.5: Four-helix bundle topologies	25
Figure 1.6: Helical wheel diagram.....	28
Figure 1.7: Layers in natural proteins	29
Figure 1.8: Canonical carboxylate-bridge diiron protein active site	36
Figure 2.1: Charge separation in BT6 using a sacrificial electron donor.....	60
Figure 2.2: BT6 crystals not suitable for X-ray diffraction	63
Figure 2.3: BT6_2sl crystals that diffract X-rays to 6-7 Å resolution.....	65
Figure 2.4: BT6_3sl crystals grow with improved morphology compared to BT6 and BT6_2sl	66
Figure 2.5: Layers in natural proteins	73
Figure 2.6: Helical wheel diagram of one heptad of an antiparallel four-helix bundle protein	74
Figure 2.7: Negative design of MZH3.....	78
Figure 2.8: Size exclusion chromatography elution profiles of MZH3	80
Figure 2.9: Size exclusion chromatography calibration curves.....	81
Figure 2.10: Heme binding by MZH3 <i>in vivo</i>	82
Figure 2.11: Heme B binding titration	83
Figure 2.12: Heme B spectra in MZH3	84
Figure 2.13: CoPIX binding titration to MZH3.....	85
Figure 2.14: Ferric DADPIX binding titration with MZH3	86
Figure 2.15: ZnNP titration into MZH3.....	88
Figure 2.16: Binding titration of ZnNP into MZH3/Heme	89
Figure 2.17: ZnPCP titration into MZH3/Heme/Zn(II).....	90
Figure 2.18: Co(II) binding titration with MZH3.....	95
Figure 2.19: Ferroxidase activity of MZH3.	96
Figure 2.20: Circular dichroism measurements of MZH3	98
Figure 2.21: Exciton coupling effects of MZH3 with heme B and ZnNP by circular dichroism....	101
Figure 2.22: Redox titration of heme B bound to MZH3	103
Figure 2.23: Size exclusion chromatography elution profile of DDH2	106
Figure 2.24: Heme titration into DDH2	107
Figure 2.25: Far UV circular dichroism spectroscopy of DDH2	108
Figure 2.26: Exciton coupling between hemes B in DDH2.....	109
Figure 3.1: Crystals of MZH3 with heme B.....	117
Figure 3.2: Crystal structure of MZH3 in holo-state.	120
Figure 3.3: Seamless connection of MZH3 cofactor binding modules facilitated by layers	122
Figure 3.4: Structured loop in MZH3 and DF2t.....	124
Figure 3.5: Heme B has well-defined conformation in MZH3	125
Figure 3.6: Heme B binding site and 2 nd shell threonines.....	126
Figure 3.7: Heme flipping in MZH3	127
Figure 3.8: Heme B rotation by 90° in MZH3-L71H mutant	127
Figure 3.9: Heme-arginine interaction in MZH3	128

Figure 3.10: Structural similarity between MZH3 and cytochrome b	130
Figure 3.11: MZH3 structure without electron acceptor	131
Figure 3.12: Conformational changes associated with heme binding in MZH3	132
Figure 3.13: MZH3 structure without pigment	133
Figure 3.14: CS-A pigment site with ZnPCP	136
Figure 3.15: CS-C pigment site with ZnPCP	138
Figure 3.16: Extra ZnPCP at opening of metal binding site cavity	140
Figure 3.17: Cd(II) bound to MZH3	143
Figure 3.18: Comparison of MZH3 to bacterioferritin	143
Figure 3.19: Unintended metal binding site	144
Figure 3.20: Metal binding with extra Mn(II) and ZnPCP	145
Figure 3.21: Histidine-tyrosine hydrogen bond in MZH3-L71H mutant	147
Figure 4.1: Model of electron transfer pathway in dyad and triad versions of MZH3	154
Figure 4.2: Electron transfer predictions in MZH3	159
Figure 4.3: Schematic of setup for transient absorption experiments	161
Figure 4.4: Redox difference spectra relevant to transient absorption experiments	162
Figure 4.5: Monad and dyad transient absorption experiments	164
Figure 4.6: Transient absorption spectra of wild type MZH3 with heme B and ZnPCP at pH 7.5	167
Figure 4.7: Transient absorption and SVD of wild type MZH3 with heme and ZnPCP at pH 9.5.	168
Figure 4.8: Predicted structure of MZH3-L71H-L31D double mutant	169
Figure 4.9: Transient absorption and SVD analysis of MZH3-L71H-L31D with heme and ZnPCP at pH 9.5	170
Figure 4.10: Transient absorption and SVD analysis of MZH3-L71H with heme, ZnPCP, and 10 μ M FeCl ₂ at pH 7.5	175
Figure 4.11: Summary of transient absorption results in graphical form	177
Figure 4.12: Co(II/III)protoporphyrin IX spectra in MZH3 and myoglobin	182
Figure 5.1: Heme B binds to MZH3 mutants His110Met and His110Ala in vivo	193
Figure 5.2: Spectra of heme B bound to MZH3 mutants His9Lys, His9Cys, and His110Tyr	194
Figure 5.3: Spectroelectrochemical midpoint determination of wild type MZH3 with heme B .	196
Figure 5.4: Midpoint potential of MZH3-His110Ala with heme B	198
Figure 5.5: Ferric, deoxyferrous, carboxyferrous, and oxyferrous spectra	202
Figure 5.6: Autooxidation of oxyferrous heme B in MZH3-His110Ala	203
Figure 5.7: Autooxidation of oxyferrous Fe-DADPIX in MZH3-His110Ala	204
Figure 5.8: Displacement of oxygen ligand by carbon monoxide in MZH3-His110Ala with ferrous heme B	205
Figure 5.9: Oxyferrous state formation in MZH3-His110Ala during anaerobic argon purging ...	206
Figure 5.10: Possible H-bond to O ₂ in oxyferrous MZH3-His110Ala akin to HisE7-O ₂ H-bond of myoglobin	209

Chapter 1: Thesis statement and introduction

Given that nature conducts light driven water oxidation and hydrogenase activities using proteins, we know that *in vivo* enzymatic conversion of water and light to oxygen and hydrogen is possible. Whether it is feasible to engineer a living system that generates large quantities of clean-burning fuel efficiently enough to compete with the price of fossil fuels remains an open question. While it is sometimes taken for granted that an organic system is too susceptible to oxidative damage to be useful in the high potential oxidation of water, an *in vivo* protein system has several unique advantages over other catalysts. For instance, enzymes can create microenvironments with precise interactions that afford lower overpotentials and faster reaction kinetics than chemical reactions in solution. The ability to create these microenvironments precludes the need for non-aqueous solvents and extremes of temperature and pH. Damaged protein can be replaced by a host organism, allowing for “self-healing” capabilities. In addition, natural enzymes demonstrate that difficult high-energy reactions can be catalyzed using inexpensive, Earth-abundant elements. With these advantages, proteins designed for solar-to-fuel energy conversion could become a significant contributor to a future alternative energy economy.

In support of my thesis, I will present the design, characterization, and crystal structure of a highly soluble, thermostable, *de novo* maquette protein that expresses in high yield in *E. coli*, assembles a redox-active cofactor tetrad, and traps a long-lived charge-separated state when exposed to visible light. This represents a first step toward artificial photosynthesis in a protein system. Despite low sequence similarity to natural proteins, this maquette bears

striking structural similarity to natural proteins that were used to guide its design, suggesting that the engineering of some enzymes with sophisticated functions may be more facile than once thought.

1.1 Photosynthesis, natural and artificial

New technologies are needed to increase production of clean-burning, high-energy fuels that can compete economically with fossil fuels to mitigate the environmental impact of climate change and lessen the social and political burden of meeting our energy needs (1-9). Society's energy demands come in different forms, but fuels account for roughly 80% of global energy consumption, and approximately 20% is satisfied by electrical energy (2). Unlike electrical energy, fuel can be readily stored and transported to allow energy to be released on demand, which is one reason why the dominant fraction of our energy needs are met by fossil fuel combustion (6). Electrical energy is generated by numerous alternative energy technologies including photovoltaics, wind turbines, nuclear, and hydropower, but currently, no satisfactory method of generating renewable fuel can be relied upon to supplant fossil fuels (2).

When averaged over a year, photosynthetic organisms convert about 100 TW of solar power into chemical energy (9). For comparison, the combined rate of energy consumption by humans in 2010 was 16.3 TW and is expected to rise to at least 30 TW by 2050 (5, 10), but the total power of sunlight reaching the Earth's surface is about 120,000 TW, making solar the most abundant form of renewable energy (4, 6, 7, 11). The scientific community is looking to the potential of artificial photosynthesis to provide solar fuels on a large scale (1-9). Because of the potentially transformative impact of efficient solar-to-fuel energy conversion, Faunce et al.

argue that, “Developing and globally deploying artificial photosynthesis . . . is one of the great scientific and moral challenges of our time . . .” (1).

1.1.1 Structure and function of photosystem II and its reaction center

An in-depth understanding of photosystem II structure and function will be instrumental in the development of artificial photosynthetic technologies. Photosystem II is nature’s solar powered water oxidase and the only enzyme in biology capable of forming an oxygen-oxygen bond from two water molecules (12). The study of photosystem II is difficult owing to its size, complexity, and fragility. This membrane protein complex resides in the thylakoid membrane in cyanobacteria, algae, and plants, and it can function as either a monomer or a dimer (13). Each monomer has a mass of about 350 kDa depending on the species, and is composed of upwards of 20 subunits and 50 cofactors including chlorophylls, pheophytins, β -carotenes, plastoquinones, hemes, non-heme iron, bicarbonate, chlorides, and a Mn_4CaO_5 oxygen evolving complex (OEC) (14). In addition, an intricate network of channels conduct water, oxygen, and protons to and from the OEC (15).

Despite this complexity, researchers have succeeded in crystallizing photosystem II from thermophilic cyanobacteria *Thermosynechococcus vulcanus* and *Thermosynechococcus elongatus* (14, 16-19). In 2011, the *T. vulcanus* photosystem II was solved to 1.9 Å resolution, a breakthrough that yielded unprecedented insight into the structure-function relationship in the enzyme (14). The overall structure of the photosystem II dimer is shown in the top left of Figure 1.1 (14). Continued progress on elucidation of photosystem II structure comes from recent free-electron laser X-ray crystallography that provides “radiation damage-free” cyanobacterial

structures at cryogenic (20) and room temperature (21), as well as studies of eukaryotic photosystem II complexes using X-ray crystallography (22) and cryo-electron microscopy (23).

While the overall complexity of photosystem II is impressive, the reaction center is conceptually simple (Figure 1.1, right). The reaction center is essentially a string of redox-active cofactors that includes a light absorber in the middle (P680), electron donors on one end (tyrosine Z and the OEC), and electron acceptors on the other end (pheophytin and plastoquinones Q_A and Q_B) (24). When P680 absorbs a photon, it enters a highly reducing singlet excited state (P680*) that has a midpoint potential $E_m(\text{P680}^*/\text{P680}^{*+})$ value between -0.57 and -0.58 V vs SHE, and it initiates an electron transfer cascade (25, 26). Within picoseconds of activation, P680* reduces the nearby pheophytin (Pheo in Figure 1.1), which passes the electron to plastoquinone Q_A on a hundreds of picoseconds timescale. Q_A then reduces Q_B within hundreds of microseconds. When a second photon absorption causes Q_B to be reduced a second time, Q_B dissociates from photosystem II and is replaced by an oxidized quinone from the quinone pool in the thylakoid membrane (24, 27). Meanwhile, on the electron donating side of the reaction center, P680*+, which has an $E_m(\text{P680}/\text{P680}^{*+})$ of 1.25 to 1.26 V (25, 26), oxidizes tyrosine Z, with an $E_m(\text{Y}_Z/\text{Y}_Z^{\cdot+})$ of about 1.2 V (25), within tens of nanoseconds (28-30). This oxidation is followed by slower conformational rearrangement steps around tyrosine Z (31-33), which take tens of microseconds. $\text{Y}_Z^{\cdot+}$, in turn, oxidizes the OEC on a tens of microseconds to milliseconds timescale, depending on the oxidation state of the OEC (34-36). When the OEC is oxidized four times, it oxidizes two water molecules to make O_2 and returns to its initial state. These reaction kinetics are reviewed in more detail in Vinyard et al., 2013 (37). (All midpoint potentials in this thesis are measured against the standard hydrogen electrode (SHE), unless otherwise noted).

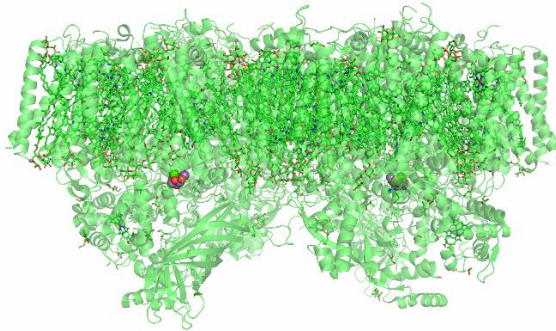
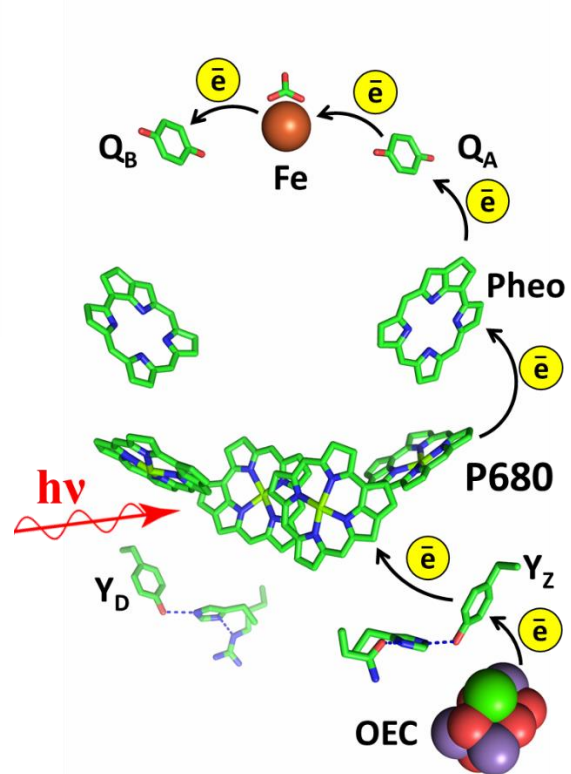


Figure 1.1: Photosystem II crystal structure

Structure at 1.9 Å resolution from (PDB ID: 3WU2) (14). Top left: Overall structure of the photosystem II dimer. The protein backbone is shown as ribbons, organic cofactors are shown as sticks, and the Mn_4CaO_5 oxygen evolving complex (OEC) is shown as spheres. Right: Reaction center of photosystem II showing light absorption and electron transfer pathway. Substituent groups of chlorophylls, pheophytins, and quinones that do not directly participate in electron transfer are removed for clarity.



Images rendered using The PyMOL Molecular Graphics System, Version 1.7 Schrödinger, LLC.

The extreme potentials necessary for water oxidation are dangerous in an organic scaffold such as a protein. Water oxidation in a protein has been likened to “setting a fire in a wicker basket, without burning the basket” (38). However, photosynthetic organisms are able to manage the risk. Replacement of the D1 polypeptide that houses the OEC occurs as frequently as every 30 minutes in full sunlight due to oxidative damage (39).

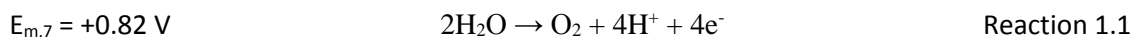
One peculiarity of the photosystem II reaction center is the nature of P680, the light-absorbing pigment. P680 consists of four weakly coupled monomeric chlorophyll *a* molecules. In the excited singlet P680* state, the excitation energy is delocalized across the chlorophylls. The special properties of the P680 chlorophylls give them exceedingly high midpoint potentials

and cause their absorbance spectra to shift to longer wavelengths. Typical antenna chlorophylls have an absorbance peak in the range of 670 to 675 nm and use energy transfer to pass photon energy to the reaction center, but in P680, this absorbance peak shifts to 680 nm. This red shift creates an “exciton trap” that is unable to transfer energy from P680* to other chlorophylls in photosystem II, because the other chlorophylls absorb higher energy light (40). The unusual association of the four chlorophylls of P680 does not necessarily need to be reproduced in order to create a working reaction center.

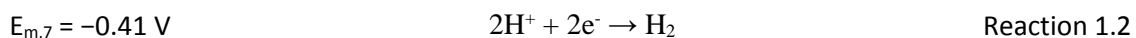
Despite detailed knowledge of photosystem II structure from high-resolution structures and decades of intense research, many important facets of photosystem II function remain elusive. As with any complex natural protein, different parts of photosystem II have interconnected and overlapping functions (41). Practical limitations have often lead researchers to make compromises such as conducting experimental studies on tyrosine Z using photosystem II in its manganese-depleted form, even though it is well known that manganese depletion affects the properties of tyrosine Z (32, 42, 43). As a result, the unraveling of mechanistic details of photosystem II has been painstaking. Debates continue with regard to the proton transfer pathway of tyrosine Z, the function of tyrosine D, the steps of the photoactivation process that assembles the OEC, the mechanism of water oxidation at the OEC, and even which water molecules and/or hydroxide/oxide ligands are the substrates of the oxygen evolving reaction (21, 31, 44-46). These shortfalls open the door to model systems to pave the way toward a deeper understanding of photosystem II functions.

1.1.2 Photosynthetic reactions and the potential for improvement

By developing the ability to extract electrons from water as a widely available substrate, the advent of oxygenic photosystem II roughly 2.5 billion years ago gave way to a “big bang of evolution” and a new age of abundant life under an oxidizing atmosphere (9, 24, 44). Electrons and protons abstracted from water could be used to convert a substrate (carbon dioxide) to a fuel (carbohydrates). The four-electron oxidation of water requires an energy input equivalent to 0.82 V vs. SHE per electron at pH 7 (47). The water oxidation half reaction of photosystem II is catalyzed upon absorption of four photons and is given below in Reaction 1.1:



In oxygenic photosynthetic organisms (plants, algae, and cyanobacteria), the second half reaction is the reduction of carbon dioxide to make carbohydrates (24). In place of carbohydrates, artificial photosynthesis seeks to produce a high energy density fuel such as hydrogen. In this case, the protons and electrons released by water oxidation could be combined, as shown in Reaction 1.2:



All oxygenic photosynthetic organisms use two separate photosystems in the oxidation of water and reduction of carbon dioxide (48). Photosystem II carries out water oxidation, while photosystem I generates NADPH to drive the carbon dioxide fixation process (9). In theory, however, only a single photosystem is necessary. The energy gap between the water oxidizing half reaction at 0.82 V (Reaction 1) and the proton reducing half reaction at -0.41 V (Reaction 2) is 1.23 eV, which is ~67% of the energy of the 680 nm (1.8 eV) photon used by P680 to enter the excited state and begin charge separation in photosystem II. This shows that photosynthetic

water oxidation and hydrogen evolution could conceivably be conducted using only a single photosystem (3). Figure 1.2 illustrates that the two half reactions fall within the range of potentials used in photosystem II. Some of the initial photon energy will need to be used to stabilize the charge separated state and allow for catalysis, but in principle, a second photosystem is not required; there is enough energy in a single photon to be used for evolution of both oxygen and hydrogen in the same reaction center. To do this, however, would require a new reaction center with inter-cofactor distances and potentials optimized to facilitate energy conversion.

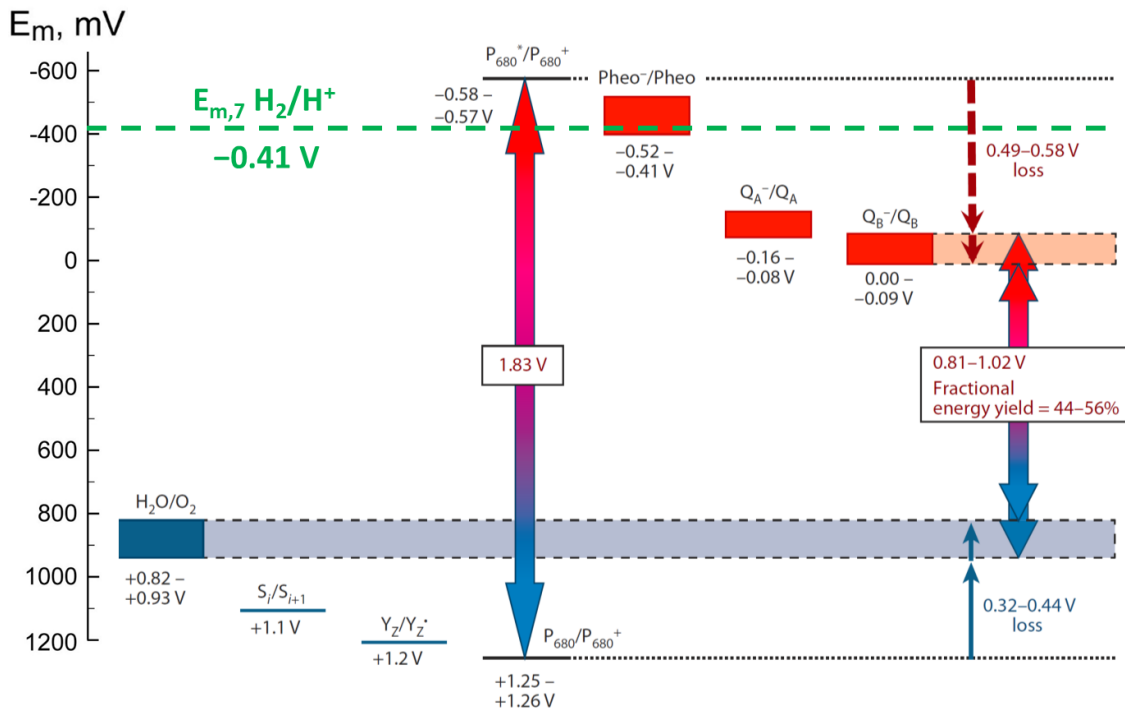


Figure 1.2: Energy diagram of photosystem II

Cofactors in the photosystem II reaction center are placed according to the scale on the left. Potentials are measured against SHE. The blue box represents the potential range where water oxidation occurs (Reaction 1), and the green dotted line represents the potential of the hydrogen evolution half reaction (Reaction 2). Modified from Vinyard, et al., 2013 (37).

1.1.3 The oxygen evolving complex (OEC) of photosystem II

In photosystem II, the water oxidation half reaction (Reaction 1.1) is catalyzed at the oxygen evolving complex (OEC), a Mn_4Ca oxo-bridged cubane-like structure (14). The OEC is the terminal cofactor on the electron donating end of the photosystem II reaction center. With each photon absorption, the OEC is progressively oxidized through the S-state cycle (Kok cycle) from S_0 (most reduced) to S_4 (most oxidized). At S_4 , the OEC converts two water molecules to dioxygen and returns to the reduced S_0 state (44, 49). In this way, the OEC couples the sequential one-electron reactions of the reaction center to the four-electron reaction of water oxidation by storing oxidizing equivalents until the OEC is oxidized four times.

The OEC catalyzes one of the most difficult reactions in biology with a low overpotential, high turnover frequency, and high turnover number and uses only Earth-abundant metals (12, 50). However, the structure of the OEC does not need to be reproduced exactly in order to achieve water oxidation. The catalyst remains functional if the calcium ion is replaced by strontium (51, 52), and most of the highly conserved amino acid ligands of the OEC can be removed by mutation without abolishing water oxidation (although the rate of the reaction is usually decreased) (44). Some small molecule manganese-containing mimics of the OEC have been shown to be capable of oxygen evolution (53-55), and various metal oxides have been used as heterogeneous water oxidation catalysts including manganese, cobalt, ruthenium, and iridium oxides (56). While iridium and ruthenium complexes can be used for impressive water oxidation activity (57, 58), the low abundance of these elements means that they are not useful as fuel generating catalysts in the long run. The Nocera group has reported a film for heterogeneous water oxidation composed of Earth-abundant cobalt oxide (59, 60). These

studies show that many different oxo-bridged metal compounds can be useful for water oxidation.

1.1.4 Photoassembly of the oxygen evolving complex (OEC)

The Mn_4Ca OEC cluster is not chemically stable when released from its binding site in photosystem II (37), and it must be assembled in place by a process known as photoactivation (61). During photoactivation, manganese ions (initially in the Mn(II) state) are oxidized using the same process of light-driven charge separation that the reaction center uses for normal water oxidation activity. It may seem counterintuitive that increasing the charge of the manganese ions would help bring them together in the OEC, but manganese oxidation is accompanied by proton release from Mn-ligating water and hydroxide ligands, exposing negatively charged oxygens that are capable of forming additional ligands to create bridging μ -hydroxo or μ -oxo ligands to multiple manganese ions (45). In the photoactivated state, five μ -oxo bridges bind the manganese and calcium ions together in the fully assembled OEC (14).

Photoactivation begins with the binding of a single Mn(II) ion to the OEC site in photosystem II with a dissociation constant of ~ 40 - $50 \mu M$ (45, 62). The Mn(II) ion is believed to bear a water ligand, and oxidation to Mn(III) by Y_z^* causes a charge-compensating release of a proton, allowing the ligating hydroxide anion to form a bridging ligation to a second metal ion (45, 62). A second oxidation event leads to a more stable state, and the cluster continues to iteratively reduce Y_z^* , release protons, and bind additional metal ions until the cluster is fully assembled, as illustrated in Figure 1.3 (45, 63).

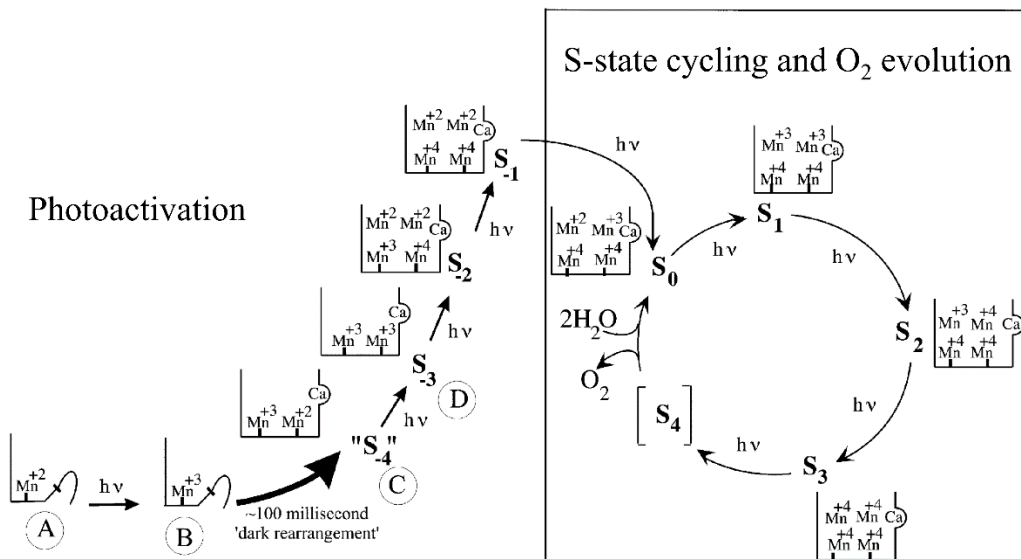


Figure 1.3: Photoactivation of the oxygen evolving complex

Left: OEC photoassembly process prepares the metal cluster for the oxygen evolving reaction. Right: Photoactivated OEC is competent for water oxidation (Reaction 1.1), and proceeds through the S-state cycle (Kok cycle). Figure adapted from Burnap, 2004 (63).

Ca(II) binds to the photoassembling OEC in the early steps of photoactivation and is required for proper formation of the Mn_4Ca cluster. In the absence of Ca(II), a runaway photoassembly of oxidized manganese ions takes place, building up to 5-10 manganese ions per photosystem II (64). The resulting cluster is not a functional OEC, but the fact that photoassembly proceeds without calcium suggests that it might be possible to engineer a similar photoassembly mechanism in a simpler protein system that is able to trap a charge separated state and bind metal ions. This would afford a path toward building an OEC in a new protein designed for artificial photosynthesis.

1.1.5 Redox active tyrosines of photosystem II: Y_D and Y_Z

In the *de novo* design of a reaction center protein, tyrosine has the supreme advantage of being a covalently attached amino acid cofactor; a specialized binding site is not needed to

pluck the cofactor out of solution and hold onto it tightly. High affinity cofactor binding sites can be difficult to engineer in *de novo* proteins, and a non-covalently bound cofactor in an *in vivo* system may require a separate cofactor production pathway to generate stoichiometric quantities of cofactor. In addition, tyrosine has a high midpoint potential, and photosystem II demonstrates the applicability of tyrosine redox reactions to water oxidation.

The oxidation and reduction of tyrosine at neutral pH is a proton coupled electron transfer (PCET) reaction. This is because the pK_a of tyrosine changes dramatically from ~ 10 in the reduced state to ~ -2 when oxidized (65, 66).

There are two redox active tyrosine residues in photosystem II, Y_z (D1-Tyr161) and Y_D (D2-Tyr160) that have symmetrically-related positions in the homologous D1 and D2 polypeptides (see Figure 1.1, right). Both of these tyrosines can participate in light-activated electron transfer reactions, are universally conserved, and lie within 9.0 to 9.3 Å of P680 according to recent crystal structures (14, 20, 21). However, only one of them, Y_z , is critical to the function of photosystem II, as Y_D is not required for water oxidation (46, 67, 68). Y_z plays an instrumental role as it directly reduces P680⁺⁺ and directly oxidizes the OEC during normal oxygen evolving activity (46).

Despite their analogous positions in homologous polypeptides, Y_z and Y_D have very different oxidation/reduction kinetics, midpoint potentials, and local environments. Tyrosine Z is a powerful oxidant, with a midpoint potential of 1.2 V (25), significantly higher than the 700-800 mV potential of Y_D (69). In the fully operational photosystem II, Y_z is oxidized by P680⁺⁺ through a PCET reaction that takes tens of nanoseconds (28, 29), exhibits no deuterium isotope effect on the kinetics (30), and is rate-limited by electron transfer (70). It has been speculated that the oxidation of Y_z by P680⁺⁺, which must involve a proton transfer that takes less than 20

ns, might be the fastest PCET reaction in nature (46). Reduction of Y_Z^\bullet by the OEC takes longer, up to 1.4 ms, depending on the S-state of the OEC (34-36). Y_D is also capable of fast reduction of $P680^{++}$ on the nanoseconds timescale (71), but reduction of Y_D^\bullet takes all day; the Y_D^\bullet radical is highly stable and remains in the oxidized state during illumination, only going reduced again when it oxidizes the OEC from the S_0 to the S_1 state after hours in the dark (46, 69, 72).

These differences in the driving forces and kinetics of Y_Z and Y_D PCET reactions can be attributed to the local environments of the residues. Y_D is located in a hydrophobic pocket that might restrict its ability to become protonated once oxidized, while Y_Z is positioned near the opening of a solvent channel that leads to the thylakoid lumen and is surrounded by water in an extensive hydrogen-bonding network that connects it to the OEC (14). Both Y_Z and Y_D make hydrogen bonds to nearby histidines that are important for modulating electron transfer function (14). D1-His190 (His-Z), which hydrogen bonds Y_Z using its imidazole N_ϵ atom, donates a second hydrogen bond to an asparagine oxygen with the N_δ atom. In contrast, D2-H189 (His-D), which hydrogen bonds Y_D with its N_ϵ atom, accepts a hydrogen bond from an arginine N-H group at the imidazole N_δ atom (Figure 1.4) (14).

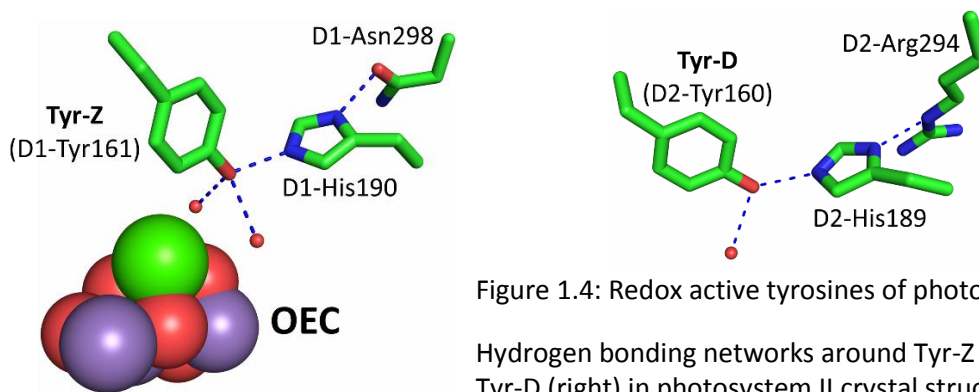


Figure 1.4: Redox active tyrosines of photosystem II

Hydrogen bonding networks around Tyr-Z (left) and Tyr-D (right) in photosystem II crystal structure (PDB ID: 3WU2) (14). Images rendered using The PyMOL Molecular Graphics System, Version 1.7 Schrödinger, LLC.

Upon oxidation, Y_Z is known to pass its proton to His-Z (32, 33, 42, 43, 46, 73). This proton transfer might be promoted by the conserved residue D1-Asn298, which accepts a hydrogen bond from the N_{δ} -H group of His-Z, thereby stabilizing the protonated form of the His-Z N_{δ} atom (14, 42, 43, 74). If the His-Z N_{δ} atom is protonated, then the neutral form of His-Z must accept a hydrogen bond from Y_Z . In this way, D1-Asn298 might force His-Z into a protonation state that is capable of accepting a proton from Y_Z when Y_Z becomes oxidized (see Figure 1.4, left). An exhaustive mutagenesis study of D1-Asn298 showed that all 19 possible mutations of D1-Asn298 resulted in either total abolition of oxygen evolving activity or a significantly decreased rate of oxygen evolution combined with a marked increase in photosensitivity (74). This supports the hypothesis that D1-Asn298 plays an important role in the electron transfer pathway of the photosystem II reaction center.

Although it has been suggested that Y_D similarly donates its proton to His-D upon oxidation to Y_D^{\bullet} (46, 69), it seems that the arginine would prevent this from happening, because the neutral state of His-D must accept a hydrogen bond from D2-Arg294, meaning that its N_{ϵ} atom is protonated and donating a hydrogen bond to the Y_D phenolic oxygen; the His-D state in the crystal structure is not competent to accept a proton from Y_D (see Figure 1.4, right) (14). Indeed, a study by Nakamura et al., 2014 provides evidence by Fourier transform infrared spectroscopy that His-Z accepts a proton when Y_Z is oxidized, but Y_D oxidation leads to proton release into a hydrogen bonding network around Y_D rather than protonation of His-D (43). This supports the hypothesis that the water molecule that hydrogen bonds Y_D in Figure 1.4 (right) is the likely proton donor and acceptor in Y_D PCET reactions, and not His-D. This water molecule only has partial occupancy in some crystal structures and is absent from others (14, 20, 21); the absence of a proton donor might restrict PCET reaction rates of Y_D and help give rise to its

observed hours-timescale stability in the oxidized state (46, 69, 72). Regardless of the precise mechanisms of proton transfer, the distal hydrogen bonds of D1-Asn298 to D1-His190 and D2-Arg294 to D2-His189 appear to play important roles in dictating PCET reaction rates of Y_Z and Y_D . Therefore, a model system involving tyrosine oxidation and reduction should use an extended hydrogen bonding network to modulate PCET properties of the tyrosine.

1.1.6 Functions of Y_D and Y_Z

When considering how to build a new reaction center for artificial photosynthesis, it is constructive to examine the purpose of including Y_D and Y_Z in photosystem II. Y_D is not necessary for oxygen-evolving activity, but it is completely conserved (46, 67, 68). No single function of Y_D stands out as obviously necessary, but some important roles have been identified. The ability of Y_D to store an oxidizing equivalent for extended periods (75) supports photoassembly of the OEC (76). In addition, if $P680^{++}$ formation outpaces S-state cycling, or if the OEC is not assembled, Y_D can reduce $P680^{++}$ and prevent a damaging side reaction (71, 77).

In contrast to Y_D , Y_Z is essential to water oxidation in photosystem II, and it serves as an intermediate electron donor between the OEC and P680 (46). Since Y_Z bridges the gap between the OEC and P680, Y_Z allows the OEC to be positioned further from P680 than it would otherwise need to be for rapid electron transfer. The distance between cofactors decreases electron transfer rates by a factor of 10 for every additional ~ 1.6 Å of distance (78, 79), so the extension of the P680-OEC distance by Y_Z may inhibit reduction of the OEC by $P680^*$. Furthermore, the increased distance may decrease quenching of the $P680^*$ excited state by manganese ions of the OEC (80). Another function of Y_Z is to quickly reduce $P680^{++}$ on a nanoseconds timescale (28-30), which helps avoid short circuiting charge recombination and damaging side reactions. The

OEC undergoes relatively slow structural reorganization steps between different S-states that result in electron transfer rates as slow as milliseconds (34-36); if P680⁺⁺ routinely persisted for milliseconds, the turnover number and quantum yield of photosystem II would be greatly diminished. As a result, Y_z couples the fast initial charge separation events to the slower S-state cycling of the OEC. In addition, the proton coupling of Y_z oxidation and reduction might serve to raise the activation energy barrier to charge recombination (81, 82).

The hydrogen abstraction model of Y_z function offers another possible function (65, 83, 84). In this model, the reduction of the deprotonated Y_z[•] radical occurs with concomitant protonation by a water molecule in the hydrogen bonding network that connects Y_z to the OEC. In this way, Y_z might help to extract protons from substrate water molecules to facilitate water oxidation and deliver protons to a solvent channel. Alternatively, the proton rocking model argues that Y_z[•] receives its proton from His-Z upon reduction and does not participate in proton transfer with the surrounding water (85-87). Y_z does not necessarily behave the same way in every S-state transition (46), and it has been suggested that hydrogen abstraction may occur between some S-state transitions, such as S₂ to S₃, but that proton rocking may be used in others (43).

A simplified reaction center protein may benefit from the use of a tyrosine residue for extension of the distance between the pigment and metal cluster, rapid reduction of the pigment radical cation, and raising the energy barrier to charge recombination by coupling electron transfer to proton transfer. Hydrogen abstraction is probably too advanced for a small, simple protein, especially if the metal binding site is exposed to bulk solvent.

1.1.7 Tyrosine Z model systems

Many different molecular mimics of Y_z have been produced to probe mechanistic details of tyrosine PCET reactions, investigate whether the Y_z to His-Z proton transfer can be reproduced easily, and begin developing bio-inspired artificial photosynthetic units. In one example, the Hammarström group synthesized a series of four different Y_z mimics in which a phenolic proton made a hydrogen bond to a benzimidazolyl or pyridyl group, and light driven phenol oxidation was carried out by an attached ruthenium tris-bipyridine moiety (88). This study showed nearly a 1000-fold decrease in the phenol oxidation rate for every ~ 0.2 Å increase in hydrogen bond length. Evidently, hydrogen bond lengths play an important role in PCET rates, which helps explain the short hydrogen bond between Y_z and His-Z of about 2.5 Å and the fast PCET reduction of $P680^{++}$ by Y_z in tens of nanoseconds (14, 20, 21, 28-30, 42, 46).

The Moore group and collaborators have developed small molecule mimics of Y_z and Y_D using hydrogen bonding phenol-benzimidazole pairs with the goal of developing an artificial photosynthetic unit. They showed that the irreversible oxidation of a phenol lacking a hydrogen bond in aprotic solvent can be made reversible by creating a hydrogen bond to a benzimidazole. The reversibility was attributed to the proton being able to shuttle between the phenol and benzimidazole groups depending on the oxidation state, instead of being lost to the solvent upon phenol oxidation (89). This proton shuttling is reminiscent of the proton rocking mechanism proposed for Y_z oxidation and reduction in photosystem II (85-87). In another mimic of Y_z and Y_D , the Moore group showed that low temperature phenol oxidation at 13 K led to an intermediate radical state that was only able to donate its proton to the benzimidazole when warmed to 100 K (90). This is very similar to the behavior of Y_D , which was shown to be trapped in an intermediate at 1.8 K that relaxed with a proton transfer at 77 K (81). The phenol-

benzimidazole pair was incorporated into a redox triad to trap a charge separated state. Using a di-pentafluorophenyl porphyrin as the pigment, the phenol-benzimidazole as the electron donor, and a tetracyanoporphyrin as the electron acceptor, the triad was able to convert light energy to a charge separated state that persisted for 3.8 μs (82). This short lifetime isn't long enough to support water oxidation chemistry, which takes milliseconds in photosystem II (34-36, 50), but it approaches the longest recorded charge separation lifetime in a synthetic triad of 34 μs (91). Small molecule tetrads can trap a charge separated state for much longer, but they must be frozen or embedded in nanoparticles to prevent intermolecular charge recombination, and their synthesis is extremely costly and time-consuming (92, 93).

The synthetic complexity and intermolecular charge recombination limitations of small molecules can be avoided through the use of proteins. Proteins can protect redox centers from recombination by shielding them in the hydrophobic core, and sometimes they can be expressed in high yield in bacteria. The Barry group and collaborators synthesized a β -hairpin peptide to study tyrosine oxidation in the presence and absence of a nearby histidine. The histidine was shown to accelerate tyrosine oxidation at pH 9, but not pH 11, consistent with PCET facilitated by the histidine. While the histidine was shown not to make a hydrogen bond to the tyrosine or affect the tyrosine pK_a , it was speculated that a proton could be passed from the oxidized tyrosine to the histidine through hydrogen bonding water molecules (94, 95). The Tommos group and collaborators designed a three-helix bundle protein to study tyrosine oxidation (96). The protein was expressible in *E. coli*, and the deeply buried tyrosyl radical was highly stable for seconds when oxidized photochemically (97). The reversibility of the tyrosine oxidation allowed detailed study of midpoint potentials (0.92 V at pH 8.4 and 1.07 V at pH 5.5) (98), and insertion of histidines in different positions was shown to modulate tyrosine

fluorescence (99). However, as with the Barry β -hairpin peptide, no conclusive evidence of a His-Tyr hydrogen bond was found.

These model systems have advanced our understanding of tyrosine oxidation and the influence of hydrogen bonds. Small molecules have reproduced the phenol-imidazole hydrogen bonds of photosystem II and demonstrated their power in influencing PCET reactions, but direct tyrosine-histidine hydrogen bonds have not been inserted into protein frameworks, and no model system has produced an extended hydrogen bonding network such as the tyrosine-histidine-asparagine network involving Y_z . If a protein could be tailored to exert precise control over tyrosine PCET reactions, a tyrosine residue might be a useful electron donor in a *de novo* designed reaction center protein for artificial photosynthesis.

1.1.8 Hydrogen evolution in artificial photosynthesis

The reducing end of a reaction center protein designed for artificial photosynthesis needs to include an active site that can reduce a substrate to make fuel such as hydrogen, as in Reaction 1.2. Natural hydrogenase enzymes demonstrate the feasibility of this approach; they exhibit efficient, reversible proton reduction with low overpotentials at neutral pH using Earth-abundant elements including nickel and iron (100). A molecular mimic of the hydrogen evolving cofactor of [Fe-Fe] hydrogenases has been shown to be capable of proton reduction activity when incorporated into different natural protein scaffolds (101-103).

Another method of generating hydrogen in a protein framework involves the use of cobalt tetrapyrroles, which have been shown to be capable of hydrogen evolution in electrocatalytic and photocatalytic systems (104, 105). Recent work has demonstrated that hydrogen production may be attainable in natural tetrapyrrole-binding proteins with modified

cofactors, such as a cobinamide cofactor in ethanolamine ammonia lyase (106) or a cobalt protoporphyrin IX cofactor in cytochrome b_{562} (107) or myoglobin (108). Proton reduction may proceed from either the Co(I) or Co(0) state of a cobalt porphyrin (109). Midpoint potentials of cobalt protoporphyrin IX in myoglobin have been reported with $E_m(\text{Co(III)Mb/Co(II)Mb})$ of 100 mV (110) and $E_m(\text{Co(II)Mb/Co(I)Mb})$ of -610 mV vs SHE (111). Unfortunately, Co(III) protoporphyrin IX reduction to the Co(II) state in proteins is slow (110-112), which may mean that a structural rearrangement occurs in the transition. However, it may be possible to adapt the local environment of the cofactor in order to facilitate faster electron transfer.

1.1.9 Reengineering natural proteins for artificial photosynthesis

One approach to artificial photosynthesis is to reengineer natural proteins with the aim of exploiting solar energy to drive proton reduction and water oxidation. For example, multiple groups have directly coupled photosystem I to a cobalt catalyst or a [Ni-Fe] or [Fe-Fe] hydrogenase in order to generate solar hydrogen (113-116). This demonstrates the feasibility of solar-to-hydrogen energy conversion in a biological system; photosystem II and the modified photosystem I could work together *in vivo* to produce hydrogen and oxygen from sunlight and water. An *in vivo* system allows for the possibility of a self-repairing mechanism in which the cell replaces protein as it becomes damaged.

However, reengineering of a photosystem I-hydrogenase complex would probably have to be done without the aid of high resolution structural characterization, because this complex is too big for NMR and crystallography would be extremely difficult. Without a precise understanding of how changes to the system improve or inactivate function, progress may not yield insights into the inner workings of the photosynthetic machinery or how best to develop

an artificial photosynthetic system. In addition, repurposing such large, complicated, and delicate proteins for a new function is no simple task. Moreover, as explained in section 1.1.2, natural photosynthetic efficiency is not as high as it could be. The efficiency of photosynthesis could be increased by covering the solar spectrum with different pigments, or by integrating both the water oxidizing and fuel generating half reactions into a single photosystem (3).

A natural reaction center protein that is not involved in oxygenic photosynthesis was reengineered by Allen, Williams, and colleagues. In this body of work, a bacterial reaction center was modified for tyrosine oxidation (117) and manganese(II) oxidation (118). The Mn-bound complex was structurally characterized by X-ray crystallography (119), and has even been used as a light-driven superoxide dismutase to convert superoxide to oxygen (120).

In another example of protein reengineering to build a reaction center, the Wydrzynski group modified the natural four-helix bundle protein bacterioferritin to bind the light-activatable zinc chlorin e_6 ($ZnCe_6$) in place of the natural cofactor heme B. The modified bacterioferritin was assembled with manganese instead of the natural iron cofactor. Under illumination, $ZnCe_6$ photo-oxidized Mn(II) to Mn(III), and three nearby tyrosine residues were found to participate in electron transfer (121-123). However, no electron acceptor was incorporated into the modified bacterioferritin reaction center, so it is unclear how the excited state of $ZnCe_6$ became oxidized.

These successes pave the way for the design of other reaction centers from scratch. When the protein scaffold is designed *de novo*, the designer has more control over the parameters that govern electron transfer rates. In order to avoid the complexities of natural proteins, the Dutton group has produced a series of *de novo* designed protein maquettes. In one example, the maquette BT6 was used for light-driven electron transfer from a zinc

tetrapyrrole to a heme B. However, because the maquette lacked an electron donor such as a metal ion or a tyrosine residue, the charge separated state could not be trapped; the reduced state of the electron acceptor was only observed when a sacrificial electron donor was introduced into the system (124). In order to improve upon this result, this thesis is aimed at stabilizing a charge separated state in a new maquette that extends the electron transfer chain so that it includes a tyrosine residue and a metal center akin to the donor side of the photosystem II reaction center. The next section will outline the design rules for four-helix bundles with a focus on the goal of building a new reaction center protein for artificial photosynthesis.

1.2 Four-helix bundle design

The field of *de novo* protein design, that is, protein design from first principles, has progressed steadily since its inception in the 1980s. Today, basic design rules for four helix bundles are firmly established. A protein designer who is well versed in the literature can readily produce an amino acid sequence with a high likelihood of folding into a stable four helix bundle. Ensuring a singular structure, however, requires some finesse, and imparting a high-level function to a *de novo* designed protein remains a challenge (125).

Four-helix bundles are very common in nature, and they perform a wide variety of functions: electron transfer using heme (cytochromes b (126), b₆ (127), b₅₆₂ (128), C' (129), bacterioferritin (130)), redox chemistry of carboxylate-bridged diiron and dimanganese proteins (ribonucleotide reductase (131), alternative oxidase (132), methane monooxygenase (133), bacterioferritin (130)), signaling (cytokines (134), growth hormone (135)), and protein oligomerization (Lac repressor) (136). All of these four-helix bundle examples have an

antiparallel helical topology, meaning that each helix is oriented antiparallel to its two adjacent helices and parallel to the one diagonally across the bundle on the other side. The abundance of antiparallel four-helix bundles in nature attests to the “designability” of this protein fold (137, 138).

Extensive work has been done on designed four-helix bundle proteins that bind heme and other tetrapyrroles (112, 124, 139-144). Heme is one of the most common and most versatile cofactors in nature, with functions that include quinone oxidation and reduction (redox) activity (cytochrome bc_1 complex) (145), electron transport (cytochrome c) (146), small molecule binding (guanylate cyclase, myoglobin) (147, 148), and carbon hydroxylation (cytochrome P450) (149). The field of *de novo* protein design has produced many proteins that can bind different tetrapyrroles like heme and use them for an impressive array of functions, but *de novo* proteins seldom rival the catalytic performance of their natural counterparts (125), and despite our progress, no high-resolution structure of a *de novo* designed protein with a tetrapyrrole cofactor has yet been solved. This limits our understanding of the structure-function relationship and makes it all the more difficult to engineer proteins with sophisticated functions.

Much of the background presented in this section was instructive in the creation of MZH3, whose design and characterization is the focus of this thesis. MZH3 was designed for high affinity binding of heme B, a zinc tetrapyrrole, and a di-metal center in an antiparallel four-helix bundle in order to absorb light and separate charge.

1.2.1 Introduction to protein maquettes

A protein maquette is a *de novo* designed functional protein that avoids reference to natural protein sequences and is minimalistic in the complexity of its design (41). Four-helix bundle maquettes use basic principles of binary patterning of polar and nonpolar amino acids to produce robust protein folds that can tolerate successive iterations of redesign without significant loss of secondary or tertiary structure (150, 151).

Four-helix bundle protein scaffolds are well suited for the design of an electron transport chain. Their elongated rod-like structure enforces a linear arrangement of the cofactors, which works in favor of charge separation, because it maximizes the distance between the electron donating and accepting ends of the maquette, thereby limiting intra-protein recombination of electrons and holes. Inter-protein collisional recombination is also restricted because cofactors are insulated within the protein frame, which prevents close contact between redox centers from different maquettes. The medium between cofactors is a dry, nonpolar core that facilitates efficient electron transfer by ensuring a low reorganization energy despite being surrounded by aqueous solvent. A coiled coil platform also allows for modularity of design. Modifying one cofactor binding site to bind a different type of cofactor typically has minimal effects on the properties of the other cofactors and the overall maquette structure (124). Distances between cofactors can be adjusted in quantized steps of 1 α -helical turn (about 5 Å) to maximize charge separation efficiency. Furthermore, while addition of cofactors to a pre-existing globular protein would typically necessitate a difficult redesign, a helical bundle can often accommodate more cofactors by a simple extension of each helix (152), and increasing the length tends to stabilize the fold (153).

Some maquettes can bind iron tetrapyrroles and zinc tetrapyrroles with high affinity. Iron tetrapyrroles are stabilized by hexacoordinate ligation of the iron ion; they prefer two axial ligands, usually histidine. Zinc tetrapyrroles, in contrast, prefer a pentacoordinate zinc ion that only requires one axial histidine (144). The special advantage of a zinc tetrapyrrole is that, like chlorophyll in photosynthetic proteins, it can absorb light to enter a high-energy excited state that is a strong reductant. Once oxidized, the zinc tetrapyrrole radical cation is a powerful oxidizing agent. If cofactors are arranged favorably, as they are in photosystem II, light activation can lead to electron transfer and trapping of the charge separated state. While maquettes that bind zinc and iron tetrapyrroles have been made to catalyze light-driven electron transfer (124), none can stabilize a charge-separated state for long enough to catalyze chemical reactions for solar energy conversion. To do so efficiently would require at least three cofactors: an electron acceptor, a pigment, and an electron donor.

Unfortunately, no high-resolution structures of tetrapyrrole binding maquettes have yet been reported in holo-state, although apo-state structures of *de novo* proteins do exist (154-157). Some tetrapyrrole binding maquettes from the Dutton laboratory have been shown to fold into an unusual mixed

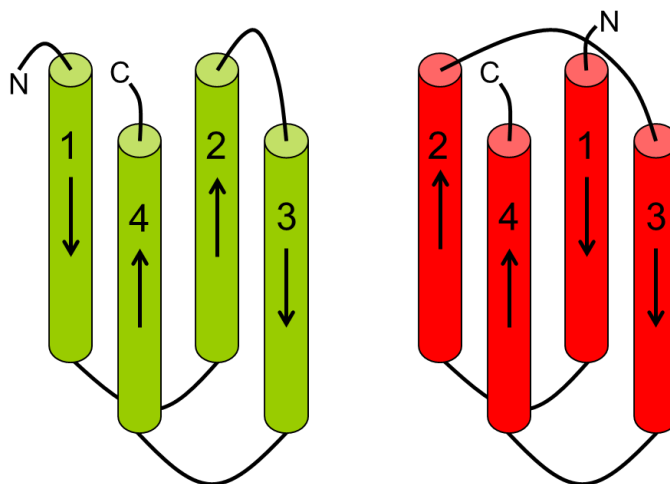


Figure 1.5: Four-helix bundle topologies

Antiparallel (left, in green), and parallel/antiparallel (right, in red) helix threading topologies. Helices are represented as cylinders with arrows pointing from N- to C-terminus. Antiparallel four-helix bundles are more common in nature.

parallel/antiparallel topology (Figure 1.5, right) rather than the more common antiparallel topology (Figure 1.5, left) (150, 154). Heme binding is accompanied by a significant structural rearrangement in which the helices rotate to ligate the heme and bury some polar groups in the process (158). Without high-resolution structures in the active holo-state, the structure-function relationship remains uncertain, and it is unclear what mutations might lead to improved function. This limits the effectiveness of the iterative redesign approach to maquette development, which is one of the prime selling points of the technique.

1.2.2 Coiled coils

In a low-energy conformation, an α -helix has approximately 3.6 residues per turn, but in coiled coils, α -helices twist together like a rope, creating a left-handed supercoil that lowers the periodicity of the right-handed α -helices to 3.5 residues per turn (150). This high-affinity wrapping of the helices is driven by “knob-into-hole” interactions, first predicted by Francis Crick, in which amino acid side chains (the knobs) pack into spaces between side chains on adjacent helices (the holes) (159). With only 3.5 amino acids per turn, a repeating unit is completed every two turns, or seven residues. This means that α -helical folds can be stabilized by a binary pattern of polar and hydrophobic amino acids arranged into repeating heptads, as demonstrated by a large library of designed proteins that follow the heptad repeat pattern (160). Following the convention set by McLachlan and Stewart (161), the seven positions in the heptad are designated *a* through *g*, where positions *a* and *d* are the most buried, *e* and *g* are interfacial, and *b*, *c*, and *f* are located on the exterior. Natural coiled coils do not always follow these coiled coil guidelines perfectly. Occasionally coiled coils have “stutters” or “skips” in the heptad pattern that can be compensated by local structural distortions; sometimes the

distinction between a coiled coils and other structures with helix-helix interactions cannot be made unambiguously (162, 163).

A common example of a dimeric coiled coil found in nature is the leucine zipper, which contains highly-conserved leucines in most *d*-positions (164). Leucine zippers provided an early platform for exploring the fundamental design rules that govern coiled coil structure.

Mutagenesis studies on leucine zippers showed that the preference of a particular heptad repeat sequence to fold as a 2-, 3-, or 4-helix coiled coil is sometimes difficult to predict, as even volume-conserving mutations from Leu to Ile at *α*- and *d*-positions in leucine zippers can result in dramatic switches between oligomerization states or between native-like and molten globular states, as observed in the classic example of GCN4 (165). For this reason, accurate prediction of coiled coil folding generally requires a broader consideration of inter-helical interactions in different possible structures. In particular, a wider surface on each helix becomes buried in a four-helix bundle compared to a two-stranded coiled coil, which means that interfacial residues can play a key role in dictating the fold. The role of interfacial residues is demonstrated in studies of various coiled coil mutants in which charged amino acids at *e*- and *g*-positions favor a two-stranded coiled coil, whereas nonpolar amino acids such as alanine at *e*- and *g*-positions stabilize four-helix bundles (166, 167).

1.2.3 Layers of hydrophobic amino acids in the core

Complementary core packing is a hallmark of native-like, uniquely-structured proteins, and the hydrophobic effect is usually the most important driving force in protein folding (168). However, hydrophobic contacts can be difficult to design, and inadequate core packing can easily lead to a molten globular fold if there is not a large enough free energy gap between the

native and non-native folded states relative to thermal energy, $k_B T$ (138, 169). In antiparallel four-helix bundles, core a - and d -position side chains can be thought of as forming “layers” where each layer consists of two a - and two d -position hydrophobic residues, with each helix contributing one residue to each layer (Figure 1.6) (170-172). Complementarity of packing is maximized when each layer has roughly the same total volume so that helices are not pushed apart to create pockets that destabilize the protein by decreasing van der Waals contact and possibly even allowing water to penetrate into the core. The crystal structure of the antiparallel four-helix bundle Rop provides a clear example of layers that has been used to guide *de novo* protein design (170, 171, 173, 174). When core d -positions are consistently large and core a -positions are consistently small, a regular packing arrangement facilitates good van der Waals contact between hydrophobic side chains (168).

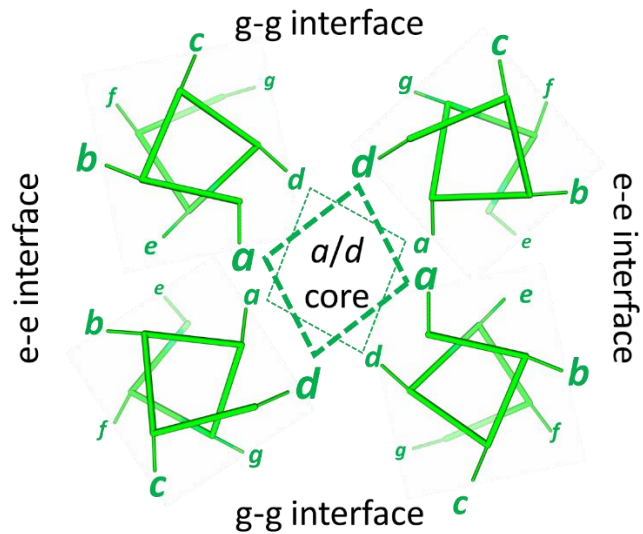


Figure 1.6: Helical wheel diagram

One heptad of an antiparallel four-helix bundle protein. The distance of an amino acid from the view is represented by the size of the heptad letter designation. Dotted lines represent hydrophobic interactions within a layer. In helices, thick ribbons connect α -carbons, while thinner lines represent C_{α} - C_{β} bonds. Image rendered using The PyMOL Molecular Graphics System, Version 1.7 Schrödinger, LLC.

Natural four-helix bundle proteins frequently have clearly segregated layers in the hydrophobic core. Figure 1.7 shows the structures of the Lac repressor tetramerization domain (136), bacterioferritin (175), and cytochrome b (176). Layers are shown as spheres with each

layer colored differently to distinguish them. The layers are sometimes more disorganized at the ends of the bundles where the four-helix bundle structure is breaking down, but in the center, the idea of layering can be a useful tool for thinking about core packing in four-helix bundles. The corresponding green layers of a bacterioferritin-like four-helix bundle and a cytochrome b-like bundle design can be matched up to create an extended bundle that assembles two tetrapyrroles and a di-metal center with an associated tyrosine.

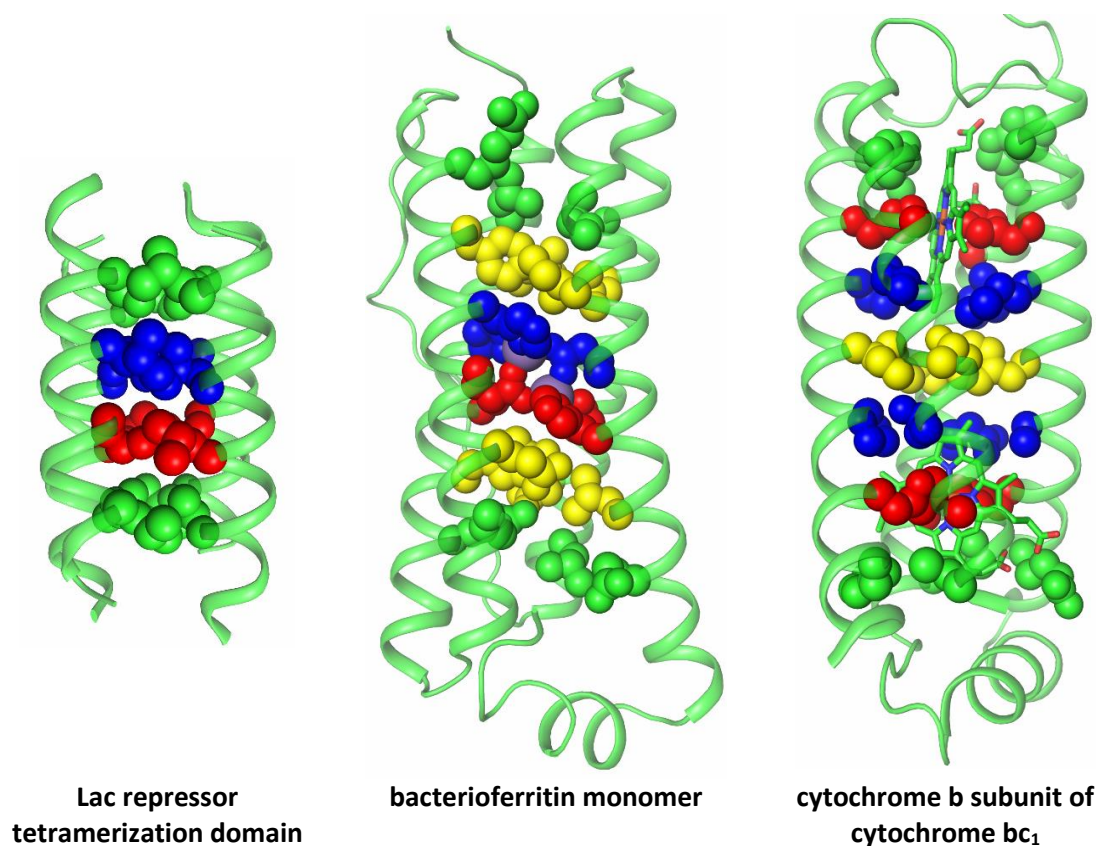


Figure 1.7: Layers in natural proteins

Structure of the Lac repressor tetramerization domain (PDB ID: 1LBI) is shown at left (136). Bacterioferritin monomer is shown at middle with Mn(II) ions represented as mauve spheres in the center and tyrosine residues in yellow layers (PDB ID: 1BCF) (175). Structure of cytochrome b subunit from cytochrome bc₁ complex is shown at right with heme B cofactors represented as sticks (PDB ID: 1EZV) (176). Core *a*- and *d*-position amino acid side chains are represented as spheres. These residues segregate into layers which are distinguished by color. Images rendered using The PyMOL Molecular Graphics System, Version 1.7 Schrödinger, LLC.

Different studies have argued for the usefulness of a layering approach to four-helix bundle core design (168, 170-172, 177, 178). One study by the Regan group showed that after substituting all eight layers of the Rop hydrophobic core with Ala in α -positions and Leu in d -positions, respectively, the protein denaturation curves exhibited signs of native-like structure, and the mutant had a 27°C increase in the thermal stability over that of wild-type Rop (172). In some cases, however, the intrinsic flexibility of leucine side chains can make a leucine-rich core dynamic, even if all the layers have the same size; it is often necessary to include some inflexible amino acids in the core such as aromatic and β -branching residues in addition to small or flexible amino acids in order to achieve a native-like structure (169). In one example, a multi-structured heme-binding four-helix bundle maquette was used as a scaffold to investigate the effects of combinations of substitutions of four d -position Leu residues for Ile, Val, and Phe. Six of the twenty mutants had a stable, unique structure as assayed by one-dimensional proton NMR, and some of these singularly-structured mutants were actually less stable than the original leucine-rich precursor (151). While not fail-safe, the layering method of hydrophobic core design offers a simple, intuitive method of building the core of a four-helix bundle.

It should be noted that not all four-helix coiled coils are said to have discreet layers. Ferritin-like Alacoils such as the Lac repressor tetramerization domain (Figure 1.7, left), which have alanine residues in e -positions, have been described as having interdigitated α - and d -positions, as measured by the relative positions of C_α atoms (179-181). It has even been argued that the idea of layers in antiparallel four-helix bundles is faulty, because α - and d -positions rarely align exactly in antiparallel coiled coils (182). However, the stringent requirement of exact alignment may be a red herring to the protein designer seeking to fill gaps in the core to

avoid destabilizing a maquette; the layering concept can still be applied even if layers appear slanted (Figure 1.7, middle). A four-helix bundle should pack well as long as there is consistency in the total volumes of the layers and in the relative sizes of adjacent α - and d -position amino acids. Layers give the designer a framework for predicting specific hydrophobic contacts in the core and the overall alignment of the helices. As with any aspect of protein design, however, the designer must be conscientious of nuances of the sequence and structure that may confound attempts to control core packing; the layering approach will not necessarily trump all other determinants of core packing. In this regard, properties of well-characterized natural proteins that are similar to the protein being designed can serve to guide the design process.

1.2.4 Heme binding in natural four-helix bundles

Both the antiparallel four-helix bundle fold and the heme cofactor are highly abundant in nature, and there is no shortage of examples of heme-binding antiparallel four-helix bundles. The cytochrome b subunit of mitochondrial respiration protein cytochrome bc_1 and the analogous photosynthetic protein cytochrome b_6 from the cytochrome b_6f complex are transmembrane antiparallel four-helix bundles that bind two hemes B (126, 127). Other examples of heme B-binding antiparallel four-helix bundles include cytochrome b_{562} (128), succinate dehydrogenase (183), and bacterioferritin (175). All of these four-helix bundle cytochromes are antiparallel and bind heme B so that the plane of the porphyrin ring is parallel to the g - g interface and cuts through the e - e interface. This may be due to inherent structural differences between the e - e and g - g interfaces. The C_α -to- C_β bond of an amino acid in an e -position points away from the hydrophobic core, while the C_α -to- C_β bond in a g -position points into the core, making it easier for e -position amino acids to move out of the way of the bulky

heme cofactor to avoid steric clashing. In addition, in all of these cases that use histidine to ligate the heme iron, the N_ε atom of the imidazole ring is used to ligate the iron, probably because an iron-N_δ ligation may cause steric clashing between the porphyrin ring and the His C_β atom or the helical backbone.

Of the four-helix bundle cytochromes mentioned above, cytochromes b and b₆ are the most relevant to the artificial photosynthetic maquette that is the centerpiece of this dissertation. This is because they each bind two B-type hemes non-covalently with an edge-to-edge distance of about 12 Å (176, 184), which is close enough for electron transfer to occur but far enough to slow electron-hole recombination, and they have a designable, layered antiparallel fold that has already been reproduced in soluble proteins by several different groups, despite the fact that cytochromes b and b₆ are transmembrane proteins (140, 141).

A few details of the structure of cytochromes b and b₆ appear to be very important to its electron transfer function. Most importantly, bis-histidine ligation of the heme iron ion is used for high-affinity binding. In addition, the four-helix bundle has binding pockets for the hemes carved out to allow space for the bulky heme cofactor (185, 186). For each pair of ligating histidines, there is also a pair of universally conserved “notch” glycines that have been shown to be essential to high-affinity heme binding; even a conservative mutation of one of these glycine residues to alanine can strain the bis-histidine coordination of the heme and inactivate the cytochrome bc₁ complex (187). These His and Gly residues form the red layers in Figure 1.7 (right panel). Helical glycines are better tolerated in a membrane environment than in solution, but active site glycines have been shown to aid metal binding in di-metal-binding maquettes as well (188, 189). Similarly, a maquette designed for anesthetic binding showed an increased affinity for halothane when four Leu residues surrounding the binding site were mutated to Ala

(190, 191). Glycines may provide space and flexibility to accommodate subtle structural rearrangements induced by cofactor binding.

Cytochromes b and b₆ also have second-shell Ser and Thr residues that make hydrogen-bonds to the heme-ligating His residues. These second-shell Thr contacts have been reproduced previously in *de novo*-designed proteins (139). The end layers (green in Figure 1.7, right panel) of cytochromes b and b₆ contain conserved arginine amino acids that make hydrogen bonds with the propionate groups of heme B (126, 184).

The core of the cytochrome b and b₆ four helix bundle can be said to have five layers between and including the layers that each contain two heme-ligating histidines and two notch glycines (red layers in Figure 1.7, right panel). The middle layer (yellow in Figure 1.7) is bulky, because it needs to fill the same volume as the layers that contain heme and two histidines; sequence alignments show that the middle layer usually contains exactly one phenylalanine and an assortment of mostly bulky hydrophobic residues that may include isoleucine, leucine, methionine, valine, and/or threonine. Layers between the heme-ligating and middle layers (blue in Figure 1.7) have part of the heme projecting into them, so they tend to have smaller and more flexible amino acids such as alanine, proline, glutamine, leucine, valine, threonine, and methionine. The presence of polar and helix-breaking amino acids may be more tolerable in a membrane than in solvent. Therefore, *a*- and *d*-positions in a water-soluble maquette should avoid these residues with the exception of the notch glycines, which appear to be critical to the heme B affinity and electron transfer function of cytochromes b and b₆.

1.2.5 *The role of the apo-state in heme binding*

It is intuitive that a heme-binding protein should have hydrophobic core packing that complements the shape of the heme cofactor to produce a native-like holo-state, but it is also instructive to consider the structure of the apo-state in the absence of heme and how it might transition to the heme-bound holo-state. Should an apo-hemoprotein be rigidly structured before the heme arrives, should folding be driven by heme binding, or is the apo-state structure irrelevant to heme binding? Studies of natural hemoproteins in the apo-state shed light on the structural requirements of the apo-state of a high-affinity heme binding structure.

One of the best-studied natural hemoproteins is myoglobin. Apo-myoglobin has relatively low stability and in some ways resembles a molten globule, but it has ordered secondary structure as well as specific and stable tertiary interactions that show it is a native-like globular protein (192). However, apo-myoglobin does have a highly plastic apo-state structure, which has led to the suggestion that heme binding drives a final transition to a stable, highly-structured, native-like holo-state (193). A similar native-like structure with folding intermediate-like properties has been observed in other apo-state B-type hemoproteins including apo-cytochrome P450 (194), apo-cytochrome b₅₆₂ (195), and apo-cytochrome b₅ (196). It should be noted, however, that proteins that bind heme transiently usually have more stable apo-state folds than proteins that bind heme permanently (197). This may reflect a decreased pressure for high affinity heme binding and increased pressure for apo-protein resistance to aggregation and proteolysis in proteins that bind heme transiently. It has been observed that natural hemoproteins in general are biased toward heme binding sites that have “low foldability” (198). This pattern suggests that a heme-binding protein, which must accommodate the bulky hydrophobic porphyrin ring of heme, needs some degree of plasticity to allow the

entry of heme into a binding pocket. Apo-protein flexibility lowers the enthalpic cost of heme binding by decreasing the number of protein-protein interactions that must be broken for heme to enter the binding site, but a partially pre-formed active site with native-like structure lowers the entropic cost of heme binding by lowering the conformational freedom of the apo-protein. In their study of cytochrome b₅, Falzone et al. termed this the “partial fold option” to convey a balance of flexibility and native-like structure in the apo-protein that facilitates high-affinity heme binding (196).

Some support for the partial fold option also comes from studies of *de novo*-designed hemoproteins. For example, the HP-1 maquette binds two hemes B with high affinity (dissociation constants less than 20 nM). HP-1 has a molten-globular apo-state but transitions to a structurally specific conformation upon the binding of heme B (154). In contrast, a maquette with a very similar sequence that has a rigid, singularly-structured apo-state transitions to a molten globular state when heme binding disrupts core packing interactions, suggesting an advantage for hemoproteins that are flexible in the apo-state (199). However, a heme maquette that is unfolded in the apo-state may not be ideal either. A D₂-symmetrical tetrameric heme maquette that was unfolded in the apo-state showed very slow heme binding that required hours to reach completion, and an unusually low extinction coefficient was reported for its Soret maximum, suggesting incomplete binding even after a day (141).

1.2.6 *Due Ferro series of maquettes*

A series of maquettes from the DeGrado and Lombardi groups and collaborators called *Due Ferro* proteins (200) were used to recapitulate functions of natural binuclear non-heme iron enzymes such as ferroxidase activity of bacterioferritin (201-205) and quinol oxidase activity of

alternative oxidase (132, 205, 206). Numerous NMR and X-ray crystallographic structures of Due Ferro maquettes have shown that the maquettes fold very similarly to the natural proteins and bind various metal ions with high affinity including Mn(II), Fe(II), Fe(III), Co(II), Zn(II), and Cd(II) (188, 202, 206-211). These natural and *de novo* four-helix bundle proteins ligate two metal ions in a deep water-filled cavity using two histidines, two bridging glutamates, and two axial glutamate residues. The histidines ligate the metal ions using the N_δ atom and typically make second shell hydrogen bonds to aspartate residues using the N_ε atom. Tyrosines are often used to make second-shell hydrogen bonds to a bidentate axial glutamates (Figure 1.8).

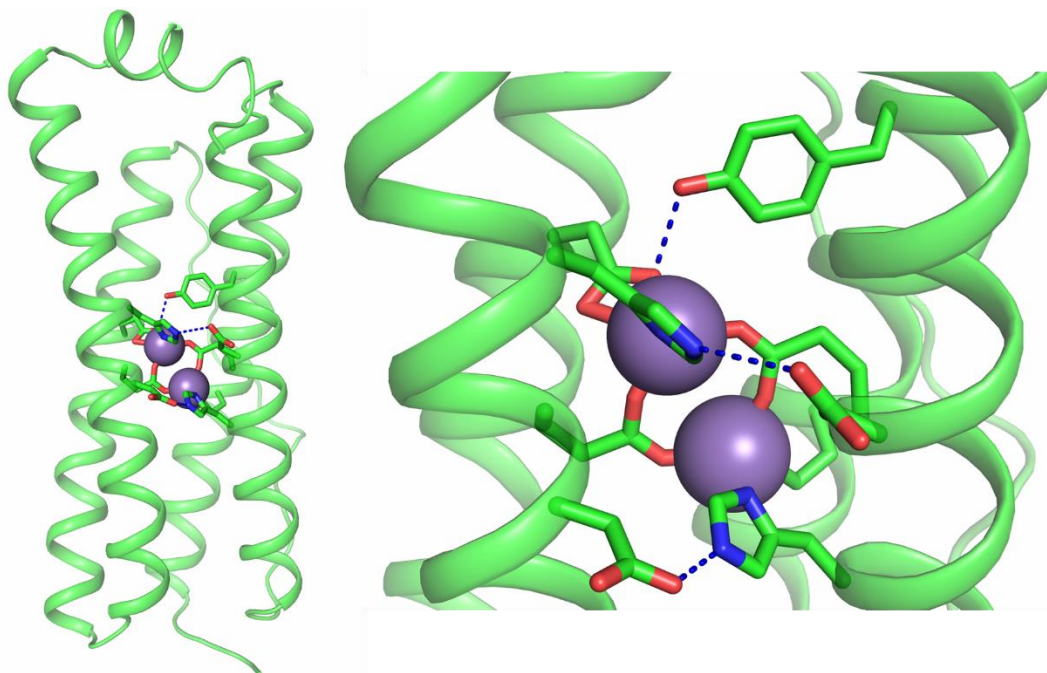


Figure 1.8: Canonical carboxylate-bridge diiron protein active site

Bacterioferritin monomer (left) and close-up of the active site (right) (PDB ID: 1BCF) (175). Manganese(II) ions are represented as mauve spheres, and hydrogen bonds between Asp and His residues and between Glu and Tyr residues are represented by blue dotted lines. Images rendered using The PyMOL Molecular Graphics System, Version 1.7 Schrödinger, LLC.

Just as notch glycines were found to be important for the function of cytochrome b, iterative redesigns of the Due Ferro series demonstrated that cofactor binding can be improved

by using active site glycine residues to make space for the cofactor. DF1 was originally designed with a set of four leucine residues occluding the di-metal binding site, and it had to be denatured and refolded in the presence of metal ions before binding could take place (207, 212). In subsequent designs, these Leu residues were changed to smaller amino acids, progressively trading stability for increasing metal ion affinity and substrate access. DF2, which had two of the Leu residues mutated to Ala, had high affinity for metal ions without the need for denaturation. In addition, DF2 exhibited ferroxidase activity, whereas DF1 did not (204, 212). In DF3, which had all four Leu residues changed to Gly, the affinity for Co(II) and Mn(II) was about two orders of magnitude higher than in DF2 (189), and DF3 was able to catalyze the oxidation of bulky phenol compounds (188).

Glycine residues at the opening of the metal site cavity in DF3 also facilitated oxygen-driven oxidation of substrate molecules including hydroquinones and anilines (188, 206, 213). A recent study showed that a semiquinone could be stabilized by binding to a di-Zn(II) site in a Due Ferro variant that had two glycines and two alanines at the opening of the cavity. Interestingly, hydrophobic interactions were identified as a critical driving force for the binding and stabilization of the semiquinone (214). Despite the highly polar contents of the metal binding cavity, hydrophobic molecules are able to make stabilizing contacts with the glycine and alanine residues at the opening of the metal site. The site is wide enough that it could conceivably accommodate a much larger molecule, such as a porphyrin.

1.2.7 Negative design

An important aim of any protein design project is to make a protein with a singular, native-like conformation. Negative design is necessary to widen the energy gap between the

intended design and alternative conformations, so that the protein cannot exist in multiple conformations at once. In a four-helix bundle, the primary concern is that the threading of the helices, or the helix topology, could be arranged incorrectly; there are many ways for the helices to align in a four-helix bundle, and in the absence of negative design, they may have similar energies. While it is true that some functions can be achieved in a protein that exchanges between multiple conformations, this is not the case for a reaction center maquette that must site-specifically assemble a di-metal center and two tetrapyrroles into an electron transport chain. In a Dye Ferro-type active site (177, 200, 207), any alternative helix threading topology other than the intended design would change the organization of metal-ligating histidines and glutamates such that metal affinity would be greatly reduced. In the tetrapyrrole-binding section of a reaction center maquette, a reversal of the threading from left-turning antiparallel to right-turning antiparallel would not affect the geometry of ligation, but a parallel/antiparallel topology would leave a distorted binding cavity and the histidines would be in the wrong positions for stable tetrapyrrole ligation. Furthermore, a maquette without a singular, native-like conformation is not suited for high-resolution structure determination, so it would be difficult to verify that the protein folded as designed or to ascribe structural features to functional effects.

We have at our disposal several tools to favor the target design including factors that can destabilize the unintended helix topology relative to the correctly folded state and factors that can stabilize the intended topology relative to the misfolded state. For one thing, a single-chain monomeric four-helix bundle would need to have inter-helical loops that are at least as long as a helix in order to have more than two helices with a parallel orientation. Short loops obviate the possibility of a topology with all helices parallel or with three helices parallel and

one antiparallel. Structured loops can be designed to favor a left- or right-turning topology, although loops usually have a weaker effect on topology than helix-helix interactions. Another significant factor in determining helix topology is hydrophobic core packing. Four-helix bundle stability is maximized when hydrophobic contact between helices is complementary, so a loss of complementarity in an alternative topology favors the intended design (170, 171).

Perhaps the most easily controlled structural element that influences helix topology is inter-helical charge pairing interactions. Early work on leucine zippers demonstrated the power of charge pairing in dictating coiled coil folding. Mutagenesis and pH titrations on the heterodimeric leucine zipper Fos-Jun human oncoprotein showed that charge pairing *e*- and *g*-positions destabilized the Fos and Jun homodimers while stabilizing the heterodimeric state (215). A rigorous study of mutants of the homodimeric VBP leucine zipper showed that altered charge patterning at *e*- and *g*-positions could make VBP fold as a heterodimer of two mutants with complementary charges (166). Charge patterning was soon leveraged to dictate folding in simple Rop-like antiparallel *de novo* four-helix bundle designs (170, 171), and later in more complicated functional antiparallel four-helix bundles. In a set of tetrameric Due Ferro maquettes, the DeGrado group used charge pairing interactions at *b*-, *c*-, *e*-, and *g*-positions to specify heterotetrameric assembly of metal-binding maquettes. When the component peptides were kept separate, they did not fold at neutral pH, but when the peptides were mixed together in the proper stoichiometries circular dichroism measurements showed high α -helical content (216, 217). Similarly, charge pairing interactions at *c*-positions were used in a series of porphyrin array (PA) antiparallel four-helix bundle maquettes to help force the intended topology, and various methods demonstrated folding and function, but no high-resolution structures were obtained to verify the structure (139, 142, 152, 218).

1.2.8 Inter-helical loops

The inter-helical loops of a four-helix bundle protein are usually among the most dynamic parts of the protein, but they can play a role in determining the structure. A short loop can force the helices it connects to be antiparallel instead of parallel, and loops can have a significant influence on the overall stability of the bundle.

A loop that is too long will decrease the stability of the four-helix bundle by raising the entropic cost of folding. Indeed, a study on the helix-loop-helix Rop protein, which folds into a homodimeric antiparallel four-helix bundle, showed that when the native Asp-Ala loop was replaced by a polyglycine linker, increasing the number of glycines in the linker progressively lowered the melting temperature. The mutant with 10 loop glycines denatured at a temperature 23°C lower than that of the mutant with a single glycine in the loop. It was estimated that each loop glycine lowered the stability of Rop by 0.26 kcal/mol (219). A loop that is very short, however, may sometimes cause misfolding or aggregation, as was observed in the α_2 B(P) maquette (220) and Rop variants with altered loops (221). The latter study demonstrated that the wild-type homodimeric Rop could be converted to a monomeric four-helix bundle by adding polyglycine loops to connect the helices. While a 3-glycine loop resulted in aggregation, the variant with 4 loop glycines was monomeric with comparable RNA substrate affinity and higher stability than the wild-type (221). In a similar manner, the single-chain four-helix bundle maquette BT6 was developed from a homodimeric helix-loop-helix maquette by rearranging the loops. In this case, 9-residue glycine-rich linkers were used to produce the single-chain BT6, which retained its affinity for heme and was expressible in *E. coli* (124).

The designed loops described above are all glycine-rich unstructured loops, which are usually sufficient to make stable, functional maquettes, but a structured loop can add stability to the protein. However, the design of a stable loop in a four-helix bundle is difficult because it lacks a stable secondary structure, is highly exposed to solvent, and is located at the ends of the helices where the protein is most dynamic. The DeGrado group has explored the use of loop structures that are found in natural proteins to connect the helices of four-helix bundles. In the di-metal maquette DF2t, a structured loop was found to increase stability and expression yield (222), and a similar maquette, DF3, used a different loop conformation to confer even greater stability and solubility (188). X-ray crystal and NMR structures demonstrated that the loops folded as designed. While a structured loop sometimes can impart subtle improvements to a protein's structure, unstructured loops are generally sufficient, because four-helix bundle folding and function is dictated primarily by the α -helices.

1.2.9 Four-helix bundle length

Natural four-helix bundles usually have a length of about 15 to 24 residues per α -helix (223), but longer four-helix bundle proteins have been reported, and several natural 2-helix and 3-helix coiled coils are considerably longer. In 2008, a *de novo*-designed two-porphyrin array (2PA) four-helix bundle maquette with 34 residues per helix was lengthened by duplicating a three-heptad sequence (and introducing a total of five mutations per helix to ensure the correct charge pairing interactions) to make a four-porphyrin array (4PA) maquette with 55 residues per helix. The extension of the helices raised the holo-state melting temperature by 24°C (139, 152). In a systematic study of four-helix bundle length and stability, a peptide sequence based on the Lac repressor tetramerization domain was extended from 21 to 28 to 35 amino acids, and

its four-helix bundle stability increased by approximately 16 kcal/mol for each heptad added (153). The increased stabilization due to lengthening is an effect of the increased burial of hydrophobic surface area.

1.2.10 Caps at helical termini

The termini of α -helices in four-helix bundles tend to fray, making them among the least stable parts of the protein (218, 224), which means that end caps can play a significant role in stability despite their small size. For example, when a single 5-residue MTPEQ N-cap was added to the N-terminus of BT6, the apo-state melting temperature increased from 37 to about 45°C (124). Similarly, when the tetrameric four-helix bundle maquette 4PA was given four SLEEA N-caps and four FQKFQKYG C-caps, they increased the apo-state melting temperature by about 57°C; the caps had a greater stabilizing effect than the lengthening of 2PA by three heptads to make 4PA (152).

N- and C-termini are unstable because the absence of a continuing bundle leaves them solvent-exposed, and the absence of a connecting loop leaves their motion largely unrestricted. An analysis of N-caps in nature shows a significant preference for proline in the N-cap (225). This is because proline addresses both the solvent exposure and conformational freedom of helical termini: proline is the most water soluble of all natural amino acids, and it is constrained to an α -helical conformation (226). In addition, the absence of a hydrogen-bond acceptor for N-terminal backbone amine groups is not an issue for proline, because it has a pyrrolidine side chain in place of an N-H bond. Outside of an N-cap, however, proline is a strong helix breaker because the pyrrolidine group blocks the preceding residue from adopting an α -helical conformation (226). Unfortunately, an N-terminal proline presents a problem for TEV protease,

which is inhibited by a proline residue close to its site of cleavage (227). N-caps in natural proteins also show a preference for Asn, Asp, Gly, and Ser residues immediately before the Pro (225, 228). These residues can adopt non-helical conformations that can hydrogen bond backbone amines at the N-terminus of the helix (225). In addition, natural N-caps frequently contain negatively charged residues, because these help stabilize the helix dipole moment which runs from N- to C- terminus, in the direction of backbone C=O bonds and against backbone N-H bonds. In the same way, C-caps can stabilize helices by using positive charges to align the helix dipole (229). However, C-caps do not have any other simple rules of thumb. Natural proteins frequently use Gly at C-caps, but this is because they are often found in the more complicated Schellman and α_L capping motifs (225, 226, 228). While Gly residues are sometimes added to designed proteins at the C-termini (139, 207, 218), they may not affect stability unless residues around them cooperate to fold into specific capping motifs (228).

1.2.11 Summary

Taken together, the above considerations provide a framework for designing a four-helix bundle maquette. The most important tool available to a protein designer is an awareness of the literature that is relevant to the protein to be designed. The structure and function of a protein is determined by a complex system of interactions, each of which may vary in strength depending on contextual details, and intuition alone cannot be relied upon as a robust predictor of structure; rational design requires guidance from empirical observations.

1.3 References

1. Faunce, T. A., Lubitz, W., Rutherford, A. W., MacFarlane, D. R., Moore, G. F., Yang, P. D., Nocera, D. G., Moore, T. A., Gregory, D. H., Fukuzumi, S., Yoon, K. B., Armstrong, F. A., Wasielewski, M. R., and Styring, S. (2013) Energy and environment policy case for a global project on artificial photosynthesis, *Energ Environ Sci* 6, 695-698.
2. Cox, N., Pantazis, D. A., Neese, F., and Lubitz, W. (2015) Artificial photosynthesis: understanding water splitting in nature, *Interface Focus* 5, 20150009.
3. Blankenship, R. E., Tiede, D. M., Barber, J., Brudvig, G. W., Fleming, G., Ghirardi, M., Gunner, M. R., Junge, W., Kramer, D. M., Melis, A., Moore, T. A., Moser, C. C., Nocera, D. G., Nozik, A. J., Ort, D. R., Parson, W. W., Prince, R. C., and Sayre, R. T. (2011) Comparing photosynthetic and photovoltaic efficiencies and recognizing the potential for improvement, *Science* 332, 805-809.
4. Lewis, N. S., and Nocera, D. G. (2006) Powering the planet: chemical challenges in solar energy utilization, *Proc Natl Acad Sci U S A* 103, 15729-15735.
5. Hingorani, K., and Hillier, W. (2012) Perspectives for Photobiology in Molecular Solar Fuels, *Aust J Chem* 65, 643-651.
6. Crabtree, G. W., and Lewis, N. S. (2007) Solar energy conversion, *Phys Today* 60, 37-42.
7. Gust, D., Moore, T. A., and Moore, A. L. (2009) Solar fuels via artificial photosynthesis, *Acc Chem Res* 42, 1890-1898.
8. Gray, H. B. (2009) Powering the planet with solar fuel, *Nat Chem* 1, 7.
9. Barber, J., and Tran, P. D. (2013) From natural to artificial photosynthesis, *J R Soc Interface* 10, 20120984.
10. (2010) World Energy Outlook Report, International Energy Agency.
11. (2003) World Energy Assessment Report: Energy and the Challenge of Sustainability, In *United Nations Development Program*, New York, NY.
12. Armstrong, F. A. (2008) Why did Nature choose manganese to make oxygen?, *Philos Trans R Soc Lond B Biol Sci* 363, 1263-1270; discussion 1270.
13. Watanabe, M., Iwai, M., Narikawa, R., and Ikeuchi, M. (2009) Is the Photosystem II Complex a Monomer or a Dimer?, *Plant and Cell Physiology* 50, 1674-1680.
14. Umena, Y., Kawakami, K., Shen, J. R., and Kamiya, N. (2011) Crystal structure of oxygen-evolving photosystem II at a resolution of 1.9 Å, *Nature* 473, 55-60.
15. Murray, J. W., and Barber, J. (2007) Structural characteristics of channels and pathways in photosystem II including the identification of an oxygen channel, *J Struct Biol* 159, 228-237.
16. Zouni, A., Witt, H. T., Kern, J., Fromme, P., Krauss, N., Saenger, W., and Orth, P. (2001) Crystal structure of photosystem II from *Synechococcus elongatus* at 3.8 Å resolution, *Nature* 409, 739-743.
17. Ferreira, K. N., Iverson, T. M., Maghlaoui, K., Barber, J., and Iwata, S. (2004) Architecture of the photosynthetic oxygen-evolving center, *Science* 303, 1831-1838.
18. Guskov, A., Kern, J., Gabdulkhakov, A., Broser, M., Zouni, A., and Saenger, W. (2009) Cyanobacterial photosystem II at 2.9-Å resolution and the role of quinones, lipids, channels and chloride, *Nat Struct Mol Biol* 16, 334-342.
19. Kamiya, N., and Shen, J. R. (2003) Crystal structure of oxygen-evolving photosystem II from *Thermosynechococcus vulcanus* at 3.7-Å resolution, *Proc Natl Acad Sci U S A* 100, 98-103.

20. Suga, M., Akita, F., Hirata, K., Ueno, G., Murakami, H., Nakajima, Y., Shimizu, T., Yamashita, K., Yamamoto, M., Ago, H., and Shen, J. R. (2015) Native structure of photosystem II at 1.95 Å resolution viewed by femtosecond X-ray pulses, *Nature* 517, 99-103.
21. Young, I. D., Ibrahim, M., Chatterjee, R., Gul, S., Fuller, F. D., Koroidov, S., Brewster, A. S., Tran, R., Alonso-Mori, R., Kroll, T., Michels-Clark, T., Laksmono, H., Sierra, R. G., Stan, C. A., Hussein, R., Zhang, M., Douthit, L., Kubin, M., de Lichtenberg, C., Vo Pham, L., Nilsson, H., Cheah, M. H., Shevela, D., Saracini, C., Bean, M. A., Seuffert, I., Sokaras, D., Weng, T. C., Pastor, E., Weninger, C., Fransson, T., Lassalle, L., Brauer, P., Aller, P., Docker, P. T., Andi, B., Orville, A. M., Glowina, J. M., Nelson, S., Sikorski, M., Zhu, D., Hunter, M. S., Lane, T. J., Aquila, A., Koglin, J. E., Robinson, J., Liang, M., Boutet, S., Lyubimov, A. Y., Uervirojnangkoorn, M., Moriarty, N. W., Liebschner, D., Afonine, P. V., Waterman, D. G., Evans, G., Wernet, P., Dobbek, H., Weis, W. I., Brunger, A. T., Zwart, P. H., Adams, P. D., Zouni, A., Messinger, J., Bergmann, U., Sauter, N. K., Kern, J., Yachandra, V. K., and Yano, J. (2016) Structure of photosystem II and substrate binding at room temperature, *Nature* 540, 453-457.
22. Ago, H., Adachi, H., Umena, Y., Tashiro, T., Kawakami, K., Kamiya, N., Tian, L., Han, G., Kuang, T., Liu, Z., Wang, F., Zou, H., Enami, I., Miyano, M., and Shen, J. R. (2016) Novel Features of Eukaryotic Photosystem II Revealed by Its Crystal Structure Analysis from a Red Alga, *J Biol Chem* 291, 5676-5687.
23. Wei, X., Su, X., Cao, P., Liu, X., Chang, W., Li, M., Zhang, X., and Liu, Z. (2016) Structure of spinach photosystem II-LHCII supercomplex at 3.2 Å resolution, *Nature* 534, 69-74.
24. Barber, J. (2008) Photosynthetic generation of oxygen, *Philos Trans R Soc Lond B Biol Sci* 363, 2665-2674.
25. Grabolle, M., and Dau, H. (2005) Energetics of primary and secondary electron transfer in Photosystem II membrane particles of spinach revisited on basis of recombination-fluorescence measurements, *Biochim Biophys Acta* 1708, 209-218.
26. Rappaport, F., Guergova-Kuras, M., Nixon, P. J., Diner, B. A., and Lavergne, J. (2002) Kinetics and pathways of charge recombination in photosystem II, *Biochemistry* 41, 8518-8527.
27. Cardona, T., Sedoud, A., Cox, N., and Rutherford, A. W. (2012) Charge separation in photosystem II: a comparative and evolutionary overview, *Biochim Biophys Acta* 1817, 26-43.
28. Brettel, K., Schlodder, E., and Witt, H. T. (1984) Nanosecond Reduction Kinetics of Photooxidized Chlorophyll-Alpha-l_i (P-680) in Single Flashes as a Probe for the Electron Pathway, H⁺-Release and Charge Accumulation in the O₂-Evolving Complex, *Biochimica Et Biophysica Acta* 766, 403-415.
29. Eckert, H. J., and Renger, G. (1988) Temperature-Dependence of P680⁺ Reduction in O₂-Evolving Ps-l_i Membrane-Fragments at Different Redox States Si of the Water Oxidizing System, *FEBS Letters* 236, 425-431.
30. Karge, M., Irrgang, K. D., Sellin, S., Feinaugle, R., Liu, B., Eckert, H. J., Eichler, H. J., and Renger, G. (1996) Effects of hydrogen/deuterium exchange on photosynthetic water cleavage in PS II core complexes from spinach, *FEBS Lett* 378, 140-144.
31. Shen, J. R. (2015) The Structure of Photosystem II and the Mechanism of Water Oxidation in Photosynthesis, *Annu Rev Plant Biol* 66, 23-48.

32. Hays, A. M., Vassiliev, I. R., Golbeck, J. H., and Debus, R. J. (1999) Role of D1-His190 in the proton-coupled oxidation of tyrosine YZ in manganese-depleted photosystem II, *Biochemistry* 38, 11851-11865.
33. Mamedov, F., Sayre, R. T., and Styring, S. (1998) Involvement of histidine 190 on the D1 protein in electron/proton transfer reactions on the donor side of photosystem II, *Biochemistry* 37, 14245-14256.
34. Babcock, G. T., Blankenship, R. E., and Sauer, K. (1976) Reaction kinetics for positive charge accumulation on the water side of chloroplast photosystem II, *FEBS Lett* 61, 286-289.
35. Razeghifard, M. R., and Pace, R. J. (1997) Electron paramagnetic resonance kinetic studies of the S states in spinach PSII membranes, *Bba-Bioenergetics* 1322, 141-150.
36. Noguchi, T., Suzuki, H., Tsuno, M., Sugiura, M., and Kato, C. (2012) Time-resolved infrared detection of the proton and protein dynamics during photosynthetic oxygen evolution, *Biochemistry* 51, 3205-3214.
37. Vinyard, D. J., Ananyev, G. M., and Dismukes, G. C. (2013) Photosystem II: the reaction center of oxygenic photosynthesis, *Annu Rev Biochem* 82, 577-606.
38. Pace, R. J., Stranger, R., and Petrie, S. (2012) Why nature chose Mn for the water oxidase in Photosystem II, *Dalton Trans* 41, 7179-7189.
39. Keren, N., Berg, A., van Kan, P. J., Levanon, H., and Ohad, I. (1997) Mechanism of photosystem II photoinactivation and D1 protein degradation at low light: the role of back electron flow, *Proc Natl Acad Sci U S A* 94, 1579-1584.
40. Barber, J., and Archer, M. D. (2001) P680, the primary electron donor of photosystem II, *J Photoch Photobio A* 142, 97-106.
41. Lichtenstein, B. R., Farid, T. A., Kodali, G., Solomon, L. A., Anderson, J. L., Sheehan, M. M., Ennist, N. M., Fry, B. A., Chobot, S. E., Bialas, C., Mancini, J. A., Armstrong, C. T., Zhao, Z., Esipova, T. V., Snell, D., Vinogradov, S. A., Discher, B. M., Moser, C. C., and Dutton, P. L. (2012) Engineering oxidoreductases: maquette proteins designed from scratch, *Biochem Soc Trans* 40, 561-566.
42. Saito, K., Shen, J. R., Ishida, T., and Ishikita, H. (2011) Short hydrogen bond between redox-active tyrosine Y(Z) and D1-His190 in the photosystem II crystal structure, *Biochemistry* 50, 9836-9844.
43. Nakamura, S., Nagao, R., Takahashi, R., and Noguchi, T. (2014) Fourier transform infrared detection of a polarizable proton trapped between photooxidized tyrosine YZ and a coupled histidine in photosystem II: relevance to the proton transfer mechanism of water oxidation, *Biochemistry* 53, 3131-3144.
44. Barber, J. (2016) The Mn₄Ca-cluster of the photosynthetic oxygen evolving centre: its structure, function and evolution, *Biochemistry*.
45. Bao, H., and Burnap, R. L. (2016) Photoactivation: The Light-Driven Assembly of the Water Oxidation Complex of Photosystem II, *Front Plant Sci* 7, 578.
46. Styring, S., Sjöholm, J., and Mamedov, F. (2012) Two tyrosines that changed the world: Interfacing the oxidizing power of photochemistry to water splitting in photosystem II, *Biochim Biophys Acta* 1817, 76-87.
47. Krishtalik, L. I. (1986) Energetics of Multielectron Reactions - Photosynthetic Oxygen Evolution, *Biochimica Et Biophysica Acta* 849, 162-171.
48. Blankenship, R. E., and Hartman, H. (1998) The origin and evolution of oxygenic photosynthesis, *Trends Biochem Sci* 23, 94-97.

49. Kok, B., Forbush, B., and McGloin, M. (1970) Cooperation of charges in photosynthetic O₂ evolution-I. A linear four step mechanism, *Photochem Photobiol* **11**, 457-475.
50. Dau, H., Limberg, C., Reier, T., Risch, M., Roggan, S., and Strasser, P. (2010) The Mechanism of Water Oxidation: From Electrolysis via Homogeneous to Biological Catalysis, *Chemcatchem* **2**, 724-761.
51. Boussac, A., and Rutherford, A. W. (1988) Nature of the Inhibition of the Oxygen-Evolving Enzyme of Photosystem-II Induced by NaCl Washing and Reversed by the Addition of Ca²⁺ or Sr²⁺, *Biochemistry* **27**, 3476-3483.
52. Koua, F. H., Umena, Y., Kawakami, K., and Shen, J. R. (2013) Structure of Sr-substituted photosystem II at 2.1 Å resolution and its implications in the mechanism of water oxidation, *Proc Natl Acad Sci U S A* **110**, 3889-3894.
53. Brimblecombe, R., Chen, J., Wagner, P., Buchhorn, T., Dismukes, G. C., Spiccia, L., and Swiegers, G. F. (2011) Photocatalytic oxygen evolution from non-potable water by a bioinspired molecular water oxidation catalyst, *J Mol Catal a-Chem* **338**, 1-6.
54. Ruettinger, W., Yagi, M., Wolf, K., Bernasek, S., and Dismukes, G. C. (2000) O₂ evolution from the manganese-oxo cubane core Mn₄O₄⁶⁺: A molecular mimic of the photosynthetic water oxidation enzyme?, *Journal of the American Chemical Society* **122**, 10353-10357.
55. Li, G. H., Sproviero, E. M., Snoeberger, R. C., Iguchi, N., Blakemore, J. D., Crabtree, R. H., Brudvig, G. W., and Batista, V. S. (2009) Deposition of an oxomanganese water oxidation catalyst on TiO₂ nanoparticles: computational modeling, assembly and characterization, *Energ Environ Sci* **2**, 230-238.
56. Harriman, A., Pickering, I. J., Thomas, J. M., and Christensen, P. A. (1988) Metal-Oxides as Heterogeneous Catalysts for Oxygen Evolution under Photochemical Conditions, *J Chem Soc Farad T* **1 84**, 2795-2806.
57. Duan, L., Bozoglian, F., Mandal, S., Stewart, B., Privalov, T., Llobet, A., and Sun, L. (2012) A molecular ruthenium catalyst with water-oxidation activity comparable to that of photosystem II, *Nat Chem* **4**, 418-423.
58. Thomsen, J. M., Huang, D. L., Crabtree, R. H., and Brudvig, G. W. (2015) Iridium-based complexes for water oxidation, *Dalton Trans* **44**, 12452-12472.
59. Lutterman, D. A., Surendranath, Y., and Nocera, D. G. (2009) A self-healing oxygen-evolving catalyst, *J Am Chem Soc* **131**, 3838-3839.
60. Kanan, M. W., and Nocera, D. G. (2008) In situ formation of an oxygen-evolving catalyst in neutral water containing phosphate and Co²⁺, *Science* **321**, 1072-1075.
61. Chéniaie, G. M., and Martin, I. F. (1971) Photoactivation of Manganese Catalyst of O₂ Evolution .1. Biochemical and Kinetic Aspects, *Biochimica Et Biophysica Acta* **253**, 167-&.
62. Tyryshkin, A. M., Watt, R. K., Baranov, S. V., Dasgupta, J., Hendrich, M. P., and Dismukes, G. C. (2006) Spectroscopic evidence for Ca²⁺ involvement in the assembly of the Mn₄Ca cluster in the photosynthetic water-oxidizing complex, *Biochemistry* **45**, 12876-12889.
63. Burnap, R. L. (2004) D1 protein processing and Mn cluster assembly in light of the emerging Photosystem II structure, *Phys Chem Chem Phys* **6**, 4803-4809.
64. Chen, C., Kazimir, J., and Chéniaie, G. M. (1995) Calcium modulates the photoassembly of photosystem II (Mn)₄-clusters by preventing ligation of nonfunctional high-valency states of manganese, *Biochemistry* **34**, 13511-13526.
65. Tommos, C., and Babcock, G. T. (2000) Proton and hydrogen currents in photosynthetic water oxidation, *Biochim Biophys Acta* **1458**, 199-219.

66. Dixon, W. T., and Murphy, D. (1976) Determination of Acidity Constants of Some Phenol Radical Cations by Means of Electron-Spin Resonance, *J Chem Soc Farad T 2* 72, 1221-1230.
67. Debus, R. J., Barry, B. A., Babcock, G. T., and McIntosh, L. (1988) Site-directed mutagenesis identifies a tyrosine radical involved in the photosynthetic oxygen-evolving system, *Proc Natl Acad Sci U S A* 85, 427-430.
68. Vermass, W. F., Rutherford, A. W., and Hansson, O. (1988) Site-directed mutagenesis in photosystem II of the cyanobacterium *Synechocystis* sp. PCC 6803: Donor D is a tyrosine residue in the D2 protein, *Proc Natl Acad Sci U S A* 85, 8477-8481.
69. Vass, I., and Styring, S. (1991) pH-dependent charge equilibria between tyrosine-D and the S states in photosystem II. Estimation of relative midpoint redox potentials, *Biochemistry* 30, 830-839.
70. Renger, G. (2004) Coupling of electron and proton transfer in oxidative water cleavage in photosynthesis, *Biochim Biophys Acta* 1655, 195-204.
71. Faller, P., Debus, R. J., Brettel, K., Sugiura, M., Rutherford, A. W., and Bousac, A. (2001) Rapid formation of the stable tyrosyl radical in photosystem II, *Proc Natl Acad Sci U S A* 98, 14368-14373.
72. Styring, S., and Rutherford, A. W. (1987) In the Oxygen-Evolving Complex of Photosystem-II the S0 State Is Oxidized to the S1 State by D+ (Signal-Islow), *Biochemistry* 26, 2401-2405.
73. Hays, A. M., Vassiliev, I. R., Golbeck, J. H., and Debus, R. J. (1998) Role of D1-His190 in proton-coupled electron transfer reactions in photosystem II: a chemical complementation study, *Biochemistry* 37, 11352-11365.
74. Kuroda, H., Kodama, N., Sun, X. Y., Ozawa, S., and Takahashi, Y. (2014) Requirement for Asn298 on D1 protein for oxygen evolution: analyses by exhaustive amino acid substitution in the green alga *Chlamydomonas reinhardtii*, *Plant Cell Physiol* 55, 1266-1275.
75. Babcock, G. T., and Sauer, K. (1973) Electron paramagnetic resonance signal II in spinach chloroplasts. I. Kinetic analysis for untreated chloroplasts, *Biochim Biophys Acta* 325, 483-503.
76. Ananyev, G. M., Sakiyan, I., Diner, B. A., and Dismukes, G. C. (2002) A functional role for tyrosine-D in assembly of the inorganic core of the water oxidase complex of photosystem II and the kinetics of water oxidation, *Biochemistry* 41, 974-980.
77. Magnuson, A., Rova, M., Mamedov, F., Fredriksson, P. O., and Styring, S. (1999) The role of cytochrome b559 and tyrosineD in protection against photoinhibition during in vivo photoactivation of photosystem II, *Biochim Biophys Acta* 1411, 180-191.
78. Moser, C. C., Keske, J. M., Warncke, K., Farid, R. S., and Dutton, P. L. (1992) Nature of biological electron transfer, *Nature* 355, 796-802.
79. Page, C. C., Moser, C. C., Chen, X., and Dutton, P. L. (1999) Natural engineering principles of electron tunnelling in biological oxidation-reduction, *Nature* 402, 47-52.
80. Sun, L. C., Hammarstrom, L., Akermark, B., and Styring, S. (2001) Towards artificial photosynthesis: ruthenium-manganese chemistry for energy production, *Chemical Society Reviews* 30, 36-49.
81. Faller, P., Goussias, C., Rutherford, A. W., and Un, S. (2003) Resolving intermediates in biological proton-coupled electron transfer: a tyrosyl radical prior to proton movement, *Proc Natl Acad Sci U S A* 100, 8732-8735.

82. Megiatto, J. D., Jr., Antoniuk-Pablant, A., Sherman, B. D., Kodis, G., Gervaldo, M., Moore, T. A., Moore, A. L., and Gust, D. (2012) Mimicking the electron transfer chain in photosystem II with a molecular triad thermodynamically capable of water oxidation, *Proc Natl Acad Sci U S A* 109, 15578-15583.
83. Hoganson, C. W., and Babcock, G. T. (1997) A metalloradical mechanism for the generation of oxygen from water in photosynthesis, *Science* 277, 1953-1956.
84. Tommos, C., Tang, X. S., Warncke, K., Hoganson, C. W., Styring, S., Mccracken, J., Diner, B. A., and Babcock, G. T. (1995) Spin-Density Distribution, Conformation, and Hydrogen-Bonding of the Redox-Active Tyrosine Y-Z in Photosystem-II from Multiple Electron Magnetic-Resonance Spectroscopies - Implications for Photosynthetic Oxygen Evolution, *Journal of the American Chemical Society* 117, 10325-10335.
85. Ahlbrink, R., Haumann, M., Cherepanov, D., Bogershausen, O., Mulkidjanian, A., and Junge, W. (1998) Function of tyrosine Z in water oxidation by photosystem II: electrostatical promotor instead of hydrogen abstractor, *Biochemistry* 37, 1131-1142.
86. Junge, W., Haumann, M., Ahlbrink, R., Mulkidjanian, A., and Clausen, J. (2002) Electrostatics and proton transfer in photosynthetic water oxidation, *Philos Trans R Soc Lond B Biol Sci* 357, 1407-1417; discussion 1417-1420.
87. Rappaport, F., and Lavergne, J. (1997) Charge recombination and proton transfer in manganese-depleted photosystem II, *Biochemistry* 36, 15294-15302.
88. Zhang, M. T., Irebo, T., Johansson, O., and Hammarstrom, L. (2011) Proton-coupled electron transfer from tyrosine: a strong rate dependence on intramolecular proton transfer distance, *J Am Chem Soc* 133, 13224-13227.
89. Moore, G. F., Hambourger, M., Gervaldo, M., Poluektov, O. G., Rajh, T., Gust, D., Moore, T. A., and Moore, A. L. (2008) A bioinspired construct that mimics the proton coupled electron transfer between P680*+ and the Tyr(Z)-His190 pair of photosystem II, *J Am Chem Soc* 130, 10466-10467.
90. Megiatto, J. D., Jr., Mendez-Hernandez, D. D., Tejeda-Ferrari, M. E., Teillout, A. L., Llansola-Portoles, M. J., Kodis, G., Poluektov, O. G., Rajh, T., Mujica, V., Groy, T. L., Gust, D., Moore, T. A., and Moore, A. L. (2014) A bioinspired redox relay that mimics radical interactions of the Tyr-His pairs of photosystem II, *Nat Chem* 6, 423-428.
91. Imahori, H., Tamaki, K., Guldi, D. M., Luo, C., Fujitsuka, M., Ito, O., Sakata, Y., and Fukuzumi, S. (2001) Modulating charge separation and charge recombination dynamics in porphyrin-fullerene linked dyads and triads: Marcus-normal versus inverted region, *J Am Chem Soc* 123, 2607-2617.
92. Imahori, H., Guldi, D. M., Tamaki, K., Yoshida, Y., Luo, C., Sakata, Y., and Fukuzumi, S. (2001) Charge separation in a novel artificial photosynthetic reaction center lives 380 ms, *J Am Chem Soc* 123, 6617-6628.
93. Fukuzumi, S., Ohkubo, K., and Suenobu, T. (2014) Long-lived charge separation and applications in artificial photosynthesis, *Acc Chem Res* 47, 1455-1464.
94. Sibert, R. S., Josowicz, M., and Barry, B. A. (2010) Control of proton and electron transfer in de novo designed, biomimetic beta hairpins, *ACS Chem Biol* 5, 1157-1168.
95. Pagba, C. V., McCaslin, T. G., Chi, S. H., Perry, J. W., and Barry, B. A. (2016) Proton-Coupled Electron Transfer and a Tyrosine-Histidine Pair in a Photosystem II-Inspired beta-Hairpin Maquette: Kinetics on the Picosecond Time Scale, *J Phys Chem B* 120, 1259-1272.

96. Tommos, C., Skalicky, J. J., Pilloud, D. L., Wand, A. J., and Dutton, P. L. (1999) De novo proteins as models of radical enzymes, *Biochemistry* 38, 9495-9507.
97. Glover, S. D., Jorge, C., Liang, L., Valentine, K. G., Hammarstrom, L., and Tommos, C. (2014) Photochemical tyrosine oxidation in the structurally well-defined alpha3Y protein: proton-coupled electron transfer and a long-lived tyrosine radical, *J Am Chem Soc* 136, 14039-14051.
98. Berry, B. W., Martinez-Rivera, M. C., and Tommos, C. (2012) Reversible voltammograms and a Pourbaix diagram for a protein tyrosine radical, *Proc Natl Acad Sci U S A* 109, 9739-9743.
99. Martinez-Rivera, M. C., Berry, B. W., Valentine, K. G., Westerlund, K., Hay, S., and Tommos, C. (2011) Electrochemical and structural properties of a protein system designed to generate tyrosine Pourbaix diagrams, *J Am Chem Soc* 133, 17786-17795.
100. Lubitz, W., Ogata, H., Rudiger, O., and Reijerse, E. (2014) Hydrogenases, *Chem Rev* 114, 4081-4148.
101. Sano, Y., Onoda, A., and Hayashi, T. (2012) Photocatalytic hydrogen evolution by a diiron hydrogenase model based on a peptide fragment of cytochrome c556 with an attached diiron carbonyl cluster and an attached ruthenium photosensitizer, *J Inorg Biochem* 108, 159-162.
102. Sano, Y., Onoda, A., and Hayashi, T. (2011) A hydrogenase model system based on the sequence of cytochrome c: photochemical hydrogen evolution in aqueous media, *Chem Commun (Camb)* 47, 8229-8231.
103. Jones, A. K., Lichtenstein, B. R., Dutta, A., Gordon, G., and Dutton, P. L. (2007) Synthetic hydrogenases: incorporation of an iron carbonyl thiolate into a designed peptide, *J Am Chem Soc* 129, 14844-14845.
104. Lee, C. H., Dogutan, D. K., and Nocera, D. G. (2011) Hydrogen generation by hangman metalloporphyrins, *J Am Chem Soc* 133, 8775-8777.
105. Losse, S., Vos, J. G., and Rau, S. (2010) Catalytic hydrogen production at cobalt centres, *Coord Chem Rev* 254, 2492-2504.
106. Robertson, W. D., Bovell, A. M., and Warncke, K. (2013) Cobinamide production of hydrogen in a homogeneous aqueous photochemical system, and assembly and photoreduction in a (betaalpha)₈ protein, *J Biol Inorg Chem* 18, 701-713.
107. Sommer, D. J., Vaughn, M. D., Clark, B. C., Tomlin, J., Roy, A., and Ghirlanda, G. (2016) Reengineering cyt b562 for hydrogen production: A facile route to artificial hydrogenases, *Biochim Biophys Acta* 1857, 598-603.
108. Sommer, D. J., Vaughn, M. D., and Ghirlanda, G. (2014) Protein secondary-shell interactions enhance the photoinduced hydrogen production of cobalt protoporphyrin IX, *Chem Commun (Camb)* 50, 15852-15855.
109. Dogutan, D. K., McGuire, R., Jr., and Nocera, D. G. (2011) Electrocatalytic water oxidation by cobalt(III) hangman beta-octafluoro corroles, *J Am Chem Soc* 133, 9178-9180.
110. Li, C. Z., Nishiyama, K., and Taniguchi, I. (2000) Electrochemical and spectroelectrochemical studies on cobalt myoglobin, *Electrochim Acta* 45, 2883-2888.
111. Gao, J. X., and Rusling, J. F. (1998) Electron transfer and electrochemical catalysis using cobalt-reconstituted myoglobin in a surfactant film, *J Electroanal Chem* 449, 1-4.
112. Fahnenschmidt, M., Bittl, R., Schlodder, E., Haehnel, W., and Lubitz, W. (2001) Characterization of de novo synthesized four-helix bundle proteins with metalloporphyrin cofactors, *Phys Chem Chem Phys* 3, 4082-4090.

113. Utschig, L. M., Silver, S. C., Mulfort, K. L., and Tiede, D. M. (2011) Nature-driven photochemistry for catalytic solar hydrogen production: a Photosystem I-transition metal catalyst hybrid, *J Am Chem Soc* **133**, 16334-16337.
114. Krassen, H., Schwarze, A., Friedrich, B., Ataka, K., Lenz, O., and Heberle, J. (2009) Photosynthetic hydrogen production by a hybrid complex of photosystem I and [NiFe]-hydrogenase, *ACS Nano* **3**, 4055-4061.
115. Lubner, C. E., Knorz, P., Silva, P. J., Vincent, K. A., Happe, T., Bryant, D. A., and Golbeck, J. H. (2010) Wiring an [FeFe]-hydrogenase with photosystem I for light-induced hydrogen production, *Biochemistry* **49**, 10264-10266.
116. Ihara, M., Nishihara, H., Yoon, K. S., Lenz, O., Friedrich, B., Nakamoto, H., Kojima, K., Honma, D., Kamachi, T., and Okura, I. (2006) Light-driven hydrogen production by a hybrid complex of a [NiFe]-hydrogenase and the cyanobacterial photosystem I, *Photochem Photobiol* **82**, 676-682.
117. Kalman, L., LoBrutto, R., Allen, J. P., and Williams, J. C. (1999) Modified reaction centres oxidize tyrosine in reactions that mirror photosystem II, *Nature* **402**, 696-699.
118. Kalman, L., Williams, J. C., and Allen, J. P. (2011) Energetics for oxidation of a bound manganese cofactor in modified bacterial reaction centers, *Biochemistry* **50**, 3310-3320.
119. Thielges, M., Uyeda, G., Camara-Artigas, A., Kalman, L., Williams, J. C., and Allen, J. P. (2005) Design of a redox-linked active metal site: manganese bound to bacterial reaction centers at a site resembling that of photosystem II, *Biochemistry* **44**, 7389-7394.
120. Allen, J. P., Olson, T. L., Oyala, P., Lee, W. J., Tufts, A. A., and Williams, J. C. (2012) Light-driven oxygen production from superoxide by Mn-binding bacterial reaction centers, *Proc Natl Acad Sci U S A* **109**, 2314-2318.
121. Conlan, B., Cox, N., Su, J. H., Hillier, W., Messinger, J., Lubitz, W., Dutton, P. L., and Wydrzynski, T. (2009) Photo-catalytic oxidation of a di-nuclear manganese centre in an engineered bacterioferritin 'reaction centre', *Biochim Biophys Acta* **1787**, 1112-1121.
122. Hingorani, K., Conlan, B., Hillier, W., and Wydrzynski, T. (2009) Elucidating Photochemical Pathways of Tyrosine Oxidation in an Engineered Bacterioferritin 'Reaction Centre', *Aust J Chem* **62**, 1351-1354.
123. Hingorani, K., Pace, R., Whitney, S., Murray, J. W., Smith, P., Cheah, M. H., Wydrzynski, T., and Hillier, W. (2014) Photo-oxidation of tyrosine in a bio-engineered bacterioferritin 'reaction centre'-a protein model for artificial photosynthesis, *Biochim Biophys Acta* **1837**, 1821-1834.
124. Farid, T. A., Kodali, G., Solomon, L. A., Lichtenstein, B. R., Sheehan, M. M., Fry, B. A., Bialas, C., Ennist, N. M., Siedlecki, J. A., Zhao, Z., Stetz, M. A., Valentine, K. G., Anderson, J. L., Wand, A. J., Discher, B. M., Moser, C. C., and Dutton, P. L. (2013) Elementary tetrahelical protein design for diverse oxidoreductase functions, *Nat Chem Biol* **9**, 826-833.
125. Baker, D. (2010) An exciting but challenging road ahead for computational enzyme design, *Protein Sci* **19**, 1817-1819.
126. Esposti, M. D., De Vries, S., Crimi, M., Ghelli, A., Patarnello, T., and Meyer, A. (1993) Mitochondrial cytochrome b: evolution and structure of the protein, *Biochim Biophys Acta* **1143**, 243-271.
127. Stroebel, D., Choquet, Y., Popot, J. L., and Picot, D. (2003) An atypical haem in the cytochrome b(6)f complex, *Nature* **426**, 413-418.

128. Mathews, F. S., Bethge, P. H., and Czerwinski, E. W. (1979) The structure of cytochrome b562 from *Escherichia coli* at 2.5 Å resolution, *J Biol Chem* 254, 1699-1706.
129. Weber, P. C., Bartsch, R. G., Cusanovich, M. A., Hamlin, R. C., Howard, A., Jordan, S. R., Kamen, M. D., Meyer, T. E., Weatherford, D. W., Nguyen huu, X., and Salemme, F. R. (1980) Structure of cytochrome c': a dimeric, high-spin haem protein, *Nature* 286, 302-304.
130. Dautant, A., Meyer, J. B., Yariv, J., Precigoux, G., Sweet, R. M., Kalb, A. J., and Frolow, F. (1998) Structure of a monoclinic crystal form of cytochrome b1 (Bacterioferritin) from *E. coli*, *Acta Crystallogr D Biol Crystallogr* 54, 16-24.
131. Høgbom, M., Galander, M., Andersson, M., Kolberg, M., Hofbauer, W., Lassmann, G., Nordlund, P., and Lendzian, F. (2003) Displacement of the tyrosyl radical cofactor in ribonucleotide reductase obtained by single-crystal high-field EPR and 1.4-Å x-ray data, *P Natl Acad Sci USA* 100, 3209-3214.
132. Shiba, T., Kido, Y., Sakamoto, K., Inaoka, D. K., Tsuge, C., Tatsumi, R., Takahashi, G., Balogun, E. O., Nara, T., Aoki, T., Honma, T., Tanaka, A., Inoue, M., Matsuoka, S., Saimoto, H., Moore, A. L., Harada, S., and Kita, K. (2013) Structure of the trypanosome cyanide-insensitive alternative oxidase, *Proc Natl Acad Sci U S A* 110, 4580-4585.
133. Rosenzweig, A. C., Brandstetter, H., Whittington, D. A., Nordlund, P., Lippard, S. J., and Frederick, C. A. (1997) Crystal structures of the methane monooxygenase hydroxylase from *Methylococcus capsulatus* (Bath): implications for substrate gating and component interactions, *Proteins* 29, 141-152.
134. Rozwarski, D. A., Gronenborn, A. M., Clore, G. M., Bazan, J. F., Böhm, A., Wlodawer, A., Hatada, M., and Karplus, P. A. (1994) Structural comparisons among the short-chain helical cytokines, *Structure* 2, 159-173.
135. de Vos, A. M., Ultsch, M., and Kossiakoff, A. A. (1992) Human growth hormone and extracellular domain of its receptor: crystal structure of the complex, *Science* 255, 306-312.
136. Lewis, M., Chang, G., Horton, N. C., Kercher, M. A., Pace, H. C., Schumacher, M. A., Brennan, R. G., and Lu, P. (1996) Crystal structure of the lactose operon repressor and its complexes with DNA and inducer, *Science* 271, 1247-1254.
137. Kamtekar, S., and Hecht, M. H. (1995) Protein Motifs. 7. The four-helix bundle: what determines a fold?, *Faseb J* 9, 1013-1022.
138. Chino, M., Maglio, O., Nastri, F., Pavone, V., DeGrado, W. F., and Lombardi, A. (2015) Artificial Diiron Enzymes with a De Novo Designed Four-Helix Bundle Structure, *Eur J Inorg Chem* 2015, 3371-3390.
139. Cochran, F. V., Wu, S. P., Wang, W., Nanda, V., Saven, J. G., Therien, M. J., and DeGrado, W. F. (2005) Computational de novo design and characterization of a four-helix bundle protein that selectively binds a nonbiological cofactor, *J Am Chem Soc* 127, 1346-1347.
140. Rau, H. K., and Haehnel, W. (1998) Design, synthesis, and properties of a novel cytochrome b model, *Journal of the American Chemical Society* 120, 468-476.
141. Ghirlanda, G., Osyczka, A., Liu, W., Antolovich, M., Smith, K. M., Dutton, P. L., Wand, A. J., and DeGrado, W. F. (2004) De novo design of a D2-symmetrical protein that reproduces the diheme four-helix bundle in cytochrome bc1, *J Am Chem Soc* 126, 8141-8147.
142. Fry, H. C., Lehmann, A., Saven, J. G., DeGrado, W. F., and Therien, M. J. (2010) Computational design and elaboration of a de novo heterotetrameric alpha-helical

- protein that selectively binds an emissive abiological (porphinato)zinc chromophore, *J Am Chem Soc* 132, 3997-4005.
143. Robertson, D. E., Farid, R. S., Moser, C. C., Urbauer, J. L., Mulholland, S. E., Pidikiti, R., Lear, J. D., Wand, A. J., DeGrado, W. F., and Dutton, P. L. (1994) Design and synthesis of multi-haem proteins, *Nature* 368, 425-432.
 144. Sharp, R. E., Diers, J. R., Bocian, D. F., and Dutton, P. L. (1998) Differential binding of iron(III) and zinc(II) protoporphyrin IX to synthetic four-helix bundles, *Journal of the American Chemical Society* 120, 7103-7104.
 145. Daldal, F. (2004) Structure, function and biogenesis of the cytochrome BC1 complex in bacteria, *Bba-Bioenergetics* 1658, 63-63.
 146. Kranz, R. G., Richard-Fogal, C., Taylor, J. S., and Frawley, E. R. (2009) Cytochrome c biogenesis: mechanisms for covalent modifications and trafficking of heme and for heme-iron redox control, *Microbiol Mol Biol Rev* 73, 510-528, Table of Contents.
 147. Makino, R., Park, S. Y., Obayashi, E., Iizuka, T., Hori, H., and Shiro, Y. (2011) Oxygen binding and redox properties of the heme in soluble guanylate cyclase: implications for the mechanism of ligand discrimination, *J Biol Chem* 286, 15678-15687.
 148. Springer, B. A., Sligar, S. G., Olson, J. S., and Phillips, G. N. (1994) Mechanisms of Ligand Recognition in Myoglobin, *Chemical Reviews* 94, 699-714.
 149. Meunier, B., de Visser, S. P., and Shaik, S. (2004) Mechanism of oxidation reactions catalyzed by cytochrome p450 enzymes, *Chem Rev* 104, 3947-3980.
 150. Moser, C. C., Sheehan, M. M., Ennist, N. M., Kodali, G., Bialas, C., Englander, M. T., Discher, B. M., and Dutton, P. L. (2016) De Novo Construction of Redox Active Proteins, *Methods Enzymol* 580, 365-388.
 151. Gibney, B. R., Rabanal, F., Skalicky, J. J., Wand, A. J., and Dutton, P. L. (1999) Iterative protein redesign, *Journal of the American Chemical Society* 121, 4952-4960.
 152. McAllister, K. A., Zou, H., Cochran, F. V., Bender, G. M., Senes, A., Fry, H. C., Nanda, V., Keenan, P. A., Lear, J. D., Saven, J. G., Therien, M. J., Blasie, J. K., and DeGrado, W. F. (2008) Using alpha-helical coiled-coils to design nanostructured metalloporphyrin arrays, *J Am Chem Soc* 130, 11921-11927.
 153. Fairman, R., Chao, H. G., Mueller, L., Lavoie, T. B., Shen, L. Y., Novotny, J., and Matsueda, G. R. (1995) Characterization of a New 4-Chain Coiled-Coil - Influence of Chain-Length on Stability, *Protein Science* 4, 1457-1469.
 154. Huang, S. S., Koder, R. L., Lewis, M., Wand, A. J., and Dutton, P. L. (2004) The HP-1 maquette: from an apoprotein structure to a structured hemoprotein designed to promote redox-coupled proton exchange, *Proc Natl Acad Sci U S A* 101, 5536-5541.
 155. Arai, R., Kobayashi, N., Kimura, A., Sato, T., Matsuo, K., Wang, A. F., Platt, J. M., Bradley, L. H., and Hecht, M. H. (2012) Domain-swapped dimeric structure of a stable and functional de novo four-helix bundle protein, WA20, *J Phys Chem B* 116, 6789-6797.
 156. Patel, S. C., and Hecht, M. H. (2012) Directed evolution of the peroxidase activity of a de novo-designed protein, *Protein Eng Des Sel* 25, 445-452.
 157. Wei, Y., Kim, S., Fela, D., Baum, J., and Hecht, M. H. (2003) Solution structure of a de novo protein from a designed combinatorial library, *Proc Natl Acad Sci U S A* 100, 13270-13273.
 158. Shifman, J. M., Moser, C. C., Kalsbeck, W. A., Bocian, D. F., and Dutton, P. L. (1998) Functionalized de novo designed proteins: mechanism of proton coupling to oxidation/reduction in heme protein maquettes, *Biochemistry* 37, 16815-16827.

159. Crick, F. H. C. (1953) The Packing of Alpha-Helices - Simple Coiled-Coils, *Acta Crystallogr* 6, 689-697.
160. Kamtekar, S., Schiffer, J. M., Xiong, H., Babik, J. M., and Hecht, M. H. (1993) Protein design by binary patterning of polar and nonpolar amino acids, *Science* 262, 1680-1685.
161. McLachlan, A. D., and Stewart, M. (1975) Tropomyosin coiled-coil interactions: evidence for an unstaggered structure, *J Mol Biol* 98, 293-304.
162. Lupas, A. N., and Gruber, M. (2005) The structure of alpha-helical coiled coils, *Adv Protein Chem* 70, 37-78.
163. Strelkov, S. V., and Burkhard, P. (2002) Analysis of alpha-helical coiled coils with the program TWISTER reveals a structural mechanism for stutter compensation, *J Struct Biol* 137, 54-64.
164. Landschulz, W. H., Johnson, P. F., and Mcknight, S. L. (1988) The Leucine Zipper - a Hypothetical Structure Common to a New Class of DNA-Binding Proteins, *Science* 240, 1759-1764.
165. Harbury, P. B., Zhang, T., Kim, P. S., and Alber, T. (1993) A Switch between 2-Stranded, 3-Stranded and 4-Stranded Coiled Coils in Gcn4 Leucine-Zipper Mutants, *Science* 262, 1401-1407.
166. Krylov, D., Mikhailenko, I., and Vinson, C. (1994) A Thermodynamic Scale for Leucine-Zipper Stability and Dimerization Specificity - E-Interhelical and G-Interhelical Interactions, *Embo Journal* 13, 2849-2861.
167. Alberti, S., Oehler, S., Vonwilckenbergmann, B., and Mullerhill, B. (1993) Genetic-Analysis of the Leucine Heptad Repeats of Lac Repressor - Evidence for a 4-Helical Bundle, *Embo Journal* 12, 3227-3236.
168. Bryson, J. W., Betz, S. F., Lu, H. S., Suich, D. J., Zhou, H. X., O'Neil, K. T., and DeGrado, W. F. (1995) Protein design: a hierarchic approach, *Science* 270, 935-941.
169. Betz, S. F., Raleigh, D. P., and Degrado, W. F. (1993) De-Novo Protein Design - from Molten Globules to Native-Like States, *Curr Opin Struc Biol* 3, 601-610.
170. Betz, S. F., and DeGrado, W. F. (1996) Controlling topology and native-like behavior of de novo-designed peptides: design and characterization of antiparallel four-stranded coiled coils, *Biochemistry* 35, 6955-6962.
171. Betz, S. F., Liebman, P. A., and DeGrado, W. F. (1997) De novo design of native proteins: characterization of proteins intended to fold into antiparallel, rop-like, four-helix bundles, *Biochemistry* 36, 2450-2458.
172. Munson, M., O'Brien, R., Sturtevant, J. M., and Regan, L. (1994) Redesigning the hydrophobic core of a four-helix-bundle protein, *Protein Sci* 3, 2015-2022.
173. Banner, D. W., Kokkinidis, M., and Tsernoglou, D. (1987) Structure of the ColE1 rop protein at 1.7 Å resolution, *J Mol Biol* 196, 657-675.
174. Westerlund, K., Moran, S. D., Privett, H. K., Hay, S., Jarvet, J., Gibney, B. R., and Tommos, C. (2008) Making a single-chain four-helix bundle for redox chemistry studies, *Protein Eng Des Sel* 21, 645-652.
175. Frolov, F., Kalb, A. J., and Yariv, J. (1994) Structure of a unique twofold symmetric haem-binding site, *Nat Struct Biol* 1, 453-460.
176. Hunte, C., Koepke, J., Lange, C., Rossmann, T., and Michel, H. (2000) Structure at 2.3 Å resolution of the cytochrome bc(1) complex from the yeast *Saccharomyces cerevisiae* co-crystallized with an antibody Fv fragment, *Structure* 8, 669-684.

177. Summa, C. M., Lombardi, A., Lewis, M., and DeGrado, W. F. (1999) Tertiary templates for the design of diiron proteins, *Curr Opin Struct Biol* 9, 500-508.
178. Willis, M. A., Bishop, B., Regan, L., and Brunger, A. T. (2000) Dramatic structural and thermodynamic consequences of repacking a protein's hydrophobic core, *Structure* 8, 1319-1328.
179. Solan, A., Ratia, K., and Fairman, R. (2002) Exploring the role of alanine in the structure of the Lac repressor tetramerization domain, a ferritin-like Alacoil, *J Mol Biol* 317, 601-612.
180. Liu, J., Zheng, Q., Deng, Y., Li, Q., Kallenbach, N. R., and Lu, M. (2007) Conformational specificity of the lac repressor coiled-coil tetramerization domain, *Biochemistry* 46, 14951-14959.
181. Gernert, K. M., Surles, M. C., Labean, T. H., Richardson, J. S., and Richardson, D. C. (1995) The Alacoil: a very tight, antiparallel coiled-coil of helices, *Protein Sci* 4, 2252-2260.
182. Grigoryan, G., and DeGrado, W. F. (2011) Probing designability via a generalized model of helical bundle geometry, *J Mol Biol* 405, 1079-1100.
183. Yankovskaya, V., Horsefield, R., Tornroth, S., Luna-Chavez, C., Miyoshi, H., Leger, C., Byrne, B., Cecchini, G., and Iwata, S. (2003) Architecture of succinate dehydrogenase and reactive oxygen species generation, *Science* 299, 700-704.
184. Huang, L. S., Cobessi, D., Tung, E. Y., and Berry, E. A. (2005) Binding of the respiratory chain inhibitor antimycin to the mitochondrial bc(1) complex: A new crystal structure reveals an altered intramolecular hydrogen-bonding pattern, *Journal of Molecular Biology* 351, 573-597.
185. Tron, T., Crimi, M., Colson, A. M., and Esposti, M. D. (1991) Structure-Function-Relationships in Mitochondrial Cytochrome-B Revealed by the Kinetic and Circular Dichroic Properties of 2 Yeast Inhibitor-Resistant Mutants, *European Journal of Biochemistry* 199, 753-760.
186. Berry, E. A., and Walker, F. A. (2008) Bis-histidine-coordinated hemes in four-helix bundles: how the geometry of the bundle controls the axial imidazole plane orientations in transmembrane cytochromes of mitochondrial complexes II and III and related proteins, *J Biol Inorg Chem* 13, 481-498.
187. Saribas, A. S., Ding, H., Dutton, P. L., and Daldal, F. (1997) Substitutions at position 146 of cytochrome b affect drastically the properties of heme bL and the Qo site of *Rhodobacter capsulatus* cytochrome bc1 complex, *Biochim Biophys Acta* 1319, 99-108.
188. Faiella, M., Andreozzi, C., de Rosales, R. T., Pavone, V., Maglio, O., Natri, F., DeGrado, W. F., and Lombardi, A. (2009) An artificial di-iron oxo-protein with phenol oxidase activity, *Nat Chem Biol* 5, 882-884.
189. Torres Martin de Rosales, R., Faiella, M., Farquhar, E., Que, L., Jr., Andreozzi, C., Pavone, V., Maglio, O., Natri, F., and Lombardi, A. (2010) Spectroscopic and metal-binding properties of DF3: an artificial protein able to accommodate different metal ions, *J Biol Inorg Chem* 15, 717-728.
190. Ma, D., Brandon, N. R., Cui, T., Bondarenko, V., Canlas, C., Johansson, J. S., Tang, P., and Xu, Y. (2008) Four-alpha-helix bundle with designed anesthetic binding pockets. Part I: structural and dynamical analyses, *Biophys J* 94, 4454-4463.
191. Cui, T., Bondarenko, V., Ma, D., Canlas, C., Brandon, N. R., Johansson, J. S., Xu, Y., and Tang, P. (2008) Four-alpha-helix bundle with designed anesthetic binding pockets. Part II: halothane effects on structure and dynamics, *Biophys J* 94, 4464-4472.

192. Eliezer, D., and Wright, P. E. (1996) Is apomyoglobin a molten globule? Structural characterization by NMR, *J Mol Biol* 263, 531-538.
193. Lin, L., Pinker, R. J., Forde, K., Rose, G. D., and Kallenbach, N. R. (1994) Molten globular characteristics of the native state of apomyoglobin, *Nat Struct Biol* 1, 447-452.
194. Pfeil, W., Nolting, B. O., and Jung, C. (1993) Apocytochrome P450cam is a native protein with some intermediate-like properties, *Biochemistry* 32, 8856-8862.
195. Feng, Y., Sligar, S. G., and Wand, A. J. (1994) Solution structure of apocytochrome b562, *Nat Struct Biol* 1, 30-35.
196. Falzone, C. J., Mayer, M. R., Whiteman, E. L., Moore, C. D., and Lecomte, J. T. (1996) Design challenges for hemoproteins: the solution structure of apocytochrome b5, *Biochemistry* 35, 6519-6526.
197. Smith, L. J., Kahraman, A., and Thornton, J. M. (2010) Heme proteins-Diversity in structural characteristics, function, and folding, *Proteins-Structure Function and Bioinformatics* 78, 2349-2368.
198. Landfried, D. A., Vuletich, D. A., Pond, M. P., and Lecomte, J. T. (2007) Structural and thermodynamic consequences of b heme binding for monomeric apoglobins and other apoproteins, *Gene* 398, 12-28.
199. Skalicky, J. J., Gibney, B. R., Rabanal, F., Urbauer, R. J. B., Dutton, P. L., and Wand, A. J. (1999) Solution structure of a designed four-alpha-helix bundle maquette scaffold, *Journal of the American Chemical Society* 121, 4941-4951.
200. Calhoun, J. R., Natri, F., Maglio, O., Pavone, V., Lombardi, A., and DeGrado, W. F. (2005) Artificial diiron proteins: from structure to function, *Biopolymers* 80, 264-278.
201. Bradley, J. M., Svistunenko, D. A., Lawson, T. L., Hemmings, A. M., Moore, G. R., and Le Brun, N. E. (2015) Three Aromatic Residues are Required for Electron Transfer during Iron Mineralization in Bacterioferritin, *Angew Chem Int Ed Engl* 54, 14763-14767.
202. Calhoun, J. R., Bell, C. B., 3rd, Smith, T. J., Thamann, T. J., DeGrado, W. F., and Solomon, E. I. (2008) Oxygen reactivity of the biferrous site in the de novo designed four helix bundle peptide DFsc: nature of the "intermediate" and reaction mechanism, *J Am Chem Soc* 130, 9188-9189.
203. Bell, C. B., Calhoun, J. R., Bobyr, E., Wei, P. P., Hedman, B., Hodgson, K. O., DeGrado, W. F., and Solomon, E. T. (2009) Spectroscopic Definition of the Biferrous and Biferic Sites in de Novo Designed Four-Helix Bundle DFsc Peptides: Implications for O-2 Reactivity of Binuclear Non-Heme Iron Enzymes, *Biochemistry* 48, 59-73.
204. Pasternak, A., Kaplan, J., Lear, J. D., and Degrado, W. F. (2001) Proton and metal ion-dependent assembly of a model diiron protein, *Protein Sci* 10, 958-969.
205. Snyder, R. A., Butch, S. E., Reig, A. J., DeGrado, W. F., and Solomon, E. I. (2015) Molecular-Level Insight into the Differential Oxidase and Oxygenase Reactivities of de Novo Due Ferri Proteins, *J Am Chem Soc* 137, 9302-9314.
206. Reig, A. J., Pires, M. M., Snyder, R. A., Wu, Y., Jo, H., Kulp, D. W., Butch, S. E., Calhoun, J. R., Szyperski, T. G., Solomon, E. I., and Degrado, W. F. (2012) Alteration of the oxygen-dependent reactivity of de novo Due Ferri proteins, *Nat Chem* 4, 900-906.
207. Lombardi, A., Summa, C. M., Geremia, S., Randaccio, L., Pavone, V., and DeGrado, W. F. (2000) Retrostructural analysis of metalloproteins: application to the design of a minimal model for diiron proteins, *Proc Natl Acad Sci U S A* 97, 6298-6305.

208. Calhoun, J. R., Liu, W., Spiegel, K., Dal Peraro, M., Klein, M. L., Valentine, K. G., Wand, A. J., and DeGrado, W. F. (2008) Solution NMR structure of a designed metalloprotein and complementary molecular dynamics refinement, *Structure* 16, 210-215.
209. Calhoun, J. R., Kono, H., Lahr, S., Wang, W., DeGrado, W. F., and Saven, J. G. (2003) Computational design and characterization of a monomeric helical dinuclear metalloprotein, *J Mol Biol* 334, 1101-1115.
210. Wade, H., Stayrook, S. E., and DeGrado, W. F. (2006) The structure of a designed diiron(III) protein: implications for cofactor stabilization and catalysis, *Angew Chem Int Ed Engl* 45, 4951-4954.
211. Geremia, S., Di Costanzo, L., Randaccio, L., Engel, D. E., Lombardi, A., Natri, F., and DeGrado, W. F. (2005) Response of a designed metalloprotein to changes in metal ion coordination, exogenous ligands, and active site volume determined by X-ray crystallography, *J Am Chem Soc* 127, 17266-17276.
212. Di Costanzo, L., Wade, H., Geremia, S., Randaccio, L., Pavone, V., DeGrado, W. F., and Lombardi, A. (2001) Toward the de novo design of a catalytically active helix bundle: a substrate-accessible carboxylate-bridged dinuclear metal center, *J Am Chem Soc* 123, 12749-12757.
213. Kaplan, J., and DeGrado, W. F. (2004) De novo design of catalytic proteins, *Proc Natl Acad Sci U S A* 101, 11566-11570.
214. Ulas, G., Lemmin, T., Wu, Y., Gassner, G. T., and DeGrado, W. F. (2016) Designed metalloprotein stabilizes a semiquinone radical, *Nat Chem* 8, 354-359.
215. O'Shea, E. K., Rutkowski, R., and Kim, P. S. (1992) Mechanism of specificity in the Fos-Jun oncoprotein heterodimer, *Cell* 68, 699-708.
216. Summa, C. M., Rosenblatt, M. M., Hong, J. K., Lear, J. D., and DeGrado, W. F. (2002) Computational de novo design, and characterization of an A(2)B(2) diiron protein, *J Mol Biol* 321, 923-938.
217. Marsh, E. N., and DeGrado, W. F. (2002) Noncovalent self-assembly of a heterotetrameric diiron protein, *Proc Natl Acad Sci U S A* 99, 5150-5154.
218. Bender, G. M., Lehmann, A., Zou, H., Cheng, H., Fry, H. C., Engel, D., Therien, M. J., Blasie, J. K., Roder, H., Saven, J. G., and DeGrado, W. F. (2007) De novo design of a single-chain diphenylporphyrin metalloprotein, *J Am Chem Soc* 129, 10732-10740.
219. Nagi, A. D., and Regan, L. (1997) An inverse correlation between loop length and stability in a four-helix-bundle protein, *Folding & Design* 2, 67-75.
220. Ho, S. P., and DeGrado, W. F. (1987) Design of a 4-Helix Bundle Protein - Synthesis of Peptides Which Self-Associate into a Helical Protein, *Journal of the American Chemical Society* 109, 6751-6758.
221. Predki, P. F., and Regan, L. (1995) Redesigning the topology of a four-helix-bundle protein: monomeric Rop, *Biochemistry* 34, 9834-9839.
222. Lahr, S. J., Engel, D. E., Stayrook, S. E., Maglio, O., North, B., Geremia, S., Lombardi, A., and DeGrado, W. F. (2005) Analysis and design of turns in alpha-helical hairpins, *J Mol Biol* 346, 1441-1454.
223. Cohen, C., and Parry, D. A. (1990) Alpha-helical coiled coils and bundles: how to design an alpha-helical protein, *Proteins* 7, 1-15.
224. Maglio, O., Natri, F., Calhoun, J. R., Lahr, S., Wade, H., Pavone, V., DeGrado, W. F., and Lombardi, A. (2005) Artificial di-iron proteins: solution characterization of four helix

- bundles containing two distinct types of inter-helical loops, *J Biol Inorg Chem* 10, 539-549.
225. Richardson, J. S., and Richardson, D. C. (1988) Amino acid preferences for specific locations at the ends of alpha helices, *Science* 240, 1648-1652.
 226. Aurora, R., and Rose, G. D. (1998) Helix capping, *Protein Sci* 7, 21-38.
 227. Dougherty, W. G., Cary, S. M., and Parks, T. D. (1989) Molecular genetic analysis of a plant virus polyprotein cleavage site: a model, *Virology* 171, 356-364.
 228. Doig, A. J., and Baldwin, R. L. (1995) N- and C-capping preferences for all 20 amino acids in alpha-helical peptides, *Protein Sci* 4, 1325-1336.
 229. Huyghues-Despointes, B. M., Scholtz, J. M., and Baldwin, R. L. (1993) Helical peptides with three pairs of Asp-Arg and Glu-Arg residues in different orientations and spacings, *Protein Sci* 2, 80-85.

Chapter 2: Design and characterization of a reaction center maquette

In order to stabilize a light-activated charge separated state, a working reaction center requires, at a minimum, an electron acceptor, a light-absorbing pigment molecule, and an electron donor. Various cofactors can be used to satisfy these roles, and previous work in *de novo* protein design has produced helical bundle maquettes capable of assembling hemes (1-3), zinc tetrapyrroles (2, 4, 5), redox-active amino acids (6-8), and di-metal centers (9, 10), but no maquette has been made to assemble all of these cofactors into a single working scaffold. Such a maquette would have to be larger and more complex than a typical maquette in order to assemble all of these cofactors. Furthermore, a reaction center maquette has added constraints; cofactors must be recognized by their respective active sites and not bind to incorrect sites, and the inter-cofactor distances and local environments need to be tuned to enable light-driven electron transfer with rates appropriate for charge separation. This chapter will describe the design and initial characterization of a working reaction center maquette.

2.1 Crystallization trials with BT6, a multifunctional heme-binding maquette

2.1.1: Structure and function of BT6

The *de novo*-designed four-helix bundle protein BT6, named after its designers Bruce Lichtenstein and Tammer Farid, is a heme binding maquette from the Dutton lab that is capable of multiple functions (2). BT6 has demonstrated light-activated electron transfer functions

involving zinc porphyrins, zinc chlorins, flavins, and heme. It is also capable of electron transfer to cytochrome c, energy transfer, and oxygen binding (2).

The light-driven electron transfer function of BT6 represents a first step toward a working reaction center. The wild type form of BT6 has two bis-histidine heme binding sites, and mutation of one heme-ligating histidine amino acid to alanine in one of the heme sites renders that site unable to bind heme but still able to bind zinc tetrapyrroles. Light absorption by the zinc tetrapyrrole (the pigment) creates a high-energy zinc tetrapyrrole excited state that reduces the heme electron acceptor. Since there is no electron donor in BT6 to trap heme in the reduced state, the electron quickly tunnels back to the strongly oxidizing zinc tetrapyrrole radical cation and to regenerate the ground state. If a sacrificial electron donor such as aniline is added to the solution, it can reduce the zinc tetrapyrrole radical cation before reduced heme does, which would trap the heme in the reduced state. Since heme is bound to same protein as the zinc tetrapyrrole $\sim 19 \text{ \AA}$ away, it usually outcompetes the aniline reaction, but over extended periods of continuous illumination and at high aniline concentrations, heme can be converted from the oxidized to the reduced form over several minutes, as shown in Figure 2.1 (2).

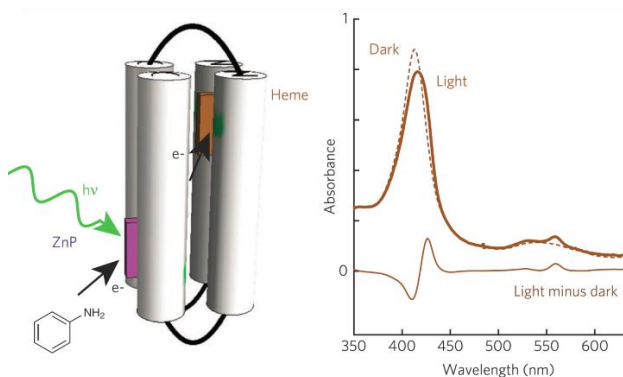


Figure 2.1: Charge separation in BT6 using a sacrificial electron donor

A BT6 mutant with heme B and Zn protoporphyrin IX (ZnP) is able to drive heme reduction under illumination in the presence of aniline. This is observed by a band shift in the ultraviolet/visible spectrum. The light minus dark difference spectrum is identical to a reduced heme minus oxidized heme difference spectrum. Figure reproduced from Farid et al., 2013 (2).

BT6 is a four-helix bundle but does not appear to be a canonical coiled coil; a precursor of BT6 with a very similar sequence, L31M, was crystallized in the apo-state and showed very straight α -helices with a slight right-handed supercoil instead of the typical left-handed twist of normal coiled coils (11). Also, the helices of BT6 and its precursors rotate to allow heme binding, which partially buries several glutamic acid residues, giving rise to an unusual, strained conformation (2, 12). As a result, BT6 in the holo-state might be quite different from the previously solved apo-state structure of L31M (11). No high-resolution structure of BT6 has been solved, but the many functions and unusual structural properties of BT6 make it a worthwhile target of structural studies.

The sequence of BT6 is given below, with each helix on a new line and loops separated from helical sequences by a space. Heme-ligating histidines are shown in red. The sequences of all four helices are identical, as are all three flexible 9-residue glycine-rich loops (2):

```
(N-terminus) : GEIWKQHEDALQKFEEALNQFEDLKQL GSGSGSGG
                EIWKQHEDALQKFEEALNQFEDLKQL GSGSGSGG
                EIWKQHEDALQKFEEALNQFEDLKQL GSGSGSGG
                EIWKQHEDALQKFEEALNQFEDLKQL (C-terminus)
```

2.1.1 Efforts to crystallize BT6

BT6 has all the requirements for crystallographic structure determination. It binds its heme B cofactors with high affinity (both heme dissociation constants are less than 2 nM), it is stable in the holo-state (with a melting temperature close to 80°C), and it has well-dispersed NMR peaks in the holo-state (2). Unfortunately, its highly repetitive sequence makes structure determination by NMR extremely difficult. Past attempts at crystallography have shown BT6 and similar maquettes to be recalcitrant to crystallization, possibly because of the long, flexible

loops and the many charged surface amino acids that give the maquette an overall charge of about -16 at neutral pH.

Here, another attempt at BT6 crystallization was made. BT6 was expressed in *E. coli* with an N-terminal His₆ tag and purified by Ni-NTA column chromatography. This His₆ tag was removed by TEV protease, and the TEV protease, His₆ tag, and uncleaved maquette were removed with a second Ni-NTA column. A size exclusion column yielded monomeric BT6 protein, and after adding heme B, BT6 was ready for crystallization trials.

Several months of crystallization trials eventually yielded small red crystals that were not suitable for diffraction. A 500 μM BT6 stock solution was prepared in 10 mM MgCl₂ with 10 mM 4-(2-hydroxyethyl)-1-piperazineethanesulfonic acid (HEPES) buffer at pH 7.5. Small, irregular crystals were grown in hanging drop experiments at 4°C over well solutions of 50-600 mM MgCl₂ and ~28-34% w/v polyethylene glycol monomethyl ether with an average molecular weight of 2000 Da (PEGMME 2000). Well solutions were not buffered, as several different buffers were found to disrupt crystal formation. Shown below in Figure 2.2 is an example of the crystals observed. This crystallization drop includes crystals of various morphologies including needles, semicircular plates, and roughly hexagonal plates. Their red color shows that heme is present in the crystals. Lengths of BT6 crystals rarely exceeded ~1 μm .

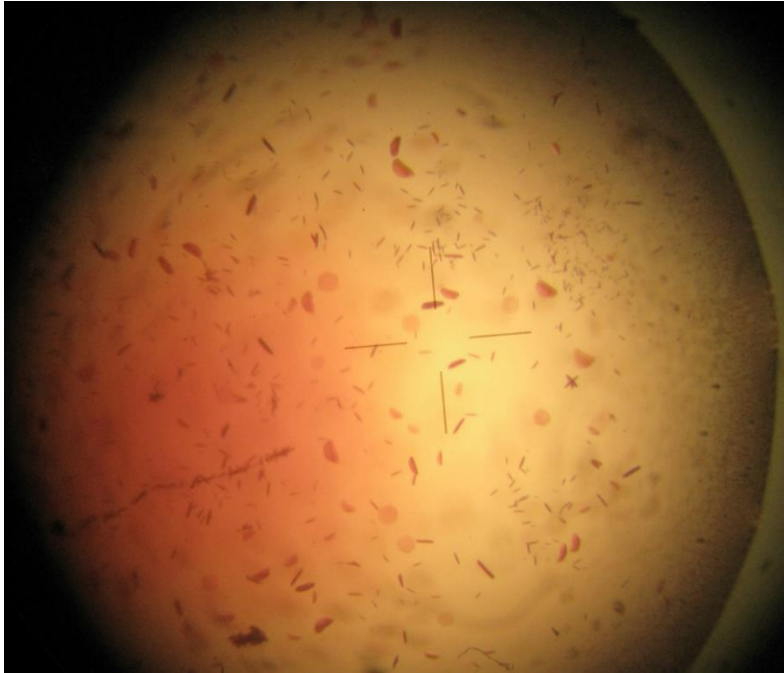


Figure 2.2: BT6 crystals not suitable for X-ray diffraction

Crystals were photographed after 3 weeks of growth at 4°C. Well solution was 300 mM MgCl₂, 32% w/v PEGMME 2000, and 1 mM HCl to adjust the pH. The crystallization drop contained 2 µL BT6 stock solution and 2 µL well solution. (Crystallization drop is labeled Tray B24, well D2).

2.1.2 Improved crystal growth in a modified BT6, BT6_2sl

Crystallization is often inhibited by flexible protein domains. The three long, 9-residue loops of BT6 are designed to be unstructured linkers. This length is unlikely to be necessary, as previous work has shown that four-helix bundles rarely require more than four residues in inter-helical loops for proper folding (13, 14). For this reason, crystallization trials were attempted with a BT6 variant with shortened loops. The middle loop of BT6 is believed to cross the bundle diagonally from helix 2 to helix 3, and may need to be longer; the second loop was left at 9 residues. The onerous task of site-directed mutagenesis in a maquette with such a repetitive sequence was tackled by fellow graduate student Joshua Mancini, who shortened loops 1 and 3 to 5 residues. The resulting sequence of BT6_2sl (also referred to as BT6sloop) is given below. The BT6_2sl sequence is identical to BT6, except for the two shortened loops.

```
(N-terminus) : GEIWKQHEDALQKFEEALNQFEDLKQL GGSGG
                EIWKQHEDALQKFEEALNQFEDLKQL GGSGSGSGG
                EIWKQHEDALQKFEEALNQFEDLKQL GGSGG
                EIWKQHEDALQKFEEALNQFEDLKQL (C-terminus)
```

A new round of crystallography with BT6_2sl following the same procedure as with BT6 gave improved results, including X-ray diffraction to $\sim 6\text{-}7$ Å resolution using rotating copper anode X-ray generator (see section 7.5 of the appendix for details). However, this resolution is not high enough to solve the crystal structure. BT6_2sl crystals were grown using a 760 μM BT6_2sl stock solution in 10 mM MgCl_2 , 10 mM HEPES buffer at pH 7.5. BT6_2sl crystals grew in similar conditions to BT6: hanging drops at 4°C over well solutions of 100-600 mM MgCl_2 and $\sim 20\text{-}34\%$ w/v PEGMME 2000. Crystals grew with an unusual semicylindrical morphology and were embedded in films that formed on the surface of the drops or on the cover slides and were somewhat difficult to extract for X-ray diffraction. Shown below in Figure 2.3 are two examples of BT6_2sl crystals that diffracted to $\sim 6\text{-}7$ Å resolution using a rotating copper anode X-ray source. The spacing between reflections was consistent with an asymmetric unit similar to the expected dimensions of a BT6_2sl monomer. However, many X-ray reflections appeared to be missing from the diffraction pattern, suggesting significant disorder in the crystals. A full data set was not collected.

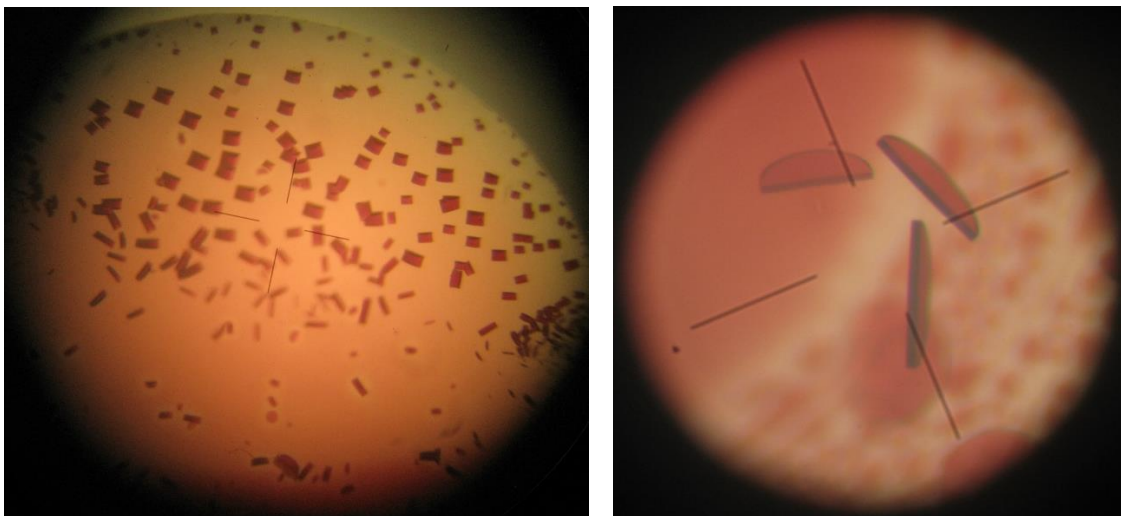


Figure 2.3: BT6_2sl crystals that diffract X-rays to 6-7 Å resolution

Two examples of BT6_2sl crystals that diffracted to 6-7 Å resolution. Before X-ray diffraction, crystals were dipped in a cryoprotectant similar to the well solution with increased PEGMME 2000 and MgCl₂ concentrations. Left: Three-week old BT6_2sl crystals grown at 4°C over a well solution of 600 mM MgCl₂ and 26% w/v PEGMME 2000. Right: Two-year old BT6_2sl crystals grown at 4°C over a well solution of 400 mM MgCl₂ and 23% w/v PEGMME 2000.

2.1.3 Promising results from BT6_3sl crystallography

Given the impact that shortened loops made on crystal quality in BT6_2sl, it was hypothesized that shortening the second loop also would further improve the crystal morphology and diffraction quality. Joshua Mancini used site-directed mutagenesis to shorten the second loop to create BT6_3sl, in which all three loops are shortened to five residues:

```
(N-terminus) : GEIWKQHEDALQKFEEALNQFEDLKQL GGSGG
                EIWKQHEDALQKFEEALNQFEDLKQL GGSGG
                EIWKQHEDALQKFEEALNQFEDLKQL GGSGG
                EIWKQHEDALQKFEEALNQFEDLKQL (C-terminus)
```

BT6_3sl was expressed and purified using a similar procedure to BT6. There was no sign of weakened affinity for heme B in BT6_3sl, and initial attempts at crystallographic structure determination have been pursued using a stock solution of 870 μM BT6_3sl with 10 mM MgCl₂ and 5 mM HEPES buffer at pH 7.5. Like BT6, BT6_3sl crystals grew at 4°C over well solutions of

~24-30% w/v PEGMME 2000 and 100-600 mM MgCl₂. BT6_3sl growth was best when the crystallization drop had a pH of about 7.0, but crystal growth was disrupted by buffer, as with other BT6 variants. BT6_3sl crystal morphology is greatly improved relative to BT6_2sl and BT6. While the crystals remain small (less than 10 μm in length), they tend to grow in the shapes of hexagonal prisms rather than thin semicylinders. Crystals appeared within a day and continued growing for about 5 days. Only one crystal so far has been mounted for X-ray diffraction, and it only diffracted to ~12 Å resolution, but there did not appear to be any missing reflections as there were with BT6_2sl. The preliminary low resolution of BT6_3sl X-ray diffraction is probably limited by the small size of the crystals (~1-10 μm in length) rather than problems with disorder in the crystals. Some examples of BT6_3sl crystals are shown in Figure 2.4.

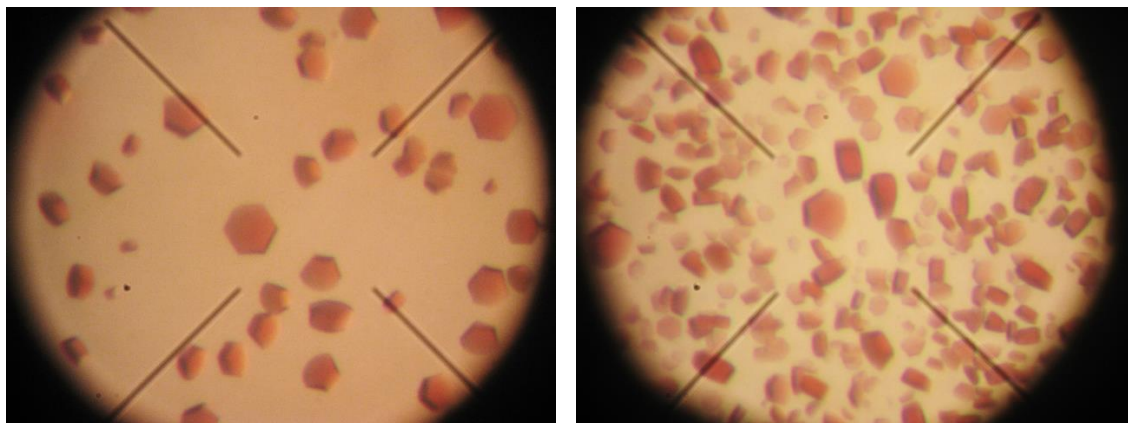


Figure 2.4: BT6_3sl crystals grow with improved morphology compared to BT6 and BT6_2sl

Left: Five-month old BT6_3sl crystals grown at 4°C over a well solution of 300 mM MgCl₂ and 25.5% w/v PEGMME 2000. Right: Five-month old BT6_3sl crystals grown at 4°C over a well solution of 200 mM MgCl₂ and 26% w/v PEGMME 2000.

While the crystal structure of BT6 has not yet been solved, the current results are very promising. It is interesting to note that the crystallization conditions of BT6 are similar to the conditions used for crystallization of the apo-state of its precursor, the L31M maquette. L31M crystals grew from well solutions with 30% w/v PEGMME 2000, similar to BT6. However, the

L31M condition also had 100 mM HEPES buffer (which disrupts BT6 crystal growth), it did not contain MgCl_2 , and the crystals grew at 28°C instead of 4°C. Still, it may be worthwhile to test the cryoprotectant that was favored for L31M (30% v/v PEG 550 and 30 mM HEPES buffer at pH 7.4) (11). Better crystals might also grow from the use of higher purity protein, such as that purified by high-performance liquid chromatography (HPLC). Future work is likely to produce a high-resolution BT6_3sl structure that may elucidate the mechanisms of different functions in BT6.

2.2 Design of the reaction center maquette MZH3

The trapping of a reduced heme state in BT6 is an important step toward developing an artificial reaction center maquette, but the ultimate goal is water oxidation and fuel generation. BT6 is not equipped to incorporate additional cofactor binding sites that will be necessary to achieve this function.

A new maquette was designed to function as a simplified reaction center by incorporating electron donors, a pigment, and an electron acceptor. The maquette was named MZH3 for the cofactors it binds: Metal, Zinc tetrapyrrole, and Heme. The design of MZH3 makes use of the extensive literature on four-helix bundle design that has been built up since Regan and DeGrado made their first *de novo* four-helix bundle protein in 1988 (15). MZH3 was designed to have an antiparallel topology, which is common to the natural carboxylate-bridged diiron and dimanganese family of proteins as well as cytochromes b and b_6 . MZH3 is a 196-amino acid protein with an extinction coefficient of $12,490 \text{ M}^{-1}\text{cm}^{-1}$ at 280 nm, a molecular weight of 22.5 kDa, and a theoretical isoelectric point at pH 5.5 in the apo-state (calculations

performed using ExPASy ProtParam online server) (16). The sequence of MZH3 in its single-letter amino acid code is:

GSPELRQEHQQLAQEFQQLLQEIQQLGRELLKGELQGIGKQLREASEKARNPEKKSVLQKILEDEEKHIELLETLQ
 QTGQEAQQLLQELQQTGQELWQLGGSGGPPELRQKHQQLAQKIQQLLQKHQQLGAKILEDEEKHIELLETILG
 GSGGDELRELLKGELQGIGKQYRELQQLGQKAQQLVQKLQQTGQKLWQLG

A more informative depiction of the sequence of MZH3 is given in Table 2.1. The winding “snaked” sequence in the second row, which is written backwards in helices 2 and 4, shows which amino acids form layers together in the hydrophobic core.

<i>heptad positions</i>	(N) <i>Forward</i> : efgabcdefgabcdefgabcdefgabcdefgabcdefgabcdef (C) (C) <i>Reverse</i> : gfedcbagfedcbagfedcbagfedcbagfedcbagfedcbagf (N)
MZH3 “snaked” sequence	(N-term) → GSPELRQEHQQLAQEFQQLLQEIQQLGRELLKGELQGIGKQLREASEK ARN → (C) (C) ← GGSGG LQWLEQGTQQLLQQLLQQAEGTQQLTELEIHKEDDELKQLVSKKEP ← (N) (N) → PELRQKHQQLAQKIQQLLQKHQQLGAKILEDEEKHIELLETIL GGSGG → (C) (C-term) ← GLQWLKCGTQQLKQVLQQAQKGLQCLERYQKIQQLGKILERLED ← (N)
MZH3 N-to-C forward sequence	(N-term) GSPELRQEHQQLAQEFQQLLQEIQQLGRELLKGELQGIGKQLREASEK ARN (C) (N) PEKKSVLQKILEDEEKHIELLETLQQTGQEAQQLLQELQQTGQELWQL GGSGG (C) (N) PELRQKHQQLAQKIQQLLQKHQQLGAKILEDEEKHIELLETIL GGSGG (C) (N) DELRELLKGELQGIGKQYRELQQLGQKAQQLVQKLQQTGQKLWQLG (C-term)

Table 2.1: Amino acid sequence of MZH3

Coiled coil heptad positions *a* through *g* are denoted in the top row for both forward (N- to C-terminus) and reverse (C- to N-terminus) sequences, and they are aligned with corresponding positions in the MZH3 amino acid sequences. Residues highlighted yellow are *a*-position residues. The MZH3 amino acid sequences have each helix written on a new line with loops separated from the helices by a space. The N- and C-terminal ends of each helix are denoted by the letter in parentheses at either end of each helix, and “N-term” and “C-term” denote termini of the protein. Green amino acids belong to the cytochrome b-like tetrapyrrole binding section of MZH3, whereas blue amino acids belong to the Due Ferro-like di-metal binding section of the protein. In the MZH3 “snaked” sequence, helices 2 and 4 are written in reverse so that amino acids that are spatially close together in the folded protein are close together in the snaked sequence diagram. Red boxes enclose layers of the hydrophobic core, each of which includes two *a*- and two *d*-position residues. The N-to-C forward sequence is written conventionally, from the N-terminus to the C-terminus.

2.2.1 Use of the Due Ferro maquette sequences in MZH3

The electron donating section of the photosystem II reaction center has a Mn_4Ca water oxidizing cluster and tyrosine Z, which transfer electrons to the pigment P680 when it becomes oxidized (17). The design of MZH3 sought to reproduce this electron transfer pathway in a four-helix bundle, and perhaps the most obvious template for such a design is the family of carboxylate-bridged diiron and dimanganese proteins that are diverse in function but similar in structure (18). This scaffold was recreated in the Due Ferro series of maquettes created by the DeGrado and Lombardi groups and collaborators (9). The carboxylate-bridged diiron fold usually includes one or two tyrosine amino acids that form hydrogen bonds with glutamates. In some cases, such as bacterioferritin and ribonucleotide reductase, these tyrosines function as redox-active cofactors (19, 20). Given the success of the Due Ferro maquettes, the sequence of one of these proteins was used as the metal and tyrosine section of the protein with some adaptations.

The Due Ferro section of MZH3 was based primarily on the sequence of DF3, a helix-loop-helix dimeric 4-helix bundle maquette protein that can bind two metal ions and was originally used for ferroxidase and phenol oxidase activity (21, 22). DF3 has higher affinity for metal ions than previous Due Ferro proteins, and its four active site glycines allow for a wide cavity that facilitates efficient entry and exit of substrate molecules and may allow space for a larger metal cluster to assemble, such as one close to the size of the oxygen evolving cluster of photosystem II. However, these helical glycines make DF3 less stable than previous Due Ferro proteins. The design of MZH3 compensates for this instability with its length and by using a single-chain monomeric rather than noncovalent dimeric folded state.

To avoid undesirable side reactions, redox-active amino acids near the di-metal site were removed. A single tyrosine was kept between the metal center and the pigment as an

intermediate electron donor, similar to tyrosine Z of photosystem II. Two interfacial Trp residues were changed to Leu, one Tyr was changed to Glu, and one of the two active site second-shell Tyr residues was mutated to Leu (see Table 2.2). A Tyr to Phe mutation might have been more conservative than Tyr to Leu, but studies involving the single-chain Due Ferro variant DFsc showed that the Y51F mutation resulted in sample heterogeneity and was not amenable to spectral analysis. Instead, the Y51L mutation was selected as an alternative because Leu has a similar Stokes radius to Tyr; Y51L was useful for spectroscopy (23).

<i>heptad positions</i>	(N) Forward:	efgabcde fga bcde fga bcde fg	(C)
	(C) Reverse:	gfedcbagfedcbagfedcbagfe	(N)
DF section of MZH3 “snaked” sequence	(N-term) →	... RELLK GE L Q G IKQ L R EASEK ARN	→ (C)
	(C) ←	... TEL L E I H KE E DEL I KQ L V SKKEP	← (N)
	(N) →	... AKI L E DE E KH I EL L ET IL GGSGG	→ (C)
	(C-term) ←	... ER Y Q KI G Q L E G KLL ER L E D	← (N)
DF3 “snaked” sequence	(N-term) →	DY RELLK GE L Q G IKQ Y REALEY THN	→ (C)
	(C-term) ←	GL IT L WE I H KE E DEL I K A L V P	← (N)
	(N) →	PV AKI L E DE E KH I E W L ETILG	→ (C-term)
	(C) ←	NHT YEL A E R Y Q KI G Q L E G KLL ER L Y D	← (N-term)
DF2t “snaked” sequence	(N-term) →	MDY RELY KLE Q Q AM KLY REASEK ARN	→ (C)
	(C-term) ←	GN IT L WE I H KE E DEL I KQ L V SKKEP	← (N)
	(N) →	PE K KS V Q KI L E DE E KH I E W L ETING	→ (C-term)
	(C) ←	NRA KES A E R Y L KM A Q Q EL K Y L ER L Y DM	← (N-term)

Table 2.2: Comparison of the Due Ferro section of MZH3 to DF2t and DF3 sequences

Residues written in orange line the active site and are thought to be important for metal binding affinity and catalysis (21). Residues of MZH3 in red are found in neither DF2t nor DF3, and were selected in order to remove redox-active amino acids or to connect helices using a flexible linker. Loops are separated from the helices by a space. Residues highlighted yellow are in α -positions. The termini of each helix are denoted by the letter in parentheses at either end of each helix.

2.2.2 Tetrapyrrole binding section of MZH3

While Due Ferro maquettes are compatible with the envisioned structure and function of MZH3, no tetrapyrrole binding maquette precisely suits the needs for the tetrapyrrole section

of MZH3. In addition, high-resolution structures of any maquette with tetrapyrroles bound do not exist, so the predicted structures have not been confirmed. By designing a new tetrapyrrole binding section, inter-cofactor distances can be more precisely controlled, the structure can be tailored to help it join seamlessly to the Due Ferro section of the maquette, and important lessons learned from years of research on four-helix bundle sequence and structure that appear to have been neglected in some maquettes can be implemented in full force to build a uniquely-structured high-affinity multi-cofactor binding protein.

Charge separation in an MZH3 tetrad should be optimized if the rate of electron transfer between the pigment and acceptor is slowed relative to the donor-to-pigment rate. This can be accomplished by using a long pigment-acceptor distance and short donor-pigment distance. If the pigment-acceptor distance is too long, however, the excited state of the zinc tetrapyrrole will decay before electron transfer can take place. Cytochrome b from the bc_1 complex, with its ~ 12 Å distance between hemes (24), is close to optimal for the purposes of MZH3. For this reason, general structural attributes of cytochrome b were reproduced in the MZH3 design. The sequence of cytochrome b, however, would not work in a soluble maquette, because cytochrome b is a transmembrane four-helix bundle. Cytochrome b has many nonpolar residues on its exterior, and helical propensities of amino acids are very different in nonpolar membrane environments; while glycines, prolines, and buried polar groups like glutamines and threonines are all tolerated quite well in a helical membrane protein, these residues would induce misfolding and aggregation in a water soluble maquette.

Layers of core α - and d -position amino acids in MZH3 followed the general layering pattern of cytochrome b. The design of MZH3 made use of the universally conserved heme-ligating histidines and notch glycines of cytochrome b (24). The histidines were placed at d -

positions and the glycines at α -positions. At the zinc tetrapyrrole site, one histidine was changed to isoleucine, since zinc tetrapyrroles have a pentacoordinate zinc ion and only one ligand is needed. Isoleucine was the residue chosen for a similar role in a four-helix bundle maquette that bound a synthetic zinc porphyrin (25). The d -position histidines were designed to make second shell hydrogen bonds to g -position threonines, as in cytochrome b. A hydrogen bond between a porphyrin-ligating histidine and a threonine has been incorporated into a maquette previously, and electron paramagnetic resonance (EPR) measurements with and without the second shell threonine indicated that the hydrogen bond tilted the imidazole rings of the histidines (26). Two α -position arginines were placed near the N-termini of helices 1 and 3 in order to try to make salt bridging interactions with propionate groups as observed in cytochrome b and to prevent hydrophobic collapse of the apo-state of the acceptor site, which might inhibit cofactor binding.

The three layers between the hemes of cytochrome b are subject to considerable variation across different species, but there are patterns in the total sizes of the layers (27). The bulkiest amino acids are in the middle layer (yellow in Figure 2.5, left). In the corresponding positions in MZH3, Phe and Ile were placed at the d -positions and Leu and Val were placed at the α -positions. The intermediate layers between the middle and histidine layers (blue in Figure 2.5, left) were composed of small and flexible Ala and Leu residues to accommodate the presence of part of the tetrapyrrole ring.

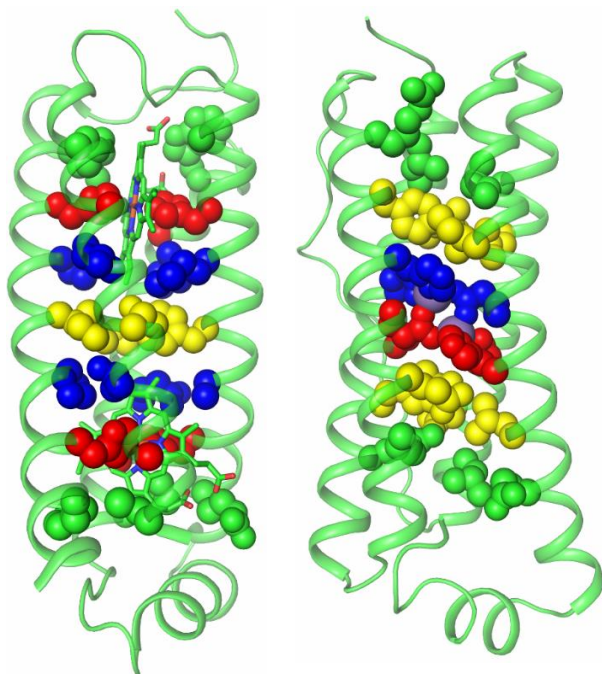


Figure 2.5: Layers in natural proteins

Structure of cytochrome b subunit from cytochrome bc_1 complex is shown at left with heme B cofactors represented as sticks (PDB ID: 1EZV) (24).

Bacterioferritin monomer is shown at right with Mn(II) ions represented as mauve spheres in the center (PDB ID: 1BCF) (28). Core α - and d -position amino acid side chains are represented as spheres. These residues segregate into layers which are distinguished by color. The basic idea of the MZH3 design is to merge a green layer from a cytochrome b-like structure and a green layer from a bacterioferritin-like structure to make a reaction center maquette. Images rendered using The PyMOL Molecular Graphics System, Version 1.7 Schrödinger, LLC.

2.2.3 Helix-helix interfaces in MZH3

Designing MZH3 to have proper distances between adjacent helices (interface widths), is a serious concern in the joining of these two very different protein modules. (Figure 2.6 shows a helical wheel diagram of an antiparallel four-helix bundle). Natural carboxylate-bridged diiron proteins tend to have e -position alanines to stabilize narrow, tightly packed e - e interfaces to make the canonical ferritin-like Alacoil (18, 29). In contrast, as described in the introduction, cytochrome b and other heme-binding antiparallel four-helix bundle proteins tend to bind heme so that the porphyrin ring lies parallel to the g - g interface and expands the e - e interface. As a result, the exceptionally wide e - e interface in the tetrapyrrole section of MZH3 must transition to become very narrow in the bacterioferritin-like section of the maquette. In addition, the g - g interface of carboxylate-bridged diiron proteins tends to be wide in order to accommodate the entry and departure of substrate and product molecules (18). Crystal structures of cytochrome

b show a slightly narrower *g-g* interface than is observed in diiron proteins (24). Some tetrapyrrole binding maquettes in the past have used a Rop-like Alacoil fold with alanines in *g*-positions to narrow the *g-g* interface (26, 30, 31).

In this way, the geometries of the cytochrome *b*-like and bacterioferritin-like four-helix bundles appear to be at odds with each other; if too much strain is exerted by one module onto the

other, cofactor binding in one module could affect the structure of the other. One advantage of using a Due Ferro sequence for the metal binding section of MZH3 is that its narrow *e-e* interface is unusually wide compared to most natural diiron and dimanganese proteins, and its wide *g-g* interface is unusually narrow compared to the natural proteins (32). In order to prevent a conflict between the tetrapyrrole and metal sections of the protein, the Rop-like Alacoil fold of earlier porphyrin binding maquettes (26, 30, 31) was rejected in favor of a wider *g-g* interface. To this end, the amino acid for most of the *g*-positions in the tetrapyrrole section of MZH3 was leucine. (The exceptions were the second shell threonines that were meant to make hydrogen bonds to histidines). Mutations of *e*-position interfacial alanines to leucines in

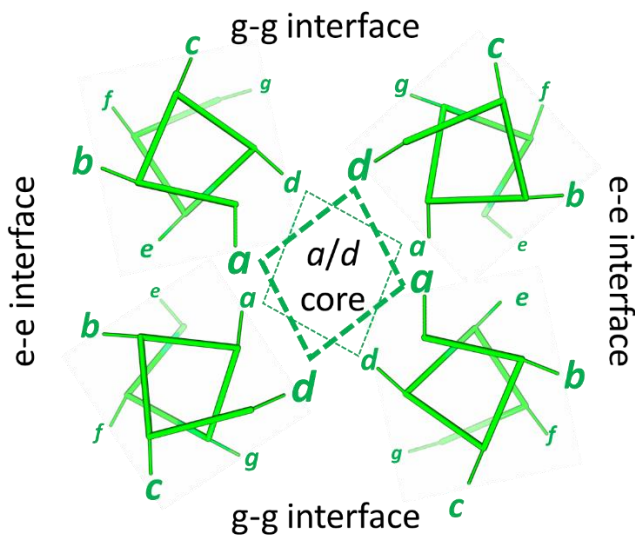


Figure 2.6: Helical wheel diagram of one heptad of an antiparallel four-helix bundle protein

The distance of an amino acid from the view is represented by the size of the heptad letter designation. Dotted lines represent hydrophobic interactions within a layer. In helices, thick ribbons connect α -carbons, while thinner lines represent C_{α} - C_{β} bonds. Image rendered using The PyMOL Molecular Graphics System, Version 1.7 Schrödinger, LLC.

the Lac repressor tetramerization domain have been predicted to force helices to rotate and move apart to accommodate the increased side chain volume (33). In addition, interfacial leucines are significantly more stabilizing than alanines (29, 33). Using *g*-position leucines in MZH3 allows for the expansion of the *g-g* interface to prevent strain in the transition between the tetrapyrrole and metal binding sections of MZH3.

Another way to prevent strain between the modules might be to ensure flexibility in the helices where the two modules meet. The pigment binding site already has two α -position glycine residues in the same layer as the histidine because of the similar notch glycine positions in cytochrome b, but it was given two more α -position glycines, G27 and G128, in the layer adjacent to the histidine layer nearest the metal binding module. This further expands the zinc tetrapyrrole binding pocket, which is at risk of hydrophobic collapse that could prevent binding of the pigment. Glycine residues G27 and G128 were also intended to increase the flexibility to allow a seamless transition from one module to the next.

2.2.4 Inter-helical loops in MZH3

In MZH3, the joining of a Due Ferro protein to a tetrapyrrole-binding protein required careful consideration of loop placement. On the electron acceptor end of MZH3, some solvent access is required to solubilize the propionate groups of protoporphyrin IX derivatives like heme B, and flexibility in the apo-state is believed to facilitate entry of the large, bulky tetrapyrrole cofactor into the binding cleft (34-36). In contrast, the DF3-like di-metal site of MZH3 is destabilized by four α -helical glycine residues and a water-filled active site containing four charged glutamates. In fact, the stability of DF3 was poor enough that it required the design of its own structured loop (21). For these reasons, the heme-binding end of MZH3 was chosen as

the end with N- and C-termini, and the DF end was given two loops in order to increase its stability (see Table 2.1). One of these loops came from DF2t (37), because the DF3 loop contains a solvent-exposed histidine, which may be capable of ligating metallo-tetrapyrroles (38) and thereby complicating characterization of MZH3. Similarly, the redesign of bacterioferritin for zinc chlorin binding called for the removal of surface histidines to avoid unintentional cofactor ligation (39). The metal site was chosen to be DF3-like because of the high metal binding affinity of DF3, but some parts of the sequence beyond the loop and active site regions differed between DF2t and DF3. Amino acids that were close to the loop were chosen to be DF2t-like, because loop stability depends on the overall structure of the protein (40). The other loop on the DF end is simply a flexible linker. This Gly-Gly-Ser-Gly-Gly linker unites the DF maquette into a single chain, as was done similarly in Rop and BT6 (2, 14). An identical linker was used on the heme-binding end of MZH3. A length of 5 residues was chosen for the glycine-rich linkers in order to guarantee sufficient length to prevent misfolding but also ensure high stability.

2.2.5 Inter-helical charge pairing interactions

The helical topology in Due Ferro proteins appears to be dictated by the sum of many interactions throughout the bundle including complementarity of core packing, inter-helical hydrogen bonds, and short, structured loops (37, 41). In MZH3, most core layers of the tetrapyrrole binding section are symmetrical, meaning that these hydrophobic contacts would not select for the left-turning antiparallel topology over the right-turning antiparallel topology. In addition, two of the loops in MZH3 are unstructured and cannot determine the topology. Interfacial *g*-position leucine pairing would strongly favor the antiparallel fold over the four other possible topologies that are all mixed parallel/antiparallel folds, but the right-turning

antiparallel topology would have the same leucine-leucine interactions as the left (see Figure 2.7). In order to help constrain the topology, charge pairing interactions were included in *c*-positions, as has been done previously in maquettes to dictate the topology (26, 42). Each helix in MZH3 included three charged *c*-position amino acids to pair with its adjacent helix across the *g-g* interface. Helices 1 and 2 were given *c*-position glutamates and helices 3 and 4 were given lysines, as depicted in Figure 2.7. As a result, each of the five alternative helix threading topologies that are possible given the short loops have helix-helix interactions that destabilize them relative to the intended helix topology. In order to prevent the *c*-position charged residues from being steered away from their intended hydrogen bonding partners, *b*- and *f*-position surface-exposed residues were made uncharged polar amino acids. There is really only one polar, uncharged amino acid with a reasonably high helical propensity, and that is glutamine (43). The decision to include many glutamine residues on the exterior of MZH3 along with *c*-position charged residues gives it an exterior that is very similar to the porphyrin array maquettes from the DeGrado group (25, 26, 44).

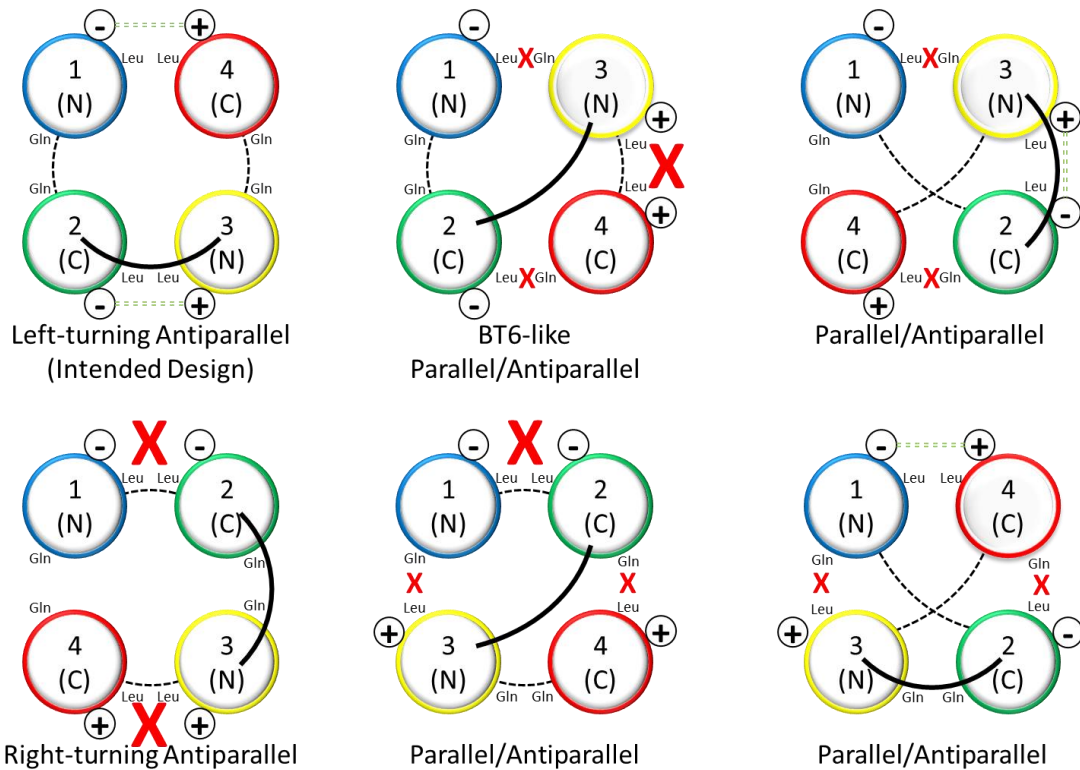


Figure 2.7: Negative design of MZH3

Possible four-helix bundle conformations are viewed from the heme-binding end. The helix number of each helix is given along with which end (N- or C-terminus) is facing the viewer. Thick black arcs represent connecting inter-helical loops on side facing viewer, and thin black dotted arcs represent inter-helical loops on far end of maquette. The circled + and – symbols stand for charged c-position lysine and glutamate residues, respectively. Green dotted lines represent charge pairing interactions, and large red X's represent charge clashes. Small red X's symbolize that the leucine zipper-like interaction of *g*-position leucines is disrupted.

This careful approach to the design of a four-helix bundle leans heavily upon specific examples of natural and *de novo* designed proteins in the literature. Can the many disparate lessons learned from all of these studies be integrated into a single design of a new protein? Or does each protein have such important nuances in its structure that takeaway messages from studies of other proteins cannot be relied upon to produce general rules for four-helix bundle

design? In order to evaluate the effectiveness this approach, the next section will describe the expression and routine characterization of MZH3.

2.3 Routine characterization of MZH3

In order to determine whether the design of MZH3 succeeded in creating a stable, folded protein maquette with the intended functions, MZH3 was subjected to a battery of routine tests. These included size exclusion chromatography to check the oligomeric state, ultraviolet/visible spectroscopy to measure cofactor binding, circular dichroism to test the stability, and redox titration to measure midpoint potentials. Methods for each technique are described in the appendix.

2.3.1 Size exclusion chromatography

Size exclusion chromatography (SEC) was used to determine the oligomerization state of MZH3. A mixture of monomeric and oligomeric MZH3 was observed after overexpression in *E. coli*, purification by Ni-NTA affinity chromatography, and cleavage of the His₆ tag by TEV protease (Figure 2.8, panel A). Addition of stoichiometric heme B or 4-fold excess ZnSO₄ to MZH3 injectant solution was not found to significantly affect the elution profile (data not shown). Monomeric and oligomeric MZH3 were collected and stored at 4°C overnight. To determine whether MZH3 monomers and oligomers rapidly interconvert, the samples were injected onto the SEC column again the next day (Figure 2.8, panels C and D). The chromatograms show that monomers remained monomeric and oligomers remained oligomeric. Oligomers can be converted to monomers by denaturing with 6.5 M GdnHCl and refolding by dilution.

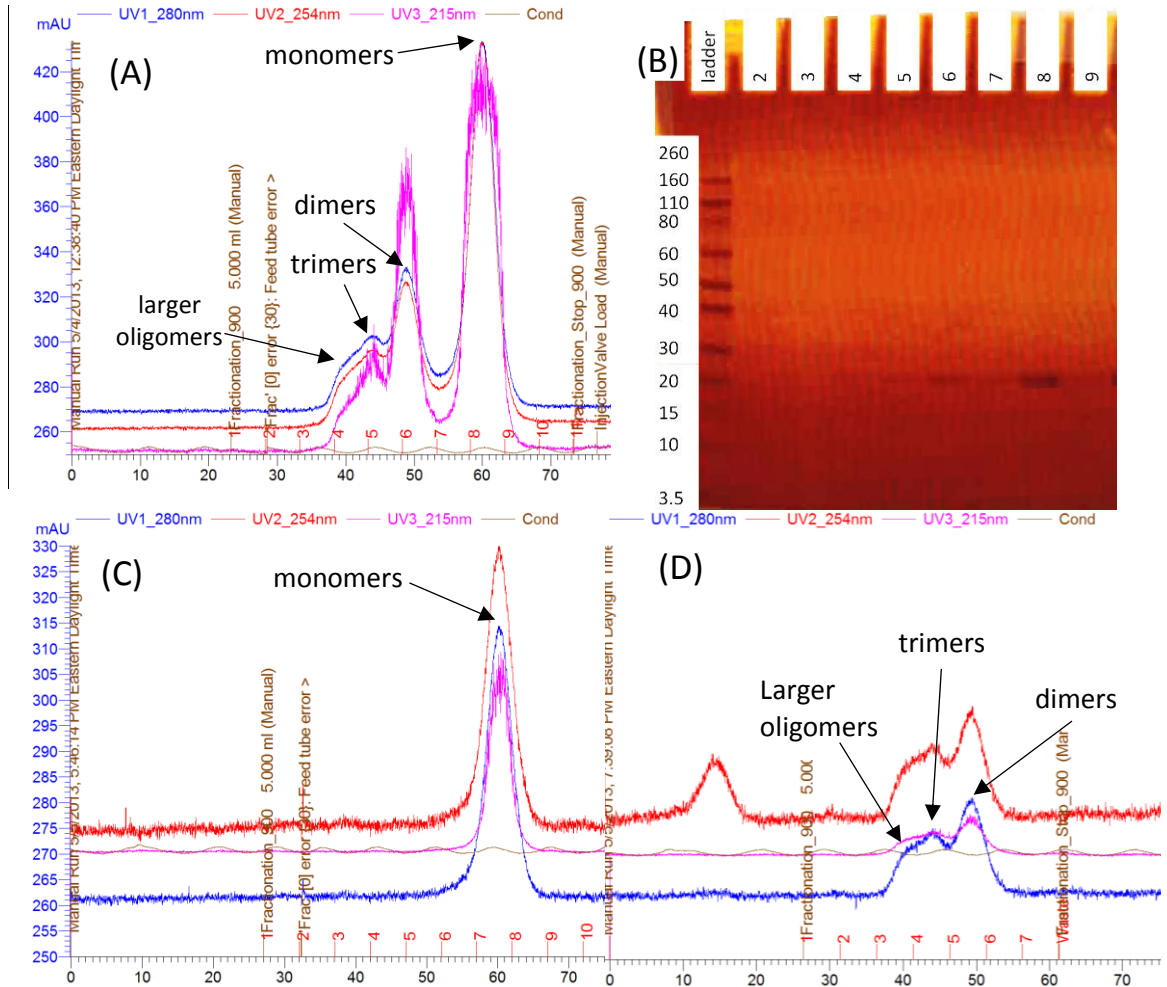


Figure 2.8: Size exclusion chromatography elution profiles of MZH3

(A) Chromatogram for initial SEC injection, with fraction numbers given at bottom. Fractions were collected separately and stored overnight at 4°C. (B) SDS-PAGE gel on SEC eluates from panel (A). Molecular weights of ladder bands are given at left in kDa. Well numbers given at the top of each well correspond to fraction numbers from SEC chromatogram in panel (A). After 1 day, (C) monomeric fraction was injected again, followed by (D) oligomeric fraction. Blue, red, and pink lines represent absorbance at indicated wavelengths vs. elution volume (mL). Running buffer was 50 mM NaCl, 10 mM MOPS buffer, pH 7.

To verify that the putative oligomeric MZH3 eluates were composed of MZH3 and not a higher molecular weight contaminant, samples from SEC fractions (labeled at the bottom of Figure 2.8A) were run in an SDS-PAGE gel, which denatures proteins so that they run as

monomers (Figure 2.8B). SDS-PAGE showed that a single band at ~22 kDa was present in all SEC fractions that had light-absorbing eluates, demonstrating that MZH3 (which has a molecular weight of 22.5 kDa) was present in each elution peak of the SEC column. No other significant bands were observed in SDS-PAGE.

MZH3 was designed to have a rod-like cylindrical shape with a diameter of about 2 nm and a length of about 7 nm, but roughly spherical globular proteins were used to standardize the size exclusion column. Given that SEC columns separate proteins based on Stokes radius rather than molecular weight (45), the rod-like shape of MZH3 is expected to decrease its elution volume relative to spherical proteins of the same molecular weight. This effect is observed for monomeric, dimeric, and trimeric states of MZH3, as shown in Figure 2.9.

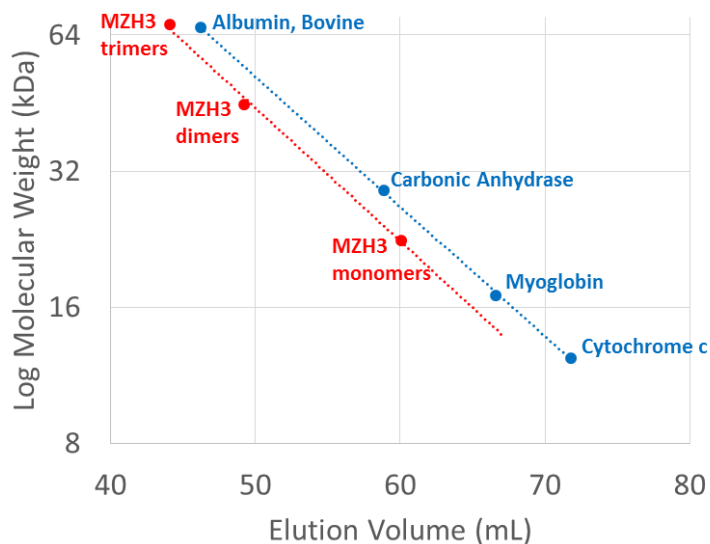


Figure 2.9: Size exclusion chromatography calibration curves

Blue: calibration curve for the XK 16/70 column (GE Healthcare Life Sciences) packed with 110 mL of Superdex 75 prep grade gel filtration medium (GE Healthcare Life Sciences). Red: MZH3 peak positions on same column for monomers, dimers, and trimers. Running buffer was 50 mM NaCl, 10 mM MOPS buffer, pH 7.5.

2.3.2 Ultraviolet/visible spectroscopy

Tetrapyrroles are strong absorbers of ultraviolet and visible light, and their absorption spectra are sensitive to their environments. Ligation of *the* central metal ion of a

metallotetrapyrrole by ligating amino acids such as histidine can trigger a pronounced band shift that can be used to monitor binding by ultraviolet/visible spectroscopy (UV/vis).

Overexpression of MZH3 in *E. coli* results in a red cell pellet, suggesting that MZH3 overexpression increases heme B biosynthesis. The red color of the sample persists during purification of MZH3 by Ni-NTA column chromatography, His-tag cleavage by TEV protease, and SEC. After purification, MZH3 is found to contain approximately 0.1 equivalents of heme B

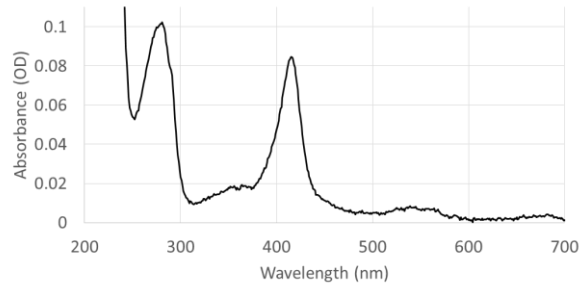


Figure 2.10: Heme binding by MZH3 *in vivo*

Spectrum of MZH3 after overexpression and purification, but before addition of heme B. The peak at 280 nm is due to absorbance of Trp and Tyr residues, and the peak at 415 nm is the Soret band of heme B. Conditions: 150mM NaCl, 6 mM phosphate buffer, pH 7.4.

per mole of MZH3, as estimated from the UV/vis spectra (Figure 2.10). When necessary, heme can be removed by high-performance liquid chromatography (HPLC) or by denaturation and washing with 2-butanone (46).

In the spectroscopic titrations presented below, cofactor solutions were titrated into protein solutions. Absorbance values at a selected wavelength were fitted to Equation 2.1, a one-site binding equation that relates the cofactor concentration c (the independent variable), absorbance A (the dependent variable), and four parameters: the total protein concentration P , the extinction coefficient of the cofactor bound to the protein ϵ_b , the extinction coefficient of the unbound cofactor ϵ_u , and the dissociation constant K_D :

$$A = c \cdot \epsilon_u + \frac{(\epsilon_b - \epsilon_u) \cdot \left[(K_D + P + c) - \sqrt{(K_D + P + c)^2 - 4 \cdot P \cdot c} \right]}{2} \quad \text{Equation 2.1}$$

2.3.3 UV/vis spectroscopy: Acceptor site

High-affinity binding of ferric heme B by MZH3 was demonstrated by UV/vis titration. The absorbance spectrum of MZH3 in complex with ferric heme has a Soret band at 415 nm with an extinction coefficient of $115,000 \text{ M}^{-1}\text{cm}^{-1}$ and broad Q bands at about 534 nm and 566 nm. This is similar to the yeast cytochrome b absorbance features which include a Soret band at 416 nm with an extinction coefficient of about $120,000 \text{ M}^{-1}\text{cm}^{-1}$ (47). Heme B is not soluble in aqueous solutions, so the unbound heme B spectrum is easily distinguished from the bound spectrum. Unbound heme B has broadened bands with significantly decreased extinction coefficients at the peaks. Fitting the absorbance of the Soret band at 415 nm vs. heme B concentration to Equation 2.1 gives a dissociation constant of less than 10 nM, which is near the resolution limit for the procedure (see Figure 2.11). This ferric heme B dissociation constant is very close to that of the natural soluble four-helix bundle hemoprotein cytochrome b_{562} , which is estimated at about 9 nM (48), although some other natural hemoproteins have much higher affinities (35).

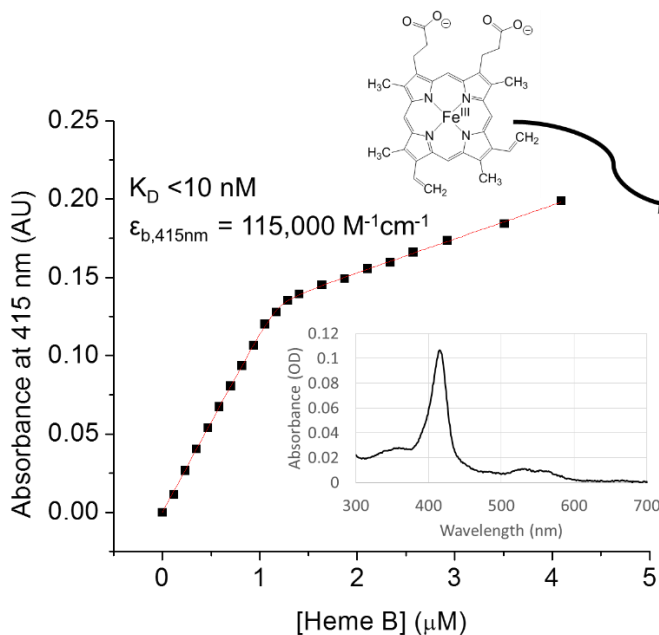


Figure 2.11: Heme B binding titration

UV/vis binding titration of ferric heme B into $1.2 \mu\text{M}$ MZH3. The structure of heme is shown at upper left and the spectrum at 0.8 equivalents of heme B per MZH3 is shown at beneath the curve. The schematic at right shows where heme B is expected to bind. Conditions: $10 \text{ mM Na}_2\text{HPO}_4$, 15 mM NaCl , pH 7.

A measurement of the reduced, ferrous heme B spectrum was made by adding dithionite to a solution of MZH3 with ferric heme B (Figure 2.12). The dithionite absorbance peak centered at 319 nm may interfere with the estimation of the Soret extinction coefficient in the reduced state, but it is about $160,000 \text{ M}^{-1}\text{cm}^{-1}$ at 430 nm.

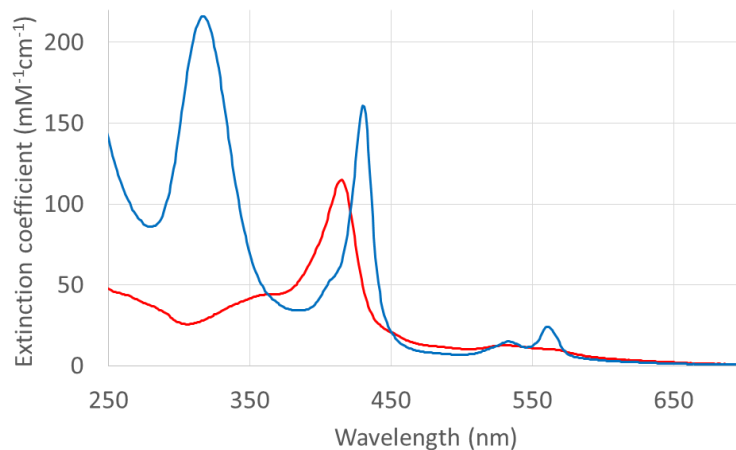


Figure 2.12: Heme B spectra in MZH3

Ferric heme B (red) and ferrous heme B (blue) spectra in MZH3. Ferrous spectrum was prepared by reduction with dithionite compared. Peak at 319 nm is due to excess dithionite. Conditions: 8 μM MZH3 with 1 equivalent of heme B, 15mM NaCl, 10mM phosphate buffer, pH7.

Replacement of the iron ion of heme B with cobalt gives cobalt protoporphyrin IX (CoPPIX), which is stable to oxygen in the Co(III) (cobaltic) state. CoPPIX is interesting as a potential electron acceptor because reduced cobalt tetrapyrroles are capable of proton reduction (49, 50). Co(III)PPIX does not have the pronounced spectral difference between the bound and unbound states that heme B has in aqueous solutions, partly because CoPPIX is more soluble. As a result, fitting the absorbance of the Soret band vs. CoPPIX concentration is difficult, because the curve is almost a straight line. However, the absorbance difference between 426 and 419 nm vs. CoPPIX concentration has a much sharper change in slope around 1.0 equivalent of cofactor per protein, allowing curve fitting with Equation 2.1 (see Figure 2.13).

The result of this fit was a dissociation constant of approximately 250 nM and an extinction coefficient of 220,000 M⁻¹cm⁻¹ for the Soret band at 426 nm in the MZH3-bound state. The estimated extinction coefficient of the Soret maximum for unbound Co(III)PPIX was 190,000 M⁻¹cm⁻¹, in agreement with previous work that found a value of 170,000 M⁻¹cm⁻¹ under similar conditions (49). The dissociation constant of 250 nM of MZH3 for Co(III)PPIX is about 25 times weaker than it is for heme B, but 35-fold stronger than the Co(III)PPIX affinity of cytochrome b₅₆₂ of 8.9 μM (49).

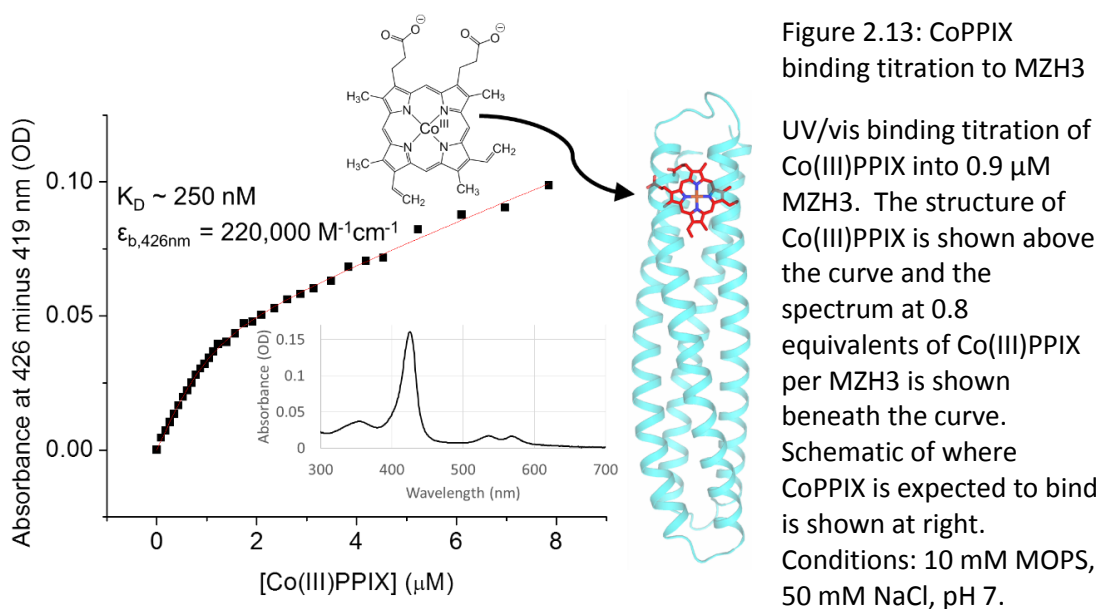


Figure 2.13: CoPPIX binding titration to MZH3

UV/vis binding titration of Co(III)PPIX into 0.9 μM MZH3. The structure of Co(III)PPIX is shown above the curve and the spectrum at 0.8 equivalents of Co(III)PPIX per MZH3 is shown beneath the curve. Schematic of where CoPPIX is expected to bind is shown at right. Conditions: 10 mM MOPS, 50 mM NaCl, pH 7.

Another iron tetrapyrrole with a structure similar to heme B is Fe(III) 2,4-diacetyl deuteroporphyrin IX (Fe-DADPIX), and it binds to MZH3 with a K_D of less than 10 nM, similar to heme B (Figure 2.14). Fe-DADPIX is similar in structure to heme B, but it has a higher electrochemical midpoint potential and red-shifted absorption bands relative to heme B. Its Soret maximum in MZH3 is about 90,000 M⁻¹cm⁻¹ at 431 nm.

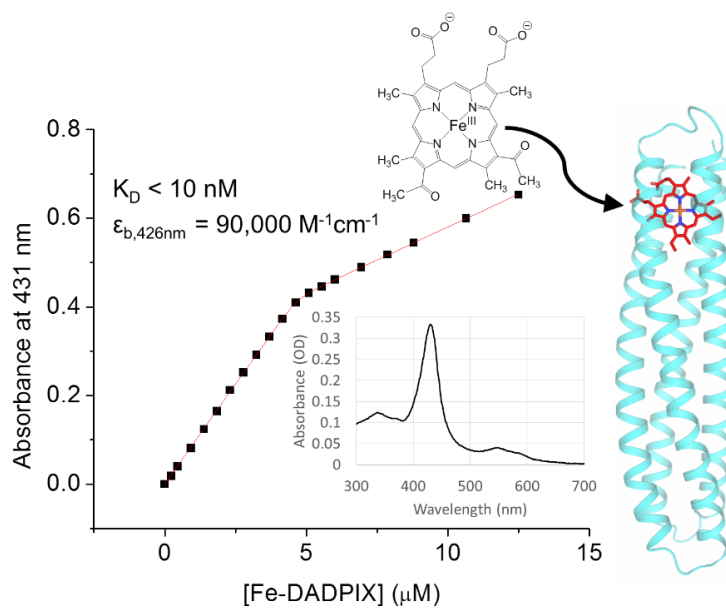


Figure 2.14: Ferric DADPIX binding titration with MZH3

UV/vis binding titration of Fe(III)-DADPIX into 4.4 μM MZH3. The structure of Fe(III)-DADPIX is shown at upper left and the spectrum at 0.8 equivalents of Fe(III)-DADPIX per MZH3 is shown above the curve. Schematic of where Fe-DADPIX is expected to bind is shown at right. Conditions: 50 mM NaCl, 20 mM phosphate buffer, pH 7.

A fourth possible electron acceptor, Fe(III) 5,10,15-tri-(*p*-carboxyphenyl) corrole (provided by Nicholas Roach from the laboratory of David Officer and referred to as PM56) showed no evidence of binding to MZH3 (see Table 2.3).

These UV/vis titrations are consistent with high-affinity bis-histidine ligation of iron and cobalt tetrapyrroles, and the 1:1 binding stoichiometry indicates that only one site in MZH3 is involved in ligation of these electron accepting cofactors. Of four cofactors tested, three bind tightly. The MZH3 electron acceptor site shows some discrimination between cofactors, but its ability to ligate different cofactors suggests a degree of plasticity in the binding site. This is similar to natural heme B proteins which can frequently bind cofactors slightly different from heme B (49). It is likely that many other iron and cobalt tetrapyrroles will bind to the acceptor site, and, as shown in the next section, some zinc tetrapyrroles will bind to this site as well, although they are intended for the mono-histidine pigment site.

Cofactor	Heme B	Fe-DADPIX	CoPPIX	PM56
K_D	< 10 nM	< 10 nM	~250 nM	None detected
Soret λ	415 nm	431 nm	426 nm	N/A
Soret ϵ_b	115,000 M ⁻¹ cm ⁻¹	90,000 M ⁻¹ cm ⁻¹	220,000 M ⁻¹ cm ⁻¹	N/A
Table 2.3: Summary of properties of tetrapyrroles tested for binding to MZH3 acceptor site Structures, dissociation constants (K_D), Soret band wavelengths in the bound state (Soret λ), and Soret extinction coefficients in the bound state (Soret ϵ_b) are given.				

2.3.4 UV/vis spectroscopy: Pigment site

Zinc tetrapyrroles are useful as pigments for light-driven electron transfer, because they can absorb light to enter a high-energy, reducing, photo-excited state similar to chlorophyll in natural reaction centers (2, 38, 39). The iron ion of iron tetrapyrroles prefers a hexacoordinate geometry, but zinc tetrapyrroles are stable with the zinc ion in a pentacoordinate geometry. This means that zinc tetrapyrroles can bind with high affinity to a binding pocket that has only one histidine (such as the pigment site of MZH3), but they could also bind to a pocket with two histidines (such as the electron acceptor site of MZH3). For this reason, it was necessary to first add an electron accepting cofactor such as heme B prior to zinc tetrapyrrole titrations of MZH3 in order to prevent the electron acceptor site from binding the zinc tetrapyrrole.

To demonstrate the necessity of an electron acceptor to block binding of the pigment to the acceptor site, a zinc Newkome porphyrin (ZnNP, provided by Tatiana Esipova in the laboratory of Sergei Vinogradov) was titrated into an MZH3 solution (Figure 2.15: ZnNP titration into MZH3). A band shift indicated binding of the ZnNP to MZH3. Using Equation 2.1, the binding stoichiometry appeared to be roughly 3.75 ZnNP molecules per protein. Cofactors at

different sites in the protein could have slightly different spectra, but this method can still give a rough estimate of binding affinities, assuming the spectra are similar. The dissociation constant was estimated at about 20 nM.

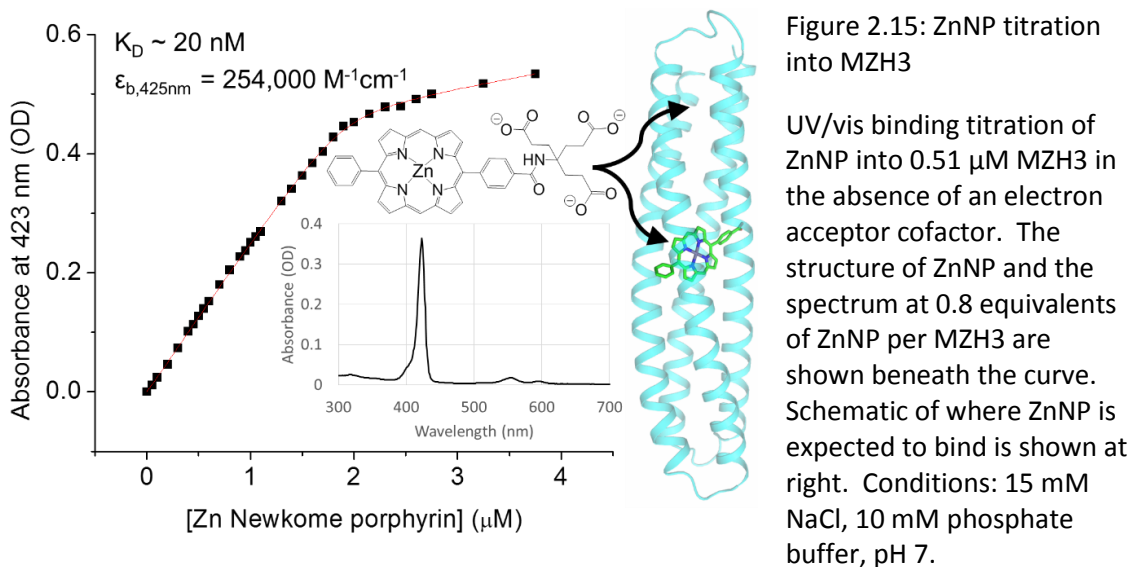
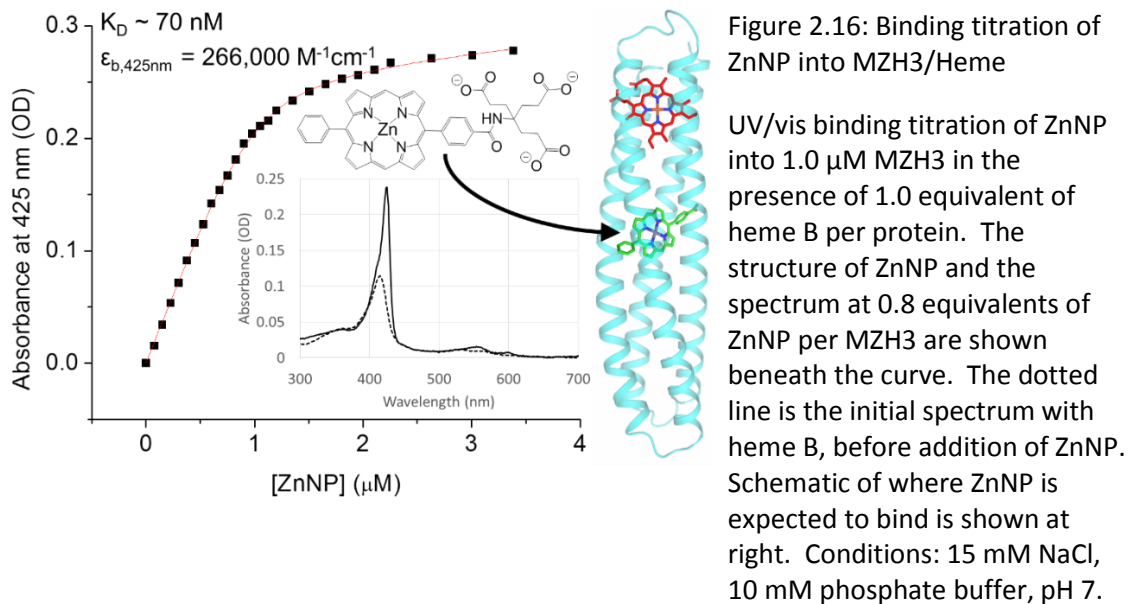


Figure 2.15: ZnNP titration into MZH3

UV/vis binding titration of ZnNP into 0.51 μM MZH3 in the absence of an electron acceptor cofactor. The structure of ZnNP and the spectrum at 0.8 equivalents of ZnNP per MZH3 are shown beneath the curve. Schematic of where ZnNP is expected to bind is shown at right. Conditions: 15 mM NaCl, 10 mM phosphate buffer, pH 7.

This titration was repeated in the presence of 1.0 equivalent of heme B per MZH3 protein (Figure 2.16). The dissociation constant for ZnNP was estimated at about 70 nM, and the binding stoichiometry appeared to be 1:1, suggesting that ZnNP binds to the pigment site and nowhere else in the protein when heme B is present.



Other titrations were performed with heme B and other zinc tetrapyrroles. Of special interest was Zn 5-phenyl-15-(*p*-carboxyphenyl) porphyrin (ZnPCP), which bound with a 1:1 stoichiometry and dissociation constant of <10 nM at pH 6.5 in the presence of 1.0 equivalent of heme B and 1.5 mM ZnCl_2 (Figure 2.17). ZnPCP was subsequently used for crystallography and transient absorption spectroscopy experiments.

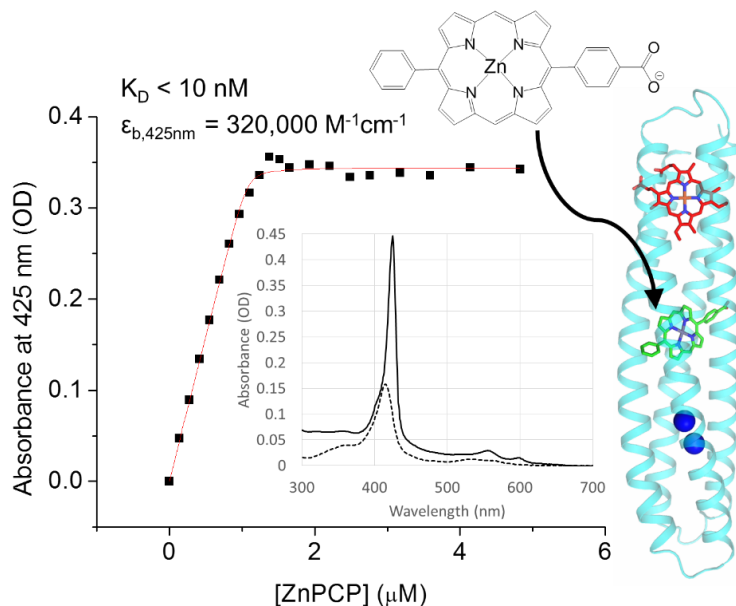


Figure 2.17: ZnPCP titration into MZH3/Heme/Zn(II)

UV/vis binding titration of ZnPCP into 1.2 μM MZH3 in the presence of 1.0 equivalent of heme B per protein. The structure of ZnPCP is shown above the curve, and the spectrum at 0.8 equivalents of ZnPCP per MZH3 is shown beneath the curve. The dotted line is the initial spectrum with heme B, before addition of ZnPCP. Schematic of where ZnPCP is expected to bind is shown at right. Conditions: 15 mM NaCl, 1.5 mM ZnCl_2 , 10 mM PIPES buffer, pH 6.5.

Synthetic zinc tetrapyrroles were prepared by collaborators following methods described previously (5, 51). The zinc porphyrins ZnNP, ZnPCP, TE312, and TE394, TE400, and TE400b were synthesized by Tatiana Esipova in the laboratory of Sergei Vinogradov following methods described previously. NR117 was provided by Nicholas Roach and the laboratory of David Officer. The zinc chlorins SE370 and SE375 were synthesized in the laboratory of Jonathan Lindsey. Other tetrapyrroles were purchased from Frontier Scientific. A list of zinc tetrapyrroles that bind MZH3 with high affinity when an acceptor cofactor is present is shown in Table 2.4, and those with low affinity are shown in Table 2.5.

Pigment name	Pigment structure	Acceptor cofactor	Metal	Stoichiometry	Binding
ZnNP		none	-	~3.75	~20 nM average
		Heme B	-	1	~70 nM
		CoPPIX	-	1	~50 nM
		Heme B	Co(II)	1	~50 nM
ZnPCP		Heme B	Zn(II)	1	< 10 nM
SE370		Heme B	-	1	~30 nM
SE375		Heme B	-	1	~70 nM
NR117		Heme B	-	inconclusive	~30 nM
ZnC		Heme B	-	inconclusive	~100 nM
		Heme B	Co(II)	1	~200-500 nM
TE312		Heme B	Zn(II)	n.d.	band shift observed, K_D was not measured
TE394		Heme B	-	n.d.	band shift observed, K_D was not measured

Table 2.4: Zinc tetrapyrroles that bind to MZH3/Heme with high affinity

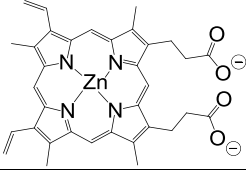
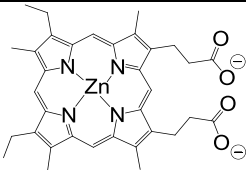
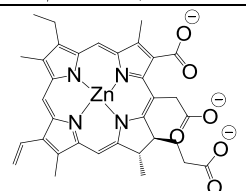
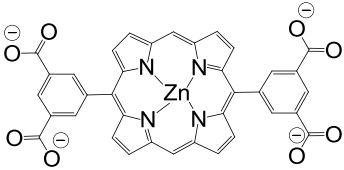
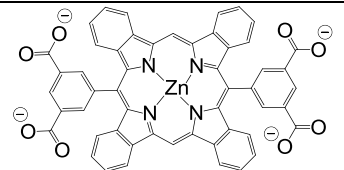
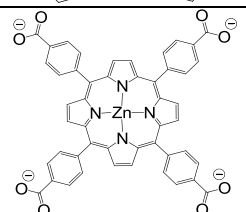
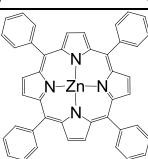
Pigment name	Pigment structure	Acceptor cofactor	Metal	Stoichiometry	Binding
ZnPPIX		Heme B	Zn(II)	1	~2 μ M
ZnMPIX		Heme B	-	0	not detected
ZnCe ₆		Heme B	-	0	not detected
TE400		Heme B	-	0	not detected
TE400b		Heme B	-	0	not detected
ZnTCP		Heme B	-	inconclusive	~5 μ M
ZnTPP		Heme B	-	0	not detected
ZnDPDP		Heme B	-	0	not detected

Table 2.5: Zinc tetrapyrroles that do not bind to MZH3/Heme with high affinity

The tests of zinc tetrapyrrole affinity for the MZH3 pigment site summarized in Table 2.4 and Table 2.5 reveal a pattern of selectivity for zinc tetrapyrroles with particular structural attributes. Consideration of the potential for steric clashes and burial of polar groups can help predict what zinc tetrapyrrole structures will bind to the pigment site of MZH3. The pigment binding cavity in the center of the maquette is a deep, narrow slit that stretches across the width of the four-helix bundle and is lined with tightly packed hydrophobic residues in layers above and below the ligating histidine. It cannot expand enough to accommodate the bulk of *meso*-tetraphenyl porphyrins (ZnTCP, ZnTPP, and ZnDPDP), and tetrapyrroles with carboxylate groups too close to the tetrapyrrole ring may be prevented from binding because the histidine cannot ligate the zinc ion without burying those negative charges (ZnPPIX, ZnMPIX, ZnCe₆, TE400, and TE400b). This issue of charge burial is believed to have prevented binding of heme B and ZnPIX to porphyrin-binding four-helix bundle maquettes that had similarly hydrophobic binding sites (25, 26, 31). The most successful zinc tetrapyrrole designs have two phenyl groups on opposite sides of the tetrapyrrole ring and lack bulky, inflexible substituents at the 10 and 20 *meso* positions that are present in the low-affinity tetraphenyl ZnTCP, ZnTPP, and ZnDPDP porphyrins. This narrower shape of the 5,15-diphenyl porphyrin better complements the shape of the binding cleft. The successful zinc tetrapyrroles also typically have polar groups in *para* positions on the phenyl rings. These polar groups might not increase the stability of the MZH3-zinc tetrapyrrole interaction, but they are likely to destabilize aggregates of zinc tetrapyrroles that might otherwise sequester the cofactor and prevent binding to MZH3, as is likely the case for the somewhat lower affinity ZnC, which has low solubility in aqueous solutions.

2.3.5 UV/vis spectroscopy: Donor site

Unlike tetrapyrroles, transition metal dications in proteins are weak absorbers of visible light and are not usually suitable for UV/vis spectroscopic titrations. A Co(II) ion bound to a protein has a maximum extinction coefficient of about one thousandth that of a typical tetrapyrrole, but this is still significantly greater than the absorbance of most other transition metals. Co(II) also has the advantage of having an absorbance spectrum that is highly sensitive to its coordination number, allowing UV/vis titrations to yield information on both binding affinity and ligation state. Extinction coefficients for Co(II) typically range from approximately 10-20 $M^{-1}cm^{-1}$ for 4-coordinate, 100-150 $M^{-1}cm^{-1}$ for 5-coordinate, and 400-600 $M^{-1}cm^{-1}$ for 6-coordinate complexes (52).

Co(II) binding to MZH3 was tested by a UV/vis titration of $Co(NO_3)_2$ into a solution of 34 μM MZH3 in a 10 cm (Figure 2.18). The result was a stoichiometry of two Co(II) ions per protein with an extinction coefficient of 90 $M^{-1}cm^{-1}$ per Co(II) ion at 545 nm and an average dissociation constant of about 3.3 μM at pH 7.3. For comparison, DF3 has a Co(II) extinction coefficient of 98 $M^{-1}cm^{-1}$ at 548 nm and an average dissociation constant of about 240 nM at pH 7 (22). Another Due Ferro maquette, DFsc, has an extinction coefficient of 136 $M^{-1}cm^{-1}$ at 550 nm and an average dissociation constant of about 160 μM at pH 6 (53). The natural diiron protein bacterioferritin has an extinction coefficient of 155 $M^{-1}cm^{-1}$ at 548 nm and an average dissociation constant of about 10 μM in the absence of heme B at pH 7.1 (54). The Co(II) affinities are similar to Mn(II) affinities in most Due Ferro maquettes (22, 40, 55). The Co(II) titration shows that MZH3 has a penta-coordinate binding site similar to the Co(II) binding properties of other di-metal proteins.

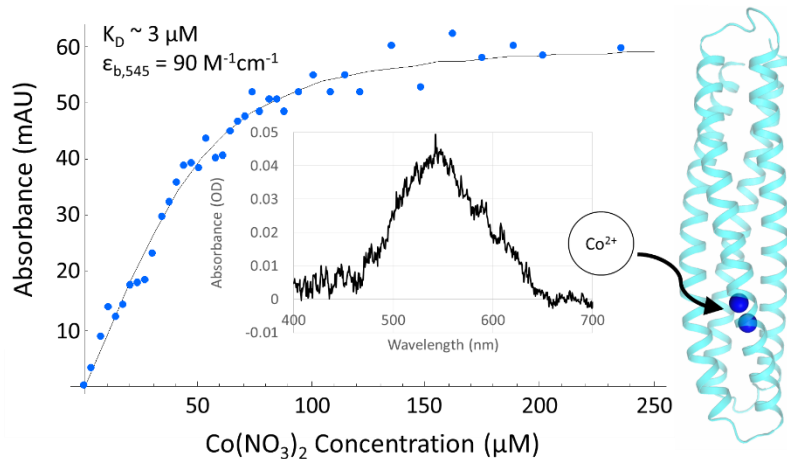


Figure 2.18: Co(II) binding titration with MZH3.

UV/vis binding titration of $\text{Co}(\text{NO}_3)_2$ into $33.7 \mu\text{M}$ MZH3 in 10 cm path length cuvette. The spectrum at 1.8 equivalents of Co(II) per MZH3 is shown beneath the curve. Schematic of where Co(II) is expected to bind is shown at right. Conditions: 150 mM KCl, 100 mM MOPS buffer, pH 7.3.

2.3.6 Ferroxidase activity

Natural diiron proteins and the Due Ferro series of *de novo* proteins catalyze ferroxidase activity, wherein a diferrous center reacts with oxygen to produce an oxo-bridged diferric site with a characteristic ligand-to-metal charge transfer (LMCT) band around 300 nm. As expected, MZH3 catalyzes this reaction as well. Figure 2.19 shows the absorbance at 300 nm of an anaerobic sample of $30 \mu\text{M}$ MZH3 in complex with stoichiometric iron chloride. At time $t=0$, the anaerobic sample was exposed to ambient oxygen, triggering a rapid conversion to the diferric species with a lifetime of roughly 3.6 minutes for the transition. The inset spectra show the rise of the LMCT band with time. The extinction coefficient for the diferric state at 300 nm is $3400 \text{ M}^{-1}\text{cm}^{-1}$, which agrees with the values for DF2 and bacterioferritin of $3240 \text{ M}^{-1}\text{cm}^{-1}$ and $3380 \text{ M}^{-1}\text{cm}^{-1}$, respectively (55, 56). Iron oxidation in MZH3 is reversible, as it is in DF3 (21). Reduction of MZH3-Fe(III)_2 by dithionite eliminated the LMCT band and subsequent air oxidation regenerated it.

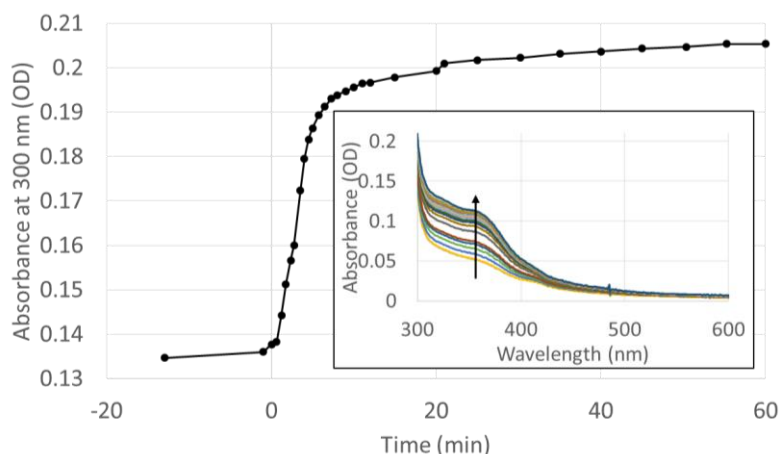


Figure 2.19: Ferroxidase activity of MZH3.

Exposure to ambient oxygen at time $t=0$ lead to rapid increase in LMCT band with lifetime of ~ 3.6 minutes. Conditions: 30 μM MZH3, 60 μM FeCl_2 , 1500 mM KCl, 50 mM MOPS buffer, pH 7.3.

In DF3, ferroxidase activity appears to give rise to a tyrosinate-Fe(III) ligation, as evidenced by a putative tyrosinate-to-Fe(III) LMCT transition with an extinction coefficient of $1,200 \text{ M}^{-1}\text{cm}^{-1}$ at 500 nm (22). In contrast, MZH3 lacks a distinct absorbance feature in this region and has only a $200 \text{ M}^{-1}\text{cm}^{-1}$ extinction coefficient at 500 nm, probably due to the broad absorbance of the oxo-to-Fe(III) charge transfer band or a small amount of Rayleigh scattering. The absence of a tyrosinate-Fe(III) in MZH3 may be because one of the tyrosine residues is replaced with leucine and because the increased stability of MZH3 prevents the structural rearrangement that would allow the other tyrosine to ligate the iron.

2.3.7 Circular dichroism to assay secondary structure

At 25°C under low salt conditions at pH 7, the mean molar ellipticity per residue at 222 nm, $[\theta_{\text{MMR}}]_{222}$, of apo-MZH3 was $-29,000 \text{ deg cm}^2 \text{ dmol}^{-1} \text{ res}^{-1}$ (see Figure 2.20 and Table 2.6). The shape of the curve and the intensity of $[\theta_{\text{MMR}}]_{222}$ are consistent with high α -helical content (57). In addition, the ratio of $[\theta_{\text{MMR}}]_{222}/[\theta_{\text{MMR}}]_{208}$ of 1.09 is high, which is consistent with a coiled coil structure (4, 58-60). The addition of 33 μM MnCl_2 to 15.2 μM MZH3 (~ 2 molar equivalents of MnCl_2 per MZH3 protein) increased the magnitude of $[\theta_{\text{MMR}}]_{222}$ and the ratio of

$[\theta_{\text{MMR}}]_{222}/[\theta_{\text{MMR}}]_{208}$, while the addition of 1 molar equivalent of heme B to 20.3 μM MZH3 lowered the magnitude of $[\theta_{\text{MMR}}]_{222}$ and the ratio of $[\theta_{\text{MMR}}]_{222}/[\theta_{\text{MMR}}]_{208}$ (see Table 2.6). Heme binding has a similar effect on $[\theta_{\text{MMR}}]_{222}$ in DDH2, a truncated

Cofactor added to MZH3	$[\theta_{\text{MMR}}]_{222}$ (deg cm ² dmol ⁻¹ res ⁻¹)	$[\theta_{\text{MMR}}]_{222}/[\theta_{\text{MMR}}]_{208}$	T_{M} (°C)
Apo	-29,000	1.09	82
1 eq. heme B	-19,400	1.04	94
2 eq. Mn(II)	-31,900	1.12	>100
3 eq. Ca(II)	n.d.	1.11	90

Table 2.6: MZH3 circular dichroism measurements

All samples contained 15 mM NaCl and 10 mM NaH₂PO₄ at pH 7. MZH3 concentration for each sample were 16.8 μM (apo), 15.2 μM (MnCl₂), 20.3 μM (Heme), and ~16 μM (CaCl₂).

version of MZH3 that binds two hemes B and lacks a metal binding site, as discussed in detail in section 2.4. This suggests that the decrease of $[\theta_{\text{MMR}}]_{222}$ is caused by the effect of heme on nearby helices rather than a long-range effect on the metal-binding section of the protein.

The effect of heme B binding in MZH3 appears to be a decrease in helicity and an increase in thermal stability. While it is common for the melting temperature to increase upon heme binding, the decrease in $[\theta_{\text{MMR}}]_{222}$ sets MZH3 apart from the behavior of other helical porphyrin-binding proteins. As described in the introduction, natural hemoproteins are usually unstable in the apo-state, and finish folding once heme is bound (34, 35). Designed porphyrin-binding proteins follow this pattern as well, showing increased ellipticity at 222 nm (26, 31, 61-63). For example, myoglobin has an apo-state $[\theta_{\text{MMR}}]_{222}$ that is only 70% of the magnitude in the holo-state (64, 65). In one exception, an iron porphyrin-binding maquette with a highly stable apo-state (similar to MZH3) showed a small decrease in $[\theta_{\text{MMR}}]_{222}$ upon porphyrin binding, but the authors attributed this to transitions of the synthetic porphyrin itself, rather than helical content (44). The decrease in $[\theta_{\text{MMR}}]_{222}$ upon heme binding by MZH3 cannot be attributed to dichroic absorption of the heme B cofactor itself, as its contribution to the CD signal at 222 nm is

negligible (57, 66, 67). The total fraction of residues that have a helical conformation accounts for much of the observed value of $[\theta_{\text{MMR}}]_{222}$, but $[\theta_{\text{MMR}}]_{222}$ is also influenced by subtle variations of α -helical structure such as lengths of the helices, dynamical motion of the protein, and the precise conformation of helical residues (68). It is not inconceivable, then, that heme binding influences the structure of MZH3 in such a way that $[\theta_{\text{MMR}}]_{222}$ decreases significantly, but the total helix content remains similar to the apo-state. However, the loss

of ellipticity upon heme binding is consistent with a disruption of core packing by heme binding, which might mean that heme affinity could be further improved by reengineering the heme site to make it less stable in the apo-state so that MZH3 is more like natural apo-hemoproteins.

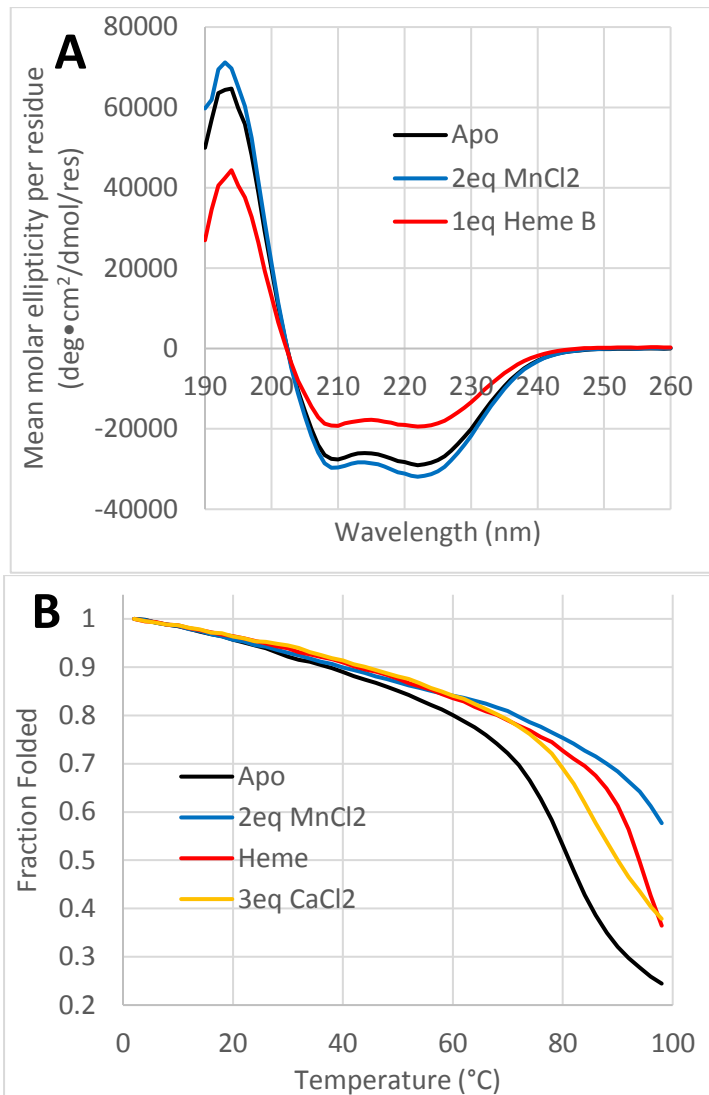


Figure 2.20: Circular dichroism measurements of MZH3

A: Far UV CD spectra at 25°C. B: Melting curves estimated from $[\theta_{\text{MMR}}]_{222}$ signal. Black curves at apo-MZH3, blue curves are have two equivalents of MnCl_2 per protein, red curves have one equivalent of heme B per protein, and orange curve is 3 equivalents of CaCl_2 per protein. All samples contained 15 mM NaCl and 10 mM NaH_2PO_4 at pH 7.

The decrease in $[\theta_{\text{MMR}}]_{222}$ could be explained if estimates of extinction coefficients were inaccurate, since the apo-MZH3 and heme-MZH3 concentrations were estimated by measuring different absorption features. However, the extinction coefficient for the heme B Soret band at 415 nm was determined from UV/vis titrations in which MZH3 concentration was determined from Trp and Tyr absorbance at 280 nm. These titrations showed a heme B stoichiometry of precisely 1.0, demonstrating consistency between concentration estimates based on the two absorption features. In addition, an error in extinction coefficients would not explain the significant decrease in $[\theta_{\text{MMR}}]_{222}/[\theta_{\text{MMR}}]_{208}$ ratio that results from heme binding.

Melting curves demonstrate that Mn(II) binds to MZH3 more tightly than Ca(II), which is expected from typical stabilities of Mn(II) and Ca(II) complexes (69). It is surprising that Mn(II) binding has a significantly greater stabilizing effect on MZH3 than the binding of heme B. Cytochrome b_{562} , which has a ferric heme B affinity similar to MZH3, increases in stability by ~ 15 kJ mol⁻¹ upon binding of ferric heme B (35, 70). In DF3, Zn(II) binding stabilizes the protein by 43.5 kJ mol⁻¹, but Mn(II) only increases the stability by 12.1 kJ mol⁻¹ (22). This is consistent with the Irving-Williams series, which predicts metal complex stabilities to follow the trend Mn(II) < Fe(II) < Co(II) < Ni(II) < Cu(II) > Zn(II), where Zn(II) affinities are generally high and close to Cu(II) (69). Given the similarities between MZH3 and these proteins, it should follow that heme B is more stabilizing than Mn(II), but the thermal melts show that the reverse is true. The pronounced difference between the stabilities of MZH3-Mn(II)₂ and MZH3-heme B could be due to an unexpected high Mn(II) affinity, but it is more likely that in the apo-state of MZH3, the Due Ferro section of the protein is less stable than the heme binding section. This would mean that

the stabilizing effect of heme B is applied primarily to a region of the maquette that is already stable, while Mn(II) increases the helicity of a more dynamic part of MZH3.

2.3.8 Circular dichroism in Soret region to assay exciton coupling

If a chromophore is either chiral, covalently bonded to a chiral center, or located in an asymmetric environment, then it is optically active and capable of producing a CD signal at wavelengths where normal absorption occurs. CD signals come from the interaction between transition dipoles of a chromophore and other transition dipoles in the molecule. If two chromophore transitions are close to degenerate, excitation of one chromophore can be delocalized across both chromophores through exciton coupling, creating a sigmoidal CD signal centered at the absorption maximum of the transition (71). Exciton coupling has been observed between the hemes of cytochrome b (47, 72) and cytochrome bd (73) and between bacteriochlorophylls of the bacterial light-harvesting antenna complex LH2 (74, 75). The phenomenon has been used in *de novo* proteins that bind two synthetic metalloporphyrins in order to determine whether the porphyrins bind in a cooperative manner (31).

CD spectra in the Soret region of MZH3 in complexes with heme B and ZnNP demonstrate that both ZnNP and Heme B are bound to MZH3 at the same time. Figure 2.21A shows weak CD signals when only one heme B or only one ZnNP is bound to the protein. Based on comparison to spectra of myoglobin and hemoglobin, these signals may be due to coupled oscillator interactions between the porphyrin and aromatic amino acids, the polypeptide backbone, or alkyl side chains (76). In contrast, Figure 2.21B shows that the addition of both heme and ZnNP or two ZnNP molecules results in CD signals more than an order of magnitude larger than the signal due to heme by itself, and about double the magnitude of the ZnNP by

itself. Such an amplification of the CD signal is expected for exciton coupling between two porphyrins with similar excitation energies bound close together in the same protein (72, 73).

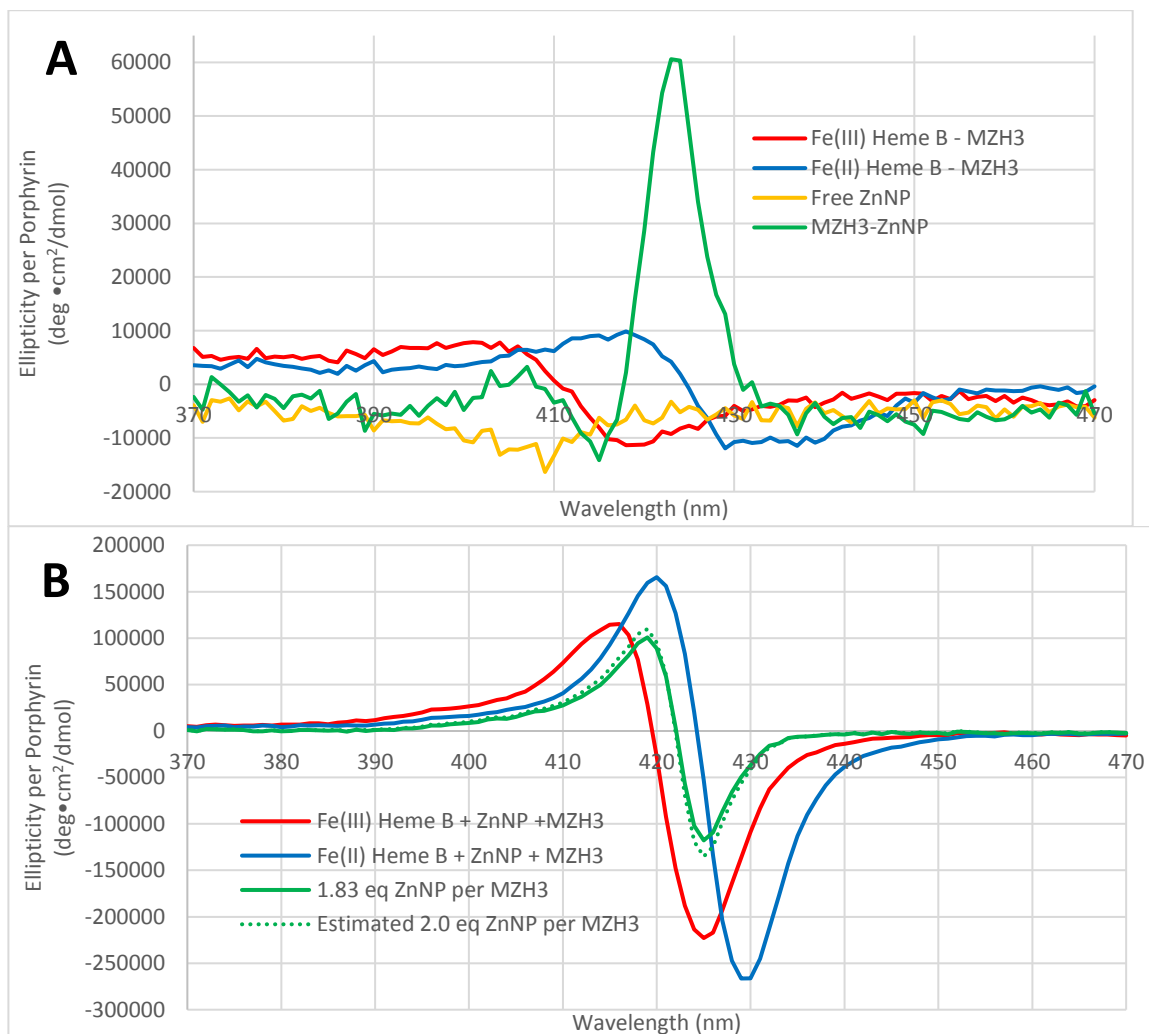


Figure 2.21: Exciton coupling effects of MZH3 with heme B and ZnNP by circular dichroism

(A) MZH3 spectra with only one porphyrin. Red trace: 5.2 μM MZH3 with 1 equivalent of ferric heme B per bundle, 1 cm path length. Blue trace: 5.2 μM MZH3 with 1 eq. ferrous heme (reduced with sodium dithionite), 1 cm path length. Green trace: 23 μM MZH3 with 19 μM ZnNP (0.83 eq.), 0.1 cm path length. Orange trace: 31 μM ZnNP, no protein, 0.1 cm path length. (B) MZH3 spectra with two porphyrins. Red trace: 33 μM MZH3 with 1.0 eq. ferric heme and 1.0 eq ZnNP, 0.1 cm path length. Blue trace: 33 μM MZH3 with 1.0 eq. ferrous heme (reduced by sodium dithionite) and 1.0 eq ZnNP, 0.1 cm path length. Green trace: 23 μM MZH3 with 42 μM ZnNP (1.83 eq.), 0.1 cm path length. All data sets were collected in 15 mM NaCl, 10 mM phosphate buffer, pH 7.

Since the heme Soret bands at 415 nm in the oxidized state and 430 nm in the reduced state are very close to the ZnNP Soret band at about 423 nm, there is significant exciton coupling, giving rise to the observed intense CD bands. Indeed, the expected ~25-45° dihedral angle between the bound porphyrin planes at the two sites will tend to enhance CD excitonic coupling signals (72).

2.3.9 Heme B Redox titration

A rate of electron transfer depends partly on the driving force of the reaction, which is determined from the difference between the midpoint potentials of the cofactors involved in the reaction. The midpoint potential of a cofactor is the potential at which half of it is oxidized and half is reduced. The Nernst equation can be used to relate the midpoint potential of a redox center E_m , the potential of the solution measured with the standard hydrogen electrode E_h , the number of electrons transferred in the reaction n , the ratio of the concentrations of oxidized to reduced cofactor $[ox]/[red]$, the universal gas constant R , temperature T , and Faraday's constant F (77):

$$E_h = E_m + \frac{RT}{nF} \cdot \ln \left(\frac{[ox]}{[red]} \right) \quad \text{Equation 2.2}$$

At room temperature, this equation reduces to following, where E_h and E_m are in volts:

$$E_h = E_m + \frac{0.059}{n} \cdot \log \left(\frac{[ox]}{[red]} \right) \quad \text{Equation 2.3}$$

A redox titration was used to determine the midpoint potential of heme B in MZH3 at pH 7 following procedures described previously (77, 78). Details are given in the Appendix. The relative concentrations of oxidized and reduced heme were monitored by UV/vis spectroscopy

of the Q-band region of the heme absorption spectrum. Increases in the absorbance difference between 560 nm and 545 nm compared to the initial oxidized spectrum were proportional to the total concentration of reduced heme, allowing absorbance changes to be fitted to the Nernst equation (Figure 2.22). The reducing and oxidizing curves were fitted with E_m values of -184 mV and -168 mV, respectively, which are the same within error, so no significant hysteresis is apparent. The fitted n values were both within 7% of 1.0, consistent with the expected one-electron transition from ferric to ferrous heme B.

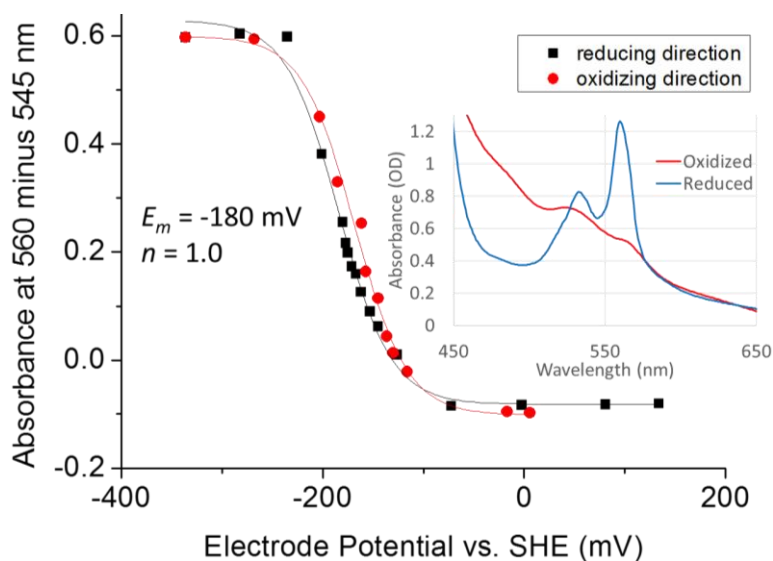


Figure 2.22: Redox titration of heme B bound to MZH3

Titration was done at pH 7.0 in reducing (black) and oxidizing (red) directions. Inset: absorbance spectra of Q band region of MZH3-heme B in reduced (blue) and oxidized (red) states.

This midpoint potential of -180 mV for heme B in MZH3 is not unusual for a four-helix bundle maquette. Midpoints of bis-histidine-ligated heme B in maquettes have ranged from -260 mV to -150 mV (79). Generally, potentials are higher when the heme is more buried.

2.4 DDH2: A truncated version of MZH3 that binds two hemes

MZH3 is essentially the joining of a well-described di-metal binding *de novo* maquette, Due Ferro, to a newly-designed and uncharacterized cytochrome b-like maquette that binds two

metallotetrapyrroles. Because the cytochrome b-like section of MZH3 has not been studied as an independent protein previously, it is difficult to compare it to other successful di-heme four-helix bundle maquettes such as BT6 (2), a di-heme binding homotetramer (62), a cytochrome b-like template-assembled synthetic protein (TASP) (61), a series of porphyrin array (PA) proteins developed by the DeGrado group (25, 26, 31), and combinatorially designed heme proteins from the Hecht group (80).

To ascertain whether the cytochrome b-like section of MZH3 remains functional in the absence of the di-metal Due Ferro section, a shortened di-heme maquette based on the sequence of MZH3, DDH2 (“Diagonal Di-Heme”), was expressed in *E. coli* with an N-terminal His₆ tag and TEV cleavage site. DDH2 is as similar in sequence to MZH3 as possible, except at the ends of the helices where DDH2 has helix caps and loops in place of helices that continue through the Due Ferro section of the protein. In addition, the pigment site of MZH3 becomes a second heme binding site in DDH2. Two α -position glycines in MZH3 were change to alanines, because the helices are expected to be relatively flexible in that region of DDH2. DDH2 is 135 amino acids long with a molecular weight of 14.99 kDa in the apo-state, an extinction coefficient of 11,000 M⁻¹cm⁻¹ at 280 nm due to two tryptophan residues, and a theoretical isoelectric point of 6.1, as estimated using the ExPASy ProtParam server (81). The sequence of DDH2 is given in below:

GGSPELRQEHQQLAQEFQQLLQEHQQLARELGGSGGDPAEELQQTGQFEAQQLLQELQQTGQELWQLGGS
GGPELRQKHQQLAQKIQQLLQKHQQLARKLGGSGGDPAEKLQQTGQKAQQLVQKLQQTGQKLWQLG

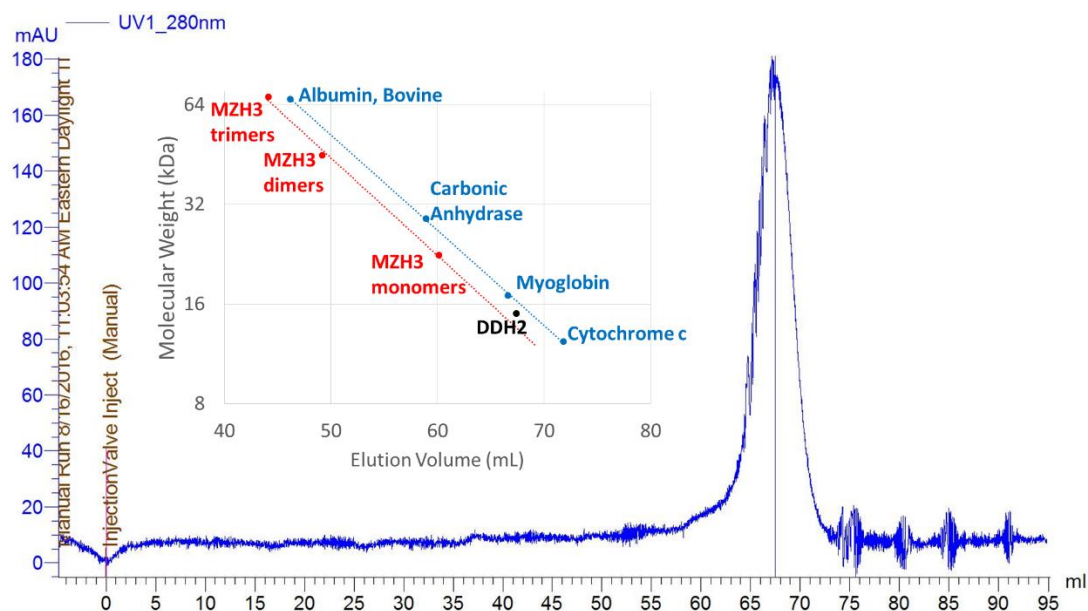


Figure 2.23: Size exclusion chromatography elution profile of DDH2

The blue line is the absorbance of the sample at 280 nm vs. elution volume. Inset: Plot of log molecular weight against elution volume for DDH2 (black), globular protein standards (blue), and MZH3 (red).

2.4.2 Ultraviolet/visible spectroscopy of DDH2 with heme B

Overexpression of DDH2 in *E. coli* produced red cell pellets, as with MZH3, and after purification, DDH2 appeared to have roughly ~0.25 equivalents of ferric heme B per DDH2 protein (or ~0.13 equivalents of heme B per binding site). DDH2 was purified by HPLC to remove heme B that was bound during expression. After purification by size exclusion chromatography, a ferric heme B binding titration was performed at pH 7.5 with 0.5 μM DDH2, as shown in Figure 2.24. The stoichiometry was two hemes B per DDH2 protein, as expected. The dissociation constant was similar to MZH3; both maquettes bind heme B with a dissociation constant of about 10 nM or less. The extinction coefficient for the Soret peak in DDH2 was 120,000 $\text{M}^{-1}\text{cm}^{-1}$, which is similar to the value for MZH3 of 115,000 $\text{M}^{-1}\text{cm}^{-1}$.

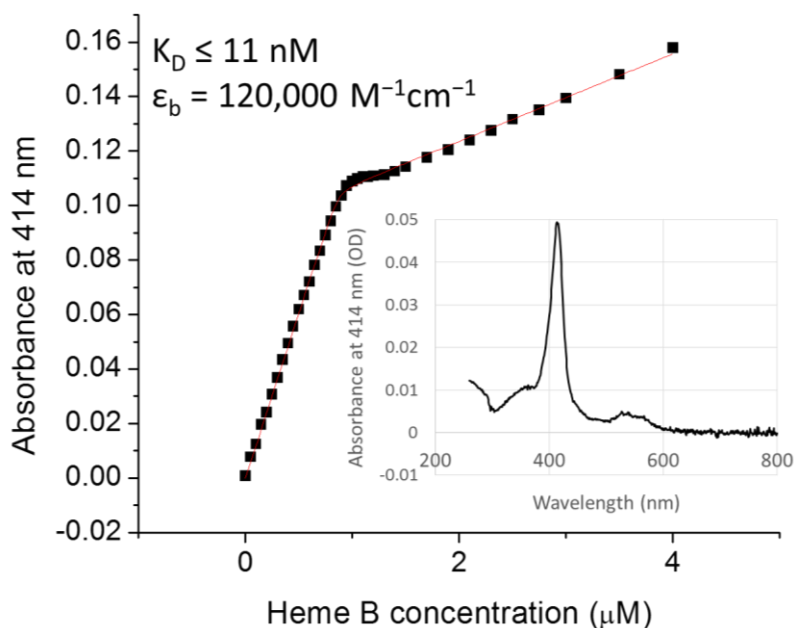


Figure 2.24: Heme titration into DDH2

UV/vis binding titration of ferric heme B into 0.5 μM DDH2. Inset: Spectrum at 0.8 equivalents of heme B per MZH3. Conditions: 50 mM NaCl, 10 mM MOPS buffer, pH 7.5.

2.4.3 Circular dichroism of DDH2 with heme B

DDH2 is highly α -helical, as demonstrated by circular dichroism (CD) spectra in Figure 2.25, top. The mean molar ellipticity per residue at 222 nm, $[\theta_{\text{MMR}}]_{222}$, in the apo-state is $-27,900 \text{ deg cm}^2 \text{ dmol}^{-1} \text{ res}^{-1}$. This ellipticity decreases progressively with the addition of heme B to $-21,100 \text{ deg cm}^2 \text{ dmol}^{-1} \text{ res}^{-1}$ when two hemes are bound. In addition, heme binding decreases the ratio of $[\theta_{\text{MMR}}]$ at 222 nm to 208 nm from 1.11 in the apo-state to 0.97 in the holo-state. This is similar to the behavior of MZH3 when it binds heme. DDH2 also exhibits relatively high thermal stability, as shown in Figure 2.25, bottom. The midpoint of unfolding in the apo-state occurs at about 71°C , which is about 11°C lower than the melting temperature of MZH3. This decreased stability is not surprising given the shortened length of DDH2 and smaller hydrophobic core. Like MZH3, heme binding has a stabilizing effect on the thermal unfolding curve, despite the decrease in $[\theta_{\text{MMR}}]_{222}$.

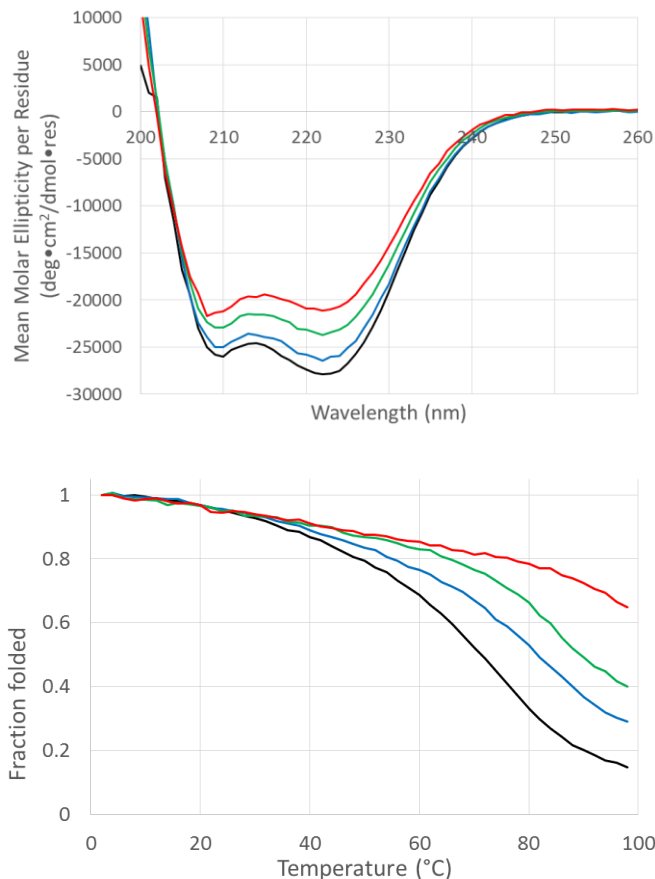


Figure 2.25: Far UV circular dichroism spectroscopy of DDH2

Used 0.1 cm path length cuvette. Black curves: 32 μM apo-DDH2. Blue curves: 18.2 μM DDH2 with 0.47 equivalents of heme B per protein. Green curves: 20.9 μM DDH2 with 0.91 equivalents of heme. Red curves: 18.3 μM DDH2 with 2.0 equivalents of heme. Top: Far UV CD spectra of DDH2. Bottom: Thermal denaturation of DDH2. Fraction folded is estimated by the decreased in measured by mean molar ellipticity at 222 nm relative to the ellipticity at 2°C.

Exciton coupling between hemes B in DDH2 is observed by CD, as shown in Figure 2.26. The addition of less than one equivalent of heme B per DDH2 protein results in a weak exciton coupling signal near the heme Soret (blue and green traces in Figure 2.26, top). However, when more than one heme B per protein is added, a pronounced exciton coupling signal is observed. In Figure 2.26, top, the trace with 0.47 hemes per protein (blue) overlaps with the trace with 0.91 hemes per protein (green), but the trace with 1.37 hemes per protein (black) has a distinct spectrum, which is increased with 2.0 hemes per protein (red). (The mean molar ellipticity is given per heme, not per protein). If we assume that the heme CD signal in the 2.0 hemes per protein spectrum (red) represents the CD spectrum for any heme in a protein with a second

heme, and the 0.91 hemes per protein spectrum (green) represents the CD spectrum for heme by itself in DDH2, we can predict the spectrum for 1.37 hemes per protein; at 1.37 hemes, 54% of the heme is in a protein where there is a second heme, and 46% is in a protein by itself. The grey dotted line represents this calculated spectrum, and it overlaps with the measured 1.37 hemes spectrum in black. It follows that heme binds to DDH2 anti-cooperatively; a second heme B does not bind to DDH2 until all of the protein has one heme B bound already. In Figure 2.26, bottom, the 0.47 equivalentents (blue) and 2.0 equivalentents (red) spectra were reduced with dithionite (dotted lines) and compared to the oxidized spectra. The red-shift and increased magnitude of exciton coupling are consistent with heme B reduction.

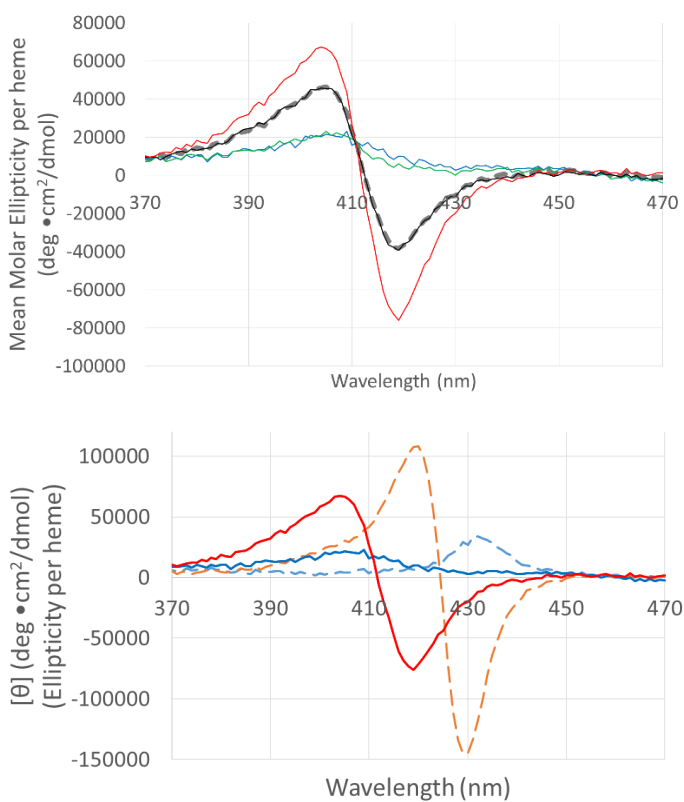


Figure 2.26: Exciton coupling between hemes B in DDH2

Measured in 1 cm path length cuvette. Blue curves: 18.2 μM DDH2 with 0.47 equivalentents of heme B per protein. Green curves: 9.4 μM DDH2 with 0.91 equivalentents of heme. Black curves: 6.6 μM DDH2 with 1.37 equivalentents of heme. Red curves: 18.3 μM DDH2 with 2.0 equivalentents of heme. Top: Grey dotted line: calculated spectrum of 1.37 equivalentents of heme B, based on spectra from 2.0 and 0.91 heme per protein spectra. Bottom: Red and blue dotted lines: heme B reduced with dithionite.

2.4.4 Significance of DDH2

DDH2 has properties that are very similar to the porphyrin binding section of MZH3. DDH2 has high affinity for heme B, binds heme B *in vivo*, is stable, and shows the same decrease in ellipticity at 222 nm upon binding heme. Therefore, the removal of the Due Ferro section of MZH3 does not significantly perturb the structure or heme-binding function of the tetrapyrrole-binding section of MZH3; both the tetrapyrrole-binding and Due Ferro sections of MZH3 can function as standalone maquettes. In effect, MZH3 can be regarded as the joining of two separate functional proteins into a single fold. DDH2 is a viable candidate for the testing of other functions performed by BT6 including electron transfer, energy transfer, and oxygen binding (2).

However, it should be noted that these experiments cannot prove that DDH2 folds as the intended left-turning antiparallel four-helix bundle and not the right-turning antiparallel structure; it remains possible that the Due Ferro section of MZH3 might help select for the correct helical topology or that charge pairing interactions in DDH2 do not sufficiently widen the energy gap between the right- and left-turning folds. Future studies of DDH2 should involve high resolution structure determination by NMR or crystallography to test the hypothesis that DDH2 folds as designed.

2.5 References

1. Robertson, D. E., Farid, R. S., Moser, C. C., Urbauer, J. L., Mulholland, S. E., Pidikiti, R., Lear, J. D., Wand, A. J., DeGrado, W. F., and Dutton, P. L. (1994) Design and synthesis of multi-haem proteins, *Nature* 368, 425-432.
2. Farid, T. A., Kodali, G., Solomon, L. A., Lichtenstein, B. R., Sheehan, M. M., Fry, B. A., Bialas, C., Ennist, N. M., Siedlecki, J. A., Zhao, Z., Stetz, M. A., Valentine, K. G., Anderson, J. L., Wand, A. J., Discher, B. M., Moser, C. C., and Dutton, P. L. (2013) Elementary tetrahelical protein design for diverse oxidoreductase functions, *Nat Chem Biol* 9, 826-833.

3. Solomon, L. A., Kodali, G., Moser, C. C., and Dutton, P. L. (2014) Engineering the assembly of heme cofactors in man-made proteins, *J Am Chem Soc* *136*, 3192-3199.
4. Sharp, R. E., Diers, J. R., Bocian, D. F., and Dutton, P. L. (1998) Differential binding of iron(III) and zinc(II) protoporphyrin IX to synthetic four-helix bundles, *Journal of the American Chemical Society* *120*, 7103-7104.
5. Kodali, G., Mancini, J. A., Solomon, L. A., Esipova, T. V., Roach, N., Hobbs, C. J., Wagner, P., Mass, O., Aravindu, K., Barnsley, J. E., Gordon, K. C., Officer, D. L., Dutton, P. L., and Moser, C. (2017) Design and engineering of water-soluble light-harvesting protein maquettes, *Chem Sci* *8*, 316-324.
6. Westerlund, K., Moran, S. D., Privett, H. K., Hay, S., Jarvet, J., Gibney, B. R., and Tommos, C. (2008) Making a single-chain four-helix bundle for redox chemistry studies, *Protein Eng Des Sel* *21*, 645-652.
7. Westerlund, K., Berry, B. W., Privett, H. K., and Tommos, C. (2005) Exploring amino-acid radical chemistry: protein engineering and de novo design, *Biochim Biophys Acta* *1707*, 103-116.
8. Tommos, C., Skalicky, J. J., Pilloud, D. L., Wand, A. J., and Dutton, P. L. (1999) De novo proteins as models of radical enzymes, *Biochemistry* *38*, 9495-9507.
9. Calhoun, J. R., Natri, F., Maglio, O., Pavone, V., Lombardi, A., and DeGrado, W. F. (2005) Artificial diiron proteins: from structure to function, *Biopolymers* *80*, 264-278.
10. Maglio, O., Natri, F., de Rosales, R. T. M., Faiella, M., Pavone, V., DeGrado, W. F., and Lombardi, A. (2007) Diiron-containing metalloproteins: Developing functional models, *Cr Chim* *10*, 703-720.
11. Huang, S. S., Gibney, B. R., Stayrook, S. E., Dutton, P. L., and Lewis, M. (2003) X-ray structure of a Maquette scaffold, *Journal of Molecular Biology* *326*, 1219-1225.
12. Shifman, J. M., Moser, C. C., Kalsbeck, W. A., Bocian, D. F., and Dutton, P. L. (1998) Functionalized de novo designed proteins: mechanism of proton coupling to oxidation/reduction in heme protein maquettes, *Biochemistry* *37*, 16815-16827.
13. Nagi, A. D., and Regan, L. (1997) An inverse correlation between loop length and stability in a four-helix-bundle protein, *Folding & Design* *2*, 67-75.
14. Predki, P. F., and Regan, L. (1995) Redesigning the topology of a four-helix-bundle protein: monomeric Rop, *Biochemistry* *34*, 9834-9839.
15. Regan, L., and DeGrado, W. F. (1988) Characterization of a helical protein designed from first principles, *Science* *241*, 976-978.
16. Gasteiger, E., Gattiker, A., Hoogland, C., Ivanyi, I., Appel, R. D., and Bairoch, A. (2003) ExpASY: the proteomics server for in-depth protein knowledge and analysis, *Nucleic Acids Research* *31*, 3784-3788.
17. Barber, J. (2008) Photosynthetic generation of oxygen, *Philos Trans R Soc Lond B Biol Sci* *363*, 2665-2674.
18. Summa, C. M., Lombardi, A., Lewis, M., and DeGrado, W. F. (1999) Tertiary templates for the design of diiron proteins, *Curr Opin Struct Biol* *9*, 500-508.
19. Bradley, J. M., Svistunenko, D. A., Lawson, T. L., Hemmings, A. M., Moore, G. R., and Le Brun, N. E. (2015) Three Aromatic Residues are Required for Electron Transfer during Iron Mineralization in Bacterioferritin, *Angew Chem Int Ed Engl* *54*, 14763-14767.
20. Ravi, N., Bollinger, J. M., Huynh, B. H., Edmondson, D. E., and Stubbe, J. (1994) Mechanism of Assembly of the Tyrosyl Radical-Diiron(III) Cofactor of Escherichia-Coli

- Ribonucleotide Reductase .1. Mossbauer Characterization of the Diferric Radical Precursor, *Journal of the American Chemical Society* 116, 8007-8014.
21. Faiella, M., Andreozzi, C., de Rosales, R. T., Pavone, V., Maglio, O., Natri, F., DeGrado, W. F., and Lombardi, A. (2009) An artificial di-iron oxo-protein with phenol oxidase activity, *Nat Chem Biol* 5, 882-884.
 22. Torres Martin de Rosales, R., Faiella, M., Farquhar, E., Que, L., Jr., Andreozzi, C., Pavone, V., Maglio, O., Natri, F., and Lombardi, A. (2010) Spectroscopic and metal-binding properties of DF3: an artificial protein able to accommodate different metal ions, *J Biol Inorg Chem* 15, 717-728.
 23. Bell, C. B., Calhoun, J. R., Bobyr, E., Wei, P. P., Hedman, B., Hodgson, K. O., DeGrado, W. F., and Solomon, E. T. (2009) Spectroscopic Definition of the Biferrous and Biferic Sites in de Novo Designed Four-Helix Bundle DFsc Peptides: Implications for O₂ Reactivity of Binuclear Non-Heme Iron Enzymes, *Biochemistry* 48, 59-73.
 24. Hunte, C., Koepke, J., Lange, C., Rossmann, T., and Michel, H. (2000) Structure at 2.3 Å resolution of the cytochrome bc(1) complex from the yeast *Saccharomyces cerevisiae* co-crystallized with an antibody Fv fragment, *Structure* 8, 669-684.
 25. Fry, H. C., Lehmann, A., Saven, J. G., DeGrado, W. F., and Therien, M. J. (2010) Computational design and elaboration of a de novo heterotetrameric alpha-helical protein that selectively binds an emissive abiological (porphinato)zinc chromophore, *J Am Chem Soc* 132, 3997-4005.
 26. Cochran, F. V., Wu, S. P., Wang, W., Nanda, V., Saven, J. G., Therien, M. J., and DeGrado, W. F. (2005) Computational de novo design and characterization of a four-helix bundle protein that selectively binds a nonbiological cofactor, *J Am Chem Soc* 127, 1346-1347.
 27. Esposti, M. D., De Vries, S., Crimi, M., Ghelli, A., Patarnello, T., and Meyer, A. (1993) Mitochondrial cytochrome b: evolution and structure of the protein, *Biochim Biophys Acta* 1143, 243-271.
 28. Frolow, F., Kalb, A. J., and Yariv, J. (1994) Structure of a unique twofold symmetric haem-binding site, *Nat Struct Biol* 1, 453-460.
 29. Gernert, K. M., Surles, M. C., Labean, T. H., Richardson, J. S., and Richardson, D. C. (1995) The Alacoil: a very tight, antiparallel coiled-coil of helices, *Protein Sci* 4, 2252-2260.
 30. Korendovych, I. V., Senes, A., Kim, Y. H., Lear, J. D., Fry, H. C., Therien, M. J., Blasie, J. K., Walker, F. A., and DeGrado, W. F. (2010) De novo design and molecular assembly of a transmembrane diporphyrin-binding protein complex, *J Am Chem Soc* 132, 15516-15518.
 31. Bender, G. M., Lehmann, A., Zou, H., Cheng, H., Fry, H. C., Engel, D., Therien, M. J., Blasie, J. K., Roder, H., Saven, J. G., and DeGrado, W. F. (2007) De novo design of a single-chain diphenylporphyrin metalloprotein, *J Am Chem Soc* 129, 10732-10740.
 32. Geremia, S., Di Costanzo, L., Randaccio, L., Engel, D. E., Lombardi, A., Natri, F., and DeGrado, W. F. (2005) Response of a designed metalloprotein to changes in metal ion coordination, exogenous ligands, and active site volume determined by X-ray crystallography, *J Am Chem Soc* 127, 17266-17276.
 33. Solan, A., Ratia, K., and Fairman, R. (2002) Exploring the role of alanine in the structure of the Lac repressor tetramerization domain, a ferritin-like Alacoil, *J Mol Biol* 317, 601-612.

34. Falzone, C. J., Mayer, M. R., Whiteman, E. L., Moore, C. D., and Lecomte, J. T. (1996) Design challenges for hemoproteins: the solution structure of apocytochrome b5, *Biochemistry* **35**, 6519-6526.
35. Landfried, D. A., Vuletich, D. A., Pond, M. P., and Lecomte, J. T. (2007) Structural and thermodynamic consequences of b heme binding for monomeric apoglobins and other apoproteins, *Gene* **398**, 12-28.
36. Smith, L. J., Kahraman, A., and Thornton, J. M. (2010) Heme proteins-Diversity in structural characteristics, function, and folding, *Proteins-Structure Function and Bioinformatics* **78**, 2349-2368.
37. Lahr, S. J., Engel, D. E., Stayrook, S. E., Maglio, O., North, B., Geremia, S., Lombardi, A., and DeGrado, W. F. (2005) Analysis and design of turns in alpha-helical hairpins, *J Mol Biol* **346**, 1441-1454.
38. Hingorani, K., Pace, R., Whitney, S., Murray, J. W., Smith, P., Cheah, M. H., Wydrzynski, T., and Hillier, W. (2014) Photo-oxidation of tyrosine in a bio-engineered bacterioferritin 'reaction centre'-a protein model for artificial photosynthesis, *Biochim Biophys Acta* **1837**, 1821-1834.
39. Conlan, B., Cox, N., Su, J. H., Hillier, W., Messinger, J., Lubitz, W., Dutton, P. L., and Wydrzynski, T. (2009) Photo-catalytic oxidation of a di-nuclear manganese centre in an engineered bacterioferritin 'reaction centre', *Biochim Biophys Acta* **1787**, 1112-1121.
40. Maglio, O., Natri, F., Calhoun, J. R., Lahr, S., Wade, H., Pavone, V., DeGrado, W. F., and Lombardi, A. (2005) Artificial di-iron proteins: solution characterization of four helix bundles containing two distinct types of inter-helical loops, *J Biol Inorg Chem* **10**, 539-549.
41. Hill, R. B., Raleigh, D. P., Lombardi, A., and DeGrado, W. F. (2000) De novo design of helical bundles as models for understanding protein folding and function, *Acc Chem Res* **33**, 745-754.
42. Summa, C. M., Rosenblatt, M. M., Hong, J. K., Lear, J. D., and DeGrado, W. F. (2002) Computational de novo design, and characterization of an A(2)B(2) diiron protein, *J Mol Biol* **321**, 923-938.
43. Pace, C. N., and Scholtz, J. M. (1998) A helix propensity scale based on experimental studies of peptides and proteins, *Biophys J* **75**, 422-427.
44. McAllister, K. A., Zou, H., Cochran, F. V., Bender, G. M., Senes, A., Fry, H. C., Nanda, V., Keenan, P. A., Lear, J. D., Saven, J. G., Therien, M. J., Blasie, J. K., and DeGrado, W. F. (2008) Using alpha-helical coiled-coils to design nanostructured metalloporphyrin arrays, *J Am Chem Soc* **130**, 11921-11927.
45. Erickson, H. P. (2009) Size and Shape of Protein Molecules at the Nanometer Level Determined by Sedimentation, Gel Filtration, and Electron Microscopy, *Biol Proced Online* **11**, 32-51.
46. Teale, F. W. (1959) Cleavage of the haem-protein link by acid methylethylketone, *Biochim Biophys Acta* **35**, 543.
47. Esposti, M. D., Palmer, G., and Lenaz, G. (1989) Circular Dichroic Spectroscopy of Membrane Hemoproteins - the Molecular Determinants of the Dichroic Properties of the B-Cytochromes in Various Ubiquinol - Cytochrome-C Reductases, *European Journal of Biochemistry* **182**, 27-36.

48. Robinson, C. R., Liu, Y., Thomson, J. A., Sturtevant, J. M., and Sligar, S. G. (1997) Energetics of heme binding to native and denatured states of cytochrome b562, *Biochemistry* *36*, 16141-16146.
49. Sommer, D. J., Vaughn, M. D., Clark, B. C., Tomlin, J., Roy, A., and Ghirlanda, G. (2016) Reengineering cyt b562 for hydrogen production: A facile route to artificial hydrogenases, *Biochim Biophys Acta* *1857*, 598-603.
50. Robertson, W. D., Bovell, A. M., and Warncke, K. (2013) Cobinamide production of hydrogen in a homogeneous aqueous photochemical system, and assembly and photoreduction in a (betaalpha)₈ protein, *J Biol Inorg Chem* *18*, 701-713.
51. Aravindu, K., Mass, O., Vairaprakash, P., Springer, J. W., Yang, E., Niedzwiedzki, D. M., Kirmaier, C., Bocian, D. F., Holten, D., and Lindsey, J. S. (2013) Amphiphilic chlorins and bacteriochlorins in micellar environments. Molecular design, de novo synthesis, and photophysical properties, *Chem Sci* *4*, 3459-3477.
52. Bertini, I., and Luchinat, C. (1984) High spin cobalt(II) as a probe for the investigation of metalloproteins, *Adv Inorg Biochem* *6*, 71-111.
53. Calhoun, J. R., Kono, H., Lahr, S., Wang, W., DeGrado, W. F., and Saven, J. G. (2003) Computational design and characterization of a monomeric helical dinuclear metalloprotein, *J Mol Biol* *334*, 1101-1115.
54. Keech, A. M., Le Brun, N. E., Wilson, M. T., Andrews, S. C., Moore, G. R., and Thomson, A. J. (1997) Spectroscopic studies of cobalt(II) binding to Escherichia coli bacterioferritin, *J Biol Chem* *272*, 422-429.
55. Pasternak, A., Kaplan, J., Lear, J. D., and DeGrado, W. F. (2001) Proton and metal ion-dependent assembly of a model diiron protein, *Protein Sci* *10*, 958-969.
56. Yang, X., Le Brun, N. E., Thomson, A. J., Moore, G. R., and Chasteen, N. D. (2000) The iron oxidation and hydrolysis chemistry of Escherichia coli bacterioferritin, *Biochemistry* *39*, 4915-4923.
57. Kelly, S. M., Jess, T. J., and Price, N. C. (2005) How to study proteins by circular dichroism, *Biochim Biophys Acta* *1751*, 119-139.
58. Zhou, N. E., Kay, C. M., and Hodges, R. S. (1992) Synthetic model proteins. Positional effects of interchain hydrophobic interactions on stability of two-stranded alpha-helical coiled-coils, *J Biol Chem* *267*, 2664-2670.
59. Zheng, T., Boyle, A., Robson Marsden, H., Valdink, D., Martelli, G., Raap, J., and Kros, A. (2015) Probing coiled-coil assembly by paramagnetic NMR spectroscopy, *Org Biomol Chem* *13*, 1159-1168.
60. Cooper, T. M., and Woody, R. W. (1990) The effect of conformation on the CD of interacting helices: a theoretical study of tropomyosin, *Biopolymers* *30*, 657-676.
61. Rau, H. K., and Haehnel, W. (1998) Design, synthesis, and properties of a novel cytochrome b model, *Journal of the American Chemical Society* *120*, 468-476.
62. Ghirlanda, G., Osyczka, A., Liu, W., Antolovich, M., Smith, K. M., Dutton, P. L., Wand, A. J., and DeGrado, W. F. (2004) De novo design of a D2-symmetrical protein that reproduces the diheme four-helix bundle in cytochrome bc1, *J Am Chem Soc* *126*, 8141-8147.
63. Huffman, D. L., Rosenblatt, M. M., and Suslick, K. S. (1998) Synthetic heme-peptide complexes, *Journal of the American Chemical Society* *120*, 6183-6184.
64. Hughson, F. M., Wright, P. E., and Baldwin, R. L. (1990) Structural characterization of a partly folded apomyoglobin intermediate, *Science* *249*, 1544-1548.

65. Griko, Y. V., Privalov, P. L., Venyaminov, S. Y., and Kutysenko, V. P. (1988) Thermodynamic study of the apomyoglobin structure, *J Mol Biol* 202, 127-138.
66. Beychok, S., and Blout, E. R. (1961) Optical rotatory dispersion of sperm whale ferrimyoglobin and horse ferrihemoglobin, *J Mol Biol* 3, 769-777.
67. Breslow, E., Beychok, S., Hardman, K. D., and Gurd, F. R. (1965) Relative Conformations of Sperm Whale Metmyoglobin and Apomyoglobin in Solution, *J Biol Chem* 240, 304-309.
68. Hirst, J. D., and Brooks, C. L., 3rd. (1994) Helicity, circular dichroism and molecular dynamics of proteins, *J Mol Biol* 243, 173-178.
69. Irving, H., and Williams, R. J. P. (1953) The Stability of Transition-Metal Complexes, *J Chem Soc*, 3192-3210.
70. Feng, Y. Q., and Sligar, S. G. (1991) Effect of heme binding on the structure and stability of Escherichia coli apocytochrome b562, *Biochemistry* 30, 10150-10155.
71. Van Holde, K. E., Johnson, W. C., and Ho, P. S. (2006) *Principles of physical biochemistry*, 2nd ed., Pearson/Prentice Hall, Upper Saddle River, N.J.
72. Palmer, G., and Degli Esposti, M. (1994) Application of exciton coupling theory to the structure of mitochondrial cytochrome b, *Biochemistry* 33, 176-185.
73. Arutyunyan, A. M., Borisov, V. B., Novoderezhkin, V. I., Ghaim, J., Zhang, J., Gennis, R. B., and Konstantinov, A. A. (2008) Strong excitonic interactions in the oxygen-reducing site of bd-type oxidase: the Fe-to-Fe distance between hemes d and b595 is 10 Å, *Biochemistry* 47, 1752-1759.
74. Alden, R. G., Johnson, E., Nagarajan, V., Parson, W. W., Law, C. J., and Cogdell, R. G. (1997) Calculations of spectroscopic properties of the LH2 bacteriochlorophyll - Protein antenna complex from Rhodospseudomonas acidophila, *Journal of Physical Chemistry B* 101, 4667-4680.
75. Kelly, S. M., and Price, N. C. (2000) The Use of Circular Dichroism in the Investigation of Protein Structure and Function, *Curr Protein Pept Sc* 1, 349-384.
76. Hsu, M. C., and Woody, R. W. (1971) The origin of the heme Cotton effects in myoglobin and hemoglobin, *J Am Chem Soc* 93, 3515-3525.
77. Dutton, P. L. (1978) Redox potentiometry: determination of midpoint potentials of oxidation-reduction components of biological electron-transfer systems, *Methods Enzymol* 54, 411-435.
78. Shifman, J. M., Gibney, B. R., Sharp, R. E., and Dutton, P. L. (2000) Heme redox potential control in de novo designed four-alpha-helix bundle proteins, *Biochemistry* 39, 14813-14821.
79. Moser, C. C., Sheehan, M. M., Ennist, N. M., Kodali, G., Bialas, C., Englander, M. T., Discher, B. M., and Dutton, P. L. (2016) De Novo Construction of Redox Active Proteins, *Methods Enzymol* 580, 365-388.
80. Patel, S. C., and Hecht, M. H. (2012) Directed evolution of the peroxidase activity of a de novo-designed protein, *Protein Eng Des Sel* 25, 445-452.
81. Gasteiger, E., Hoogland, C., Gattiker, A., Duvaud, S., Wilkins, M. R., Appel, R. D., and Bairoch, A. (2005) Protein Identification and Analysis Tools on the ExPASy Server, In *The Proteomics Protocols Handbook* (Walker, J. M., Ed.), pp 571-607, Humana Press.

Chapter 3: Structure of a reaction center maquette

No high-resolution structure of a *de novo*-designed protein has been reported in complex with heme B or any other tetrapyrrole. High-resolution structures do exist for small peptides that are covalently linked to a tetrapyrrole cofactor (1, 2), modified natural proteins with bound tetrapyrroles (3), and apo-states of *de novo* proteins that are capable of binding tetrapyrroles (4-7). This conspicuous absence is not for lack of effort, as structural characterization of designed proteins is generally pursued with purpose; experimentally-derived structures of *de novo*-designed proteins have the power to validate design methods, guide future designs, reveal structure-function relationships, and help explain the significance of structural elements of natural proteins.

3.1 Crystallographic structure determination of MZH3

Given the past difficulties in structural characterization of tetrapyrrole maquettes, crystallography of MZH3 in complex with heme B and zinc 5-phenyl,15-(*p*-carboxyphenyl) porphyrin (ZnPCP) was pursued with caution, initially. However, it was soon found that MZH3 crystallizes readily, with some limitations, in different space groups and unit cells with different cofactors and under various conditions. The very first crystal tray of MZH3 that was set to optimize results from an initial screen yielded heme-containing red crystals shown in Figure 3.1 that diffracted to 1.45 Å at the National Synchrotron Light Source (NSLS) at Brookhaven National Laboratory.

MZH3 samples that were subjected to HPLC and lyophilization prior to SEC showed no attenuation in crystal quality. MZH3 samples of only ~90% purity as estimated from SDS-PAGE gels were often easy to crystallize with heme and metal ions, but samples of MZH3 with a zinc tetrapyrrole were much more difficult to grow, and sometimes required seeding with crystals that did not contain a zinc tetrapyrrole. UV/vis spectroscopy and the quality of crystal growth and diffraction suggested that careful

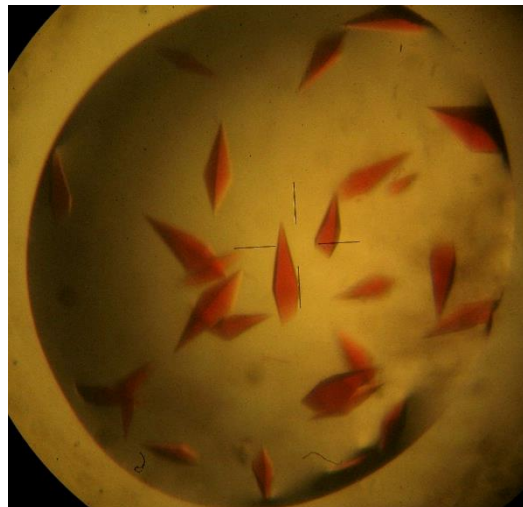


Figure 3.1: Crystals of MZH3 with heme B

These crystals were grown with heme B and Zn(II) in the first optimization tray and diffracted to 1.45 Å resolution for crystal structure CS-D (Table 3.2).

addition of 1.0 equivalent of low-solubility electron acceptor and pigment tetrapyrroles per maquette was necessary to prevent tetrapyrrole aggregates from sequestering cofactors and lowering occupancy of the acceptor and pigment binding sites. See the appendix for details concerning crystallography methods.

Three different crystallization conditions were used to solve high-resolution structures of MZH3, and a fourth condition was identified that provided only small, thin crystals that were not suitable for diffraction. These conditions and the ranges across which crystal growth was observed are shown in Table 3.1. Most crystal structures came from crystallization conditions CC-1 and CC-2, which have pH less than or equal 5.0, but crystals were also observed at pH as high 6.1 in CC-3. Lest it be surmised that MZH3 is only singularly structured at low pH, CC-4 was included in Table 3.1 to show that MZH3 crystals at higher pH have been observed, suggesting that MZH3 remains uniquely structured across a wide pH range.

Name	Salt	buffer	pH	precipitant	Notes
CC-1	2.2 – 4.0 M NaCl	100 mM Na acetate	3.2 – 5.0	–	One metal ion is located in unintended position, ligated by His138 N _ε atom instead of N _δ . Can grow with or without ZnPCP. Requires heme and metal dications.
CC-2	40 – 120 mM CdCl ₂	100 mM Na acetate	4.0 – 4.9	18 – 30% PEG 400 – 20,000	Crystals did not grow with ZnPCP. Can grow with or without heme B. Cd(II) is unavoidable in metal site.
CC-3	1 – 1.5 M Li ₂ SO ₄ 0.5M (NH ₄) ₂ SO ₄	100 mM Na ₃ citrate	5.6 – 6.1	–	Crystals grew with heme B and Zn(II) or Mn(II).
CC-4	10 – 200 mM Na/K tartrate or Na ₃ citrate	various buffers	6.8 – 9.5	24 – 40% PEG 200 – PEG 400	Crystals grew in presence of heme B, ZnPCP, and Zn(II). No diffraction-quality crystals grown

Table 3.1: Crystallization conditions used to grow MZH3 crystals

Details of the crystallization conditions for each crystal are given in the appendix. PEG is polyethylene glycol; the number beside it is the average molecular weight of PEG used.

Eight crystal structures of MZH3 are reported in this chapter, and they are listed in Table 3.2. Each of these structures contributes unique information about the assembly of cofactors. The first MZH3 structure was CS-A, which was solved by multi-wavelength anomalous dispersion (MAD) using the X-ray absorption of the three zinc ions (two from the metal site and one from the zinc tetrapyrrole) to create the phase shift and anomalous dispersion. All of the subsequent structures were solved by using molecular replacement starting from previously solved structures. Diffraction data for crystal structures CS-A and CS-D were collected using synchrotron radiation at the National Synchrotron Light Source. All others were collected using an in-house rotating copper anode X-ray generator at the University of Pennsylvania. Details of the methods and statistics for each crystal are given in the appendix.

Name	Condition	Resolution	Acceptor	Pigment	Metal	Notes
CS-A	CC-1	2.0 Å	Heme B	ZnPCP	2 Zn(II)	<ul style="list-style-type: none"> • used for MAD phasing • Zn(II) on wrong side of H138 • pH 4.5
CS-B	CC-1	2.02 Å	Heme B	ZnPCP	3 Mn(II)	<ul style="list-style-type: none"> • Tyr in two rotamers • Mn(II) on both sides of H138 • pH 4.9
CS-C	CC-1	2.10 Å	Heme B	ZnPCP	2 Mn(II)	<ul style="list-style-type: none"> • Tyr in unintended rotamer • extra ZnPCP • Mn(II) on wrong side of H138 • pH 4.8
CS-D	CC-1	1.45 Å	Heme B	–	2 Zn(II)	<ul style="list-style-type: none"> • Zn(II) on wrong side of H138 • pH 4.5
CS-E	CC-3	1.90 Å	Heme B	–	2 Mn(II)	<ul style="list-style-type: none"> • one low-occupancy Mn(II) • pH 5.9
CS-F	CC-2	2.01 Å	Heme B	–	2 Cd(II)	<ul style="list-style-type: none"> • pH 4.2
CS-G	CC-2	1.78 Å	–	–	2 Cd(II)	<ul style="list-style-type: none"> • Cd(II) bound to acceptor site • pH 4.4
CS-H	CC-2	2.02 Å	Heme B	–	2 Cd(II)	<ul style="list-style-type: none"> • L71H mutant with His-Tyr hydrogen bond • pH 4.6

Table 3.2: List of MZH3 crystal structures

Details of the crystallization conditions for each crystal are given in the appendix.

3.2 Overall structure of MZH3

As designed, MZH3 folds as a four-helix coiled coil (Figure 3.2). All eight structures are similar overall and largely consistent with the design. Helices begin and end at the intended positions, *α*- and *d*-position amino acids are directed into the core, each helix is oriented antiparallel to its two adjacent neighboring helices to form *e-e* and *g-g* interfaces, the bundle has the intended left turning topology, and, with some exceptions that will be described in subsequent sections, cofactors bind to intended sites in accordance with the design.

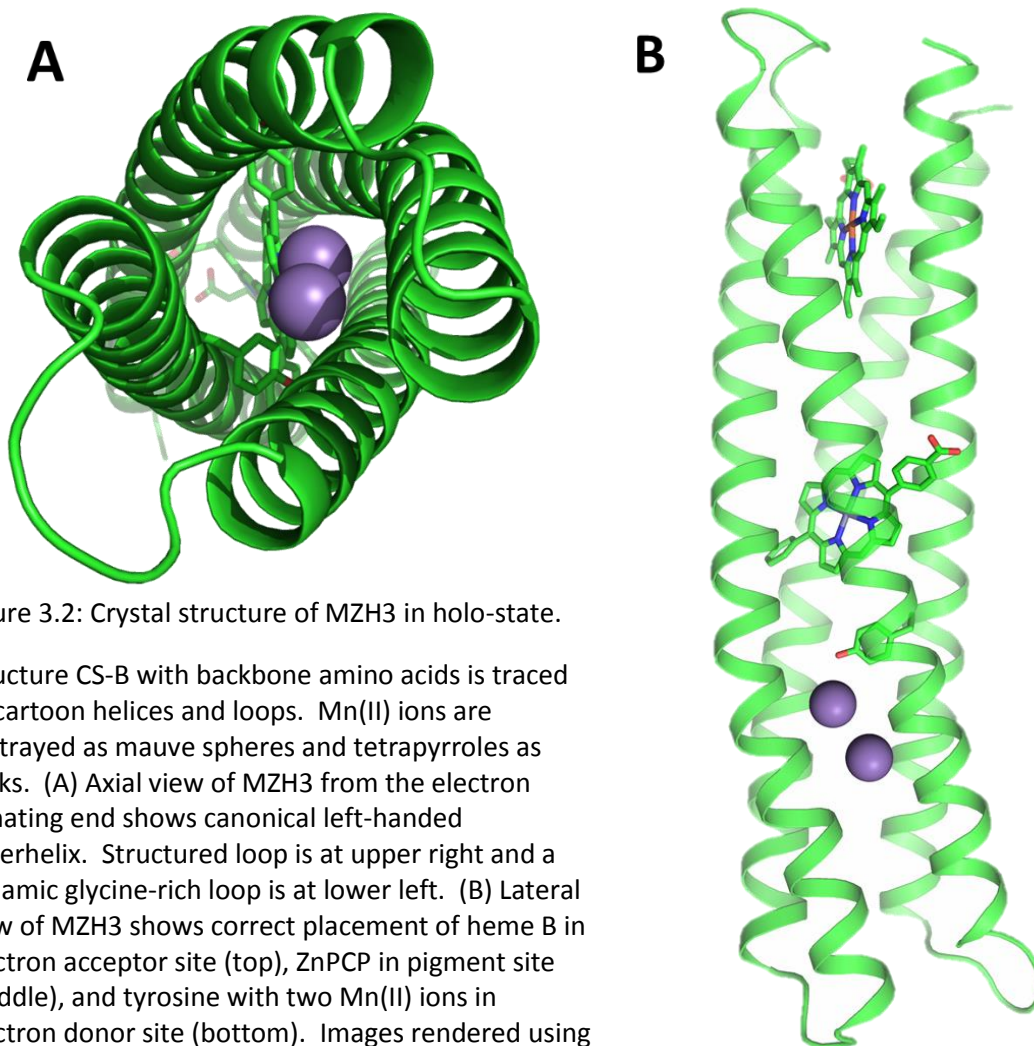


Figure 3.2: Crystal structure of MZH3 in holo-state.

Structure CS-B with backbone amino acids is traced by cartoon helices and loops. Mn(II) ions are portrayed as mauve spheres and tetrapyrroles as sticks. (A) Axial view of MZH3 from the electron donating end shows canonical left-handed superhelix. Structured loop is at upper right and a dynamic glycine-rich loop is at lower left. (B) Lateral view of MZH3 shows correct placement of heme B in electron acceptor site (top), ZnPCP in pigment site (middle), and tyrosine with two Mn(II) ions in electron donor site (bottom). Images rendered using The PyMOL Molecular Graphics System, Version 1.7 Schrödinger, LLC.

3.2.1 MZH3 is a coiled coil

Coiled coil structural parameters of MZH3 were evaluated by the programs SOCKET (8), TWISTER (9), and CCCP (10). These programs assess the structure of a coiled coil by taking atomic coordinates from a PDB file as input and searching for knob-into-hole interactions and/or determining the Crick parameters, a set of parameters that can be used to define the amino acid backbone coordinates in an idealized coiled coil (11, 12). Using the coordinates of CS-B as a prototypical MZH3 structure, all three programs find that MZH3 is a canonical coiled coil with a

left-handed superhelix. In addition, the heptad *abcdefg* positions of helical amino acids in MZH3 designated by the programs agree with the *abcdefg* assignments intended by design. For a set of coordinates that included only the residues between and including the core *a-d-a-d* layers at either end of the MZH3 bundle, CCCP calculated an average of 3.51 residues per turn (canonical coiled coils have 3.5 residues per turn) and a 0.968 Å RMSD deviation from an idealized coiled coil structure. SOCKET identified extensive knob-into-hole interactions involving *a*, *d*, *e*, and *g* positions across each helix. SOCKET also calculated the average pairwise helix crossing angle between adjacent helices to be 19.9°; idealized coiled coils with left-handed supercoils tend to have crossing angles near 20° (13). This analysis shows that the secondary and tertiary structure of MZH3 is consistent with the design.

3.2.2 Layers in the hydrophobic core

MZH3 forms layers in the hydrophobic core that are consistent with the design. Each helix contributes two heptad *a*- and two *d*-positions to each layer to make groups of four amino acids each that are roughly aligned in the same plane. This validates the original design approach of connecting the set of layers from a di-heme protein such as cytochrome b to the set of layers from a diiron protein such as bacterioferritin to form a long string of layers in an extended four-helix bundle. The left panel in Figure 3.3, shows how the *a-d-a-d* layers of cytochrome b and bacterioferritin were essentially strung together to make the core of MZH3. While the exact identities of each core *a*- and *d*-position are not copied from nature, the total size of the amino acid side chains and cofactors in each layer is kept consistent throughout the length of the holo-state bundle, with small exceptions to aid cofactor binding and function. The right panel of Figure 3.3 shows the simplified cartoon backbones and cofactors of cytochrome b

and bacterioferritin to show how MZH3 retains structural properties of both a transmembrane hemoprotein and a water soluble diiron protein. When connected, they create a metal-tyrosine-pigment-electron acceptor tetrad that should be competent for light-activated electron transfer and the trapping of a charge-separated state.

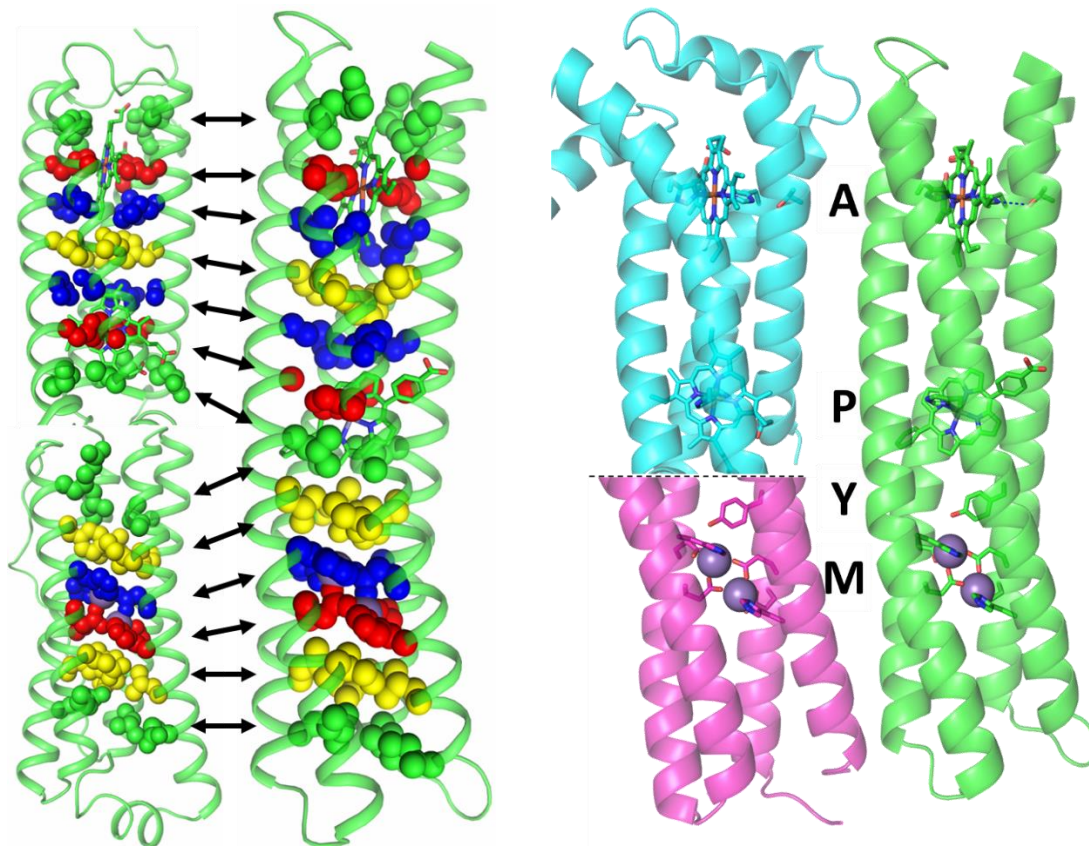


Figure 3.3: Seamless connection of MZH3 cofactor binding modules facilitated by layers

Left: layering of the hydrophobic core in MZH3 (CS-B) is similar to that of a cytochrome b-like protein joined to a bacterioferritin-like protein. The four-helix bundle on the top left is a crystal structure of cytochrome b (14). The bottom left bundle is a crystal structure of bacterioferritin (15). Layers of α - δ - α - δ positions are shown as spheres. Colors of layers in MZH3 match up with layers in cytochrome b and bacterioferritin, as indicated by arrows. Right: Cartoon of MZH3 with cofactors (green, structure CS-B) is shown alongside cytochrome b in cyan (16), and bacterioferritin in magenta (17). Cofactors are labeled A for electron acceptor, P for pigment, Y for tyrosine, and M for di-metal center. Images rendered using The PyMOL Molecular Graphics System, Version 1.7 Schrödinger, LLC.

3.2.3 *Inter-helical charge patterning interactions*

Charge patterning interactions between *c*-position glutamates and lysines in the tetrapyrrole-binding section of MZH3 did not result in stable salt-bridging hydrogen bonds. In some crystal structures, some of the distances between lysine nitrogens and glutamate oxygens are close enough for hydrogen bonding, but these flexible, solvent-exposed side chains tend to have relatively high temperature factors, indicating that hydrogen bonding interactions are transient. It may be that the *g-g* interfaces in MZH3 are too wide for persistent hydrogen bonding between *c*-position residues. In addition, the high ionic strengths of the three crystallization conditions may shield the charges to some extent and destabilize surface-exposed polar contacts. Despite the lack of stable salt bridges, the cumulative effect of all of the inter-helical electrostatic interactions may be involved in determining the topology.

3.2.4 *Inter-helical loops*

The structures of the inter-helical loops in MZH3 follow the design (Figure 3.4). The structured turn between helices 1 and 2 in MZH3 forms the same set of hydrogen bonds as the structured turn between helices 1 and 2 in MZH3 forms the same set of hydrogen bonds as the Due Ferro protein DF2t, which has the same loop sequence (18). This structured loop has backbone temperature factors that are similar to backbone temperature factors within the helices, indicating that the loop is stable and that the hydrogen bonding pattern in the turn persists. In contrast, the N- and C-termini and glycine-rich loops in MZH3 are dynamic.

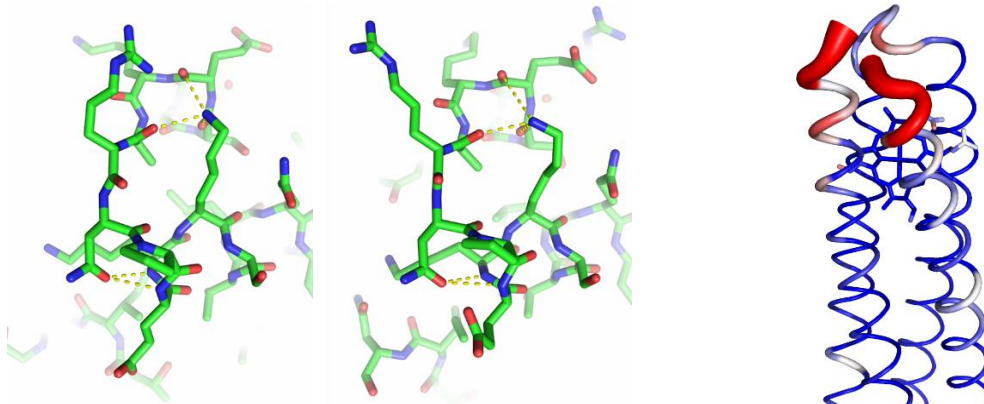


Figure 3.4: Structured loop in MZH3 and DF2t

The structured turn in MZH3 that connects helices 1 and 2 (above left, from structure CS-D) closely matches the conformation of the turn in DF2t (above right, PDB ID: 1MFT) (18). Yellow dotted lines represent hydrogen bonds between side chains and backbone atoms. Right: backbone atoms in CS-D represented by temperature factor from low (blue, narrow tube), to medium (white), to high (red, wide tube). As expected, the most dynamic parts are the N- and C- termini and glycine-rich loops. The structured loop (bottom, rear) has temperature factors similar to the center of the bundle. Images rendered using The PyMOL Molecular Graphics System, Version 1.7 Schrödinger, LLC.

The overall structure of MZH3 is consistent with the design. The following sections will examine specific interactions at cofactor binding sites to validate or challenge design methods and consider possible effects on function.

3.3 Electron acceptor site

3.3.1 Heme B binding site agrees with design

Heme B was selected as the electron acceptor in all crystallography experiments, except in crystal structure CS-G, which lacks an electron acceptor. All heme-containing structures show that the acceptor site histidine residues ligate the ferric ion of heme B with N_{ϵ} atoms, the propionate groups of the heme are directed away from the hydrophobic core and are partially

exposed to solvent, and the porphyrin ring is secured into a well-defined conformation with low temperature factors (Figure 3.5). This fixed heme conformation is surprising, because no facet of the design was consciously included to prevent free rotation of the porphyrin ring about the histidine-iron ligands while keeping propionate groups solvent exposed.

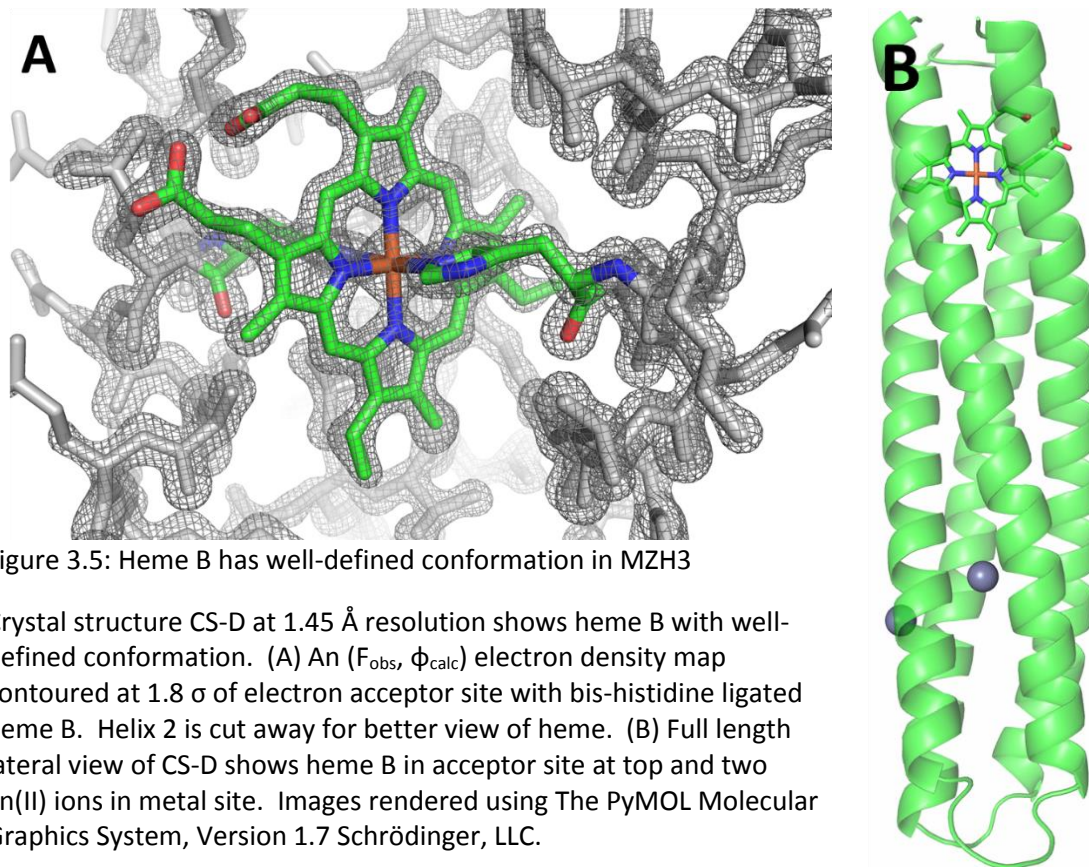


Figure 3.5: Heme B has well-defined conformation in MZH3

Crystal structure CS-D at 1.45 Å resolution shows heme B with well-defined conformation. (A) An (F_{obs} , ϕ_{calc}) electron density map contoured at 1.8 σ of electron acceptor site with bis-histidine ligated heme B. Helix 2 is cut away for better view of heme. (B) Full length lateral view of CS-D shows heme B in acceptor site at top and two Zn(II) ions in metal site. Images rendered using The PyMOL Molecular Graphics System, Version 1.7 Schrödinger, LLC.

All of the crystal structures with heme in the electron acceptor site exhibit the intended second-shell inter-helical hydrogen bonds between the N δ atoms of the heme-ligating histidines and the threonine hydroxyl groups (Figure 3.6). The lengths of the hydrogen bonds range from about 2.6 to 3.1 Å. Helices 1 and 3, which bear heme-ligating histidines are pushed outward to make room for the histidine-iron ligation, while helices 2 and 4, which contain notch glycines,

make close contact with heme. The C_α atoms of the notch glycines (shown as green spheres in Figure 3.6) are within van der Waals contact of the heme.

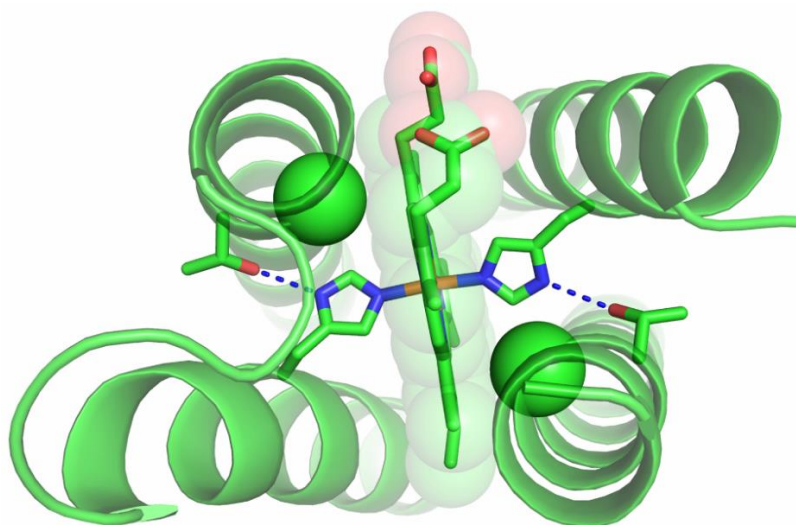


Figure 3.6: Heme B binding site and 2nd shell threonines

Axial view of crystal structure CS-D from electron acceptor end. Blue dotted lines represent hydrogen bonds between threonine residues and ligating histidines. Glycine residues (with C_α as green spheres) make close van der Waals contact with heme (translucent spheres).

Image rendered using The PyMOL Molecular Graphics System, Version 1.7 Schrödinger, LLC.

3.3.2 Multiple heme conformations in the acceptor site

Despite the low temperature factors of heme B in MZH3, different conformations are observed in the crystal structures. A close-up view of the isolated electron density map of the heme B from crystal structure CS-D at 1.45 Å shows that the diffraction data is consistent with heme B in either of two orientations related by a 180° rotation that switches the positions of the vinyl groups (Figure 3.7). A similar lack of conformational specificity with regard to the vinyl groups is observed in cytochrome b₅, neuroglobin, and others (19, 20), but some proteins display selectivity for one orientation. Protein contacts at the heme edge are generally not well conserved, suggesting that this 180° flipping of the heme has little effect on function (21).

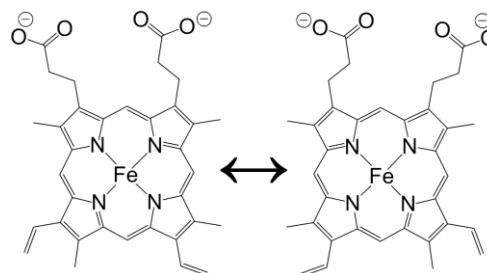
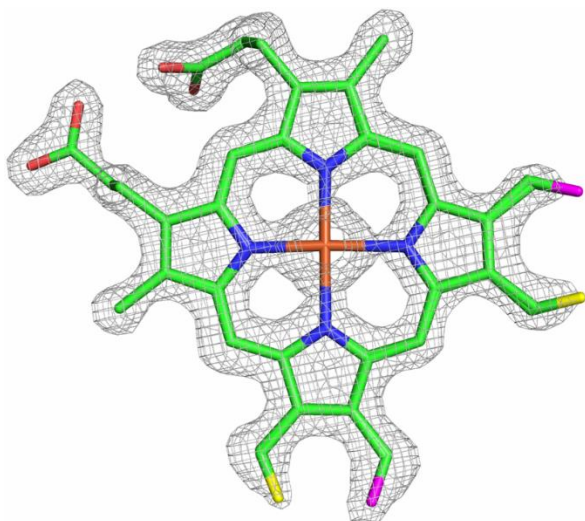


Figure 3.7: Heme flipping in MZH3

Left: Two possible orientations of heme B superimposed in structure CS-D (F_{obs} , ϕ_{calc}) map contoured at 1.8σ . One orientation has heme vinyl methylene groups colored yellow, the other magenta. Top right: Heme B has asymmetric arrangement of vinyl and methyl groups in pyrrole β -positions.

Image rendered using The PyMOL Molecular Graphics System, Version 1.7 Schrödinger, LLC.

While the positions of the vinyl groups of heme B are sometimes in a mixture of states, heme B is otherwise fixed in natural proteins. In MZH3, mutation of leucine 71 to histidine in crystal structure CS-H led to a 90° rotation of the heme porphyrin ring relative to the wild type structure, putting the propionate groups between helices 3 and 4 instead of between 1 and 2 (Figure 3.8). The MZH3-L71H mutant will be discussed in more detail in section 3.6.

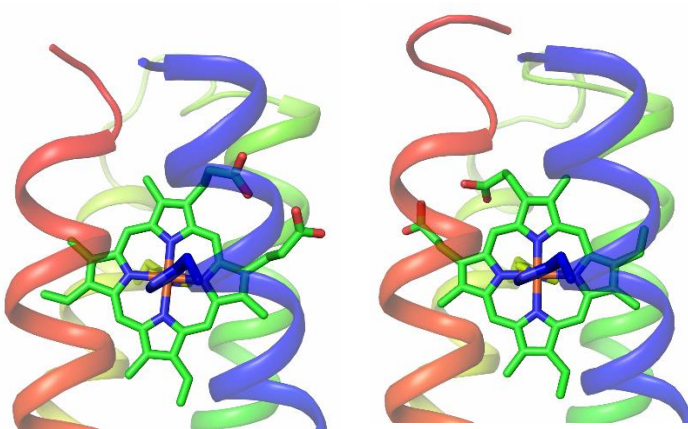


Figure 3.8: Heme B rotation by 90° in MZH3-L71H mutant

Heme B is rotated in crystal structure CS-F (left) relative to CS-H (right). Both crystals were grown in condition CC-2 with heme B and Cd(II), but CS-H has L71H mutation. Space groups were C2 for CS-F and P2₁ for CS-H. Helices 1, 2, 3, and 4 are colored blue, green, yellow, and red, respectively.

Images rendered using The PyMOL Molecular Graphics System, Version 1.7 Schrödinger, LLC.

3.3.3 Influence of arginine and tryptophan residues on heme binding in MZH3

Arginine residues in cytochrome b make stable salt bridging hydrogen bonds with the propionate groups of heme B. In MZH3, two *d*-position arginines were placed one turn N-terminal to the heme-ligating histidines in an effort to reproduce this interaction. Crystal structures indicate that these arginines do not make stable hydrogen bonds with heme propionate groups. The low pH of most of the crystal structures might inhibit salt bridging interactions by protonating the propionate groups. In structure CS-E at pH 5.9, the arginine nitrogen to propionate oxygen distance is 2.8 Å, close

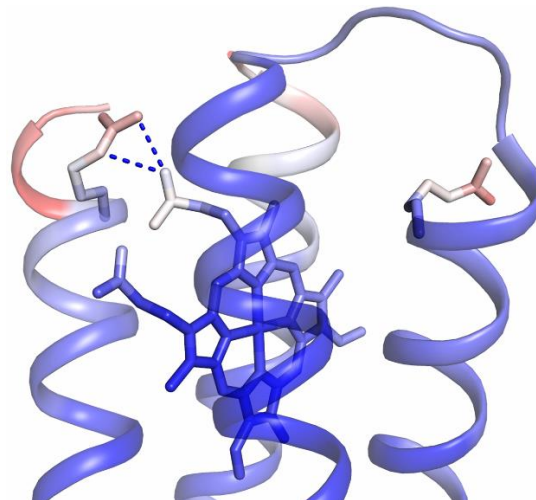


Figure 3.9: Heme-arginine interaction in MZH3

MZH3 crystal structure CS-E at pH 5.9 shows heme propionate-arginine interaction. Heme B and arginine side chains are represented as sticks. Atoms are colored by temperature factors from low (blue) to medium (white) to high (red). Temperature factors suggest propionate-arginine hydrogen bond is unstable. Image rendered using The PyMOL Molecular Graphics System, Version 1.7 Schrödinger, LLC.

enough for hydrogen bonding, but elevated temperature factors suggest that these interactions are transient (Figure 3.9). Nevertheless, *d*-position arginines may serve to prevent hydrophobic collapse of the electron acceptor site in the apo-state to make the site accessible for cofactor binding, attract the heme B cofactor (which has an overall charge of -1 in the ferric state at neutral pH), stabilize the propionate groups by electrostatic interactions, and raise the midpoint potential of the electron acceptor. Calculations performed by Dirk Auman using multi-conformer continuum electrostatics (MCCE) (22, 23) indicate that despite the conformational freedom of the two arginine residues, they each raise the heme B midpoint potential by ~ 16 mV

to a predicted midpoint of -192 mV (*personal communication*). This is consistent with the -180 mV measurement at pH 7 by redox titration (Figure 2.22).

MZH3 has two tryptophan residues in interfacial *e*-positions next to the electron acceptor site that were included mainly as spectroscopic probes for concentration measurements. They are located very close to the dynamic C-termini of helices 2 and 4, and their conformations vary widely in different crystal structures. However, most of the MZH3 crystal structures have one tryptophan residue within about 4 Å of the heme cofactor, possibly forming stabilizing T-stacking interactions. The second tryptophan side chain appears to be very close to the propionate groups of heme, which is a potentially destabilizing interaction. Despite their proximity to the heme, the effect of the tryptophan residues on heme binding is ambiguous.

3.3.4 Structural similarity between heme sites of MZH3 and cytochrome *b*

The MZH3 crystal structures that contain heme B reveal remarkable structural similarities with cytochrome *b* despite negligible sequence similarity (Figure 3.10). As intended by design, MZH3 shows similar interface widths, hydrophobic core packing, rotameric states of heme-ligating histidines, and second shell histidine-threonine hydrogen bonds. Furthermore, the orientation of the maquette heme relative to the superhelical bundle axis is conspicuously similar to that observed in cytochrome *b*, suggesting that the particular conformation of heme in cytochrome *b* is not precisely controlled for any functional purpose, but rather is an accident of the structural constraints demanded by this protein fold.

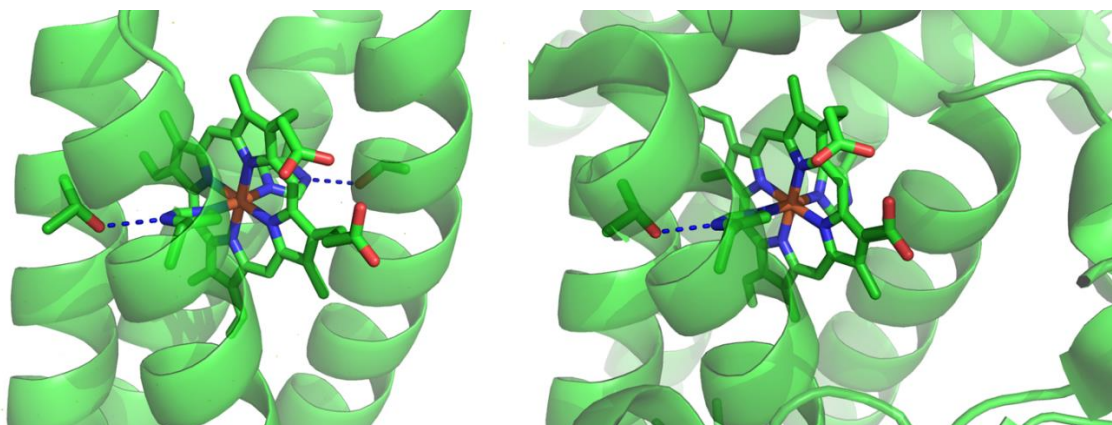


Figure 3.10: Structural similarity between MZH3 and cytochrome b

Despite low sequence similarity, MZH3 and cytochrome b bind heme B with very similar conformations. Left: MZH3 crystal structure CS-D. Right: cytochrome b crystal structure, PDB ID: 2A06 (16). Images rendered using The PyMOL Molecular Graphics System, Version 1.7 Schrödinger, LLC.

3.3.5 *Apo-state of the acceptor site*

Binding of heme B appeared to improve crystal growth in most cases, but crystallization condition CC-2 containing ~ 35 mM CdCl_2 was able to facilitate MZH3 crystal growth from a sample that lacked an electron acceptor cofactor. Because MZH3 expresses with some heme already bound, extra purification steps were required including HPLC purification to remove heme, lyophilization to remove acetonitrile, resuspension in GdnHCl to solubilize the lyophilized powder, and dilution to refold the protein. After SEC, the crystallization trays were set, and the resulting structure, CS-G, diffracted to 1.78 \AA using a rotating copper anode X-ray tube.

In CS-G and other crystal structures that came from crystallization condition CC-2, several Cd(II) ions are bound to the surface of MZH3, and some of them mediate crystal contacts. In CS-G, one of the resolved Cd(II) ions is ligated by the two histidines in the electron acceptor site. The Cd(II) takes on a tetrahedral geometry with two coordinated water molecules and the two histidines ligating with N_ϵ atoms (Figure 3.11). Because of the tetrahedral geometry of the Cd(II) ion, the histidines cannot have the same rotameric state as they do when ligating

heme. Instead, His110 has its imidazole ring flipped, disrupting the second-shell hydrogen-bond to Thr91.

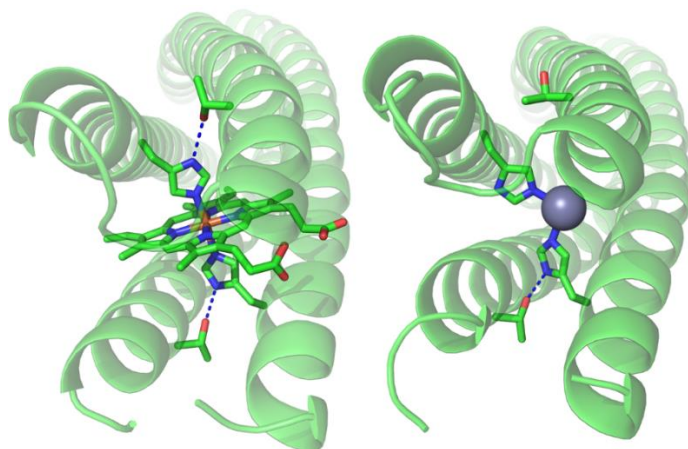


Figure 3.11: MZH3 structure without electron acceptor

MZH3 conformation is similar with heme B or Cd(II) in acceptor site. Left: crystal structure CS-D has bis-histidine ligated heme B and second shell His-Thr hydrogen bonds. Right: structure CS-G lacks an electron acceptor, but a Cd(II) ion is coordinated by the two histidine residues. One His-Thr hydrogen bond remains intact, but the other is broken.

Images rendered using The PyMOL Molecular Graphics System, Version 1.7 Schrödinger, LLC.

In comparing the structures of MZH3 with and without heme, it is important to remember that the Cd(II) ion in the acceptor site may serve to stabilize the site. As described in the introduction, natural hemoproteins typically have significant conformational variability in heme binding sites in the apo-state, and the binding of heme stabilizes secondary and tertiary structure. In contrast, the structures of MZH3 with heme and with Cd(II) in the acceptor site have relatively subtle differences. They have essentially identical helix content, and the only significant difference between their tertiary structures is a modest expansion of *e-e* interface through which the porphyrin ring lies. As shown in Figure 3.12, the most notable changes seem to be in side chain rotamers. The two tryptophan residues next to the acceptor site, W96 and W193, are fully or partially buried in the absence of heme, but heme binding displaces them into more solvent-exposed conformations. Gln residues in *e*-positions and two *d*-position Leu residues also change conformation to accommodate the steric bulk of the heme cofactor.

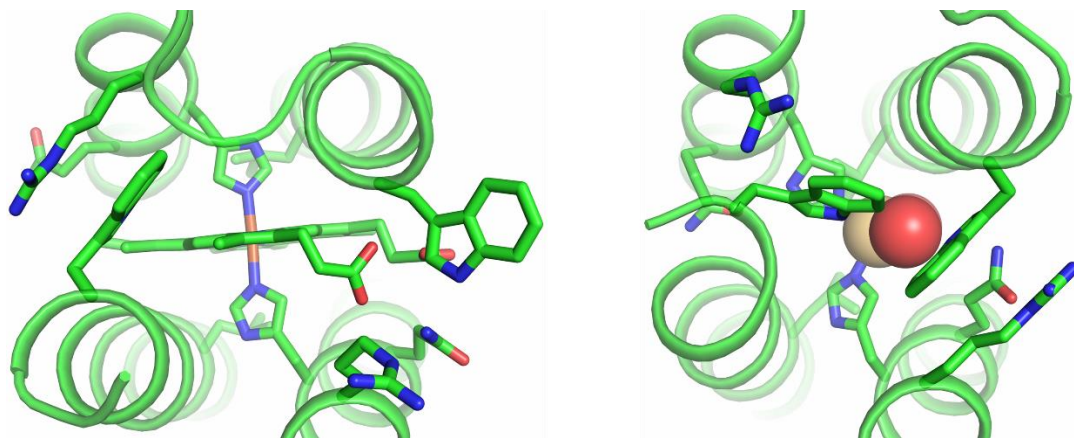


Figure 3.12: Conformational changes associated with heme binding in MZH3

Heme binding in MZH3 triggers a slight expansion of the *e-e* interface as well as rotameric changes in the side chains of Trp96, Trp193, Arg6, Arg107, Gln10, Gln111, Leu88, and Leu185. Some of these changes, particularly the removal of the tryptophans from the core, might weaken heme affinity. Left: MZH3 crystal structure CS-D. Right: MZH3 crystal structure CS-G. Images rendered using The PyMOL Molecular Graphics System, Version 1.7 Schrödinger, LLC.

The electron acceptor site probably does not bind metal ions at lower concentrations, and it is possible that the bis-histidine-ligated Cd(II) ion affects the structure. Even with Cd(II) contributing to stability, it is still surprising that the acceptor site is so structured without heme; the hydrophobic core in this part of the protein includes two *d*-position arginines, two *a*-position glycines, and two *d*-position histidines, all of which should be strongly destabilizing. It may be that interfacial interactions between *g*-position leucines and electrostatic interactions between *c*-position glutamates and lysines are the most stabilizing forces in the vicinity of the apo-state acceptor site.

3.4 Pigment site

3.4.1 Apo-state of the pigment site

Given the importance of apo-state flexibility for heme binding sites, it was deemed important to create ample space for the binding of a zinc tetrapyrrole at the pigment site of

MZH3. The pigment site lies in the center of the four-helix bundle, where the protein should be the most stable, and if the pigment site succumbs to hydrophobic collapse in the apo-state, the inherent inflexibility of the helices in this section of the bundle would prevent entry of the zinc tetrapyrrole. For this reason, MZH3 design included *a-d-a-d* layers of bulky hydrophobic amino acids adjacent to the pigment site and four helical α -position glycines in the pigment site in order to create a cavity into which a zinc tetrapyrrole could penetrate.

Figure 3.13 shows that in the absence of a pigment cofactor, the helices are indeed held apart to create a pore in the center of the bundle. The highest resolution crystal structures that lack a zinc tetrapyrrole, CS-D and CS-G, have four well-resolved water molecules in the pigment site. These four waters are found in

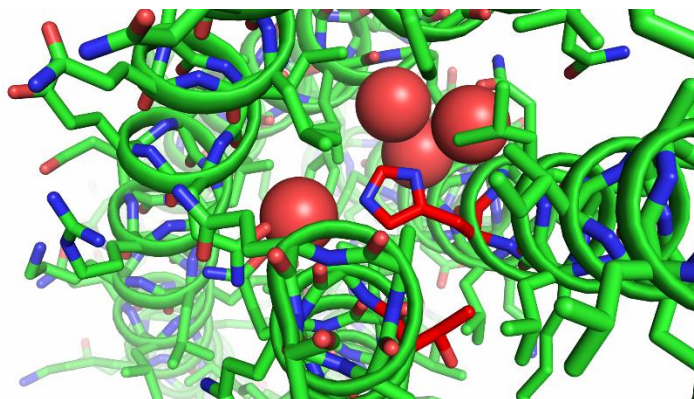


Figure 3.13: MZH3 structure without pigment

the same positions regardless of differences in the crystallization condition or whether heme B is present. The fact that water is able to penetrate into the pigment site means that a proper binding cavity has been created for the zinc tetrapyrrole.

The MZH3 pigment site contains four structured water molecules when zinc tetrapyrrole is absent. Crystal structure CS-G is shown here with the four buried waters shown as red spheres and the zinc tetrapyrrole-ligating histidine and intended second-shell threonine shown in red. Part of helix 2 is cut away for better view of pigment site. Image rendered using The PyMOL Molecular Graphics System, Version 1.7 Schrödinger, LLC.

The presence of water in the hydrophobic core is usually strongly destabilizing. However, circular dichroism showed that in the absence of cofactors, MZH3 is highly α -helical and has a high melting temperature of 82°C. Given that apo-MZH3 has poor hydrophobic core

packing in the acceptor site, water in core at the pigment site, water and four negatively charged glutamate residues in the core at the metal site, and a total of ten helical glycine residues at mostly *a*- and *d*-positions, its high stability cannot be attributed to packing of *a-d-a-d* layers alone. Interfacial hydrophobic contacts and possibly inter-helical charge pairing interactions may provide much of the driving force for folding of MZH3.

Figure 3.13 also shows that the pigment site histidine residue H124 and an interfacial threonine T77 (both shown in red) are not in rotameric states that would allow a hydrogen bond to form. These residues were designed to make a hydrogen bond when the zinc tetrapyrrole is bound, and with their C_α atoms 5.9 Å apart in CS-G, they appear to be close enough to make a hydrogen bond if their rotamers changed.

3.4.2 *Holo-state of the pigment site*

All three crystal structures that contain a pigment molecule, CS-A, CS-B, and CS-C, used Zn 5-(*p*-carboxyphenyl)-15-phenyl porphyrin (ZnPCP), which was kindly provided by Tatiana Esipova in the laboratory of Sergei Vinogradov. As shown in Figure 2.17, ZnPCP binds with a dissociation constant of <10 nM. These three structures also had heme B and either Zn(II) or Mn(II) as the metal ion. Zn(II) has the advantage of being able to form strong ligands, as predicted by the Irving-Williams series (24), and zinc was useful for MAD phasing in concert with the zinc ion of ZnPCP to solve the crystal structure CS-A.

The pigment binding site of CS-A is shown in Figure 3.14. The ZnPCP molecule in CS-A is resolved in the pigment site with a conformation that is largely consistent with the design. The phenyl groups protrude through the *e-e* interfaces on either side of the protein, as expected. Similar to heme B, the ZnPCP molecule is tilted in the binding site so that two of the pyrrole

nitrogens are closer to the central superhelical axis of MZH3 than the other two. ZnPCP has higher temperature factors and less well-defined electron density than the heme B, which suggests sub-stoichiometric occupancy of the pigment site or increased conformational variability compared to heme B.

Like the ZnPCP cofactor itself, the ZnPCP-ligating His124 has poorly-defined electron density, and its rotameric state is ambiguous. It is not clear whether His124 ligates ZnPCP with the N_δ or N_ε imidazole nitrogen, possibly because partial occupancy of the ZnPCP may result in the histidine having multiple conformations that complicate its electron density. The pigment site was designed for ligation of the zinc ion of ZnPCP by the histidine N_ε, and this conformation is consistent with the (F_{obs}, φ_{calc}) electron density map of CS-A (Figure 3.14), but not conclusive. In the conformation that has the N_ε atom as the ZnPCP ligand, the His124 N_δ is 2.7 Å from the second shell Thr77 oxygen, forming a putative hydrogen bond, as designed.

The ZnPCP molecule has one carboxylate group in the *para*-position on one of the phenyl groups. The temperature factors of this carboxylate group are high, but the electron density map is more consistent with the carboxylate being in the *e-e* interface between helices 3 and 4 than between helices 1 and 2 (Figure 3.14). This could be because the charge-pairing *c*-position amino acids in the porphyrin-binding section of MZH3 are distributed so that helices 3 and 4 are positively charged and helices 1 and 2 are negatively charged, creating a dipole moment that may cause the preference in ZnPCP orientation.

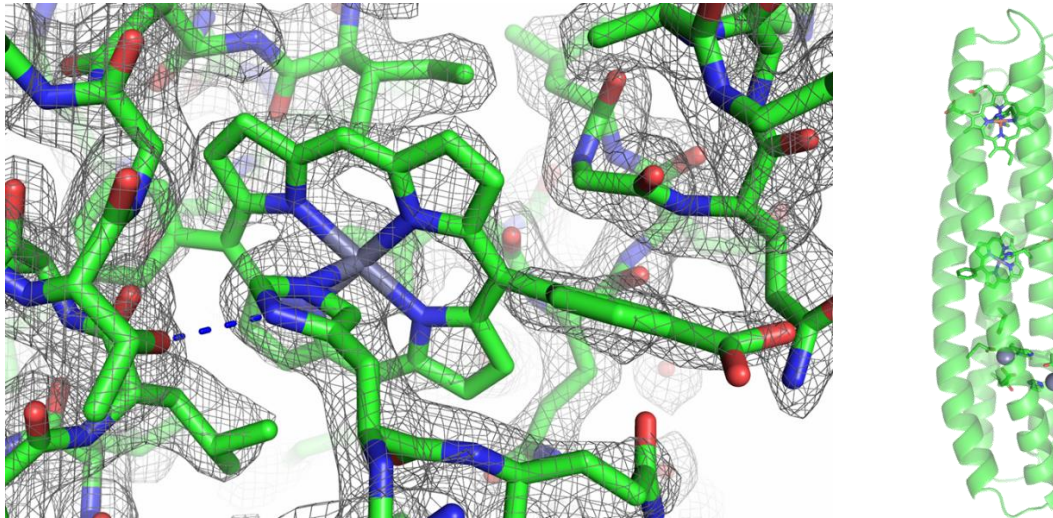
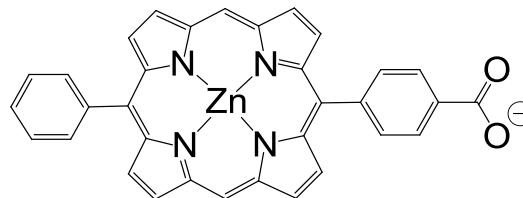


Figure 3.14: CS-A pigment site with ZnPCP

The cofactor Zn 5-(*p*-carboxyphenyl)-15-phenyl porphyrin (ZnPCP) (lower right) binds to the pigment site of MZH3 in crystal structure CS-A (upper right). An (F_{obs} , ϕ_{calc}) electron density map of CS-A contoured at 1.0 σ (upper left) shows the electron density of the ZnPCP in the pigment site. Blue dotted line shows second shell histidine-threonine hydrogen bond.



Images rendered using The PyMOL Molecular Graphics System, Version 1.7 Schrödinger, LLC.

In contrast to the heme in MZH3, the structure of the pigment site with its ZnPCP deviates slightly from the structure of cytochrome b. ZnPCP does not bind with its porphyrin ring in the same orientation relative to the helical bundle axis as the hemes of cytochrome b, possibly because the bulky phenyl groups would clash with the hydrophobic core of the maquette. Also, the metal-to-metal distance in MZH3 is about ~ 1 Å longer than in cytochrome b, probably because the four glycine residues in the core near the pigment binding cavity in MZH3 create a pocket that causes the ZnPCP to shift away from the electron acceptor. Whereas heme is ligated by two histidines, ZnPCP is ligated by only one histidine, giving it more conformational freedom to adapt to the shape of the binding cleft.

3.4.3 ZnPCP can bind to an unexpected site in MZH3

The (F_{obs} , ϕ_{calc}) electron density map of crystal structure CS-A has an unusually large peak of 3.0σ located at the opening of the metal-binding cavity. (For comparison, the peak for the zinc ion of ZnPCP in the pigment site is 9.5σ). The peak of 3.0σ is located between the carbonyl oxygen atoms of helical glycines G33 and G160, which line the opening to the metal binding cavity. The center of the peak is 2.9 \AA from the carbonyl oxygen of G160 and 3.6 \AA from the oxygen of G33. A chloride ion at this position would clash with the nearby partial negative charge of the glycine carbonyl oxygens. The peak was deemed unlikely to represent a free metal ion because carbonyl oxygens are not strong ligands, and the crystallization drop only had a stoichiometric concentration of ZnCl_2 . The 3.0σ peak is surrounded by a coplanar arc of diffuse electron density on one side, not unlike a metal ion surrounded by a partially-resolved tetrapyrrole ring. If this electron density does come from a tetrapyrrole, the occupancy of that tetrapyrrole would be very low, so the peaks in this region were assigned to water molecules instead.

Crystal structure CS-A (Figure 3.14) was solved with zinc ions in the metal site for MAD phasing with the zinc of the ZnPCP cofactor, but Zn(II) is redox-inactive and not useful as an electron donor in a reaction center maquette. The most promising metal ion for use in an oxygen evolution catalyst is manganese, because of its relevance to photosystem II, rich redox chemistry, known capacity for oxygen evolution, and abundance (25). For this reason, additional crystal structures of MZH3 with heme B and ZnPCP were grown with Mn(II) to produce structures CS-B and CS-C. Unlike the crystals from CS-A which grew spontaneously, growth of crystals for CS-B and CS-C structures required seeding with crystals that contained

heme B and Mn(II) but not ZnPCP. All pigment-containing structures came from crystallization condition CC-1. Efforts to grow crystals with ZnPCP in conditions CC-2 and CC-3 resulted in crystal structures that lacked the pigment; evidently, the ZnPCP cofactor dissociated from MZH3 before crystallization.

In crystal structure CS-C, the temperature factors and the shape of the electron density for the ZnPCP cofactor in the pigment site were improved compared to structure CS-A (Figure 3.15). In CS-C, the overall conformation of ZnPCP in the pigment site is in good agreement with the structures of CS-A and CS-B. The carboxylate group of ZnPCP is between helices 3 and 4 for all three structures, which supports the hypothesis that the ZnPCP orientation is influenced by a dipole moment created by charged *c*-position residues. The conformation of the ZnPCP-ligating histidine H124 appears to be more consistent with ligation of the zinc by the N_δ atom than the

N_ε atom. This is unusual because natural heme-binding proteins overwhelmingly favor heme ligation by histidine N_ε atoms over N_δ atoms.

Despite the flipping of the imidazole ring, there remains a 2.8 Å hydrogen bond between the H124 N_ε atom and the hydroxyl oxygen of T77.

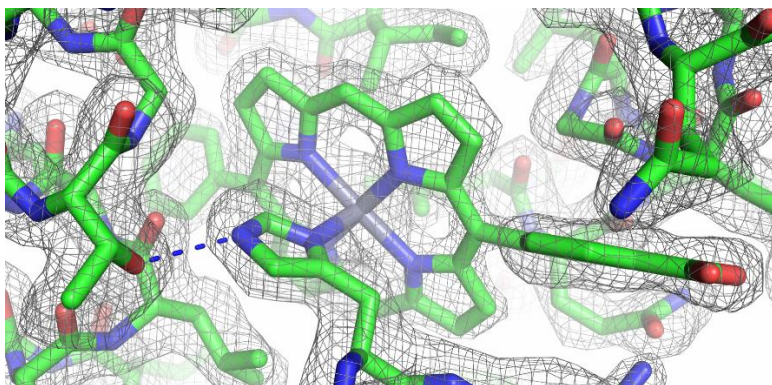


Figure 3.15: CS-C pigment site with ZnPCP

ZnPCP in MZH3 pigment binding site in crystal structure CS-C has lower B-factors than CS-A, suggesting increased occupancy of ZnPCP. An (F_{obs} , ϕ_{calc}) electron density map contoured at 1.0 σ corroborates ZnPCP conformation in CS-A, but His124 in CS-C appears to fit electron density better when ligating ZnPCP with N_δ. Image rendered using The PyMOL Molecular Graphics System, Version 1.7 Schrödinger, LLC.

Crystal structure CS-C has a clearly-resolved second ZnPCP molecule at the opening of the metal site cavity in the same position as the tetrapyrrole-like features observed in CS-A (Figure 3.16). In the (F_{obs} , ϕ_{calc}) map of CS-C, the electron density peak heights for the zinc ion in the pigment site and the metal cavity are 12.8σ and 6.7σ respectively, compared to 9.5σ and 3.0σ in CS-A. In CS-C, the G160 carbonyl oxygen appears to interact with the zinc ion which is 2.9 \AA away, and the distance between the zinc and G33 carbonyl oxygen is 3.7 \AA . The porphyrin ring of ZnPCP makes van der Waals contact with all four of the glycine residues that line the opening of the metal binding cavity, G33, G37, G160, and G164. The pyrrole group of the porphyrin ring furthest from the porphyrin-binding section of the protein packs against the side chains of residues L41 and L157. The *p*-carboxyphenyl group of ZnPCP projects out of the protein into the solvent and is not resolved at all. The other phenyl group projects into the core of MZH3 and displaces the tyrosine 168 side chain so that Y168 rotates outward into a partially solvent-exposed interfacial position, pushing Gln172 into a strained conformation. The phenyl group makes hydrophobic contacts with side chains of L30, L71, I131, and Y168.

The binding of ZnPCP to the metal site is reminiscent of work done on Due Ferro proteins that has shown quinone molecules binding to the metal cavity for redox reactions with iron ions (26). While interesting in its own rite, the ZnPCP binding at the metal cavity presents a problem for light-driven electron transfer studies, because it changes the rotameric state of tyrosine 168, which changes the distances between cofactors and therefore electron transfer rates, impedes binding of metal ions and potential substrates to the metal site, and may participate in light-activated redox chemistry that would interfere with charge separation. All three ZnPCP-containing structures, CS-A, CS-B, and CS-C, have some evidence of this metal cavity ZnPCP, but it is clearest in CS-C and nearly undetectable in CS-A.

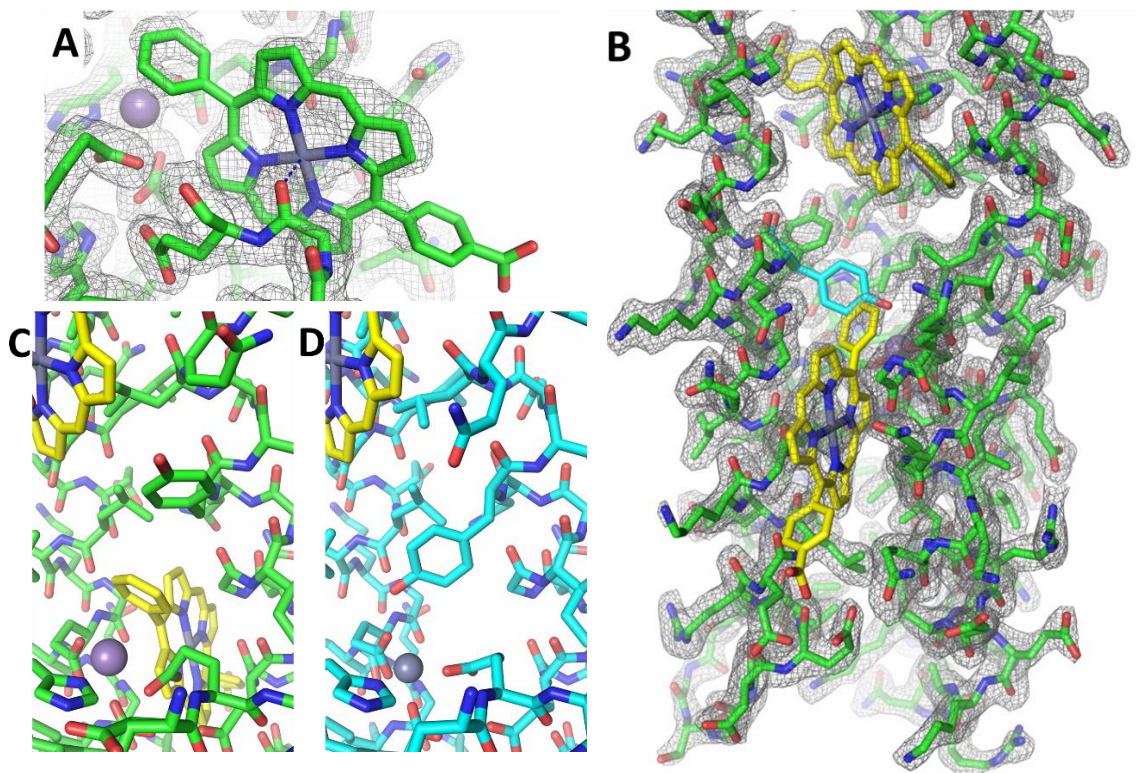


Figure 3.16: Extra ZnPCP at opening of metal binding site cavity

ZnPCP is well-resolved in an unintended site at the opening of the metal binding cavity in crystal structure CS-C, but not CS-A. (A) (F_{obs} , ϕ_{calc}) map of CS-C contoured at 1.0σ shows electron density of ZnPCP at opening of metal-binding cavity. Dotted blue line shows proximity of G160 carbonyl oxygen to zinc ion of ZnPCP. Solvent-exposed *p*-carboxyphenyl of ZnPCP is not resolved. Part of helix 4 is cut away for better view. (B) (F_{obs} , ϕ_{calc}) map of CS-C at 1.0σ contour level showing the two ZnPCP cofactors in yellow and the change in Tyr168 rotamer with ZnPCP binding to metal cavity. Tyr168 of structure CS-A, shown in cyan, would clash with ZnPCP phenyl group if it did not adopt interfacial conformation observed in CS-C. Part of helix 1 is removed. (C) CS-C interfacial Tyr168 side chain rotamer avoids steric clash with ZnPCP phenyl group. Gln172 (top right) in strained conformation avoids steric clash with Tyr168. (D) CS-A Tyr168 side chain is located in the core in the absence of ZnPCP at metal cavity, and Gln172 adopts relaxed conformation. Images rendered using The PyMOL Molecular Graphics System, Version 1.7 Schrödinger, LLC.

The crystal structures indicate that ZnPCP binds with higher affinity to the intended pigment site than the metal cavity. In all three structures, the electron density of the zinc ion of ZnPCP at the pigment site is significantly higher than the zinc ion of ZnPCP at the metal cavity.

All three crystal structures grew from crystallization condition CC-1 well solutions with pH between 4.5 and 4.9, and this may disfavor binding to the pigment site, which involves coordination by histidine 124. His124 is likely to be protonated in this pH range the absence of ZnPCP, because the solution pK_a of histidine is about 6.4, and His124 is surrounded by water in the apo-state (see Figure 3.13). Acidic conditions have been observed to weaken histidine-metalloporphyrin interactions in maquettes previously (27). In contrast, the ZnPCP at the metal cavity is not contingent upon ligation by any protonatable groups, suggesting that acidic conditions would favor ZnPCP binding to the metal cavity over the pigment site. Despite the low pH, however, the electron density maps clearly show more density for ZnPCP at the pigment site, and this disparity may be higher at neutral pH.

The unexpected binding of ZnPCP to the metal cavity likely cannot be reproduced in other zinc tetrapyrroles that bind to MZH3 with high affinity. Table 2.4 shows that SE375, NR117, TE312, and TE394 have different substituents on the porphyrin ring, and they would not be able to make the same interactions that ZnPCP makes at the metal cavity. NR117, for example, has two *p*-carboxyphenyl groups which would not easily be buried in the core to pack against L30, L71, and I131 as ZnPCP does. TE312 and TE394 have benzyl substituents fused to two of the pyrrole units, and these are likely to clash with glutamate residues in the metal binding site and core leucine residues L30 or L157 on either side of the opening to the metal binding cavity. In SE375, an alkyne group connects the porphyrin ring to a phenyl group, and this long, inflexible substituent would create severe steric clashes if the porphyrin ring were lodged at the opening of the metal cluster as it is in CS-C. Despite these potential clashes at the metal binding cavity, SE375, NR117, TE312, and TE394 all bind to MZH3 with high affinity, suggesting that the intended pigment binding site is the preferred site for zinc tetrapyrroles.

3.5 Metal-binding site

3.5.1 *Di-metal site structure consistent with design*

All MZH3 crystals grown in crystallization conditions CC-2 and CC-3 had metal binding sites that closely match the design. Histidines H67 and H138 ligate the metal ions with N_δ atoms and make second-shell hydrogen bonds with N_ε atoms to aspartates D134 and D63, respectively. Glutamates E34 and E161 make bidentate axial ligands with the metal ions, while E64 and E135 make bridging ligands to connect the two metal ions. In one exception, the Mn(II)₂ site of CS-E has a low-occupancy Mn(II) in the site closest to the tyrosine, and E34 appears to be out of place. This crystal was grown with a slightly sub-stoichiometric amount of MnCl₂, which may not have been enough to fill the metal sites, given the relatively weak affinity of Mn(II) compared to other metals (28). In the highest resolution structure that came from CC-2 or CC-3, CS-G, a bridging μ-aqua or μ-hydroxo ligand is resolved between the two cadmium ions. Crystal structures CS-F and CS-H, which both have Cd(II) and heme B, look very similar to the CS-G structure, which has only Cd(II). In all three structures containing CdCl₂, the Cd(II) ions are 3.6 Å apart. In the Mn(II) structure CS-E, the distance between the ions is 5.5 Å. This change is likely due to the lengthening of the ligands between the Mn(II) ions and the amino acid ligands compared to Cd(II). Figure 3.17 shows an electron density map of the metal site in CS-G and the overall structure.

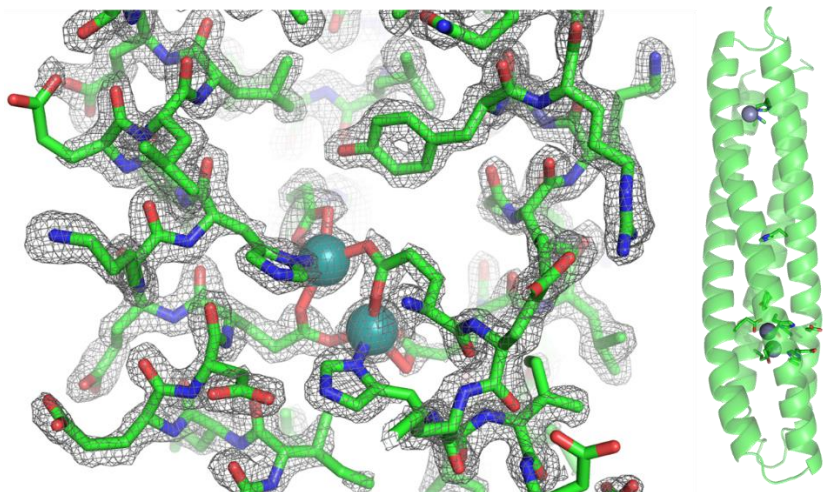


Figure 3.17: Cd(II) bound to MZH3

Crystal structure CS-G shows high-affinity metal binding. Left: (F_{obs}, ϕ_{calc}) map contoured at 1.0σ with part of helix 3 cut away. Cd(II) ions are shown as grey spheres. Right: overall fold of MZH3 in CS-G.

Images rendered using The PyMOL Molecular Graphics System, Version 1.7 Schrödinger, LLC.

The metal binding site of MZH3 in crystals from crystallization conditions CC-2 and CC-3 are very similar to the metal site of bacterioferritin. As an example, structure CS-G is shown in a side-by-side comparison with bacterioferritin in Figure 3.18.

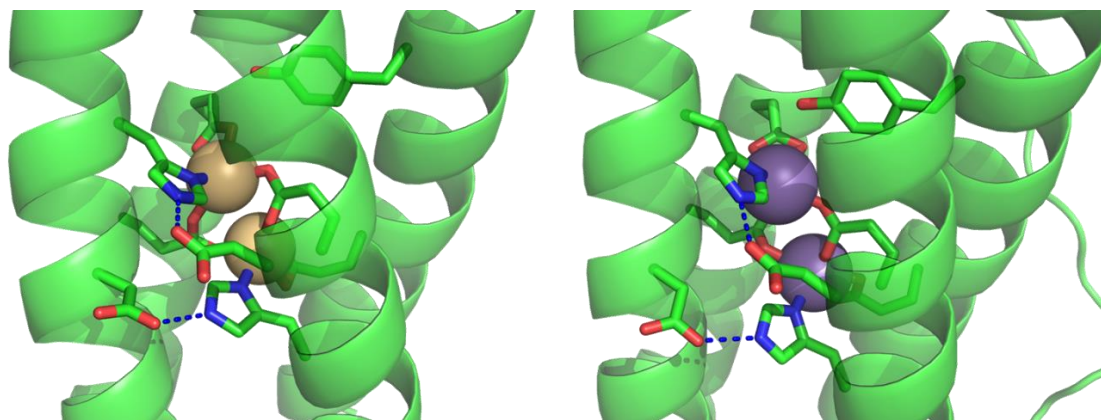


Figure 3.18: Comparison of MZH3 to bacterioferritin

Metal binding site of crystal structure CS-G with Cd(II) (left) closely matches the structure of the natural diiron protein bacterioferritin with Mn(II) (right). Side chain rotamers of first shell histidines and glutamates and second-shell asparates and tyrosine are nearly identical in the two structures. Bacterioferritin structure comes from PDB ID: 1BFR (17). Images rendered using The PyMOL Molecular Graphics System, Version 1.7 Schrödinger, LLC.

3.5.2 Di-metal site structure with metal in unintended position

In contrast to structures from crystallization conditions CC-2 and CC-3, all structures from condition CC-1, including CS-A, CS-B, CS-C, and CS-D, had a misplaced metal ion on the outside of the metal binding site and corresponding lowered or absent occupancy of a metal in the intended site on the interior of the protein (Figure 3.19). The unexpected external metal ion was coordinated in a tetrahedral

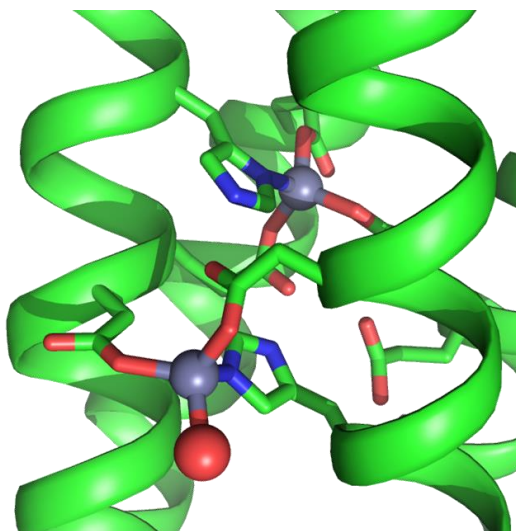


Figure 3.19: Unintended metal binding site

Crystal structure CS-D exemplifies the external metal binding site from crystallization condition CC-1 structures. While the Zn(II) ion nearest the porphyrin-binding section of the protein is ligated correctly, the far site is empty and an external Zn(II) coordinates the active site His138 and second shell residues D63 and D134. Image rendered using The PyMOL Molecular Graphics System, Version 1.7 Schrödinger, LLC.

geometry by active site residue H138, a water molecule, and the two aspartates, D63 and D134, which were intended to be second shell contacts to the histidines. H138 is designed to ligate a metal ion in the interior of the protein using the N_{δ} atom, and in structures from condition CC-1, H138 retains the conformation it was intended to have, but ligates the external metal ion using its N_{ϵ} atom. The (F_{obs}, ϕ_{calc}) electron density maps from condition CC-1 structures show that the external metal has very strong scattering intensity that is higher than that of the internal metal at the site nearest the porphyrin binding section of MZH3.

Structures CS-A and CS-D contained Zn(II), a metal that commonly adopts a tetrahedral geometry, but Mn(II) is rarely stable in this geometry (29). Crystals of MZH3 with Mn(II), heme

B, and ZnPCP were grown in condition CC-1 with the expectation that Mn(II) would not be able to bind to the external site because it would have to be tetrahedral. Instead, structures CS-B and CS-C showed that Mn(II) did, in fact, bind with a tetrahedral geometry to the unusual

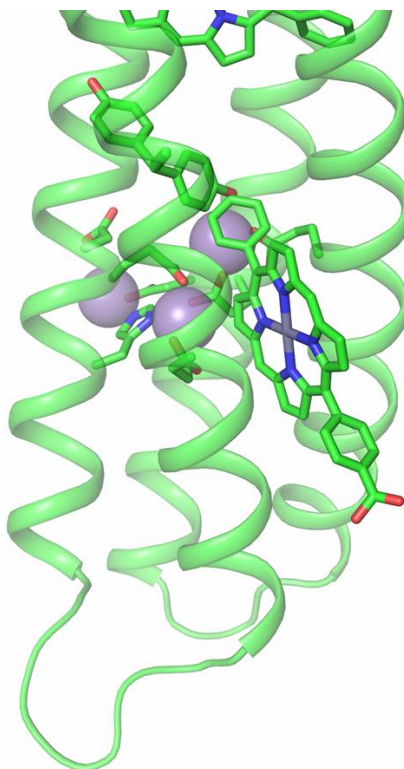


Figure 3.20: Metal binding with extra Mn(II) and ZnPCP

Crystal structure of CS-B with three Mn(II) ions. His138 is shown ligating internal Mn(II) with N_δ and external Mn(II) with N_ε. Tyr168 adopts two rotamers, presumably because of partial occupancy of ZnPCP at metal binding cavity. Tyr168 in core would clash with ZnPCP, so it moves to the interfacial rotamer when ZnPCP is present. Image rendered using The PyMOL Molecular Graphics System, Version 1.7 Schrödinger, LLC.

external metal site (Figure 3.20). In structure CS-C, which had 2 mM MnCl₂ in the protein stock solution (about 3 equivalents of MnCl₂ per protein), only two metal ions were observed with one in the internal site close to the porphyrin section of the protein and one in the external site, similar to the Zn(II) structures CS-A and CS-D. In crystal structure CS-B, however, ~35 mM MnCl₂ was added in an attempt to fill the intended metal binding site. The result was electron density consistent with a Mn(II) ion on both sides of His138, suggesting that either His 138 was ligating two Mn(II) ions at once or that there was a mixture of states of Mn(II) binding. The (F_{obs}, φ_{calc}) map showed the internal and external Mn(II) ions ligated by His138 had peaks of 3.7 σ and 4.8 σ, respectively.

The metal binding site of structures from condition CC-1 may not be an accurate representation of the metal binding site of MZH3 in solution. The CC-1 metal site structure is

not consistent with structures from the other two crystallization conditions, which suggests that the external metal ion may be an artifact of crystal packing. This external metal ion is not observed in any structure reported for Due Ferro proteins, and UV/vis titration of $\text{Co}(\text{NO}_3)_2$ into an MZH3 solution produced a spectrum and extinction coefficients for MZH3-Co(II) that are consistent with pentacoordinate ligation and not tetrahedral ligation, similar to Due Ferro proteins (Figure 2.18) (28, 30, 31). As a result, structures from crystallization conditions CC-2 and CC-3 are presumed to be more reliable representations of the mode of metal binding by MZH3 in solution at neutral pH.

3.6 Leu71His mutation and His-Tyr hydrogen bond

The redox active tyrosine Z of Photosystem II has a hydrogen bonding interaction with a histidine side chain (32). The histidine is necessary for rapid proton transfer to and from tyrosine Z to enable efficient oxidation and reduction of the tyrosine side chain. In order to reproduce this effect in MZH3, Leu71 was mutated to histidine to make MZH3-L71H. The MZH3-L71H mutant was crystallized in the cadmium-containing condition CC-2 with heme B in the electron acceptor site. Figure 3.21 (bottom) shows that a hydrogen bond forms in MZH3-L71H with a length of 2.6 Å between the His71 N_ϵ atom and the Tyr168 oxygen. This relatively short distance is consistent with a stable hydrogen bond. The L71H mutation does not seem to affect binding of the Cd(II) ions.

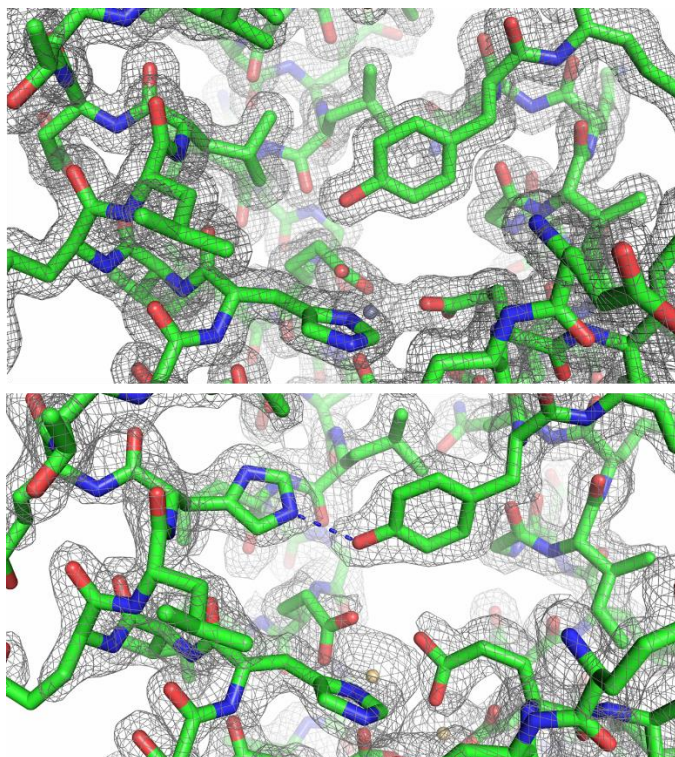


Figure 3.21: Histidine-tyrosine hydrogen bond in MZH3-L71H mutant

Electron density (F_{obs} , ϕ_{calc}) maps of crystal structures CS-D (top) and CS-H (bottom) contoured at 1.0σ . Blue dotted line in L71H mutant, structure CS-H, shows that a hydrogen bond forms between H71 and Y168, as designed. Image rendered using The PyMOL Molecular Graphics System, Version 1.7 Schrödinger, LLC.

The length of the hydrogen bond in MZH3-L71H shown in Figure 3.21 appears to be typical of a strong hydrogen bond, but not unusually strong. In contrast, the hydrogen bond in photosystem II between tyrosine Z and a histidine has special characteristics. It has a 2.5 Å donor-acceptor distance, and analysis of the 1.9 Å crystal structure suggests that the proton is shared equally between the tyrosine and the histidine, facilitating rapid proton coupled electron transfer reactions of the tyrosine (32, 33). The MZH3-L71H hydrogen bond, with a length of 2.6 Å, probably does not have these special features, but can still act as a probe to explore the role of hydrogen bonding in tyrosine electron transfer kinetics.

As noted above in Figure 3.8, the heme B of L71H is rotated by 90° relative to the wild type MZH3 structures so that the propionate groups project out of the core in a different direction. It is not obvious why L71H would cause such a conformational change on the other end of the protein. The change could be due to differences in crystal contacts; one of the heme

propionate groups in the L71H structure appears to be involved in a 3.3 Å inter-protein hydrogen bond with Gln7 from a neighboring protein. However, all six heme-containing wild type MZH3 structures from all three crystallization conditions in different states of cofactor assembly have the same heme conformation. In addition, dogged attempts to crystallize MZH3-L71H in crystallization condition CC-1 produced only long needle-like crystals that were not useful for diffraction. Wild type MZH3 crystal structures from CC-1 have a heme propionate inter-protein hydrogen bond with Lys32 with a length of 2.8 Å (as measured in CS-D), and crystals did not grow in CC-1 without heme B. While wild type MZH3 crystallized readily in CC-1, the needle-like crystals of L71H were difficult to grow. It is likely, therefore, that a subtle shift in core packing created by the L71H mutation is translated up the helices to the electron acceptor site, causing a different heme B conformation. The fact that such a subtle shift could tip the balance to favor a different heme conformation is not surprising given the symmetry of the heme binding site and the fact that no design element was consciously included to favor one orientation over the other. What is surprising is that all of the wild type structures have a consistent heme orientation with the propionate groups in the same position.

3.7 Summary

X-ray crystal structures of MZH3 from 1.45 to 2.10 Å resolution show that the overall structure of MZH3 closely matches the design; the maquette folds as a left-turning antiparallel four-helix coiled coil, with heptad *a*- and *d*-positions forming layers in the hydrophobic core. The protein retains its fold in the absence of a pigment or electron acceptor, despite the penetration of solvent into the hydrophobic core. The apo-state stability may be the result of stabilizing interactions between interfacial *g*-position leucines. Stable inter-helical salt bridging

interactions were not observed in these crystal structures, but charge pairing interactions might still play an important role in determining helix topology.

Heme B and metal ions bind to the correct sites with structures very similar to natural proteins cytochrome b and bacterioferritin, respectively, despite the absence of sequence identity between these proteins. Heme and metal ions are coordinated exactly as intended by design, complete with second-shell hydrogen bonding interactions. In crystallization condition CC-1, ZnPCP is shown to bind to the pigment site, and is ligated by the intended histidine 124. The rotameric state of His124 when it ligates ZnPCP is not resolved conclusively, but it appears to make the intended second-shell hydrogen bond to Thr77. Unexpected details emerged from crystals grown in CC-1, including the improper binding of a tetrahedral metal ion to the exterior of MZH3 and the unintended binding of ZnPCP to the opening of the metal binding cavity. The exterior metal was not present in other crystallization conditions, and only a single ZnPCP is observed to bind to MZH3 by UV/vis spectroscopy. These results suggest that crystal packing may have distorted the metal site of MZH3 in condition CC-1 and given rise to these unexpected results.

There is room for improvement of the sequence of MZH3. Some glutamine residues in the vicinity of tetrapyrrole binding sites appear to be pushed into strained rotameric states by the binding of the cofactor. In addition, two tryptophan residues are buried in the apo-state and must be solvated to allow heme binding. Mutation of some of these amino acids to smaller residues may increase the binding affinity of the tetrapyrroles. It may also be wise to change the metal binding site so that metals and ZnPCP cannot bind to unintended sites in the manner of crystals grown in condition CC-1, even though these anomalies appear to be artifacts of crystal packing. Redesign should be approached with caution, however, as increasing the

stability of the holo-state might also increase the stability of the apo-state, which could have the effect of slowing the binding rate or weakening cofactor affinity. Even without enhancements, however, these crystal structures show that MZH3 has an architecture consistent with the design, with cofactors positioned appropriately for long-lived light-activated charge separation. The next chapter will use transient absorption spectroscopy to investigate whether MZH3 can in fact function as a reaction center maquette.

3.8 References

1. Lombardi, A., Nastri, F., Marasco, D., Maglio, O., De Sanctis, G., Sinibaldi, F., Santucci, R., Coletta, M., and Pavone, V. (2003) Design of a new mimochrome with unique topology, *Chemistry* 9, 5643-5654.
2. Di Costanzo, L., Geremia, S., Randaccio, L., Nastri, F., Maglio, O., Lombardi, A., and Pavone, V. (2004) Miniaturized heme proteins: crystal structure of Co(III)-mimochrome IV, *J Biol Inorg Chem* 9, 1017-1027.
3. Thielges, M., Uyeda, G., Camara-Artigas, A., Kalman, L., Williams, J. C., and Allen, J. P. (2005) Design of a redox-linked active metal site: manganese bound to bacterial reaction centers at a site resembling that of photosystem II, *Biochemistry* 44, 7389-7394.
4. Huang, S. S., Gibney, B. R., Stayrook, S. E., Dutton, P. L., and Lewis, M. (2003) X-ray structure of a Maquette scaffold, *Journal of Molecular Biology* 326, 1219-1225.
5. Arai, R., Kobayashi, N., Kimura, A., Sato, T., Matsuo, K., Wang, A. F., Platt, J. M., Bradley, L. H., and Hecht, M. H. (2012) Domain-swapped dimeric structure of a stable and functional de novo four-helix bundle protein, WA20, *J Phys Chem B* 116, 6789-6797.
6. Patel, S. C., and Hecht, M. H. (2012) Directed evolution of the peroxidase activity of a de novo-designed protein, *Protein Eng Des Sel* 25, 445-452.
7. Wei, Y., Kim, S., Fela, D., Baum, J., and Hecht, M. H. (2003) Solution structure of a de novo protein from a designed combinatorial library, *Proc Natl Acad Sci U S A* 100, 13270-13273.
8. Walshaw, J., and Woolfson, D. N. (2001) Socket: a program for identifying and analysing coiled-coil motifs within protein structures, *J Mol Biol* 307, 1427-1450.
9. Strelkov, S. V., and Burkhard, P. (2002) Analysis of alpha-helical coiled coils with the program TWISTER reveals a structural mechanism for stutter compensation, *J Struct Biol* 137, 54-64.
10. Grigoryan, G., and Degrado, W. F. (2011) Probing designability via a generalized model of helical bundle geometry, *J Mol Biol* 405, 1079-1100.
11. Crick, F. H. C. (1953) The Fourier transform of a coiled-coil, *Acta Crystallogr* 6, 685-689.
12. Crick, F. H. C. (1953) The Packing of Alpha-Helices - Simple Coiled-Coils, *Acta Crystallogr* 6, 689-697.

13. Lupas, A. N., and Gruber, M. (2005) The structure of alpha-helical coiled coils, *Adv Protein Chem* 70, 37-78.
14. Hunte, C., Koepke, J., Lange, C., Rossmann, T., and Michel, H. (2000) Structure at 2.3 Å resolution of the cytochrome bc(1) complex from the yeast *Saccharomyces cerevisiae* co-crystallized with an antibody Fv fragment, *Structure* 8, 669-684.
15. Frolow, F., Kalb, A. J., and Yariv, J. (1994) Structure of a unique twofold symmetric haem-binding site, *Nat Struct Biol* 1, 453-460.
16. Huang, L. S., Cobessi, D., Tung, E. Y., and Berry, E. A. (2005) Binding of the respiratory chain inhibitor antimycin to the mitochondrial bc(1) complex: A new crystal structure reveals an altered intramolecular hydrogen-bonding pattern, *Journal of Molecular Biology* 351, 573-597.
17. Dautant, A., Meyer, J. B., Yariv, J., Precigoux, G., Sweet, R. M., Kalb, A. J., and Frolow, F. (1998) Structure of a monoclinic crystal form of cytochrome b1 (Bacterioferritin) from *E. coli*, *Acta Crystallogr D Biol Crystallogr* 54, 16-24.
18. Lahr, S. J., Engel, D. E., Stayrook, S. E., Maglio, O., North, B., Geremia, S., Lombardi, A., and DeGrado, W. F. (2005) Analysis and design of turns in alpha-helical hairpins, *J Mol Biol* 346, 1441-1454.
19. Mortuza, G. B., and Whitford, D. (1997) Mutagenesis of residues 27 and 78 modulates heme orientation in cytochrome b5, *FEBS Lett* 412, 610-614.
20. Vallone, B., Nienhaus, K., Brunori, M., and Nienhaus, G. U. (2004) The structure of murine neuroglobin: Novel pathways for ligand migration and binding, *Proteins* 56, 85-92.
21. Schneider, S., Marles-Wright, J., Sharp, K. H., and Paoli, M. (2007) Diversity and conservation of interactions for binding heme in b-type heme proteins, *Nat Prod Rep* 24, 621-630.
22. Georgescu, R. E., Alexov, E. G., and Gunner, M. R. (2002) Combining conformational flexibility and continuum electrostatics for calculating pK(a)s in proteins, *Biophys J* 83, 1731-1748.
23. Alexov, E. G., and Gunner, M. R. (1997) Incorporating protein conformational flexibility into the calculation of pH-dependent protein properties, *Biophys J* 72, 2075-2093.
24. Irving, H., and Williams, R. J. P. (1953) The Stability of Transition-Metal Complexes, *J Chem Soc*, 3192-3210.
25. Armstrong, F. A. (2008) Why did Nature choose manganese to make oxygen?, *Philos Trans R Soc Lond B Biol Sci* 363, 1263-1270; discussion 1270.
26. Ulas, G., Lemmin, T., Wu, Y., Gassner, G. T., and DeGrado, W. F. (2016) Designed metalloprotein stabilizes a semiquinone radical, *Nat Chem* 8, 354-359.
27. Shifman, J. M., Moser, C. C., Kalsbeck, W. A., Bocian, D. F., and Dutton, P. L. (1998) Functionalized de novo designed proteins: mechanism of proton coupling to oxidation/reduction in heme protein maquettes, *Biochemistry* 37, 16815-16827.
28. Torres Martin de Rosales, R., Faiella, M., Farquhar, E., Que, L., Jr., Andreozzi, C., Pavone, V., Maglio, O., Natri, F., and Lombardi, A. (2010) Spectroscopic and metal-binding properties of DF3: an artificial protein able to accommodate different metal ions, *J Biol Inorg Chem* 15, 717-728.
29. Harding, M. M. (2001) Geometry of metal-ligand interactions in proteins, *Acta Crystallogr D Biol Crystallogr* 57, 401-411.

30. Bertini, I., and Luchinat, C. (1984) High spin cobalt(II) as a probe for the investigation of metalloproteins, *Adv Inorg Biochem* 6, 71-111.
31. Calhoun, J. R., Kono, H., Lahr, S., Wang, W., DeGrado, W. F., and Saven, J. G. (2003) Computational design and characterization of a monomeric helical dinuclear metalloprotein, *J Mol Biol* 334, 1101-1115.
32. Saito, K., Shen, J. R., Ishida, T., and Ishikita, H. (2011) Short hydrogen bond between redox-active tyrosine Y(Z) and D1-His190 in the photosystem II crystal structure, *Biochemistry* 50, 9836-9844.
33. Umena, Y., Kawakami, K., Shen, J. R., and Kamiya, N. (2011) Crystal structure of oxygen-evolving photosystem II at a resolution of 1.9 Å, *Nature* 473, 55-60.

Chapter 4: Light-driven electron transfer in a reaction center maquette

The long-term goal of this project is to convert solar energy to fuel, and this means the energy of a light-activated charge separated state must be converted into chemical energy by oxidizing one substrate (such as water to make oxygen) and reducing another (such as protons to make hydrogen fuel). Such chemical reactions are usually much slower than the charge separating electron transfer reactions, because they need time for the comparatively slow making and breaking of chemical bonds. Previous work has demonstrated the use of *de novo*-designed protein maquettes to create light-activatable electron transfer dyads, in which a pigment molecule photo-reduces an electron acceptor (1-3). Dyads can be useful in investigating the parameters that affect electron transfer, but they are not equipped to trap a long-lived charge separated state, because the electron on the reduced electron acceptor quickly recombines with the hole on the oxidized pigment. In order to stabilize the charge separated state, a third cofactor, an electron donor, must be introduced to increase the distance between the electron and the hole in order to allow a charge separated state to persist for long enough for chemical reactions to make fuel. The electron donor should be placed close to the pigment so that oxidation of the donor can outcompete the electron-hole recombination that would quench the electrical potential energy of the charge separated state. In photosystem II, a long string of electron donors and acceptors gives the reaction center a quantum yield for producing product O₂ and reduced plastoquinone of up to 95% in favorable light conditions (4, 5). Here, MZH3 makes use of a redox-active triad to trap a long-lived charge separated state.

4.1 Electron transfer background

4.1.1 A kinetic model of electron transfer in MZH3

MZH3 was designed for tetrad activity involving an iron or cobalt porphyrin, a zinc tetrapyrrole, a tyrosine side chain, and two metal ions. Here, the discussion will focus on development of a triad, and a charge separating tetrad will be a future aim. A comparison of the electron transfer pathways of a light-activatable dyad and triad in MZH3 is shown in Figure 4.1. A dyad can be prepared by making an MZH3 mutant that lacks a tyrosine or by inhibiting tyrosine oxidation in the wild type MZH3. A model such as this can be used to predict how a system will progress after the pigment absorbs light to enter the excited state.

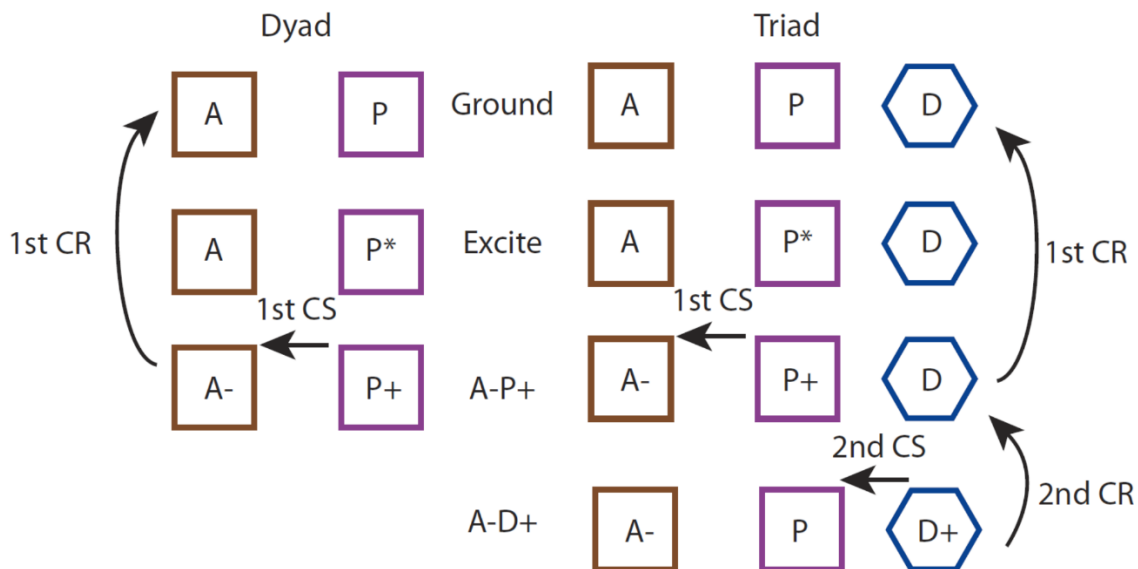


Figure 4.1: Model of electron transfer pathway in dyad and triad versions of MZH3

Cofactor A is the electron acceptor, P is the pigment, and D is an electron donor, such as a tyrosine side chain. CS is a charge separation, and CR is a charge recombination.

Figure 4.1 makes use of a few assumptions. For example, the singlet excited state of the zinc porphyrin is not relevant, because it goes through intersystem crossing to the triplet state

before electron transfer. In addition, the triplet excited state does not relax to the ground state, the A·P⁺ state does not return to the excited triplet state of the zinc porphyrin, and the A·D⁺ state in the triad case does not return directly to the ground state. These assumptions are valid because competing reactions are significantly faster than these reactions, so they do not play a significant role in the electron transfer pathway of the system.

Using Figure 4.1, a set of equations can be written to describe how the concentration of each state of the system changes with time after light absorption. For example, in the triad case, the rate of change of the concentration of the excited state, d[E]/dt, depends only on the concentration of the excited state, [E], and the rate constant for its conversion to the A·P⁺ state, k_{CS1}, as shown below:

$$\frac{d[E]}{dt} = -k_{CS1}[E]$$

Table 4.1 gives the rate of change of each state of the triad system. From this information, a system of equations can be compiled to describe how the triad system evolves after absorption of a photon.

	[E]	[A·P ⁺]	[A·D ⁺]	[G]
$\frac{d[E]}{dt}$	-k _{CS1}	0	0	0
$\frac{d[A·P^+]}{dt}$	+k _{CS1}	-k _{CR1} - k _{CS2}	+k _{CS2}	0
$\frac{d[A·D^+]}{dt}$	0	+k _{CS2}	-k _{CR2}	0
$\frac{d[G]}{dt}$	0	+k _{CR1}	0	0

Table 4.1: Rates of change of each state of the MZH3 triad system

The rate of change of the concentration of each state given on the left of each row is equal to each rate constant in that row times its corresponding concentration at the top of the column. The names of each state and rate constant are taken from Figure 4.1. E is the excited state and G is the ground state. CS is charge separation and CR is charge recombination. The rate constants k_{CS1}, k_{CS2}, k_{CR1} and k_{CR2} represent the transitions labeled 1st CS, 2nd CS, 1st CR, and 2nd CR, respectively, in Figure 4.1.

When the triad system is photo-activated at time $t = 0$, the entire system is in the excited state, E, so the occupancy of [E] is 1.0. With this starting condition and the equations from Table 4.1, the relative occupancies of each state can be determined at any time t after light absorption in terms of the electron transfer rate constants given in Table 4.1. If we can make accurate estimates of these rate constants, then we can accurately predict how the system will change with time after light absorption.

4.1.2 Parameters that govern electron transfer rates

MZH3 was designed to arrange its cofactors in a way that could manipulate light-activated electron transfer rates to maximize the yield and lifetime of charge separation. Prediction of electron transfer rates was guided by an empirical approximation of Marcus theory sometimes referred to as the Moser-Dutton ruler, shown below in Equation 4.1 (6-8). In this equation, k_{ET} is the rate constant for electron transfer from one redox center to another in s^{-1} , R is the distance between them measured in Å, ΔG is the driving force of the reaction in eV, and λ is the reorganization energy in eV.

$$\log(k_{ET}) = 15 - 0.6R - 3.1 \cdot \frac{(\Delta G + \lambda)^2}{\lambda} \quad \text{Equation 4.1}$$

The most important variable that influences electron transfer rates is the distance between the redox centers, R ; for every 1.6 Å change in distance, the rate of electron transfer changes by an order of magnitude. Crystal structures of MZH3 with heme B, ZnPCP, and Mn(II) give the distances between cofactors. The R values relevant to electron transfer rates in Equation 4.1 are measured by the distance of closest approach between the two redox centers (6, 7). The edge-to-edge distance between the porphyrin rings of pigment ZnPCP and acceptor

heme B, R_{PA} , is 13.0 to 13.1 Å in the crystal structures that contained both cofactors. Vinyl and methyl groups of the heme B cofactors are assumed not to be part of the redox-active center and are therefore ignored in this distance measurement. The edge-to-edge distance between tyrosine 168 and the pigment ZnPCP, R_{YP} , is 5.0 to 5.1 Å in crystal structures CS-A and CS-B when tyrosine is in the intended conformation. The R_{YP} distance is reduced to 3.4 to 3.5 Å in crystal structures CS-B and CS-C when the tyrosine has moved to an interfacial conformation to accommodate the binding of ZnPCP to the metal binding cavity, but this conformation may not be relevant to these electron transfer studies. The distance between tyrosine 168 and the nearest metal, R_{MY} , appears to vary by metal ion. Structures containing Cd(II) have a 4.7 Å R_{CdY} distance, Zn(II) structures have a 3.7 to 4.0 Å R_{ZnY} distance, and Mn(II) structures have a 3.2 to 3.5 Å R_{MnY} distance. If the tyrosine is not an active participant in photo-oxidation of bound metal ions, then the distance between the metal and the pigment, R_{MP} , becomes important. This distance ranges from 9.6 to 10.1 Å in crystal structures that contain ZnPCP and Mn(II) or Zn(II).

The second most important variable in calculating electron transfer rates is the driving force for electron transfer, ΔG , which is calculated from the difference in midpoint potentials of the redox centers involved in electron transfer. Redox titration provided a midpoint potential for heme B in MZH3 in the absence of ZnPCP of -180 mV vs. SHE (Figure 2.22). Zinc porphyrins in the excited state tend to be powerful reducing agents. The excited singlet state of the ZnPCP used for these experiments has a lifetime on the order of nanoseconds, which is too short for electron transfer to heme in MZH3. However, ZnPCP bound to MZH3 undergoes relatively efficient intersystem crossing to a triplet excited state that persists for milliseconds before phosphorescing (9). For this reason, it is assumed that the heme B in MZH3 transient absorption experiments is reduced only by the triplet excited state of the zinc porphyrin, and the singlet

state is not relevant to these electron transfer studies. Spectroelectrochemical titration and phosphorescence measurements of ZnPCP in MZH3 by Zhenyu Zhao gave potentials of 0.91 V for the $[\text{ZnPCP}^{++}/\text{ZnPCP}^0]$ redox couple and -0.69 V for $[\text{ZnPCP}^{++}/^3\text{ZnPCP}^*]$ (9).

The midpoint potential of tyrosine in MZH3 has not been measured. Tyrosine potentials depend upon the protonation states and the mechanism of the electron transfer or proton-coupled electron transfer (PCET) of the redox reaction. Tyrosine has a pK_a of about 10.2 in solution, and at high pH, it can exist partly in the neutral protonated form and partly as the deprotonated tyrosinate species (10). Oxidation of tyrosine in MZH3 should be treated as the oxidation of a mixture of these two components, as opposed to the oxidation of a single tyrosine species with a pH-dependent driving force for electron transfer (11). Oxidation of protonated tyrosine leads to an unstable radical cation that has a pK_a of -2 (12). If tyrosine oxidation proceeds by electron transfer followed by proton transfer (an ET-PT mechanism), then protonated tyrosine will have a high midpoint potential of ~ 1.34 V, because the radical cation product of the reaction is so unstable (13). In contrast, oxidation of the negatively charged tyrosinate anion forms the neutral tyrosyl radical that is much more stable than the radical cation, giving the $\text{Tyr-O}^-/\text{Tyr-O}^\bullet$ redox couple a lower midpoint potential of about 0.72 V, based on work by the laboratory of Cecilia Tommos (14). However, other mechanisms such as concerted proton-electron transfer (CPET) are observed in photosystem II redox active tyrosines and various phenols from model systems (15-19). The potentials of these CPET reactions depend on the nature of the proton acceptor, among other environmental details.

Unfortunately, reorganization energy, λ , is very difficult to measure. The reorganization energy for electron tunneling within the hydrophobic core of proteins is typically around 0.7 eV, but inter-protein electron transfer, which usually involves tunneling through solvent, has a

reorganization energy closer to about 1.3 eV (6). An intermediate reorganization energy of 1.2 eV may be most appropriate for electron transfer rate calculations in MZH3, because some cofactors are solvent-exposed while others are buried. A summary of the measured and predicted electron transfer parameters is given in Table 4.2. Figure 4.2 illustrates these

R_{PA}	13.1 Å
R_{YP}	5.0 Å
R_{MY}	3.7 Å
R_{MP}	9.6 Å
$E_{m, [Fe(II)\text{-Heme B}/Fe(III)\text{-Heme B}]}$	-0.18 V
$E_{m, [{}^3ZnPCP^*/ZnPCP^{**}]}$	-0.69 V
$E_{m, [ZnPCP^0/ZnPCP^{**}]}$	0.91 V
$E_{m, [Tyr\text{-OH}/Tyr\text{-OH}^{**}]}$	~1.34 V
$E_{m, [Tyr\text{-O}^-/Tyr\text{-O}^{\cdot}]}$	~0.72 V
λ	~1.2 eV

Table 4.2: Summary of parameters that determine electron transfer rates in MZH3

Parameters listed with a tilde (~) are estimates, and the other values have been measured experimentally. Midpoint potentials are vs. SHE.

parameters and applies them to the kinetic model described in section 4.1.1.

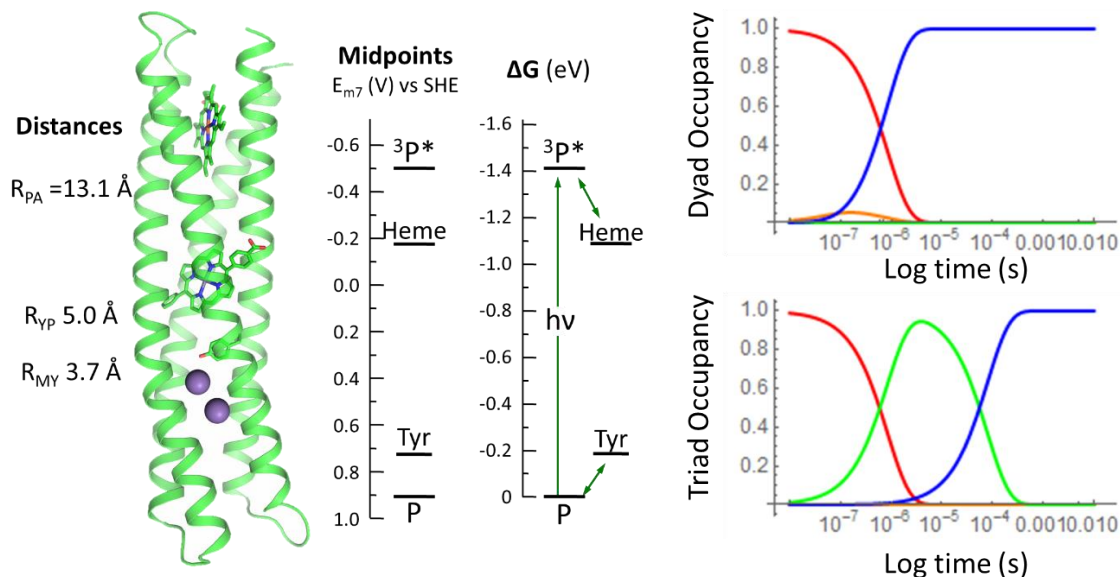


Figure 4.2: Electron transfer predictions in MZH3

Left: MZH3 crystal structure CS-B shows inter-cofactor distances, and energy diagrams show midpoint potentials and corresponding driving forces for electron transfer. Right: Once a photon is absorbed, the progression of the dyad and triad systems can be predicted using the Moser-Dutton ruler (Equation 4.1) and the parameters listed on the left and in Table 4.2. Red traces: Occupancy of the excited state. Orange trace: Occupancy of $A\cdot P^+$. Green trace: Occupancy of $A\cdot D^+$. Blue traces: Occupancy of the ground state. The triad case assumes a deprotonated tyrosinate in the starting condition.

4.2 Transient absorption

Tetrapyrroles like heme B and ZnPCP are strong absorbers of visible light, and their UV/vis absorbance spectra are highly sensitive to changes in their electronic state. This makes them amenable to characterization by transient absorption spectroscopy, in which a sample is photo-excited by a short pulse of bright light, and a measurement of the absorbance is made after a series of set time delays to track changes in electronic states. Here, transient absorption is used to examine light-driven electron transfer rates and yields of charge separated states in MZH3.

4.2.1 Transient absorption experimental approach

Here, a transient absorption setup was used that included a 2 ns excitation pulse of 532 nm light from an Nd:YAG laser directed toward one end of a 1 mL, 1 cm path length quartz cuvette containing a sample of interest; the other end of the sample was not exposed to the laser light. After a time delay, the excitation pulse was followed by emission of white light from a Xe flash lamp as a probe beam to determine absorbance spectra of the sample that was kept in the dark and the sample that was exposed to the excitation pulse. A monochromator separated the light by wavelength, and a PiMax CCD detector recorded the spectra. The dark reference spectrum was subtracted from the photoexcited sample spectrum for data analysis. After each measurement, a magnetic stir bar stirred the sample. Sets of 50 spectra per time point were recorded from about 350 nm to 650 nm at time points from 1 μ s to up to 10 s after the laser pulse. The gate width of the Xe flash lamp for the experiments described here ranged from 600 ns to 1 μ s to maximize the signal-to-noise ratio, but the limit of the time resolution for

this setup is about 30 ns. Transient absorption samples were held at 20°C using a Peltier temperature controller. Figure 4.3 illustrates the transient absorption setup.

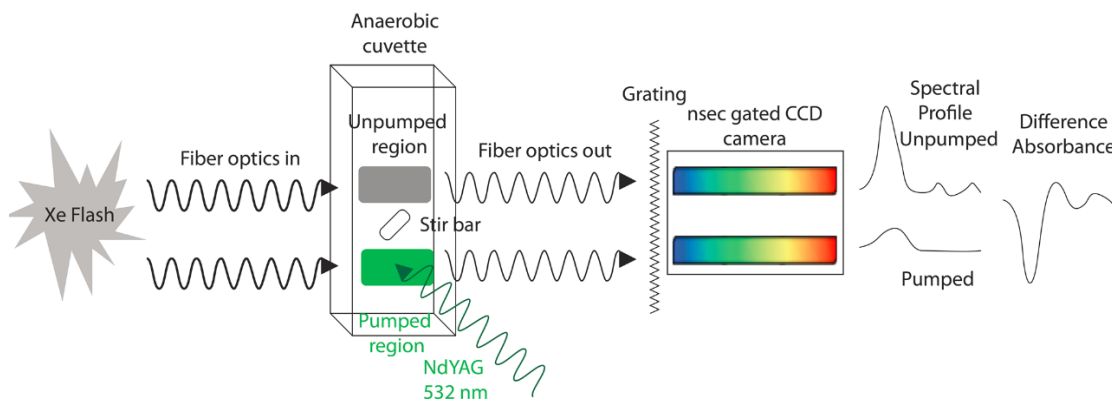


Figure 4.3: Schematic of setup for transient absorption experiments

An excitation flash of 532 nm laser light is absorbed by pigment cofactor in one part of the cuvette, while the other part remains dark. After a variable time delay t , the Xe flash lamp emits a probe beam to measure the absorbance spectra of the photo-excited and dark sample at time t . A monochromator separates light by wavelength and a PiMax CCD detector collects the absorbance spectra. The light minus dark difference spectrum shows the redox states of light-absorbing cofactors.

To avoid redox reactions with oxygen, all transient absorption experiments reported here were done with samples that were sealed in a quartz cuvette and thoroughly purged with argon purified through an oxygen-scrubbing gas train as described previously (20). Argon purging was continued during the experiment. Exposure to ambient oxygen resulted in gradual attenuation of transient absorption signals and an increased rate of photo-degradation of the sample, consistent with production of reactive oxygen species from the zinc porphyrin excited triplet state. Under anaerobic conditions, absorbance spectra at time $t = 1 \mu\text{s}$ after the laser flash were measured at the beginning and end of each experiment, and the magnitude of the ZnPCP Soret bleach in the final measurement at $1 \mu\text{s}$ was usually within 5-10% of the first.

Transient absorption experiments with MZH3 sought to track two signals with time: one from the conversion of the ground state of ZnPCP to the excited triplet state $^3\text{ZnPCP}^*$ and one from ferric Fe(III)-heme B reduction to ferrous Fe(II)-heme. The difference absorption spectra corresponding to these transitions are shown in Figure 4.4. The ZnPCP^{++} radical cation species was not observed, presumably because it had a short lifetime and its spectrum is similar to $^3\text{ZnPCP}^*$ in the measured wavelength range. Oxidized tyrosyl radicals have a weak absorbance, measured at $2,750 \text{ M}^{-1}\text{cm}^{-1}$ at 408 nm in a three-helix bundle maquette (14), but this signal was not resolved in experiments described here, probably because the tyrosyl radical absorbance is too low and it overlaps with larger absorbance signals from the other cofactors.

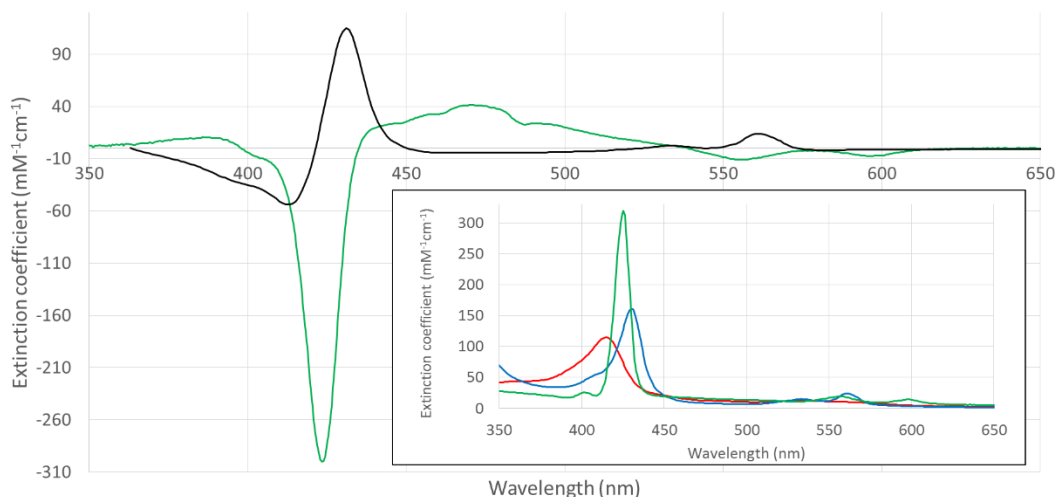


Figure 4.4: Redox difference spectra relevant to transient absorption experiments

Green: $^3\text{ZnPCP}^*$ minus ground state of ZnPCP in MZH3-Y168L mutant at pH 7.5, 1 μs after flashing with 532 nm light. Extinction coefficients are rough estimates based on the ground state spectrum. Black: Fe(II)-heme minus Fe(III)-heme difference spectrum in MZH3 wild type at pH 7. Fe(II)-heme spectrum was prepared by reducing the Fe(III)-heme sample with excess dithionite, which may cause slight overestimate of Fe(II)-heme extinction coefficients. Inset: Spectra of ZnPCP ground state (green), Fe(III)-heme (red), and Fe(II)-heme (blue) bound to MZH3. The ZnPCP spectrum was measured in MZH3 that also contained heme; the heme spectrum was subtracted out.

4.2.2 *Monad and Dyad in MZH3*

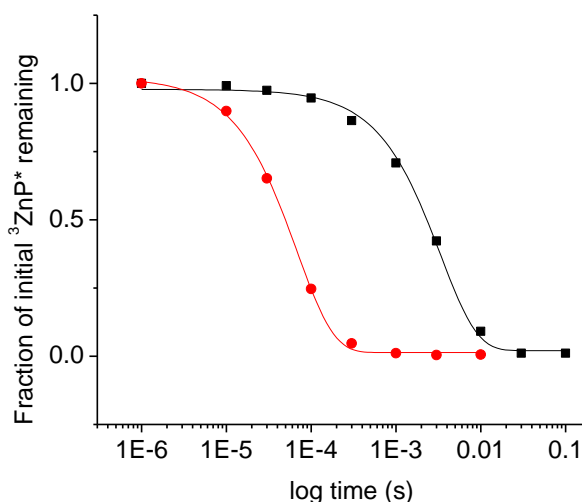
The first step was to reproduce light-activated electron transfer dyad results involving zinc tetrapyrroles and heme B that were demonstrated previously in *de novo* four-helix bundle maquettes (1). To confirm electron transfer between the two cofactors of a dyad, the behavior of the dyad must be compared to a monad (a pigment by itself), in order to determine the effect of the electron acceptor. This is because the P^+A^- state (Figure 4.1) is transient in the dyad and is difficult to observe directly.

A monad maquette was prepared by adding zinc Newkome porphyrin (ZnNP) to MZH3 at pH 7.3 in the absence of any other cofactor, and the lifetime of the triplet excited state was measured by transient absorption. The lifetime of $^3\text{ZnNP}^*$ is similar to $^3\text{ZnPCP}^*$. All other transient absorption experiments presented in this chapter use ZnPCP as the pigment. The addition of ZnNP to an MZH3 protein that lacks an electron acceptor might allow the ZnNP to bind preferentially to the acceptor site or to a mixture of both the pigment and acceptor sites. This is not a concern, because the decay rate of the triplet excited state is not expected to be sensitive to the relatively modest differences between the environments of the pigment and acceptor sites. The recovery of the ground state spectrum was estimated by the absorbance of the Soret band at 423 nm. Fitting to a single exponential fit gave an estimated lifetime of 3.3 ms (Figure 4.5, upper left, black curve).

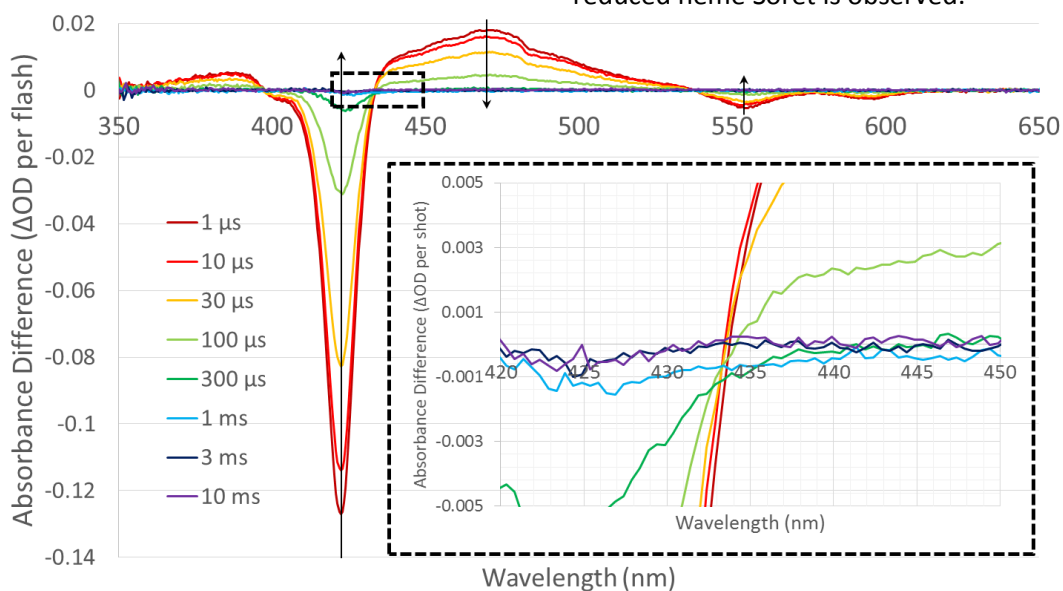
A dyad maquette was prepared using an MZH3 mutant in which the tyrosine was removed and replaced with leucine. Leucine was chosen over phenylalanine to avoid a structural disruption of the Due Ferro section of the protein, as was observed in a previous Due Ferro mutant (21). As a result MZH3-Y168L/Heme B/ZnPCP has only two redox centers available to participate in electron transfer. Transient absorption measurements were performed at pH

7.5, and fitting the Soret absorbance to a single exponential curve showed that the ground state recovery was 70 μs , 50 fold faster than in the monad (Figure 4.5). The Y168L mutant behaved similarly at pH 9.5. This demonstrates that heme B quenched the energy of the excited triplet state and is consistent with quenching by an electron transfer mechanism. However, no Fe(II)-heme Soret band at 432 nm is evident, even in a close-up view of the heme Soret region (Figure 4.5, bottom).

Figure 4.5: Monad and dyad transient absorption experiments



The lifetime of the zinc porphyrin P^* state in MZH3 is greatly reduced when heme B is also bound to MZH3. Upper left: Scaled absorbance at 423 nm of the ZnNP monad (black square points) and the ZnPCP-Heme B dyad in MZH3-Y168L (red circular points) are fitted to single exponential curves (lines). The P^* lifetimes of the monad and dyad are 3.3 ms and 70 μs , respectively. Bottom: Dyad spectra show progression of the recovery of the ground state spectrum from 1 μs to 10 ms. Inset: Close-up view of the area in the dotted box, where no reduced heme Soret is observed.



As expected, MZH3-Y168L containing heme B in the acceptor site and ZnPCP in the pigment site does not stabilize a long-lived charge-separated state; no peaks suggesting heme reduction were observed. The results are consistent with the behavior of a redox active dyad; electrons are transferred from one cofactor to the other, but cannot trap the charge separated state for long enough for chemical reactions to occur.

4.2.3 Triad with tyrosine in MZH3

Some precautions were necessary to ensure that MZH3 triad transient absorption results were reproducible and did not contain artifacts from improper cofactor incorporation. First, given the impact of the second ZnPCP on the conformation of the tyrosine residue as was shown in Figure 3.16, only ~0.8 equivalents of ZnPCP per protein were added to ~3.5 μM MZH3 samples for triad experiments. This is to avoid the possibility of an extra ZnPCP binding to the metal cavity and interfering with electron transfer. Second, MZH3 chelates metals, and after purification, MZH3 often contains bound metal ions, presumably Ni(II) from a Ni-NTA column. For this reason, it was necessary to treat MZH3 samples with a metal chelating agent such as 100-500 μM ethylenediaminetetraacetic acid (EDTA), and then remove the chelator by desalting column or dialysis.

In transient absorption experiments where the signal-to-noise ratio is large and signals from different species do not overlap, the change in concentration of a species with time can be approximated by its absorbance at a single wavelength. In MZH3 triad experiments, however, absorbance features from different species overlap extensively, as shown in Figure 4.4, and if the yield is low, the heme redox spectrum may be noisy. For this reason, it was necessary to use singular value decomposition (SVD) to separate spectral components and determine the rates of

electron transfer reactions (22), following methods described in the appendix. Quantum yields were calculated using an approximate ratio of -2.8 between the extinction coefficient at 423 nm at $1 \mu\text{s}$ (due to the ZnPCP excited triplet minus ground state) and the extinction coefficient at 431 nm of the peak of the heme redox spectrum from SVD analysis. In this way, rough estimates of the yields of the charge separated state for different triad experiments were calculated in a self-consistent manner in order to make comparisons between experiments with different MZH3 mutants and at varying pH. For consistency, all of the following triad experiments used the following conditions: $\sim 3.5 \mu\text{M}$ MZH3, 1.0 equivalent of heme B per protein, ≤ 0.8 equivalents of ZnPCP per protein, and 50 mM NaCl. Experiments at pH 7.5 used 10 mM 3-(N-morpholino)propanesulfonic acid (MOPS) as a buffer, and at pH 9.5, 10 mM N-cyclohexyl-2-aminoethanesulfonic acid (CHES) buffer was used.

Transient absorption with wild type MZH3 at pH 7.5 produced results that had similarities to the MZH3-Y168L dyad, but a distinct peak at 432 nm was observed, consistent with the reduced heme difference spectrum in Figure 4.4. SVD analysis showed that the recovery of the ground state of ZnPCP had a lifetime of $40 \mu\text{s}$, similar to the $70 \mu\text{s}$ lifetime in Y168L, but the absorbance peak at 432 nm persisted for 4 ms. The Q-band absorbance at 560 nm could not be resolved. The relatively weak putative heme Soret band at 432 nm corresponds to a quantum yield of the charge separated state of 2%. The wild type MZH3 transient absorption spectra are shown in Figure 4.6.

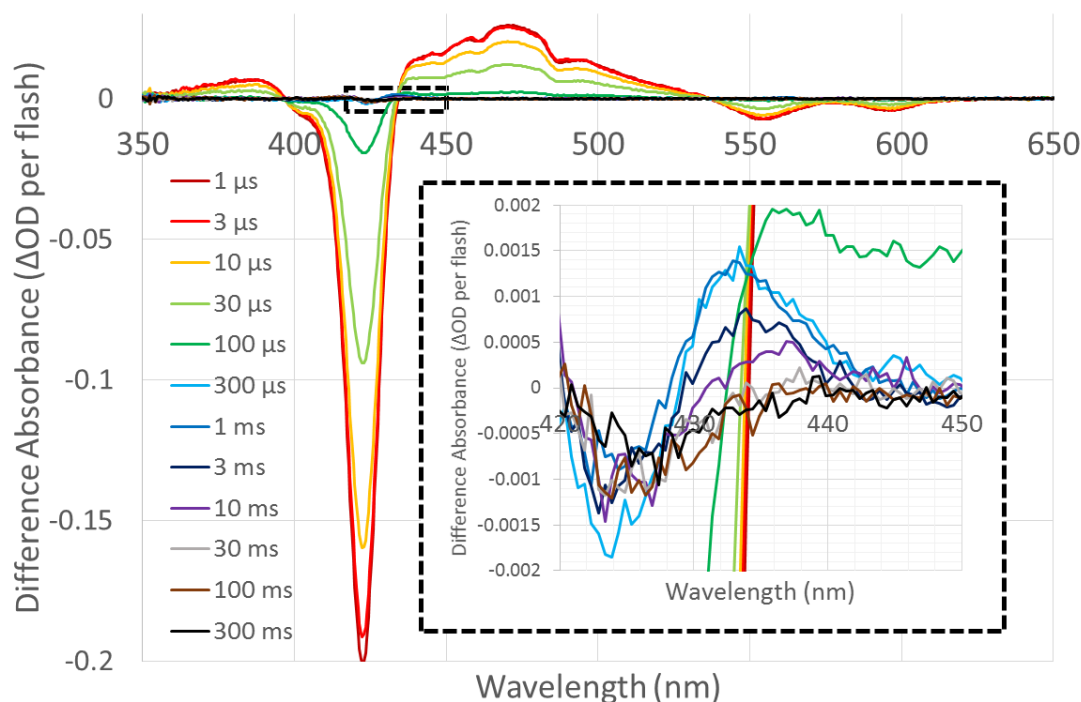


Figure 4.6: Transient absorption spectra of wild type MZH3 with heme B and ZnPCP at pH 7.5

Inset: Close-up view of the region in the dotted box shows an absorbance feature at 432 nm, where the ferrous heme Soret band absorbs.

Given that tyrosine oxidation depends on protonation state, pH was expected to have a pronounced effect on electron transfer kinetics. For this reason, the wild type MZH3 transient absorption experiment was repeated at pH 9.5. The results were similar to the wild type results at pH 7.5 in some regards, with a weak feature at 432 nm corresponding to a quantum yield of 2.5% and a triplet excited state lifetime of 50 μ s. However, the lifetime of the putative charge separated state increased to 150 ms at pH 9.5. This is 38-fold longer than the 4 ms lifetime of the charge separated state at pH 7.5. In addition, SVD analysis found that weaker absorbance features at 560 nm and \sim 533 nm were correlated with a stronger absorbance feature at 532 nm; this SVD component strongly resembled the heme redox spectrum from Figure 4.4. The transient absorption spectra and SVD analysis are shown in Figure 4.7.

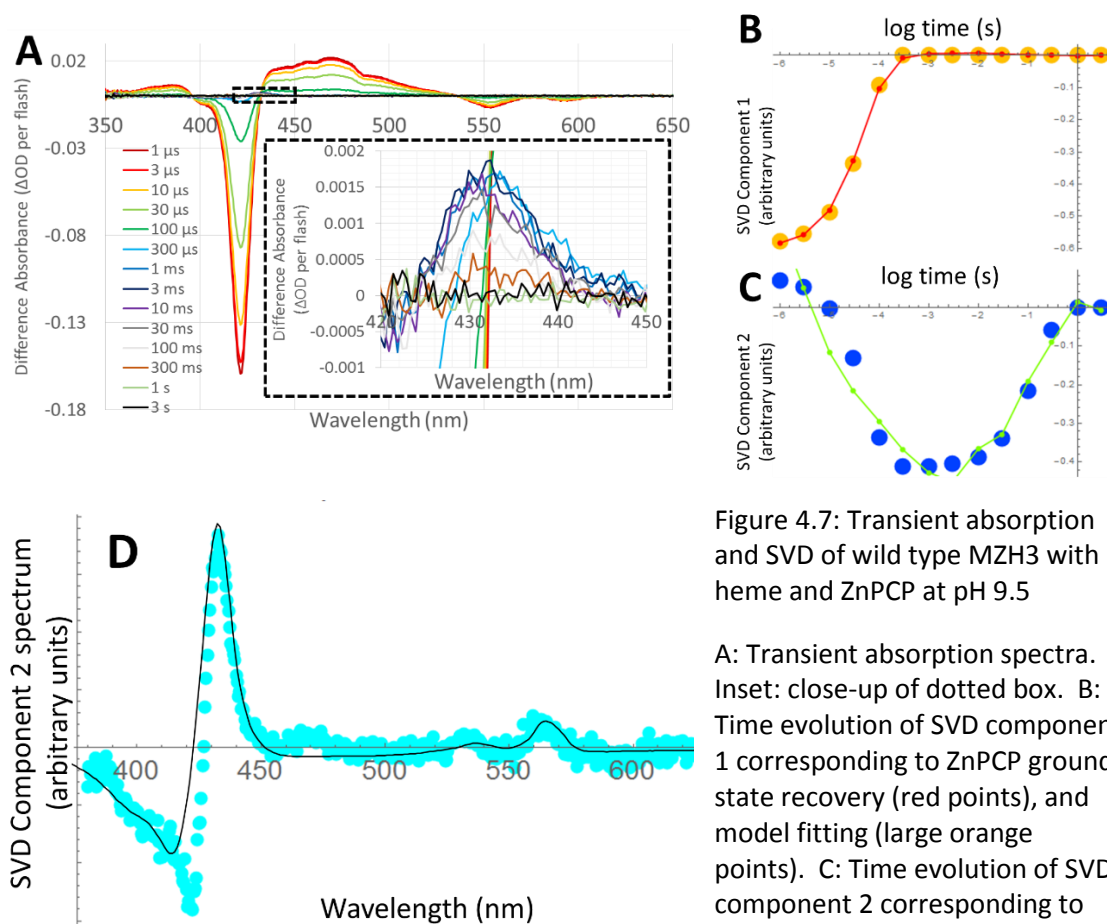


Figure 4.7: Transient absorption and SVD of wild type MZH3 with heme and ZnPCP at pH 9.5

A: Transient absorption spectra. Inset: close-up of dotted box. B: Time evolution of SVD component 1 corresponding to ZnPCP ground state recovery (red points), and model fitting (large orange points). C: Time evolution of SVD component 2 corresponding to the heme redox signal (green points), and model fitting (large blue points). D: Spectrum of SVD component 2 (cyan points) and overlay of heme redox spectrum (black line).

The MZH3-L71H mutant was made to facilitate proton-coupled electron transfer reactions involving the tyrosine, similar to the interaction between tyrosine Z and a histidine side chain in photosystem II. The crystal structure of MZH3-L71H was solved with heme B and Cd(II) bound, and the mutant succeeded in forming the intended histidine-tyrosine hydrogen bond, as was shown in Figure 3.21. Transient absorption results show that the MZH3-L71H mutant also succeeded in increasing the yield of the charge separated state compared to the

wild type. At pH 7.5, the calculated yield was 6%, and at pH 9.5 the yield was 4%. The increased yield was accompanied by a decreased lifetime of the charge separated state. The lifetimes of the MZH3-L71H charge separated state at pH 7.5 and 9.5 were 1.2 ms and 32 ms, respectively. Once again, the lifetime was shorter at pH 7.5 than at 9.5. (Transient absorption results with tyrosine are summarized in Table 4.3).

Other MZH3 mutants were made to further examine the dependence of tyrosine oxidation kinetics on the presence of protonatable groups. In photosystem II, the histidine that hydrogen bonds the redox active tyrosine Z shares a second hydrogen bond with the side chain of asparagine 298 on the D1 protein (23). An exhaustive mutagenesis study of the 19 possible mutants at position 298 found that 12 mutants were incapable of oxygen evolving activity and the other 7 had significantly decreased activity and increased photosensitivity (24). Evidently, this distal hydrogen bond plays a significant role in tyrosine oxidation kinetics. To try to reproduce this effect, an aspartate residue was placed at position 31 in the mutant MZH3-L71H-L31D. Asp31 was meant to make a hydrogen bond to His71 to keep the His71 N_δ atom protonated so that the His71 N_ε atom would accept a hydrogen bond from tyrosine. In addition, the aspartate was intended to stabilize the protonated histidine imidazolium cation and increase the yield of the charge separated state in MZH3. The intended structure is shown in Figure 4.8.

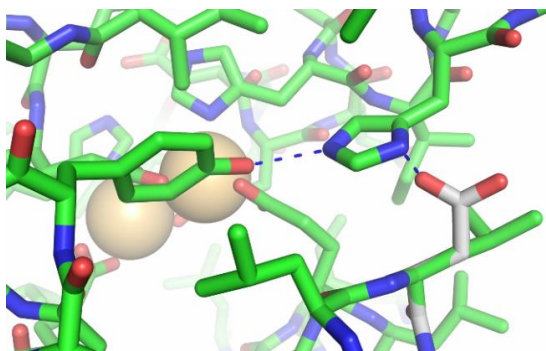


Figure 4.8: Predicted structure of MZH3-L71H-L31D double mutant

The crystal structure of MZH3-L71H with Cd(II) and heme B is shown with carbon atoms in green. The predicted preferred rotamer of D31 is overlaid onto the position of L31 in the crystal structure and colored with white carbon atoms. The histidine and aspartate are within hydrogen bonding distance.

Image rendered using The PyMOL Molecular Graphics System, Version 1.7 Schrödinger, LLC.

Transient absorption experiments showed that the MZH3-L71H-L31D mutant succeeded in increasing the yield of the charge separated state over the yield of the MZH3-L71H mutant and the wild type protein. The addition of Asp31 increased the yield to 8% at pH 7.5 and 12% at pH 9.5. In addition, the lifetimes of the charge separated state decreased to 140 μ s and 2.5 ms at pH 7.5 and 9.5, respectively; as with other MZH3 variants, the charge separated state lasted longer at higher pH. The lifetime of the ground state recovery of ZnPCP was similar to other variants, about 30 μ s at pH 7.5 and 50 μ s at pH 9.5. The MZH3-L71H-L31D transient absorption results at pH 9.5 are presented in Figure 4.9.

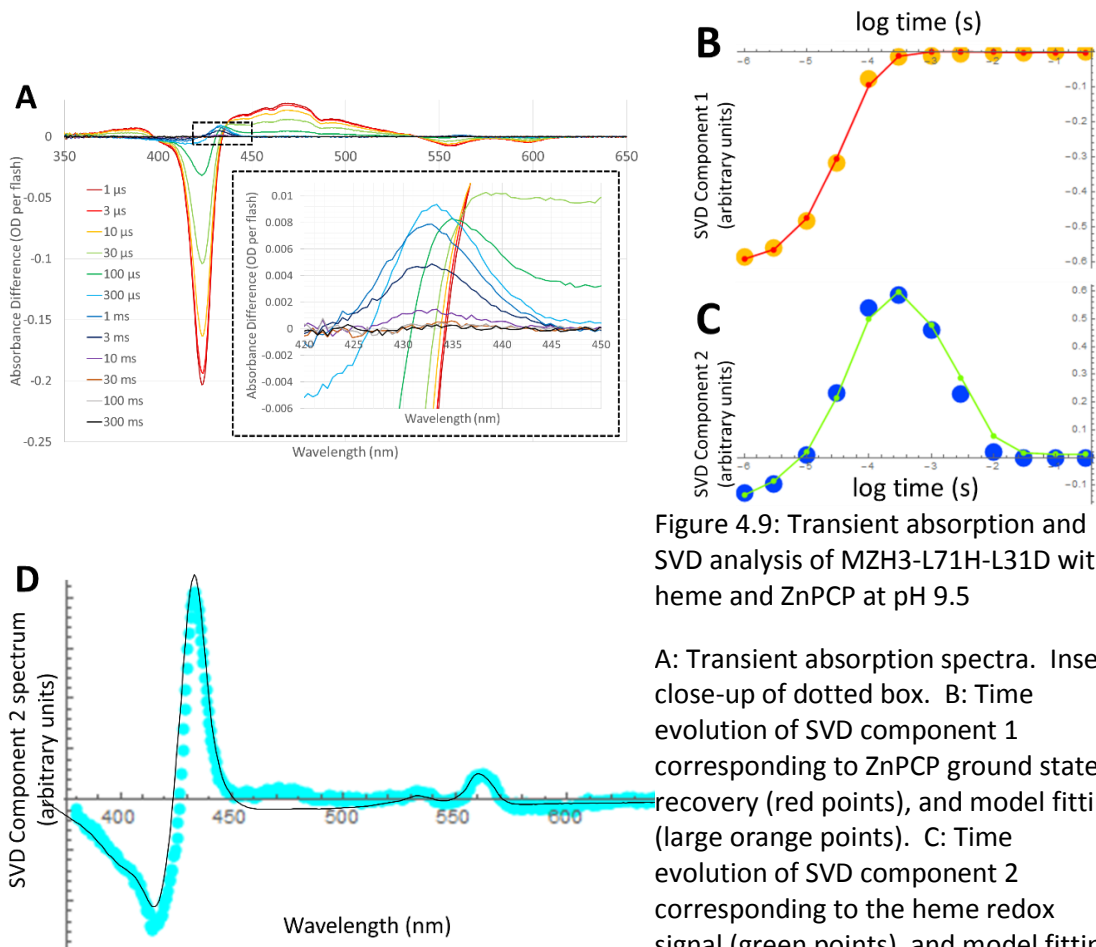


Figure 4.9: Transient absorption and SVD analysis of MZH3-L71H-L31D with heme and ZnPCP at pH 9.5

A: Transient absorption spectra. Inset: close-up of dotted box. B: Time evolution of SVD component 1 corresponding to ZnPCP ground state recovery (red points), and model fitting (large orange points). C: Time evolution of SVD component 2 corresponding to the heme redox signal (green points), and model fitting (large blue points). D: Spectrum of SVD component 2 (cyan points) and overlay of heme redox spectrum (black line).

The tyrosine 168 side chain of MZH3 and MZH3-L71H makes a hydrogen bond to the metal-ligating residue glutamate 34 (see Figure 3.21). This reproduces an interaction that is observed in DufF proteins and natural diiron proteins such as bacterioferritin (25, 26). In order to probe the involvement of Glu34 in tyrosine redox activity, the MZH3-L71H-E34A mutant was prepared. Transient absorption results showed a significant drop in the yield of the charge separated state and a modest increase in lifetime. At pH 7.5, MZH3-L71H-E34A had a yield of only 1% and a lifetime of roughly 3 ms. At pH 9.5, the yield was about 3%, and the lifetime was about 40 ms. The significant drop in yield upon removal of Glu34 suggests that Glu34 is involved in modulating the midpoint potential of the tyrosine, its pK_a , or the efficiency of the proton transfer step in tyrosine oxidation.

Bacterioferritin binds heme B by bis-methionine ligation, and the Wydrzynski group has shown that a modified bacterioferritin can bind zinc chlorin e_6 ($ZnCe_6$) in place of heme B, and this pigment is able to photo-oxidize tyrosine amino acids in bacterioferritin (27, 28). To our knowledge, methionine ligation of zinc tetrapyrroles has not been tested in protein maquettes. Substitution of a hydrophobic methionine ligand for a polar histidine could serve to raise the midpoint potential of a zinc tetrapyrrole to increase the yield of tyrosine and metal ion oxidation. To test whether a methionine ligation of the zinc tetrapyrrole affects oxidation of tyrosine, the histidine in the pigment site was mutated to a methionine residue in the MZH3-L71H-H124M mutant. An ultraviolet/visible spectroscopic titration showed that MZH3-L71H-H124M binds heme B with high affinity, albeit slightly more weakly than wild type MZH3. The dissociation constant for ZnPCP binding was weakened from 10 nM with His124 to about 100 nM with Met124. The titration of ZnPCP into a solution of MZH3-L71H-H124M that contained heme B showed that the ZnPCP Soret band absorbance was centered at 420 nm, representing a

blue-shift of about 2 nm relative to the wild type. Despite these differences between the histidine- and methionine-ligated ZnPCP, transient absorption experiments of MZH3-L71H-H124M were not radically different from MZH3-L71H. At pH 7.5, the yield was 8% and the charge separated state lifetime was 3.4 ms (compared to 6% and 1.2 ms for MZH3-L71H). At pH 9.5, the yield for MZH3-L71H-H124M was 5% and the lifetime was 60 ms (compared to 4% and 32 ms for MZH3-L71H).

A summary of these transient absorption results is shown in Table 4.3. In each protein tested, the lifetime of the charge separated state was extended by an increase in the pH. In general, measurements of the lifetimes of the charge separated states were found to be highly reproducible, but yield estimates were subject to a larger error. These transient absorption experiments do not provide direct experimental evidence of tyrosine oxidation, but the observed changes in electron transfer kinetics would be difficult to explain without invoking

tyrosine redox activity. The replacement of tyrosine with leucine completely eliminates detection of a long-lived charge separated state, and the introduction of polar groups near the tyrosine residue effects pronounced changes in yield and lifetime that are consistent with the known

MZH3 mutant	pH	CS lifetime	CS yield
wt	7.5	~4 ms	2%
Y168L	7.5	N/A	N/A
L71H	7.5	1.2 ms	6%
L31D/L71H	7.5	140 μ s	8%
E34A/L71H	7.5	~3 ms	1%
L71H/H124M	7.5	3.4 ms	8%
wt	9.5	150 ms	2.5%
Y168L	9.5	N/A	N/A
L71H	9.5	32 ms	4%
L31D/L71H	9.5	2.5 ms	12%
E34A/L71H	9.5	40 ms	3%
L71H/H124M	9.5	60 ms	5%
Table 4.3: Transient absorption results in MZH3 with heme B and ZnPCP			
Summary of quantum yields and lifetimes of charge separated (CS) states in MZH3 and MZH3 variants with Heme B and ZnPCP and in the absence of metal ions.			

proton dependence of tyrosine oxidation.

4.2.4 Triad with iron in MZH3

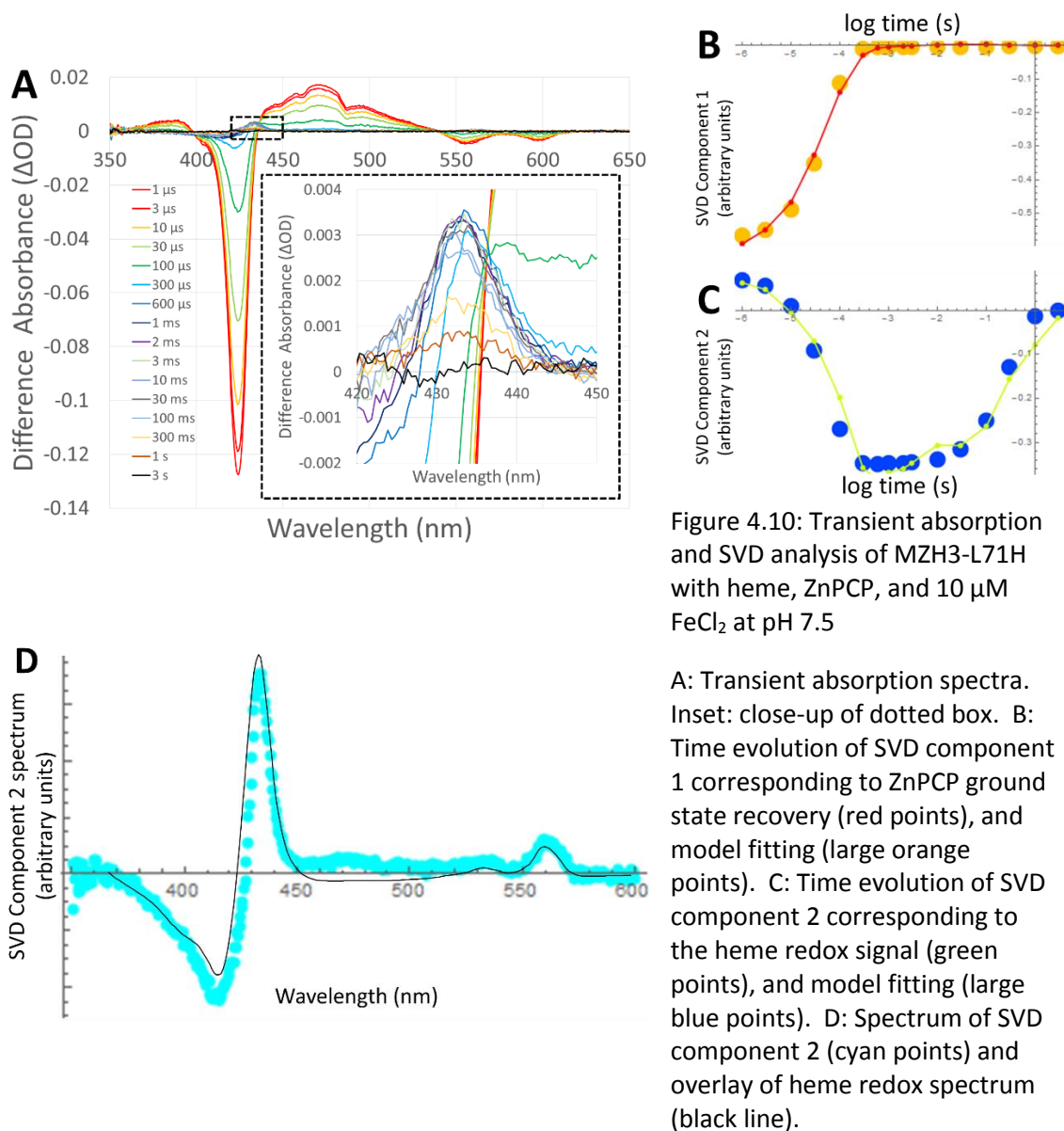
MZH3 was originally intended to function as a redox-active tetrad involving an iron or cobalt tetrapyrrole, a zinc tetrapyrrole, a tyrosine side chain, and a metal ion. However, the ZnPCP-to-metal distance is close enough for direct electron transfer to occur, and tyrosine oxidation could be bypassed if the driving force and reorganization energy are favorable. The metal-to-ZnPCP distance for Zn(II) is 10.1 Å, and it is 9.6 Å for Mn(II). The metal dication that would be easiest to photo-oxidize in MZH3 transient absorption experiments would probably be Fe(II), because it should bind to the di-metal site with high affinity, and it has a lower midpoint potential than Mn(II) or Co(II). Due Ferro maquettes and natural diiron proteins like bacterioferritin can alternately oxidize and reduce iron using oxygen and a reductant (26, 29-31), so it is a natural starting point for tests of metal photo-oxidation in MZH3. All transient absorption experiments with metal ions were carried out at pH 7.5 and not pH 9.5 because of the risk of precipitation of metal hydroxide complexes, which could complicate results.

Addition of large concentrations of FeCl₂ (in excess of 500 μM) in transient absorption experiments with 3.5 μM MZH3 appears to have led to the use of Fe(II) as an unbound sacrificial electron donor. Treatment of MZH3-L71H, MZH3-Y168L, and MZH3-L71H-E34A with high Fe(II) concentrations always resulted in the trapping of a reduced state of heme B for at least 10 s; recombination was not observed.

The MZH3-L71H-E34A mutant is likely to have impaired metal binding activity at the site closest to the ZnPCP, because Glu34 is a bidentate ligand of the metal at that site. Removal of either of the corresponding bidentate axial glutamate residues from bacterioferritin results in a

protein that can only bind one Co(II) ion per bundle (32). Therefore, it is likely that E34A prevents binding of metal ions to the site nearest the tyrosine. Transient absorption experiments of 3.0 μM MZH3-L71H-E34A with heme B, ZnPCP, and 1 mM FeCl_2 led to heme B remaining reduced for longer than 10 s, but when the experiment was repeated with only 10 μM FeCl_2 , the lifetime of the charge separated state was roughly 5 ms, which is similar to the ~ 3 ms lifetime that was observed in the absence of FeCl_2 . In addition, the yields of MZH3-L71H-E34A experiments with and without 10 μM FeCl_2 were both about 1%, but at 1 mM FeCl_2 , the yield was 6%. At 50 μM FeCl_2 , the yield and lifetime of the charge separated state were 1.5% and ~ 10 ms, which are only slightly different from the metal-free MZH3-L71H-E34A.

In contrast, MZH3-L71H, which binds metal ions with high affinity, had a dramatic increase in the lifetime of the charge separated state when only 10 μM FeCl_2 was added. In the absence of Fe(II) the lifetime was 1.3 ms, but the presence of 10 μM FeCl_2 increased the lifetime to 300 ms. The 10 μM FeCl_2 experiment also had a modest increase in yield to 8% from 6% without FeCl_2 . These results are presented in Figure 4.10. The lifetime of the recovery of the ground state bleach of the ZnPCP was close to the lifetime without iron, 60 μs .



The MZH3-Y168L mutant should be competent to bind metal ions, but its metal affinity might be weakened slightly, because the Tyr168 makes a hydrogen bond to Glu34, which stabilizes Glu34 in the metal-binding conformation. The metal ligand Glu161 is intended to make a bidentate ligation of a metal ion in the same way that Glu34 ligates the other metal ion, and Glu161 has consistently higher temperature factors in its side chain than Glu34 in almost all

MZH3 crystal structures. Glu161 lacks a second shell hydrogen bond to a tyrosine, which suggests a stabilizing role for the second shell tyrosine contact. For this reason, removal of Tyr168 in MZH3-Y168L could weaken metal ion affinity. When 10 μM FeCl_2 was added to 3.5 μM MZH3-Y168L for a transient absorption experiment, the results showed a clear heme redox signal with a low yield of approximately $\sim 2\%$ and a lifetime of roughly ~ 500 ms. This charge separated lifetime is similar to the lifetime in MZH3-L71H with 10 μM FeCl_2 , which suggests that the tyrosine is not involved in formation of the charge separated state. The decreased quantum yield in MZH3-Y168L compared to MZH3-L71H can be attributed to the presumed decreased affinity for metal ions.

These results show that a bound iron ion can act as the electron donor in a redox-active triad in MZH3. In MZH3-L71H, addition of 10 μM FeCl_2 increases the lifetime of the charge separated state by a factor of 220. The same concentration of FeCl_2 does not significantly affect the lifetime of MZH3-L71H-E34A, a mutant that probably does not bind Fe(II) with high affinity at the metal site that is proximal to the pigment site. The disparity in the effect of 10 μM FeCl_2 shows that at this low concentration, Fe(II) is not an effective sacrificial electron donor in transient absorption experiments. Because 10 μM FeCl_2 gives MZH3-L71H a longer lifetime and higher yield but eventually recombines after 300 ms, MZH3-L71H must be photo-oxidizing bound Fe(II) and not free Fe(II) .

Since heme reduction in MZH3-Y168L is not observed in transient absorption spectroscopy unless 10 μM FeCl_2 is present, tyrosine 168 is not essential to photo-oxidation of bound Fe(II) in MZH3. Therefore, MZH3 containing heme B, ZnPCP, tyrosine, and Fe(II) functions as a triad and not as a tetrad that involves the activity of tyrosine. This could be the result of the

relatively low potential of iron compared to manganese or cobalt; Fe(II) may have a sufficiently high driving force for oxidation by ZnPCP that it can outcompete tyrosine oxidation.

A summary of the transient absorption results presented so far is given in graphical form in Figure 4.11.

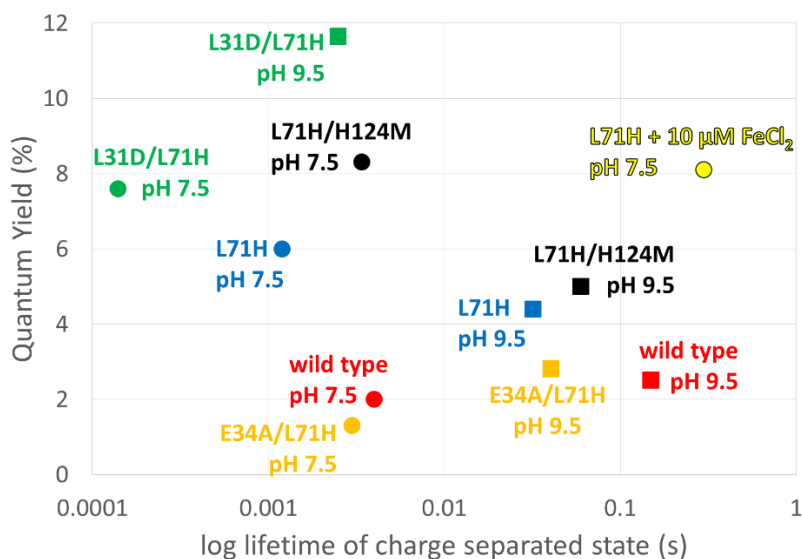


Figure 4.11: Summary of transient absorption results in graphical form

Circular and square data points represent experiments at pH 7.5 and pH 9.5, respectively. Unless otherwise noted, data points represent experiments in the absence of metal ions.

4.2.5 MZH3 reverts to dyad behavior in the presence of Zn, Cd, or Mn

The addition of MnCl₂ or ZnSO₄ eliminated the long-lived charge separated state in transient absorption experiments. Zn(II) is not redox active, but the potential of the Mn(II)/Mn(III) redox couple should make Mn(II) susceptible to oxidation in this system. In one experiment with 2.4 μ M MZH3-L71H with heme B and ZnPCP and no metal ions at pH 7.5, a charge separated state had a lifetime of 1.2 ms and a yield of 6%. A ZnSO₄ stock solution was added to a final concentration of 10 μ M, and the experiment was repeated. The ZnPCP Soret bleach was red-shifted with the addition of ZnSO₄ by about 2-3 nm from 422 nm to 425 nm. The heme redox signal was not observed in the presence of ZnSO₄. The lifetime of the recovery of

ZnPCP ground state was 70 μ s with Zn(II), similar to the 60 μ s lifetime in the absence of metal ions. Evidently, Zn(II) binding to MZH3-L71H inhibits oxidation of the tyrosine.

This experiment was repeated with 3.4 μ M MZH3-L71H-L31D with heme B and ZnPCP. Despite the addition of Asp31 to increase the polarity of the tyrosine environment, the same result was observed; a charge separated state was trapped in the absence of metal ions, but 10 μ M ZnSO₄ eliminated the heme redox signal.

Preliminary results have shown that the same inhibitory effect and red-shifted ZnPCP Soret absorbance was observed in the presence of MnCl₂. No long-lived charge separated state was observed by transient absorption in MZH3-L71H-H124M with 10 μ M MnCl₂, MZH3-L71H with 4 mM MnCl₂, or wild type MZH3 with 1 mM MnCl₂ at pH 7.5. All of these MZH3 variants trap a long-lived charge separated state in the absence of Mn(II), but lose the ability to do so in high yield when Mn(II) binds.

It is unclear why the binding of metal ions would inhibit formation of the charge separated state in MZH3. One possibility is that metal binding alters the midpoint potential of the tyrosine. The presence of the metal could alter the tyrosine potential by an electrostatic effect, but crystal structures show that Glu34 appears to shield the positive charge of the metal ion from the tyrosine. In addition, at pH 7.5, the initial and final states of the tyrosine are both expected to be neutral, because the electron transfer is coupled to proton transfer. This would make the electrostatic influence of the metal irrelevant if tyrosine oxidation follows a concerted PCET mechanism.

It is unlikely that tyrosine 168 of MZH3 ligates a metal ion, which could change its midpoint potential from the expected value. A tyrosinate-Fe(III) ligand has been detected in Due Ferro proteins, but not a tyrosinate-Fe(II) ligand (21, 33, 34). A tyrosinate-Fe(III) spectral

signature was not observed in MZH3 (Figure 2.19), and crystal structures show that the distance between the tyrosine phenolic oxygen and metal ion is at least 3.2 Å. This is much longer than the tyrosinate-Fe(III) ligand in Due Ferro variant DFsc, which has an Fe(III)-O bond length of 1.89 Å (21). In addition, the carboxylate group of Glu34 stands between Y168 and the metal to make a hydrogen bond with the tyrosine and a bidentate ligation of the metal. The Tyr-to-Zn(II) distance is even longer than the Tyr-to-Mn(II) distance; crystal structure CS-A, which has one ZnPCP in the pigment site and Zn(II), has 3.7 Å between the tyrosine phenolic oxygen and the Zn(II). Both Mn(II) and Zn(II) were shown to inhibit formation of the charge separated state, so a tyrosinate-metal ligand in MZH3 is not supported by experimental evidence.

Metal binding may inhibit efficient deprotonation of the tyrosine. It could be that when a metal ion binds, Tyr168 donates a hydrogen bond to Glu34 which cannot accept a proton because it is ligating a metal ion. This would stabilize the proton on Tyr168 and inhibit oxidation. However, a study of bacterioferritin shows that a tyrosine in an analogous hydrogen bonding interaction with an iron-ligating glutamate residue, Tyr25, is oxidized during normal function of the protein (29). Another study in a modified bacterioferritin showed photo-oxidation of this same tyrosine in the presence of manganese and further showed that tyrosine could not be photo-oxidized in the absence of metal ions (27, 28, 35). The metal dependence of Tyr25 oxidation in bacterioferritin is the opposite of what is observed for Tyr168 in MZH3. Despite the difference in tyrosine oxidation activity, MZH3 and bacterioferritin have highly similar overall folds (see Figure 3.18); specific interactions may be significant in achieving tyrosine oxidation in the presence of bound metal ions. Unlike the Tyr168 residue of wild type MZH3, which contacts only hydrophobic residues apart from the metal-ligating Glu34, Tyr 25 of bacterioferritin is surrounded by a total of four carboxylate amino acids: the metal-ligating

Glu94 as well as Glu44, Glu47, and Asp90 (36). The difference in the polarity of the environment of the tyrosines in MZH3 and bacterioferritin might be the source of the difference in redox activity. The highly polar environment around Tyr25 in bacterioferritin could facilitate proton transfer from Tyr25 even if Glu94 is unable to accept a proton.

The flexibility of MZH3 could play a role in tyrosine oxidation. DF3 is known to have relatively low stability in the apo-state (33), and MZH3 does not crystallize in the absence of metal ions and its helicity and stability increase significantly in the presence of MnCl_2 and CaCl_2 (Table 2.6 and Figure 2.20). This metal-dependent stability suggests that apo-MZH3 may have structural fluctuations in the vicinity of the metal binding site that could increase solvent exposure of tyrosine 168. Metal binding may restrict these motions and thereby lower the solvent exposure of Tyr168. This would decrease the rate of deprotonation of the tyrosine so that its oxidation is no longer able to compete with the rate of reduction of ZnPCP^{2+} by Fe(II)-heme B. The 2-3 nm redshift in the ZnPCP Soret band when metal ions bind might also be caused by a decrease in the degree of penetration of solvent into the core of MZH3.

Photo-oxidation of manganese ions has been achieved before in modified natural proteins (27, 37, 38), and there is no reason why it can't be done in a maquette. Future work should seek to determine why metal binding inhibits tyrosine oxidation in MZH3 and how to oxidize Mn(II). It may be possible to achieve efficient manganese oxidation by altering the driving forces by raising the pH, using a higher potential zinc tetrapyrrole, or altering the environment of the Mn(II) ion or Tyr168 through mutagenesis.

4.2.6 Photo-reduction of cobalt protoporphyrin IX

Cobalt protoporphyrin IX (CoPPIX) has been used for photo-catalytic hydrogen generation in modified natural proteins (39, 40). Co(III)PPIX binds to wild type MZH3 with a dissociation constant of 250 nM, 35 times stronger than the Co(III)PPIX affinity of cytochrome b_{562} (39), as described in section 2.3.3. For this reason, CoPPIX may be a viable candidate for catalytic hydrogen production in MZH3. One of the natural proteins that promoted hydrogen evolution using CoPPIX was cytochrome b_{562} , which uses a histidine and a methionine to ligate the cofactor (39). In order to reproduce this His-Met ligation scheme, the MZH3-His110Met mutation was made.

Before testing for photo-reduction of CoPPIX, reference spectra of Co(III)PPIX and Co(II)PPIX bound to MZH3-His110Met were determined in order to confirm binding and to aid data analysis. The Co(III)PPIX state is more stable under aerobic conditions; the midpoint potential of the [Co(III)PPIX/Co(II)PPIX] redox couple was measured at 100 mV vs. SHE in myoglobin and 16 mV vs. SHE in cytochrome b_{562} (39, 41). These potentials should make it possible for the excited state $^3\text{ZnPCP}^*$ cofactor to reduce Co(III)PPIX, since the [ZnPCP⁺/³ZnPCP*] midpoint potential is -0.69 V. The Co(III)PPIX Soret absorbance peak had a wavelength of 429 nm in MZH3-His110Met and 426 nm in wild type MZH3, similar to the 424-430 nm range found for cobalt cytochrome b_{562} variants, cobalt myoglobin, and a four-helix bundle maquette (39, 41, 42). Co(III)PPIX was reduced in MZH3-His110Met and wild type MZH3 using dithionite, but the reduction was slow. This is consistent with observations that the Co(III)PPIX/Co(II)PPIX transition in myoglobin and in maquettes is orders of magnitude slower than heme reduction, and these slow kinetics have been attributed to a structural rearrangement (41, 42). During reduction of Co(III)PPIX in MZH3 variants, the decrease in the

Co(III)PPIX Soret band absorbance was accompanied by a concomitant increase in a weaker, broader Co(II)PPIX Soret band increase at 399 nm in MZH3-His110Met or 397 nm in wild type MZH3. Similar Co(II)PPIX Soret absorbance wavelengths have been reported between 394 nm and 406 nm in myoglobin and at 401 nm in a four-helix bundle maquette (40-42). The CoPPIX spectra in MZH3-His110Met and in myoglobin are shown in Figure 4.12.

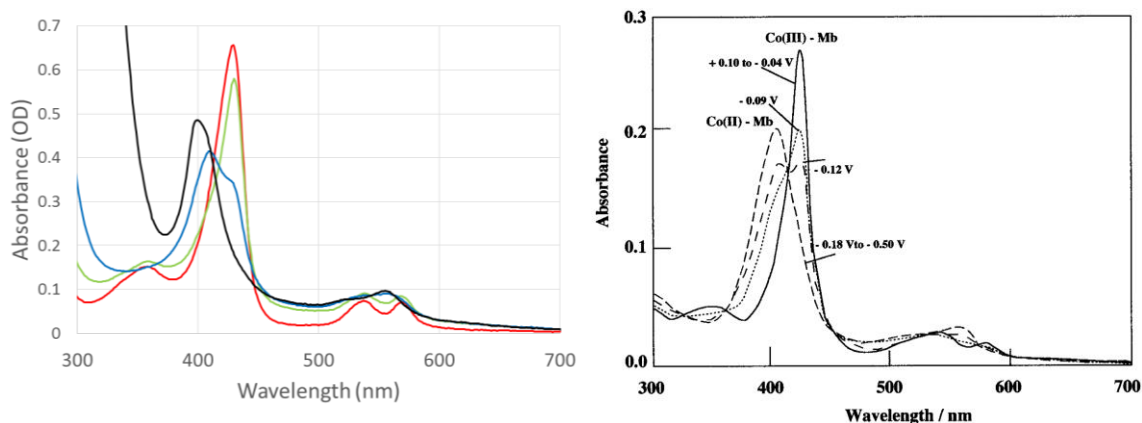


Figure 4.12: Co(II/III)protoporphyrin IX spectra in MZH3 and myoglobin

Left: Spectra of 3 μM MZH3-His110Met bound to CoPPIX in 20 mM sodium phosphate, 50 mM NaCl at pH 7.5. Red trace is Co(III)PPIX and black trace is Co(II)PPIX reduced with excess dithionite. (Dithionite accounts for the steep increase in absorbance of the Co(II)PPIX trace near 319 nm). The green and blue traces are mixtures of Co(III) and Co(II)PPIX collected before the slow reduction was complete. Right: Literature Co(III)-myoglobin and Co(II)-myoglobin spectra collected at pH 6.8 in a spectroelectrochemical cell. Potentials at which spectra were measured are given vs Ag|AgCl (saturated KCl). Figure reproduced from Li et al., 2000 (41).

CoPPIX photo-reduction was tested by transient absorption spectroscopy in MZH3 variants that also had ZnPCP bound. The experiment was run at pH 7.5 and pH 9.5 using wild type MZH3 and MZH3-His110Met. There was no sign of a Co(II)PPIX peak in any of the transient absorption experiments. However, in all cases, the excited $^3\text{ZnPCP}^*$ triplet state lifetime was decreased from 3.3 ms in the ZnPCP-MZH3 monad to roughly 100 μs when Co(III)PPIX was present. This could mean that Co(III)PPIX is transiently reduced to the Co(II)PPIX state, but that

reduction of ZnPCP⁺⁺ by Co(II)PPIX outcompetes tyrosine oxidation. Energy transfer is another possible explanation for the reduced lifetime of the ³ZnPCP* excited state.

The fact that Co(III)PPIX reduction kinetics are slow might explain the absence of Co(II)PPIX in transient absorption. To test whether CoPPIX reduction is possible in MZH3 over longer timescales, continuous illumination experiments were used to look for Co(II)PPIX production on a minutes to hours timescale. A CUDA model I-150 halogen lamp with a 150 W bulb illuminated the sample using a fiber optic cable, and the anaerobic sample was held at 20°C using a Peltier temperature controller. Anaerobic samples of ~3 μM wild type MZH3 and MZH3-His110Met were prepared with CoPPIX and ZnPCP at pH 9.5 with 1 mM EDTA, 0.5-1 mM ascorbate, 50 mM NaCl, and 10 mM CHES buffer. Under these conditions, a distinct Co(II)PPIX Soret peak was observed at 397-399 nm within a few minutes of the start of illumination, and it was accompanied by a concomitant decrease of the Co(III)PPIX Soret at 427-429 nm. Reduction continued over the course of about 1 hour. However, no CoPPIX reduction was observed when the pH was lowered to 7.5 or if either ascorbate or EDTA were not included in the sample.

In previous maquettes, CoPPIX has been reported to dissociate from the maquette after reduction to the Co(II)PPIX state (42). For this reason, the wild type MZH3 sample was tested for Co(II)PPIX dissociation. After 2 hours of illumination, when reduction to the Co(II)PPIX state had been completed, the light source was turned off. About 0.2 μM Co(III)PPIX was added to the anaerobic sample to test for binding; if Co(II)PPIX remains bound, then no Co(III)PPIX should bind to MZH3. Unexpectedly, the added Co(III)PPIX was reduced within the time it took to record a spectrum (less than one minute). This suggests that the solution potential had been lowered over the course of the experiment. After removal of free CoPPIX by a PD-10 desalting

column (GE Healthcare Life Sciences), a Co(II)PPIX Soret peak at ~398 nm remained, suggesting that Co(II)PPIX remained bound to wild type MZH3 after reduction.

These results clearly establish that light-driven reduction of Co(III)PPIX to Co(II)PPIX occurs slowly in MZH3. The requirements of high pH and the presence of both ascorbate and EDTA are not easily explained, but the pH dependence suggests involvement of the tyrosine in electron transfer. It could be that either EDTA or ascorbate serves as the sacrificial electron donor, while the other performs an unexpected function such as storing reducing equivalents or directly interacting with the protein in a way that influences electron transfer rates. This line of research is ongoing, but current results show that CoPPIX photo-reduction occurs in MZH3.

4.3 Summary of electron transfer in MZH3

4.3.1 ZnPCP binding to metal cavity is not consistent with transient absorption results

If ZnPCP binds to the opening of the metal cavity in transient absorption experiments, it would push the tyrosine side chain out of the core, as observed in crystal structures CS-B and CS-C and shown in Figure 3.16. This would break the hydrogen bond with the histidine in the MZH3-L71H mutant, and a more solvent-exposed tyrosine side might be easier to oxidize than a buried tyrosine, because it might be more stable in the charged tyrosinate form. There are several reasons why it is unlikely that a second ZnPCP binds to the metal cavity.

All transient absorption experiments were done with sub-stoichiometric ZnPCP to avoid the possibility of a second ZnPCP binding to the opening of the metal binding site cavity. Ultraviolet/visible spectroscopic titrations showed high-affinity binding of ZnPCP at neutral pH with a stoichiometry of 1:1, and changing the pigment site His124 to Met124 results in changes in binding affinity and creates a blue-shift in the ZnPCP spectrum. Crystal structures CS-B and

CS-C showed a clear preference of the ZnPCP for the pigment site rather than the metal cavity. This suggests that ZnPCP is not present in the metal binding site under the conditions of the transient absorption experiments.

If a ZnPCP molecule were to bind to the metal cavity in these experiments, it would be 30 Å from the heme, meaning that this ZnPCP could not reduce the heme because the maximum rate of heme reduction by $^3\text{ZnPCP}^*$ to the heme would have a lifetime of about 1000 s. The fact that heme is reduced on a μs timescale shows that a ZnPCP must be bound to the pigment site.

Despite this reasoning, it may be worthwhile to confirm that ZnPCP does not bind to the opening of the metal cavity in transient absorption experiments. One way to do this would be to repeat these experiments with zinc tetrapyrroles that are unlikely to bind to MZH3 at the metal site, such as NR117 or SE375 (see Table 2.4). Another alternative is to make mutations to MZH3 that would destabilize the ZnPCP at the opening of the metal cavity and the interfacial conformation of the tyrosine.

4.3.2 Analysis of transient absorption results

The rate of the electron transfer from the excited triplet state $^3\text{ZnPCP}^*$ to Fe(III)-heme B, k_{CS1} , was consistently measured at about $10^{4.5} \text{ s}^{-1}$ (30 to 70 μs lifetime) for all transient absorption experiments. This lifetime is more than an order of magnitude slower than the estimated 1 μs lifetime (10^6 s^{-1} rate of k_{CS1}) calculated using the Moser-Dutton ruler (Equation 4.1) from parameters in Table 4.2. This discrepancy is surprising, but could be explained by an unusually large reorganization energy ($\sim 1.6 \text{ eV}$) or an uneven distribution of the $^3\text{ZnPCP}^*$ wavefunction that creates a longer effective distance R_{PA} .

Regardless of reorganization energy or distance, the rate of charge recombination between the Fe(II)-heme and ZnPCP⁺⁺, k_{CR1} , should be about 20 times faster than the forward electron transfer rate, k_{CS1} . Based on the measured rate of k_{CS1} , this would put k_{CR1} close to $10^{5.8} \text{ s}^{-1}$. Therefore, less than 5% of the A⁻P⁺ intermediate should be observable in the dyad. This is consistent with transient absorption results that did not detect the intermediate A⁻P⁺ state.

At pH 9.5, around 30% of Tyr168 will be deprotonated before the flash, assuming a tyrosine pK_a of 10. Using the parameters in Table 4.2, tyrosinate oxidation by ZnPCP⁺⁺ should proceed with a rate k_{CS2} of $10^{9.5} \text{ s}^{-1}$, and the recombination rate, k_{CR2} , should be $10^{6.3} \text{ s}^{-1}$, so the rate of charge separation is favored by a factor of $10^{3.2}$. Since the rate of the first recombination k_{CR1} is $10^{5.8} \text{ s}^{-1}$, the return to the ground state should proceed at a rate of $10^{5.8-3.2} \text{ s}^{-1}$, or $10^{2.6} \text{ s}^{-1}$ corresponding to a lifetime of 2.5 ms. Transient absorption experiments with MZH3-L71H-L31D are in agreement with this model; the measured lifetime of the MZH3-L71H-L31D charged separated state at pH 9.5 is 2.5 ms and the yield is 12%. Other mutants that have lower yields and longer lifetimes of the charge separated state are consistent with higher tyrosine pK_a values and corresponding lower midpoint potentials of the [Tyr-O⁻/Tyr-O[•]] redox couple.

At pH 7.5, the fraction of tyrosine in the tyrosinate state is small, assuming a pK_a of 10, and tyrosine oxidation might proceed through the tyrosyl radical cation, which would have a midpoint potential of ~1.34 V. The 0.43 eV uphill driving force for tyrosine oxidation by ZnPCP⁺⁺ would have a lifetime of around 400 μs, and give <1% yield. However, if the tyrosine potential were slightly lower, at 1.28 V, then 40 μs electron transfer could take place, and this could account for a 4% yield, assuming proton transfer can also take place in 40 μs. This mechanism is consistent with the wild type MZH3 yield of 2% at pH 7.5.

Upon binding of Fe(II), the lifetime of the charge separated state becomes 300 ms. This recombination rate is about $10^{5.3}$ times slow than the dyad short circuit k_{CS1} , and corresponds to a [Fe(II)/Fe(III)] midpoint potential of about 0.59 V. This potential would be high for iron but is not unreasonable, as iron midpoint potentials in diiron proteins can vary across a wide range.

4.3.3 Conclusion and future directions

The transient absorption results presented in this chapter demonstrate that MZH3 can assemble a charge separating triad that involves heme B as the acceptor, ZnPCP as the pigment, and either tyrosine or Fe(II) as the donor. A stable charge separated state is formed when tyrosine is present in the protein, and the quantum yield and lifetime of charge separation can be manipulated by hydrogen bonding interactions with the tyrosine. Hydrogen bonding partners of the tyrosine seem to have the effect of increasing the yield of charge separation, but decreasing the lifetime. It should be noted, however, that in photosystem II, the Y_z^* radical is a transient species that is not itself used for bond making and breaking; Y_z^* has a short lifetime so it can pass oxidizing equivalents to the OEC. In MZH3, bound Fe(II) enables lifetimes of charge separation of 300 ms, long enough for chemical reactions to take place.

The transient absorption results strongly support electron transfer from the donors, but the oxidized states of the donors could not be detected directly. Future studies of this system by electron paramagnetic resonance may be able to detect a tyrosyl radical signal to confirm its oxidation.

Cobalt tetrapyrroles are known to be capable of hydrogen production (39, 43). Preliminary results have shown that when CoPPIX is used as the electron acceptor in place of heme in MZH3, a charge separated state is not detected by transient absorption. However,

continuous illumination experiments of MZH3 with CoPPIX and ZnPCP in the presence of ascorbate and EDTA suggest Co(III)PPIX photo-reduction to Co(II)PPIX, as evidenced by a large blue-shift of the Soret band of CoPPIX. Experimental complications and uncertainties have so far left ambiguity as to whether direct electron transfer from ZnPCP to CoPPIX occurs, but CoPPIX is being investigated as a possible path toward hydrogen production.

The MZH3 scaffold provides a starting point to begin to assemble a redox-active metal cluster akin to the oxygen evolving complex of photosystem II. Photo-oxidation of tyrosine and Fe(II) have already been demonstrated in this chapter, and this represents an important first step toward a water oxidation catalyst. If oxidation of Mn(II) can be achieved, it may be possible to use a photo-assembly mechanism to build a multinuclear metal center similar to the OEC of photosystem II. The simple, robust reaction center maquette MZH3 could thus be used to investigate the properties necessary to build a functional water-oxidizing metal cluster.

4.4 References

1. Farid, T. A., Kodali, G., Solomon, L. A., Lichtenstein, B. R., Sheehan, M. M., Fry, B. A., Bialas, C., Ennist, N. M., Siedlecki, J. A., Zhao, Z., Stetz, M. A., Valentine, K. G., Anderson, J. L., Wand, A. J., Discher, B. M., Moser, C. C., and Dutton, P. L. (2013) Elementary tetrahelical protein design for diverse oxidoreductase functions, *Nat Chem Biol* 9, 826-833.
2. Lichtenstein, B. R., Farid, T. A., Kodali, G., Solomon, L. A., Anderson, J. L., Sheehan, M. M., Ennist, N. M., Fry, B. A., Chobot, S. E., Bialas, C., Mancini, J. A., Armstrong, C. T., Zhao, Z., Esipova, T. V., Snell, D., Vinogradov, S. A., Discher, B. M., Moser, C. C., and Dutton, P. L. (2012) Engineering oxidoreductases: maquette proteins designed from scratch, *Biochem Soc Trans* 40, 561-566.
3. Rau, H. K., DeJonge, N., and Haehnel, W. (1998) Modular synthesis of de novo designed metalloproteins for light-induced electron transfer, *P Natl Acad Sci USA* 95, 11526-11531.
4. Ananyev, G., and Dismukes, G. C. (2005) How fast can Photosystem II split water? Kinetic performance at high and low frequencies, *Photosynth Res* 84, 355-365.
5. Vinyard, D. J., Ananyev, G. M., and Dismukes, G. C. (2013) Photosystem II: the reaction center of oxygenic photosynthesis, *Annu Rev Biochem* 82, 577-606.

6. Moser, C. C., Keske, J. M., Warncke, K., Farid, R. S., and Dutton, P. L. (1992) Nature of biological electron transfer, *Nature* 355, 796-802.
7. Page, C. C., Moser, C. C., Chen, X., and Dutton, P. L. (1999) Natural engineering principles of electron tunnelling in biological oxidation-reduction, *Nature* 402, 47-52.
8. Moser, C. C., Anderson, J. L., and Dutton, P. L. (2010) Guidelines for tunneling in enzymes, *Biochim Biophys Acta* 1797, 1573-1586.
9. Zhao, Z. (2016) Engineering principles of photosystems and their practical application as long-lived charge separation in maquettes, University of Pennsylvania.
10. Ishimitsu, T., Hirose, S., and Sakurai, H. (1976) Acid dissociation of tyrosine and its related compounds, *Chem Pharm Bull (Tokyo)* 24, 3195-3198.
11. Bonin, J., Costentin, C., Robert, M., Routier, M., and Saveant, J. M. (2013) Proton-coupled electron transfers: pH-dependent driving forces? Fundamentals and artifacts, *J Am Chem Soc* 135, 14359-14366.
12. Dixon, W. T., and Murphy, D. (1976) Determination of Acidity Constants of Some Phenol Radical Cations by Means of Electron-Spin Resonance, *J Chem Soc Farad T* 2 72, 1221-1230.
13. Tommos, C., and Babcock, G. T. (2000) Proton and hydrogen currents in photosynthetic water oxidation, *Biochim Biophys Acta* 1458, 199-219.
14. Martinez-Rivera, M. C., Berry, B. W., Valentine, K. G., Westerlund, K., Hay, S., and Tommos, C. (2011) Electrochemical and structural properties of a protein system designed to generate tyrosine Pourbaix diagrams, *J Am Chem Soc* 133, 17786-17795.
15. Megiatto, J. D., Jr., Mendez-Hernandez, D. D., Tejeda-Ferrari, M. E., Teillout, A. L., Llansola-Portoles, M. J., Kodis, G., Poluektov, O. G., Rajh, T., Mujica, V., Groy, T. L., Gust, D., Moore, T. A., and Moore, A. L. (2014) A bioinspired redox relay that mimics radical interactions of the Tyr-His pairs of photosystem II, *Nat Chem* 6, 423-428.
16. Jenson, D. L., Evans, A., and Barry, B. A. (2007) Proton-coupled electron transfer and tyrosine D of photosystem II, *J Phys Chem B* 111, 12599-12604.
17. Pagba, C. V., McCaslin, T. G., Chi, S. H., Perry, J. W., and Barry, B. A. (2016) Proton-Coupled Electron Transfer and a Tyrosine-Histidine Pair in a Photosystem II-Inspired beta-Hairpin Maquette: Kinetics on the Picosecond Time Scale, *J Phys Chem B* 120, 1259-1272.
18. Zhang, M. T., Irebo, T., Johansson, O., and Hammarstrom, L. (2011) Proton-coupled electron transfer from tyrosine: a strong rate dependence on intramolecular proton transfer distance, *J Am Chem Soc* 133, 13224-13227.
19. Manbeck, G. F., Fujita, E., and Concepcion, J. J. (2016) Proton-Coupled Electron Transfer in a Strongly Coupled Photosystem II-Inspired Chromophore-Imidazole-Phenol Complex: Stepwise Oxidation and Concerted Reduction, *J Am Chem Soc* 138, 11536-11549.
20. Englander, S. W., Calhoun, D. B., and Englander, J. J. (1987) Biochemistry without Oxygen, *Analytical Biochemistry* 161, 300-306.
21. Bell, C. B., Calhoun, J. R., Bobyr, E., Wei, P. P., Hedman, B., Hodgson, K. O., DeGrado, W. F., and Solomon, E. T. (2009) Spectroscopic Definition of the Biferrous and Biferric Sites in de Novo Designed Four-Helix Bundle DFsc Peptides: Implications for O-2 Reactivity of Binuclear Non-Heme Iron Enzymes, *Biochemistry* 48, 59-73.
22. Shrager, R. I., and Hendler, R. W. (1982) Titration of Individual Components in a Mixture with Resolution of Difference Spectra, Pks, and Redox Transitions, *Anal Chem* 54, 1147-1152.

23. Umena, Y., Kawakami, K., Shen, J. R., and Kamiya, N. (2011) Crystal structure of oxygen-evolving photosystem II at a resolution of 1.9 Å, *Nature* **473**, 55-60.
24. Kuroda, H., Kodama, N., Sun, X. Y., Ozawa, S., and Takahashi, Y. (2014) Requirement for Asn298 on D1 protein for oxygen evolution: analyses by exhaustive amino acid substitution in the green alga *Chlamydomonas reinhardtii*, *Plant Cell Physiol* **55**, 1266-1275.
25. Dautant, A., Meyer, J. B., Yariv, J., Precigoux, G., Sweet, R. M., Kalb, A. J., and Frolov, F. (1998) Structure of a monoclinic crystal form of cytochrome b₁ (Bacterioferritin) from *E. coli*, *Acta Crystallogr D Biol Crystallogr* **54**, 16-24.
26. Faiella, M., Andreozzi, C., de Rosales, R. T., Pavone, V., Maglio, O., Natri, F., DeGrado, W. F., and Lombardi, A. (2009) An artificial di-iron oxo-protein with phenol oxidase activity, *Nat Chem Biol* **5**, 882-884.
27. Conlan, B., Cox, N., Su, J. H., Hillier, W., Messinger, J., Lubitz, W., Dutton, P. L., and Wydrzynski, T. (2009) Photo-catalytic oxidation of a di-nuclear manganese centre in an engineered bacterioferritin 'reaction centre', *Biochim Biophys Acta* **1787**, 1112-1121.
28. Hingorani, K., Pace, R., Whitney, S., Murray, J. W., Smith, P., Cheah, M. H., Wydrzynski, T., and Hillier, W. (2014) Photo-oxidation of tyrosine in a bio-engineered bacterioferritin 'reaction centre'-a protein model for artificial photosynthesis, *Biochim Biophys Acta* **1837**, 1821-1834.
29. Bradley, J. M., Svistunenko, D. A., Lawson, T. L., Hemmings, A. M., Moore, G. R., and Le Brun, N. E. (2015) Three Aromatic Residues are Required for Electron Transfer during Iron Mineralization in Bacterioferritin, *Angew Chem Int Ed Engl* **54**, 14763-14767.
30. Reig, A. J., Pires, M. M., Snyder, R. A., Wu, Y., Jo, H., Kulp, D. W., Butch, S. E., Calhoun, J. R., Szyperski, T. G., Solomon, E. I., and DeGrado, W. F. (2012) Alteration of the oxygen-dependent reactivity of de novo Due Ferri proteins, *Nat Chem* **4**, 900-906.
31. Snyder, R. A., Butch, S. E., Reig, A. J., DeGrado, W. F., and Solomon, E. I. (2015) Molecular-Level Insight into the Differential Oxidase and Oxygenase Reactivities of de Novo Due Ferri Proteins, *J Am Chem Soc* **137**, 9302-9314.
32. Keech, A. M., Le Brun, N. E., Wilson, M. T., Andrews, S. C., Moore, G. R., and Thomson, A. J. (1997) Spectroscopic studies of cobalt(II) binding to *Escherichia coli* bacterioferritin, *J Biol Chem* **272**, 422-429.
33. Torres Martin de Rosales, R., Faiella, M., Farquhar, E., Que, L., Jr., Andreozzi, C., Pavone, V., Maglio, O., Natri, F., and Lombardi, A. (2010) Spectroscopic and metal-binding properties of DF3: an artificial protein able to accommodate different metal ions, *J Biol Inorg Chem* **15**, 717-728.
34. Calhoun, J. R., Bell, C. B., 3rd, Smith, T. J., Thamann, T. J., DeGrado, W. F., and Solomon, E. I. (2008) Oxygen reactivity of the biferrous site in the de novo designed four helix bundle peptide DFsc: nature of the "intermediate" and reaction mechanism, *J Am Chem Soc* **130**, 9188-9189.
35. Hingorani, K., Conlan, B., Hillier, W., and Wydrzynski, T. (2009) Elucidating Photochemical Pathways of Tyrosine Oxidation in an Engineered Bacterioferritin 'Reaction Centre', *Aust J Chem* **62**, 1351-1354.
36. Frolov, F., Kalb, A. J., and Yariv, J. (1994) Structure of a unique twofold symmetric haem-binding site, *Nat Struct Biol* **1**, 453-460.

37. Allen, J. P., Olson, T. L., Oyala, P., Lee, W. J., Tufts, A. A., and Williams, J. C. (2012) Light-driven oxygen production from superoxide by Mn-binding bacterial reaction centers, *Proc Natl Acad Sci U S A* 109, 2314-2318.
38. Kalman, L., Williams, J. C., and Allen, J. P. (2011) Energetics for oxidation of a bound manganese cofactor in modified bacterial reaction centers, *Biochemistry* 50, 3310-3320.
39. Sommer, D. J., Vaughn, M. D., Clark, B. C., Tomlin, J., Roy, A., and Ghirlanda, G. (2016) Reengineering cyt b562 for hydrogen production: A facile route to artificial hydrogenases, *Biochim Biophys Acta* 1857, 598-603.
40. Sommer, D. J., Vaughn, M. D., and Ghirlanda, G. (2014) Protein secondary-shell interactions enhance the photoinduced hydrogen production of cobalt protoporphyrin IX, *Chem Commun (Camb)* 50, 15852-15855.
41. Li, C. Z., Nishiyama, K., and Taniguchi, I. (2000) Electrochemical and spectroelectrochemical studies on cobalt myoglobin, *Electrochim Acta* 45, 2883-2888.
42. Fahnenschmidt, M., Bittl, R., Schlodder, E., Haehnel, W., and Lubitz, W. (2001) Characterization of de novo synthesized four-helix bundle proteins with metalloporphyrin cofactors, *Phys Chem Chem Phys* 3, 4082-4090.
43. Robertson, W. D., Bovell, A. M., and Warncke, K. (2013) Cobinamide production of hydrogen in a homogeneous aqueous photochemical system, and assembly and photoreduction in a (betaalpha)₈ protein, *J Biol Inorg Chem* 18, 701-713.

Chapter 5: Oxygen binding and alternative heme ligations

Light-driven water oxidation and hydrogen evolution will require fine-tuning of the properties of the various cofactors. One way to effect significant changes in heme redox properties is by altering the ligand sphere (1). Wild type MZH3 ligates the heme B iron ion using two histidine imidazole groups from His9 and His110 to form hexacoordinate iron. This bis-histidine ligation scheme is similar to the heme coordination found in cytochromes b and b₆ of the cytochrome bc₁ and b₆f complexes, where the heme is used for electron transfer functions (2, 3). Changes to the coordination in the MZH3 acceptor site could modulate heme B and cobalt protoporphyrin IX (CoPPIX) midpoint potentials and possibly enable hydrogen evolution activity from a cobalt tetrapyrrole.

Different heme ligation schemes in natural hemoproteins help to impart diverse functions. For example, P450 enzymes ligate heme with a cysteine residue (4), bovine liver catalase uses a tyrosinate ligand (5), cytochrome c and cytochrome b₅₆₂ use a His-Met ligation pattern (6, 7), and cytochrome f uses a histidine and an N-terminal amino group as heme ligands (8). Myoglobin and hemoglobin ligate heme B with only one histidine, and the other site is left open for a small molecule such as oxygen to bind (9, 10). This chapter will show heme B binding by MZH3 mutants in which acceptor site histidine residues were changed to either tyrosine, lysine, methionine, or alanine. The His110Ala mutant exhibits evidence of high-affinity oxygen binding and a slow rate of autoxidation, similar to myoglobin and hemoglobin.

5.1 MZH3 mutants bind heme B with ligands other than histidine

Wild type MZH3 ligates heme or CoPPIX in the electron acceptor site using His9 and His110, and this section presents heme binding by MZH3 mutants His9Cys, His110Cys, His9Lys, His9Tyr, His110Met, and His110Ala. All of these mutants retain the ability to bind heme B, as evidenced by their ultraviolet/visible (UV/vis) spectra. Unbound ferric heme B in aqueous solutions has a relatively weak, broad absorbance at about 390-395 nm, whereas all of the MZH3 heme site mutants exhibit strongly absorbing Soret bands between 407 and 424 nm. In addition, MZH3 heme site mutants bind heme B *in vivo* during overexpression in *E. coli*. Figure 5.1 shows absorbance spectra of MZH3 variants after cell lysis and purification by Ni-NTA column; no heme was added to these spectra.

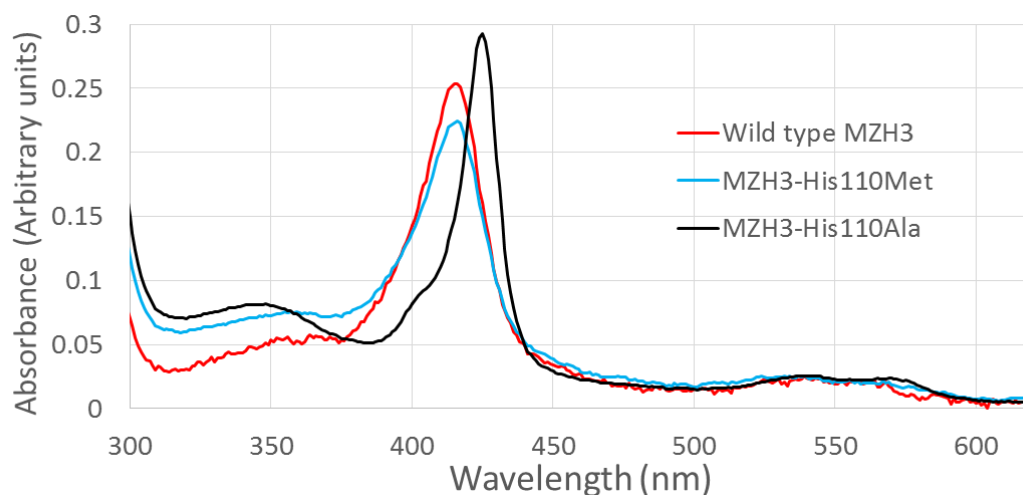


Figure 5.1: Heme B binds to MZH3 mutants His110Met and His110Ala *in vivo*

Conditions for wild type MZH3: 150 mM NaCl, 6 mM sodium phosphate, pH 7.4. Conditions for MZH3-His110Met and His110Ala mutants: 100 mM NaCl, 600 μ M EDTA, 30 mM Tris buffer, pH 8.0. (His₆ tags of the mutants had not yet been cleaved by TEV protease when these spectra were collected, but the wild type MZH3 did have its His₆ tag cleaved. Subsequent studies showed that the His₆ tag does not affect the spectrum).

Figure 5.2 shows the spectra of three more MZH3 variants with ferric heme bound. These spectra were collected after adding heme B to the maquettes *in vitro*.

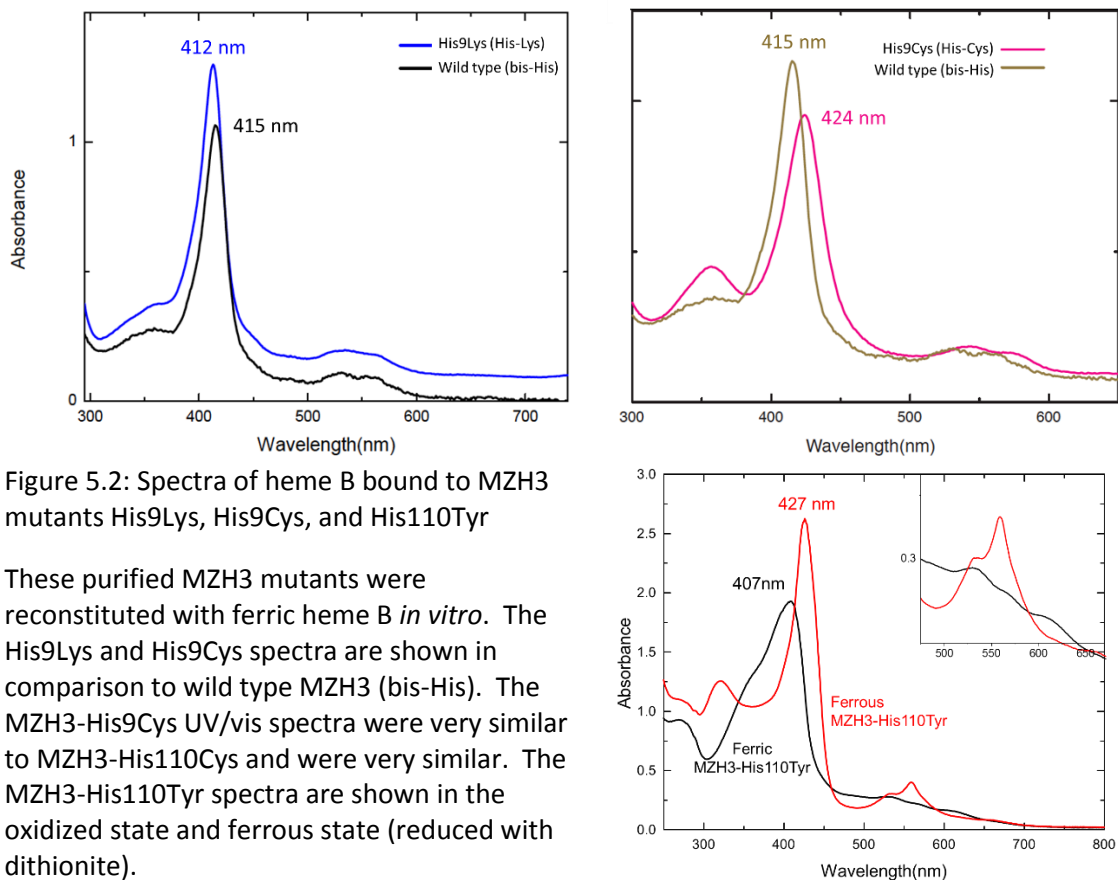


Figure 5.2: Spectra of heme B bound to MZH3 mutants His9Lys, His9Cys, and His110Tyr

These purified MZH3 mutants were reconstituted with ferric heme B *in vitro*. The His9Lys and His9Cys spectra are shown in comparison to wild type MZH3 (bis-His). The MZH3-His9Cys UV/vis spectra were very similar to MZH3-His110Cys and were very similar. The MZH3-His110Tyr spectra are shown in the oxidized state and ferrous state (reduced with dithionite).

In Figure 5.1 and Figure 5.2, absorbance is shown in arbitrary units, because extinction coefficients of heme B in MZH3 mutants have not been determined. Assuming similar heme extinction coefficients in the different mutants, roughly 5-10% of samples of MZH3-His110Met and His110Ala contained heme B from *E. coli* after lysis and purification by Ni-NTA column. MZH3-His9Lys appeared to overexpress with approximately 15-20% heme B incorporation (data not shown). The fact that MZH3 binds heme B *in vivo* similarly regardless of the ligation state indicates that heme binding is not wholly dependent upon coordination by ligating amino acids; other factors such as the shape of the binding pocket play a significant role in heme binding in MZH3.

Of particular interest is the fact that heme binds to MZH3-His110Ala, which only has one histidine in the heme binding site. Previous maquettes from the Dutton group lacked the ability to bind heme B using only one histidine instead of two, and this feature has been used to create tetrapyrrole binding sites that select for zinc tetrapyrroles over iron tetrapyrroles (11, 12). In addition, the heme B of MZH3-His110Ala remains in a reduced ferrous state even after several hours of exposure to oxygen during cell lysis, Ni-NTA column purification, and dialysis. Ferric heme B in MZH3-His110Ala has a Soret absorbance band at 415 nm, but Figure 5.1 (black trace) shows that the Soret absorbance of MZH3-His110Ala is 425 nm immediately after purification, which is consistent with an oxygen-bound oxyferrous state (1, 12). Other heme binding maquettes, including other MZH3 variants, are rapidly oxidized in the presence of oxygen. The oxyferrous MZH3-His110Ala species will be examined more closely in section 5.3.

5.2 Heme B midpoint potentials in MZH3 mutants

Alteration of heme-ligating amino acids can lead to new functions by changing the midpoint potential of the heme. The midpoint potentials of iron porphyrins are particularly sensitive to the ligating amino acids, presumably because the redox active electron in iron porphyrins is localized to the iron ion; in some cases, amino acid substitutions can lead to midpoint potential shifts of over 600 mV (13). Using a honeycomb spectroelectrochemical cell (Pine Research Instrumentation), heme B midpoint potentials were determined for wild type MZH3 and the mutants His9Lys, His9Tyr, His110Met, and His110Ala at pH 7.5. The methods used for the spectroelectrochemical midpoint determinations are detailed in the appendix.

To demonstrate reproducibility, the midpoint potential of wild type MZH3 (with bis-His heme ligation) was measured using the spectroelectrochemical honeycomb apparatus and the

result was compared to the redox titration method described in section 2.2.9. The redox titration previously showed a reversible one-electron transfer event at a midpoint of -180 mV (Figure 2.22). Figure 5.3 shows that the results from the honeycomb spectroelectrochemical cell are in agreement with the redox titration result. The heme redox spectrum from the

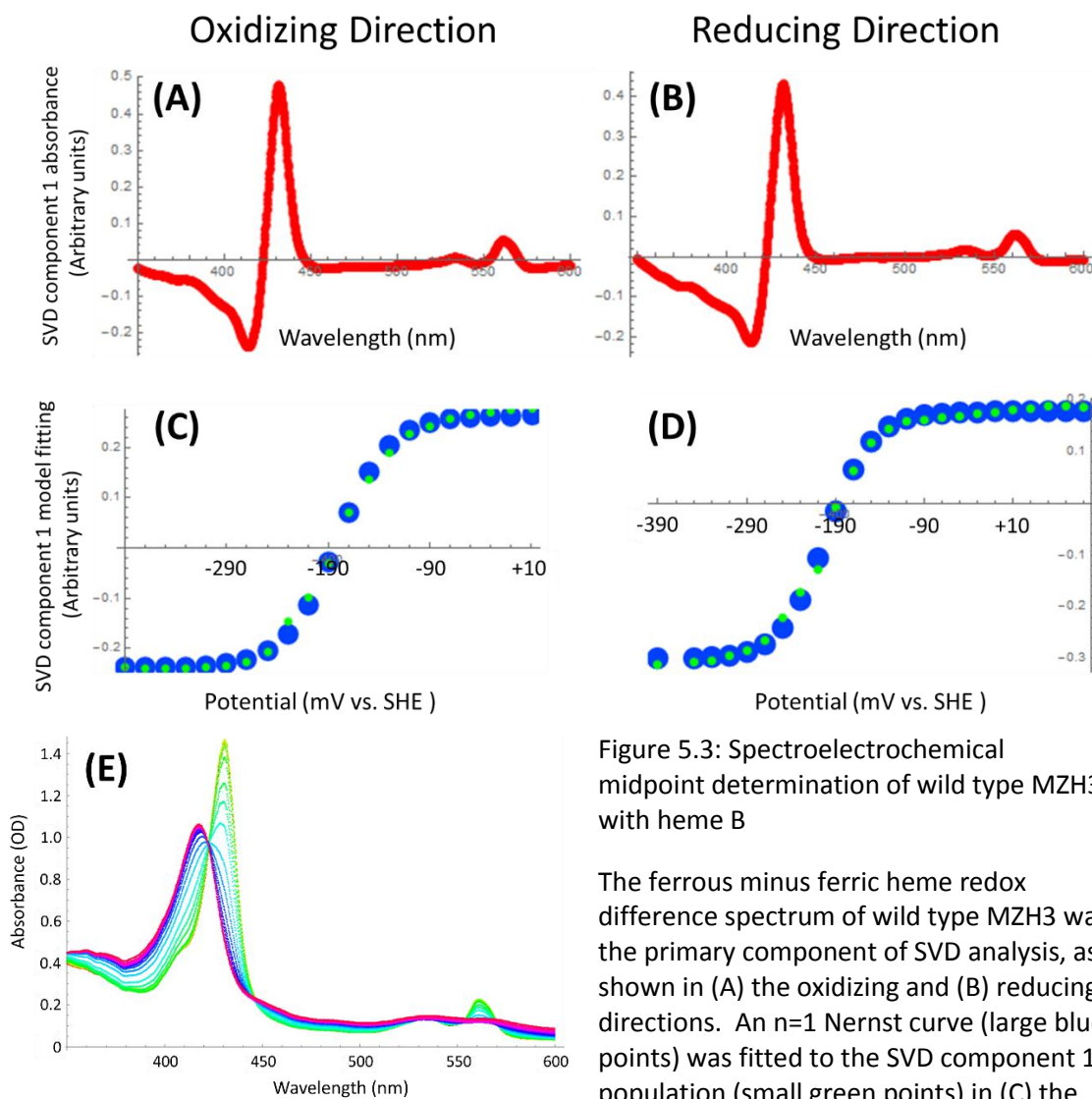


Figure 5.3: Spectroelectrochemical midpoint determination of wild type MZH3 with heme B

The ferrous minus ferric heme redox difference spectrum of wild type MZH3 was the primary component of SVD analysis, as shown in (A) the oxidizing and (B) reducing directions. An $n=1$ Nernst curve (large blue points) was fitted to the SVD component 1 population (small green points) in (C) the oxidizing and (D) reducing directions. (E): Absorbance spectra from the oxidizing scan going from high potentials (ferric heme, purple traces) to low potentials (ferrous heme, green traces).

spectroelectrochemical measurement was identified by SVD and fitted to a Nernst equation that gave a one-electron reaction with a potential of about -183 mV in the oxidizing direction and -195 mV in the reducing direction, demonstrating negligible hysteresis. The estimate of -190 mV using the spectroelectrochemical cell is within error of the -180 mV value from the redox titration.

The spectroelectrochemical apparatus was used to determine midpoint potentials of MZH3 mutants including MZH3-His110Ala (Figure 5.4). As with the wild type, MZH3-His110Ala showed no sign of hysteresis, and Figure 5.4 shows the data from both the reducing and oxidizing directions analyzed together. The low reducing potentials created an anaerobic environment, and there was no sign of an oxygen-bound ferrous heme state in the reduced spectra of Figure 5.4 (C); note the difference in Q-band shape between 500 and 600 nm in Figure 5.1 (black trace) compared to Figure 5.4 (C) (blue and purple traces). (This is shown more clearly in Figure 5.5A). The midpoint potential of heme B bound to MZH3-His110Ala was estimated at -110 mV vs. SHE.

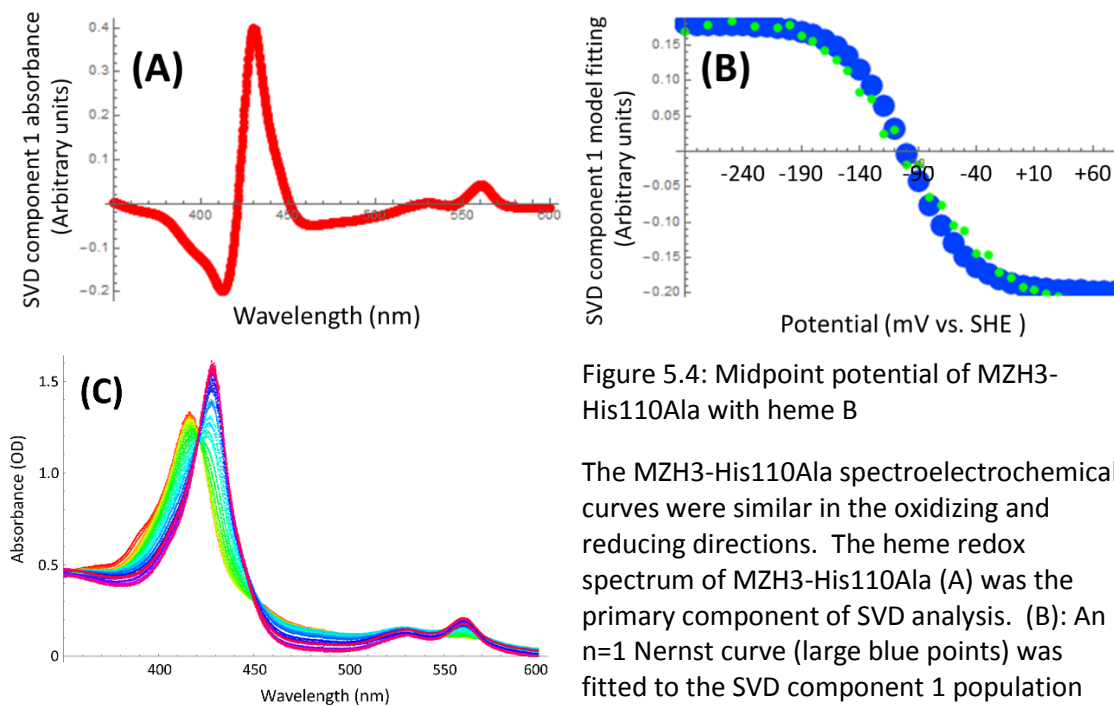


Figure 5.4: Midpoint potential of MZH3-His110Ala with heme B

The MZH3-His110Ala spectroelectrochemical curves were similar in the oxidizing and reducing directions. The heme redox spectrum of MZH3-His110Ala (A) was the primary component of SVD analysis. (B): An $n=1$ Nernst curve (large blue points) was fitted to the SVD component 1 population (small green points). Absorbance spectra from the oxidizing scan going from low potentials (ferric heme, red traces) to high potentials (ferrous heme, purple traces).

In contrast to other mutants, heme B in MZH3-His110Met exhibited signs of hysteresis. A partially reversible midpoint potential was observed at +70 mV vs. SHE, but in the reducing direction, there was a second distinct midpoint at approximately -80 mV. This secondary -80 mV potential may represent a state similar to the MZH3-His110Ala ligation state in which the protein contributes only one amino acid ligand and the potential is -110 mV. The fact that this secondary low potential transition is only observed in the reducing direction may be because methionine is a soft ligand that forms a stable interaction with the soft Lewis acid Fe(II) of ferrous heme, but has a much weaker affinity for the hard Lewis acid Fe(III) of ferric heme. The increased affinity of methionine ligands for ferrous heme over ferric heme has been shown to stabilize the reduced state in other His-Met hemoproteins (14). The MZH3-His9Lys and His9Tyr

mutants were found to have reversible Nernstian one-electron transfer events at midpoint potentials of -65 mV and -180 mV, respectively. The MZH3 mutant spectroelectrochemistry results are summarized in Table 5.1.

MZH3 variant	Ligation Pattern	Natural Protein	Abs Peaks Natural (nm)	Abs Peaks Maquette (nm)	Em (mV)
Wild type	His (●) His	Neuroglobin	426, 560 (red) 413, 529 (ox)	426, 560 (red) 412, 529 (ox)	-190
His9Cys/ His110Cys	His (●) Cys	Rr CooA, Cysathione b-synthase	422, 540, 570 360, 424, 535	421, 540, 570 360, 424, 535	not done
His110Met	His (●) Met	b562 Cyt c	430, 562 406, 534	429, 562 409, 529	70
His9Tyr	His (●) Tyr	Bovine liver catalase	436, 558 406, 534, 620	427, 558 407, 530, 615	-180
His9Lys	His (●) Lys	Cyt f (amino)	421, 554 412	427, 532, 560 414	-65
His110Ala	His (●) Ala	Myoglobin	435, 555 409, 505, 635	428, 530, 562 416, 531	-110

Table 5.1: Summary of heme B properties in different MZH3 mutants

The properties of heme B in MZH3 variants and natural proteins with similar ligation schemes are compared. Table is adapted from Moser et al., 2016 (1).

5.3 Oxygen binding in MZH3-His110Ala

Many important medical procedures depend on blood transfusion to save lives and improve health. The fact that this blood comes from voluntary donors means that healthcare systems are susceptible to blood shortages, and blood transfusions present the risk of transfusion-transmissible infections. An oxygen transport maquette that reproduces the function of hemoglobin or myoglobin could potentially provide a safe, inexpensive blood

substitute. This section examines the unexpected MZH3-His110Ala property of stable, high-affinity oxygen binding and the possibility of developing it into a novel blood substitute.

5.3.1 Introduction to oxygen transport proteins

Oxygen transport proteins including myoglobin and hemoglobin use ferrous heme B to bind oxygen at the heme iron; the oxidized ferric state cannot form a stable interaction with oxygen. The relatively low potential of heme B compared to oxygen means that the heme is vulnerable to oxidation to the inactive ferric state, and the protein environment must modulate the redox properties to prevent electron transfer. At room temperature, free heme B in aqueous solutions autooxidizes within seconds, but myoglobin and hemoglobin autooxidation takes hours or days (15, 16). Myoglobin and hemoglobin bind oxygen with dissociation constants in the hundreds of nanomolar range: 830 nM for sperm whale myoglobin (17).

Oxygen binding has been observed in *de novo*-designed maquettes and redesigned natural proteins. In these model systems, autooxidation is generally orders of magnitude faster than in myoglobin or hemoglobin. In one example, human serum albumin (HSA) was redesigned to introduce a heme B binding pocket. The modified HSA had an autooxidation lifetime of ~10 minutes, and its oxygen affinity in two different conformational states was 2.8 and 0.4% of the myoglobin oxygen affinity (17, 18). In a series of maquettes from the Dutton group, an oxyferrous state was identified with an autooxidation lifetime of seconds to tens of seconds at 16°C, and one maquette had an oxygen affinity that was 5% of the myoglobin oxygen affinity (12, 17, 19, 20). These results demonstrate significant progress toward a designed oxygen transport protein, but the oxyferrous stability and oxygen affinity must be increased significantly before such a protein could become useful for medical applications.

5.3.2 Oxygen binding results in MZH3-His110Ala

Natural oxygen transport proteins and previous oxygen binding maquettes show a clear difference in the UV/vis absorbance spectra in the ferric, deoxyferrous, carboxyferrous, and oxyferrous spectra. MZH3-His110Ala spectra at pH 7.5 (Figure 5.5A) are similar to those of the earlier maquette BT6, which binds two hemes B via bis-histidine ligation and is able to bind oxygen and carbon monoxide (Figure 5.5B) (12). In both MZH3-His110Ala and BT6, anaerobic reduction of ferric heme (green traces) to deoxyferrous heme (blue traces) yields a significant red shift in the Soret band from ~412-415 nm to ~426-431 nm and a significant sharpening and increase in the intensity of the Q-bands at ~530 and ~560 nm. Exposure of the deoxyferrous species to oxygen produces the oxyferrous state (red traces), and exposure to carbon monoxide produces the carboxyferrous state (black traces). The oxyferrous and carboxyferrous spectra have Soret bands that peak between the ferric and deoxyferrous Soret peaks and Q-bands that are red-shifted and are more pronounced than the ferric Q-bands but less pronounced than the deoxyferrous Q-bands. Further confirmation that MZH3-His110Ala binds oxygen comes from comparison to spectra of bovine myoglobin (purchased from Sigma). Figure 5.5C shows the deoxyferrous minus oxyferrous difference absorbance spectra of myoglobin (orange) and MZH3-His110Ala (black). While the relative intensities of the absorption bands differ slightly, the wavelengths of each band and the overall shapes of the spectra are similar.

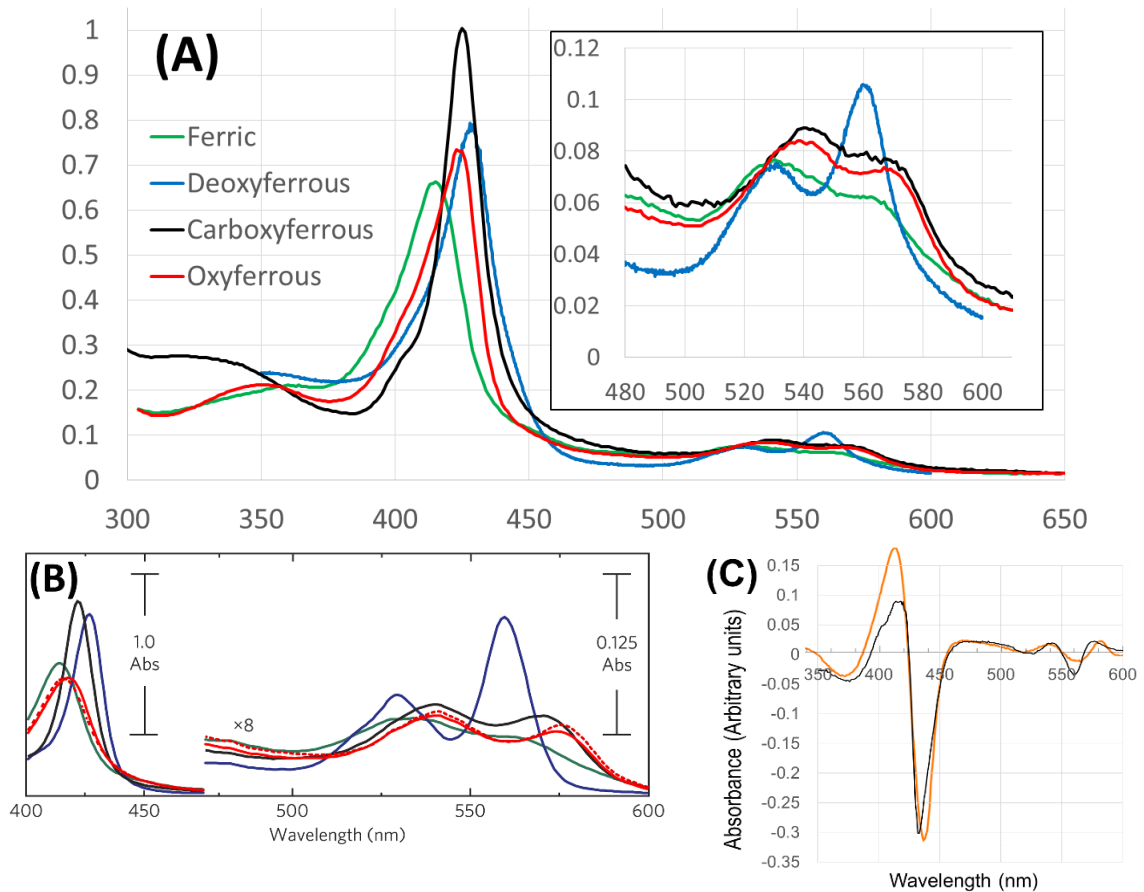


Figure 5.5: Ferric, deoxyferrous, carboxyferrous, and oxyferrous spectra

(A): MZH3-His110Ala spectra are shown with heme B in ferric (green), deoxyferrous (blue), carboxyferrous (black), and oxyferrous (red) states. Samples were prepared in 50 mM NaCl, 10 mM MOPS buffer at pH 7.5 and are scaled to approximately the same concentration ($\sim 6 \mu\text{M}$). Inset: Q-band region of MZH3-His110Ala spectra. (B): Reference spectra reproduced from earlier bis-His two-heme maquette BT6 publication (Farid et al., 2013) (12), following same color scheme as in (A). (The dotted red line is the oxyferrous species with only one heme B bound to BT6 instead of two). (C): Deoxyferrous minus oxyferrous difference spectra of myoglobin (orange trace) and MZH3-His110Ala (black trace).

The seconds to minutes lifetimes of oxyferrous states of earlier designed oxygen transport proteins is too short for a blood substitute (12, 17-20), but the oxyferrous state of MZH3-His110Ala is detectable for hours after cell lysis and protein purification (Figure 5.1). In order to determine the rate of autooxidation, oxyferrous MZH3-His110Ala was prepared by reduction of $\sim 10 \mu\text{M}$ ferric MZH3-His110Ala with 10 mM ascorbate in 50 mM NaCl, 10 mM

MOPS buffer at pH 7.5 at room temperature. Reduction with ascorbate was slow, probably because of the relatively low heme B midpoint potential of MZH3-His110Ala of -110 mV vs SHE. After one hour, reduction was complete, and ascorbate was removed by filtration through a PD-10 desalting column (GE Healthcare Lifesciences). The ~ 6 μ M sample was exposed to ambient oxygen and UV/vis spectra were recorded every 0.25 to 4 hours for about 4 days. SVD fitting identified two spectral components that were similar to the oxyferrous and ferric species shown in Figure 5.5A. The oxyferrous lifetime was about 38 hours (Figure 5.6).

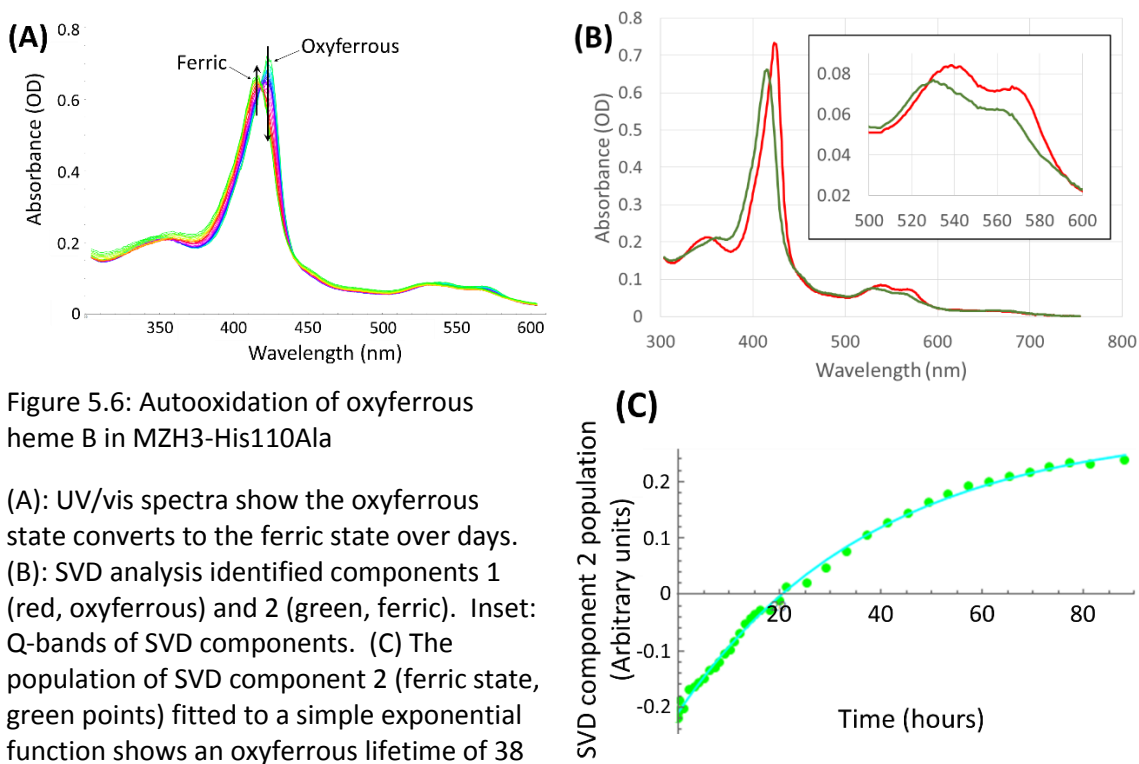


Figure 5.6: Autooxidation of oxyferrous heme B in MZH3-His110Ala

(A): UV/vis spectra show the oxyferrous state converts to the ferric state over days. (B): SVD analysis identified components 1 (red, oxyferrous) and 2 (green, ferric). Inset: Q-bands of SVD components. (C) The population of SVD component 2 (ferric state, green points) fitted to a simple exponential function shows an oxyferrous lifetime of 38 hours.

There is no requirement for a blood substitute to use heme B, and other iron tetrapyrrole cofactors might be preferable to heme B. MZH3 binds the higher potential Fe(III) 2,4-diacetyl deuteroporphyrin IX (Fe-DADPIX) with high affinity, as described in section 2.3.3. As with heme B, MZH3-His110Ala is able to stabilize an oxyferrous state of Fe-DADPIX. A sample of

30 μM MZH3-His110Ala bound to Fe-DADPIX was incubated with 150 μM ascorbate for several hours to prepare the oxyferrous state, and ascorbate was removed using a PD-10 column. The sample was kept exposed to ambient oxygen at room temperature at pH 7.5, and autooxidation was monitored by the decay of the Fe-DADPIX oxyferrous Soret band at 447 nm for 6 days. About $\sim 8\%$ of the MZH3-His110Ala sample contained heme B leftover from expression instead of Fe-DADPIX, but the absorbance difference between the ferric and oxyferrous states of heme B is very small at 447 nm. Fitting the autooxidation curve at 447 nm with a simple exponential fit gave an Fe-DADPIX oxyferrous lifetime of ~ 80 hours, or 3.3 days (Figure 5.7).

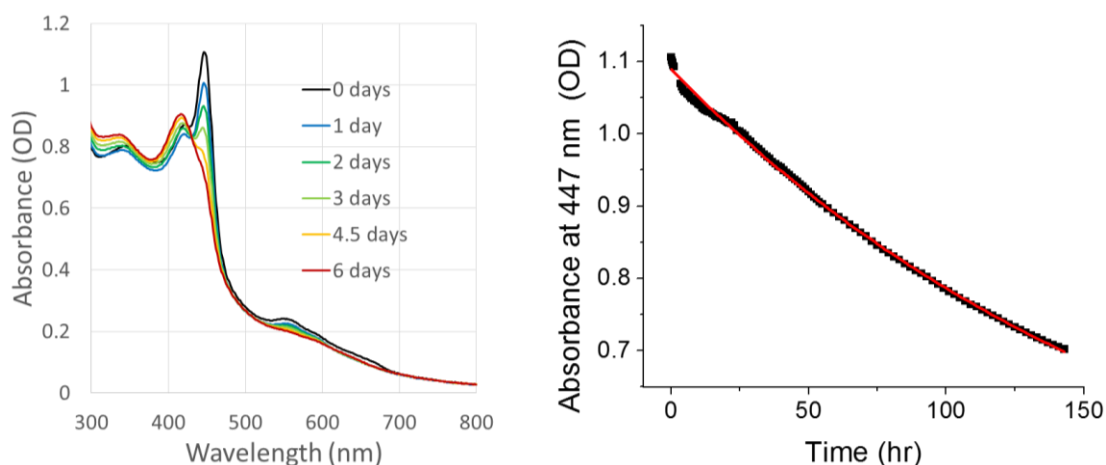


Figure 5.7: Autooxidation of oxyferrous Fe-DADPIX in MZH3-His110Ala

Left: Absorbance spectra of MZH3-His110Ala with Fe-DADPIX at selected time points after beginning the autooxidation reaction. Right: Absorbance at 447 nm fitted to a single exponential curve gives oxyferrous Fe-DADPIX lifetime of roughly 80 hours or 3.3 days.

Carbon monoxide tends to bind to ferrous heme more tightly than oxygen, so introduction of carbon monoxide should be able to convert oxyferrous MZH3-His110Ala to the carboxyferrous state. The carboxyferrous and oxyferrous spectra are similar, but can be distinguished by the large difference in the extinction coefficient of the Soret band (see Figure 5.5A, black and red traces, respectively). To test for the displacement of oxygen by carbon

monoxide, a 1 mL sample of MZH3-His110Ala with ferric heme B was degassed and reduced with dithionite. Addition of 15 μ L of water containing ambient oxygen led to a mixture of ferric and oxyferrous MZH3-His110Ala. About 10 mL of carbon monoxide gas was bubbled through the anaerobic sample, and a slow increase in the Soret band at 425 nm was monitored over the ensuing 40 minutes. After 40 minutes, more dithionite was added to sample to reduce the oxygen and ferric heme B. The result was an immediate significant increase in the Soret absorbance at 425 nm corresponding to rapid binding of carbon monoxide to ferrous heme B. The result in Figure 5.8 shows that the presence of oxygen inhibited carbon monoxide binding to MZH3-His110Ala, limiting its binding rate to tens of minutes. When oxygen was eliminated by reduction with dithionite, carbon monoxide binding was complete within seconds.

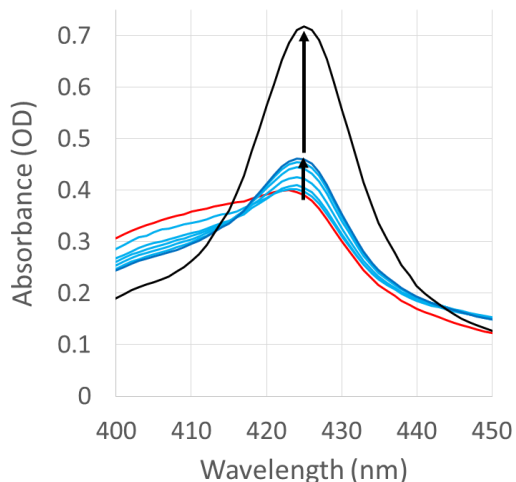


Figure 5.8: Displacement of oxygen ligand by carbon monoxide in MZH3-His110Ala with ferrous heme B

UV/vis spectra show slow carbon monoxide binding when oxygen is present and fast carbon monoxide binding once oxygen is reduced. Red trace: mixture of oxyferrous and ferric heme B. Blue traces: after adding carbon monoxide, Soret band slowly rose over 40 minutes in the direction of the arrow. Spectrum after 40 minutes is shown in slightly darker blue. Black trace: addition of dithionite reduced ferric heme B and eliminated oxygen, allowing rapid carbon monoxide binding in seconds or less.

Nature calibrated the dissociation constants of oxygen binding by myoglobin and hemoglobin to be in the hundreds of nanomolar range (17, 21-23) so that these proteins can bind oxygen from oxygen-rich environments and release it in oxygen-poor environments. To probe the oxygen affinity of MZH3-His110Ala, a 5.6 μ M sample in 50 mM NaCl, 10 mM MOPS

buffer at pH 7.5 was degassed for 3.5 hours with argon that was bubbled through an acid vanadyl sulfate-granular zinc oxygen scrubbing gas train (24). An ascorbate stock solution was purged similarly, and ascorbate was added to the sample to a 500 μM final concentration at time $t=0$ in Figure 5.9, below. The sample was purged continuously with argon throughout the experiment. A peak began to increase at the oxyferrous Soret band wavelength of 425 nm. No sign of a deoxyferrous state with a sharp Q-band feature at 560 nm was observed. Presumably, oxyferrous formation was allowed by a slow leakage of oxygen into the cuvette. After 15 hours, the rate of increase of absorbance at 425 nm had leveled off, and the cuvette was opened and exposed to ambient oxygen. The oxyferrous spectrum decreased slightly, then increased to a maximum after about 28 hours, showing that the oxyferrous spectrum depends on the presence of oxygen.

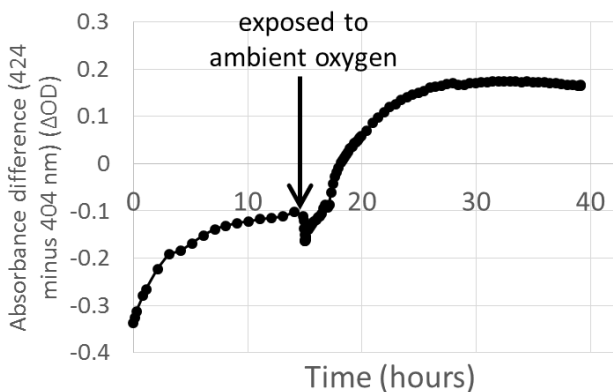


Figure 5.9: Oxyferrous state formation in MZH3-His110Ala during anaerobic argon purging

500 μM ascorbate was added to MZH3-His110Ala with ferric heme B at time $t=0$. The absorbance difference of 424 minus 404 nm represents the rise of the oxyferrous state. At the arrow, the anaerobic cuvette was opened and the sample was exposed to ambient oxygen. Conditions: 50 mM NaCl, 10 mM MOPS buffer, pH 7.5.

In the first 15 hours of the experiment in Figure 5.9, the solution was purged continuously with anaerobic argon, but the oxyferrous spectrum increased and was stable, suggesting that the dissociation constant for the MZH3-His110Ala-heme B-oxygen complex was less than the concentration of dissolved oxygen under these low-oxygen conditions. The oxyferrous state was also stable for many hours if a glucose oxidase/catalase oxygen scrubbing

system was introduced to the sample or if a weak vacuum was applied to the cuvette. These results show that the affinity of MZH3-His110Ala for oxygen is greater than that of hemoglobin or myoglobin, which release oxygen under low-oxygen conditions. Preliminary experiments suggest that deoxyferrous MZH3-His110Ala is able to absorb oxygen from oxyferrous myoglobin. This would indicate that the dissociation constant for oxygen binding by deoxyferrous MZH3-His110Ala is less than hundreds of nanomolar. More work is need to determine a precise dissociation constant.

5.3.3 Oxygen binding conclusions and future directions

The results presented here demonstrate that MZH3-His110Ala with heme B binds oxygen. The stability of the oxyferrous state is 38 hours at room temperature at pH 7.5; the autooxidation rate is orders of magnitude slower than the rates observed in earlier maquettes and redesigned natural proteins (12, 18-20). This 38 hour lifetime at room temperature is comparable to the hours to days lifetimes of various myoglobins and hemoglobins under similar conditions (15, 16). For example, at pH 7.2 and 25°C, sperm whale oxymyoglobin is stable for 150 hours (16, 25), *Aplysia kurodai* myoglobin autooxidizes in 9 hours (25), and the chicken gizzard oxymyoglobin lifetime is 59 hours (26). In addition, preliminary results suggest that the oxygen affinity of MZH3-His110Ala appears to exceed that of maquettes, redesigned natural proteins, and even natural myoglobins and hemoglobins by orders of magnitude. Extensive purging with anaerobic argon does not convert oxyferrous MZH3-His110Ala to the deoxyferrous state even over the course of hours.

It is not surprising that MZH3-His110Ala can bind oxygen; after all, several maquettes and redesigned natural proteins have already demonstrated this ability, and MZH3-His110Ala

has only one amino acid ligand available to ligate the heme iron, and the other site is left open. However, the high oxygen affinity of MZH3-His110Ala and its oxyferrous state stability are very much unexpected, and deserve explanation. The crystal structures of wild type MZH3, which has bis-histidine heme B ligation, show low solvent access to the heme iron. It is likely that the MZH3-His110Ala mutant is similar. A dry hydrophobic core might increase the oxygen affinity because water molecules do not need to be displaced for oxygen to bind (15). The BT6 maquette and related mutants demonstrated that water access to the heme increases the rate of autooxidation via water-catalyzed inner sphere electron transfer (12). However, solvent inaccessibility alone cannot account for the extremely high affinity and stability observed in oxyferrous MZH3-His110Ala.

Natural myoglobins and hemoglobins usually form a hydrogen bond between the oxygen ligand and a distal histidine on helix E, HisE7 (27). This hydrogen bonding interaction plays a pivotal role in stabilizing the oxyferrous state. The oxygen is the hydrogen bond acceptor and the histidine donates a hydrogen bond from the protonated N_ε atom. While myoglobins tend to remain functional when HisE7 is replaced by glutamine, which may also donate a hydrogen bond to oxygen, many substitutions to the E7 position result in a catastrophic increase in autooxidation rate and decrease in binding affinity (15). For example, the HisE7Gly mutation in sperm whale myoglobin accelerates autooxidation from a lifetime of 150 hours to 17 minutes (16) and decreases the oxygen affinity from 830 nM to 11 μM (17). Similar results are observed for other mutations at the E7 position (15). These HisE7 mutations weaken the oxygen binding and oxyferrous stability of myoglobin to the level of oxygen binding maquettes and redesigned natural proteins, which have lifetimes and dissociation constants on

the orders of seconds to minutes and tens of micromolar, respectively (12, 18-20). These designed proteins are presumed not to have an oxygen-amino acid hydrogen bond.

Crystal structures of wild type bis-His MZH3 show that there are two hydrogen bond donors in helix 2 that could potentially form a hydrogen bond to a bound oxygen molecule in MZH3-His110Ala (Figure 5.10). The backbone amide of Gly92 and the hydroxyl group of Thr91 are both relatively close to where oxygen might be expected to bind (~3.5-4 Å). The Gly92 amide N-H group is perpendicular to the direction of the heme iron, and might not have the proper geometry to form a stable hydrogen bond with a bound oxygen ligand. However, Thr91, which makes a stable 2.8 Å hydrogen bond with heme-ligating His110 in wild type MZH3, appears to have about the right distance and geometry to make a hydrogen bonding contact with a bound oxygen molecule. The absence of a ligating His110 in MZH3-His110Ala might result in a change in conformation that brings the threonine hydroxyl closer to the heme iron to

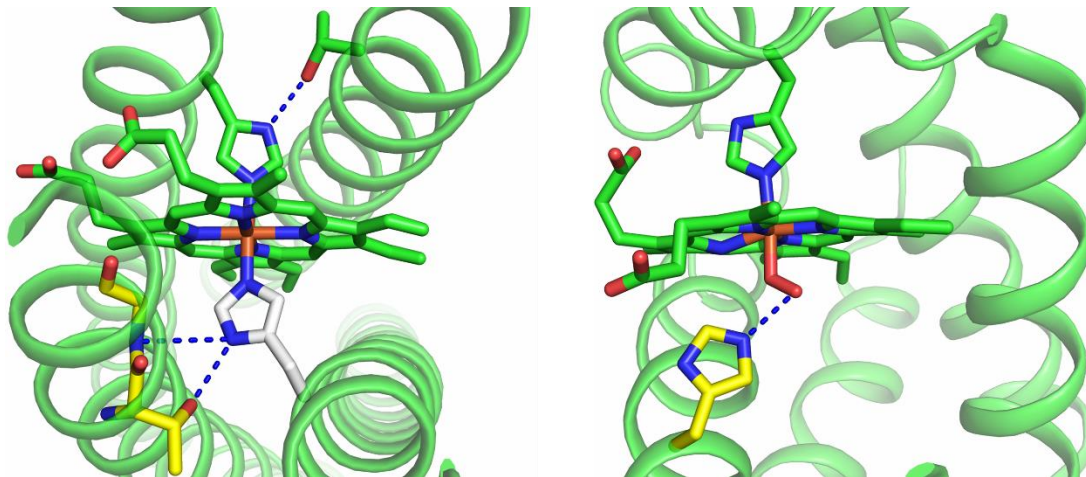


Figure 5.10: Possible H-bond to O₂ in oxyferrous MZH3-His110Ala akin to HisE7-O₂ H-bond of myoglobin

Left: Wild type MZH3 crystal structure CS-D shown with His110 carbons in white and Thr91 and Gly92 carbons in yellow. Thr91 or Gly92 might form a hydrogen bond to bound oxygen in MZH3-His110Ala. Right: Crystal structure of human myoglobin in oxyferrous state shows HisE7 with yellow carbons making hydrogen bond to bound oxygen molecule. Structure is from PDB-ID: 1MBO (9). Images rendered using The PyMOL Molecular Graphics System, Version 1.7 Schrödinger, LLC.

make a hydrogen bond closer to the His-O₂ hydrogen bond length found in natural myoglobins of ~2.8 Å (9, 28).

Future work on oxygen transport in MZH3 should be directed toward fine tuning the dissociation constant for oxygen binding so that it better resembles natural myoglobins and hemoglobins. The dissociation constant for MZH3-His110Ala should be determined precisely, followed by mutagenesis studies to elucidate the source of the high oxygen affinity and long oxyferrous lifetime. For example, study of a Thr91Val or Thr91Ala mutant might show whether Thr91 plays an important role in stabilizing the oxyferrous state. Given the stability of the complex and the fact that wild type MZH3 is readily crystallizable, it may be possible to solve the structure of oxyferrous MZH3-His110Ala by X-ray crystallography.

5.4 References

1. Moser, C. C., Sheehan, M. M., Ennist, N. M., Kodali, G., Bialas, C., Englander, M. T., Discher, B. M., and Dutton, P. L. (2016) De Novo Construction of Redox Active Proteins, *Methods Enzymol* 580, 365-388.
2. Esposti, M. D., De Vries, S., Crimi, M., Ghelli, A., Patarnello, T., and Meyer, A. (1993) Mitochondrial cytochrome b: evolution and structure of the protein, *Biochim Biophys Acta* 1143, 243-271.
3. Stroebel, D., Choquet, Y., Popot, J. L., and Picot, D. (2003) An atypical haem in the cytochrome b(6)f complex, *Nature* 426, 413-418.
4. Meunier, B., de Visser, S. P., and Shaik, S. (2004) Mechanism of oxidation reactions catalyzed by cytochrome p450 enzymes, *Chem Rev* 104, 3947-3980.
5. Bandara, D. M., Sono, M., Bruce, G. S., Brash, A. R., and Dawson, J. H. (2011) Coordination modes of tyrosinate-ligated catalase-type heme enzymes: magnetic circular dichroism studies of *Plexaura homomalla* allene oxide synthase, *Mycobacterium avium* ssp. *paratuberculosis* protein-2744c, and bovine liver catalase in their ferric and ferrous states, *J Inorg Biochem* 105, 1786-1794.
6. Mathews, F. S., Bethge, P. H., and Czerwinski, E. W. (1979) The structure of cytochrome b562 from *Escherichia coli* at 2.5 Å resolution, *J Biol Chem* 254, 1699-1706.
7. Tanaka, N., Yamane, T., Tsukihara, T., Ashida, T., and Kakudo, M. (1975) The crystal structure of bonito (katsuo) ferrocytochrome c at 2.3 Å resolution. II. Structure and function, *J Biochem* 77, 147-162.

8. Martinez, S. E., Huang, D., Szczepaniak, A., Cramer, W. A., and Smith, J. L. (1994) Crystal structure of chloroplast cytochrome f reveals a novel cytochrome fold and unexpected heme ligation, *Structure* 2, 95-105.
9. Phillips, S. E. V. (1980) Structure and Refinement of Oxymyoglobin at 1.6-Å Resolution, *Journal of Molecular Biology* 142, 531-554.
10. Shaanan, B. (1983) Structure of human oxyhaemoglobin at 2.1 Å resolution, *J Mol Biol* 171, 31-59.
11. Sharp, R. E., Diers, J. R., Bocian, D. F., and Dutton, P. L. (1998) Differential binding of iron(III) and zinc(II) protoporphyrin IX to synthetic four-helix bundles, *Journal of the American Chemical Society* 120, 7103-7104.
12. Farid, T. A., Kodali, G., Solomon, L. A., Lichtenstein, B. R., Sheehan, M. M., Fry, B. A., Bialas, C., Ennist, N. M., Siedlecki, J. A., Zhao, Z., Stetz, M. A., Valentine, K. G., Anderson, J. L., Wand, A. J., Discher, B. M., Moser, C. C., and Dutton, P. L. (2013) Elementary tetrahelical protein design for diverse oxidoreductase functions, *Nat Chem Biol* 9, 826-833.
13. Raphael, A. L., and Gray, H. B. (1991) Semisynthesis of Axial-Ligand (Position-80) Mutants of Cytochrome-C, *Journal of the American Chemical Society* 113, 1038-1040.
14. Tezcan, F. A., Winkler, J. R., and Gray, H. B. (1998) Effects of ligation and folding on reduction potentials of heme proteins, *Journal of the American Chemical Society* 120, 13383-13388.
15. Springer, B. A., Sligar, S. G., Olson, J. S., and Phillips, G. N. (1994) Mechanisms of Ligand Recognition in Myoglobin, *Chemical Reviews* 94, 699-714.
16. Suzuki, T., Watanabe, Y. H., Nagasawa, M., Matsuoka, A., and Shikama, K. (2000) Dual nature of the distal histidine residue in the autoxidation reaction of myoglobin and hemoglobin comparison of the H64 mutants, *Eur J Biochem* 267, 6166-6174.
17. Olson, J. S., Mathews, A. J., Rohlfs, R. J., Springer, B. A., Egeberg, K. D., Sligar, S. G., Tame, J., Renaud, J. P., and Nagai, K. (1988) The role of the distal histidine in myoglobin and haemoglobin, *Nature* 336, 265-266.
18. Komatsu, T., Ohmichi, N., Zunszain, P. A., Curry, S., and Tsuchida, E. (2004) Dioxygenation of human serum albumin having a prosthetic heme group in a tailor-made heme pocket, *J Am Chem Soc* 126, 14304-14305.
19. Zhang, L., Andersen, E. M., Khajo, A., Magliozzo, R. S., and Koder, R. L. (2013) Dynamic factors affecting gaseous ligand binding in an artificial oxygen transport protein, *Biochemistry* 52, 447-455.
20. Koder, R. L., Anderson, J. L., Solomon, L. A., Reddy, K. S., Moser, C. C., and Dutton, P. L. (2009) Design and engineering of an O₂ transport protein, *Nature* 458, 305-309.
21. Gibson, Q. H. (1970) The reaction of oxygen with hemoglobin and the kinetic basis of the effect of salt on binding of oxygen, *J Biol Chem* 245, 3285-3288.
22. Olson, J. S., Andersen, M. E., and Gibson, Q. H. (1971) The dissociation of the first oxygen molecule from some mammalian oxyhemoglobins, *J Biol Chem* 246, 5919-5923.
23. Steinmeier, R. C., and Parkhurst, L. J. (1975) Kinetic studies on the five principal components of normal adult human hemoglobin, *Biochemistry* 14, 1564-1572.
24. Englander, S. W., Calhoun, D. B., and Englander, J. J. (1987) Biochemistry without Oxygen, *Analytical Biochemistry* 161, 300-306.
25. Shikama, K., and Matsuoka, A. (1986) Aplysia Oxymyoglobin with an Unusual Stability Property - Kinetic-Analysis of the Ph-Dependence, *Biochemistry* 25, 3898-3903.

26. Matsuoka, A., Iwaasa, H., Takiguchi, K., Arakawa, N., Li, L., Takagi, T., and Shikama, K. (1987) Stability properties of oxymyoglobin from chicken gizzard smooth muscle, *Comp Biochem Physiol B* 88, 783-789.
27. Phillips, S. E., and Schoenborn, B. P. (1981) Neutron diffraction reveals oxygen-histidine hydrogen bond in oxymyoglobin, *Nature* 292, 81-82.
28. Unno, M., Chen, H., Kusama, S., Shaik, S., and Ikeda-Saito, M. (2007) Structural characterization of the fleeting ferric peroxo species in myoglobin: experiment and theory, *J Am Chem Soc* 129, 13394-13395.

Chapter 6: Conclusion

In this thesis, a photosynthetic reaction center maquette has been designed that can assemble iron and cobalt tetrapyrroles as electron acceptors, various zinc tetrapyrroles as pigments, and tyrosine and metal ions as electron donors. MZH3 is a singularly structured and highly stable canonical left-handed four-helix coiled coil with high affinity for all of its designated cofactors. High resolution X-ray crystal structures show that all of the intended cofactors bind to MZH3 simultaneously, and that MZH3 shares a high degree of structural similarity with the natural four-helix bundle proteins cytochrome b and bacterioferritin, despite low sequence identity. Transient absorption results indicate that MZH3 traps a charge separated state involving ferrous heme B and a tyrosyl radical for up to 150 ms at pH 7.5. In addition, binding of ferrous iron allows MZH3 to hold heme reduced for 300 ms at pH 7.5 before recombination. An unexpected oxygen binding function was also detected in an MZH3 mutant. The MZH3-His110Ala mutation led to a stable oxyferrous heme state with a lifetime comparable to natural myoglobins and hemoglobins and with higher oxygen affinity than the natural proteins. These results offer new perspectives on four-helix bundle design and advance the field toward more sophisticated functions.

6.1 Four-helix bundle protein design strategy

Robertson et al. described the first *de novo* hemoprotein in 1994 (1). Since then, a number of groups have pursued high resolution structural characterization of porphyrin binding maquettes, and some have solved apo-state structures that lend insight into the structure-

function relationship of four-helix bundle heme maquettes (2-4). Until now, holo-state structures have not been reported. Without experimental structures in the active state of the maquette, it is difficult to identify essential structural elements that give rise to function or to evaluate the degree to which maquettes fold into the intended structures.

The Dutton group has worked with a series of four-helix bundle maquettes designed by simple binary patterning to achieve diverse functions including light-driven electron transfer, iron-sulfur cluster assembly, inter-protein electron transfer, and oxygen binding (5-8). This binary patterning is appealing as a way to simplify the design approach and minimize the complexity of the sequence to tease out essential elements of the sequence-structure relationship. However, simple binary patterning alone does not always lead to singularly structured functional proteins, and it becomes less reliable in the design of increasingly complex proteins. Furthermore, simple sequences do not necessarily translate into simple structures; some maquettes lack the standard knob-into-hole interactions of coiled coils, fold with the uncommon mixed parallel/antiparallel helical topology, and have a slight right-handed, superhelical twist as opposed to the left-handed supercoil in normal coiled coils (2, 9). In addition, heme binding in some maquettes triggers a significant structural change that rotates the helices and buries glutamate residues (10). Many interesting functions have been achieved in this type of heme maquette, but the unusual structural properties and lack of a high resolution structure in the holo-state complicate our interpretation of the structure-function relationship and sometimes make redesign difficult. A more robust design procedure was necessary to design the multi-cofactor reaction center maquette MZH3.

In the successful design of MZH3, a broad and detailed view of the factors influencing protein structure was used to strike a balance between the stability needed to decrease the

entropic cost of cofactor binding, and flexibility, which is needed to decrease the enthalpic cost of binding (11-13). The sequence of the metal binding section of MZH3 was taken from Due Ferro proteins (14-16), but the tetrapyrrole binding section was designed from scratch. A truncated version of MZH3 that only has a tetrapyrrole section, DDH2, is stable, helical, and binds heme with high affinity. This shows that even in the absence of the Due Ferro section, the tetrapyrrole section of MZH3 is functional. The design process relied on close attention to interface widths, cofactor binding cavities, core packing using a layering approach, and negative design by charge patterning. This is an empirical design method in the sense that it relies primarily on takeaway messages derived from a variety of studies on natural and designed proteins that have qualities in common with the desired design, as opposed to being an intuition-driven approach guided by heptad repeat patterning. Ultimately, this method proved to be fruitful, yielding the first high resolution structure of a maquette with tetrapyrroles bound and the first maquette that separates charge for long enough for chemical reactions to occur. This puts us on a path toward artificial photosynthesis in a *de novo* designed protein maquette.

Despite these successes, it is not clear whether the design strategy is robust. MZH3 and DDH2 are promising results, but represent only two examples of proteins in which this empirical approach to *de novo* four-helix bundle design has been used. Analysis of MZH3 crystal structures in the apo-state suggests that interfacial leucine-leucine hydrophobic interactions across *g-g* interfaces might be among the most stabilizing forces in MZH3, and they might play a more important role in folding than layering of core amino acids or inter-helical charge pairing interactions, which were originally expected to be the most important features of the maquette sequence. In addition, the design strategy used for MZH3 is limited by its dependence on observations of natural and designed protein structures and their modes of cofactor binding.

MZH3 design was heavily influenced by the extensive literature on natural heme binding proteins, carboxylate-bridged di-iron and di-manganese proteins, photosystem II, and a variety of maquettes. An empirical approach to four-helix bundle design would not be suitable to the design of a maquette that binds an unusual cofactor not found in nature or one that has an atypical fold or function that has no precedent. However, when natural proteins that are structurally similar to the target design exist, their structural attributes can serve to guide design; MZH3 has striking structural similarities to cytochrome b and bacterioferritin despite negligible sequence similarity. This shows that natural and designed protein structural features can be readily included in the design of new maquettes with dissimilar sequences.

6.2 Light-driven electron transfer

Previous work has demonstrated light-driven oxidation of tyrosine side chains and metal ions in redesigned natural proteins (17-22), but MZH3 is the first example of this function in a maquette. The fact that MZH3 was designed from scratch gives it certain advantages. MZH3 was engineered to be highly stable, and the simplicity of its overall fold makes it amenable to redesign. The maquette was specifically designed to arrange cofactors so that charge separation can take place. Efficient redox-active triads have been synthesized chemically (23, 24), but the MZH3 triad is able to stabilize a charge separated state in an aqueous environment for orders of magnitude longer than synthetic triads.

Transient absorption results support the conclusion that tyrosine and Fe(II) ions are photo-chemically oxidized in MZH3 to stabilize the charge separated state. The MZH3-Y168L mutant, which lacks a tyrosine, fails to stabilize a charge separated state, and the introduction of hydrogen bonding networks involving the tyrosine in the MZH3-L71H and MZH3-L71H-L31D

mutants significantly affects the yield and lifetime of charge separation. The crystal structure of MZH3-L71H showed a 2.6 Å hydrogen bond between tyrosine 168 and histidine 71, similar to the tyrosine-histidine hydrogen bonds of photosystem II. The L71H mutation results in a pronounced increase in the yield of charge separation, and this yield is further increased by the introduction of an aspartate predicted to be within hydrogen bonding distance of His71 in the MZH3-L71H-L31D mutant. This histidine-aspartate interaction might play a role in tyrosine oxidation that is similar to D1-Asn298 in photosystem II. Addition of Fe(II) in MZH3 enables charge separation with a lifetime of 300 ms at pH 7.5 whether or not tyrosine is present. In contrast, the MZH3-L71H-E34A mutant, which is deficient in its metal binding capacity, did not exhibit a significant difference in charge separation behavior when Fe(II) was added. This shows that bound Fe(II) is involved in charge separation.

These results provide compelling evidence of tyrosine oxidation and Fe(II) oxidation in a working reaction center maquette, but further development is necessary to achieve the long-term goal of *in vivo* generation of oxygen and hydrogen. Direct evidence of tyrosine oxidation might be derived from electron paramagnetic resonance (EPR) detection of the EPR-active tyrosyl radical. Energy conversion might be made more efficient if the excited singlet state of the zinc tetrapyrrole can be used for rapid electron transfer before it relaxes to the lower energy triplet state. This would require the insertion of an additional cofactor close to the zinc porphyrin, perhaps by using a modified version of the unexpected zinc porphyrin binding site at the opening of the metal binding cavity observed in crystal structures CS-B and CS-C (Figure 3.16). In extending the electron transfer chain, a second electron acceptor cofactor might further stabilize charge separation and expedite the slow cobalt porphyrin reduction that will be

needed for hydrogen evolution. Future work is needed to establish manganese oxidation, which would be a crucial step toward photoassembly of an oxygen evolving cluster in a maquette.

6.3 Oxygen binding

The MZH3-His110Ala mutation gave rise to a long-lived oxyferrous heme state. Other heme maquettes and redesigned natural proteins have demonstrated oxygen binding capacity (5, 6, 25, 26), but the MZH3-His110Ala oxyferrous lifetime is orders of magnitude longer at 38 hours, commensurate with the lifetimes of oxygen-carrying proteins in nature. Preliminary results suggest that the oxygen affinity of MZH3-His110Ala exceeds the affinity of myoglobin and hemoglobin, and that this affinity will need to be decreased in order to create a potential blood-substitute protein.

Oxygen binding in MZH3-His110Ala was not unexpected, given that it has a vacant coordination site on the heme iron and a proximal histidine ligand similar to myoglobin, but the stability and oxygen affinity are remarkable. Unanticipated specific interactions may be responsible for the serendipitous oxygen-carrying properties of MZH3-His110Ala. The hydroxyl group of threonine 91 might be poised to make a hydrogen bond with bound oxygen, thereby stabilizing the oxygen in the manner of HisE7 in myoglobin and hemoglobin (27). The backbone amide nitrogen of glycine 92 might also be close enough to make a hydrogen bonding contact with oxygen. Given the long lifetime of the oxyferrous state and the fact that MZH3 is readily crystallizable, it may be possible to resolve these questions by X-ray crystallography of the MZH3-His110Ala mutant in the oxyferrous state. Mutagenesis studies may also be able to determine whether Thr91 plays a role in oxygen binding, and could allow the fine-tuning of the maquette to make its oxygen binding behavior more similar to natural proteins.

6.4 Summary

This thesis demonstrates the design, structure and action of a working photosynthetic reaction center maquette. The design procedure applied detailed design rules laid out by decades of research on the sequence-structure relationship in four-helix bundle proteins. High resolution X-ray crystallographic structures revealed the assembly of multiple redox cofactors into an electron transfer chain that can separate charge for hundreds of milliseconds, as verified by transient absorption spectroscopy. Without copying natural sequences, the maquette folds into a structure that strongly resembles structures of natural proteins that were used to guide the design. Ultraviolet/visible spectroscopy showed that this maquette binds oxygen in a complex with a stability comparable to oxygen transport proteins in nature. There is still a vast divide between the range of functions expertly covered by natural proteins and the developing field of *de novo* protein design. This thesis helps to narrow the gap and advance protein design toward the goal of artificial photosynthesis to serve human energy needs.

6.5 References

1. Robertson, D. E., Farid, R. S., Moser, C. C., Urbauer, J. L., Mulholland, S. E., Pidikiti, R., Lear, J. D., Wand, A. J., DeGrado, W. F., and Dutton, P. L. (1994) Design and synthesis of multi-haem proteins, *Nature* 368, 425-432.
2. Huang, S. S., Gibney, B. R., Stayrook, S. E., Dutton, P. L., and Lewis, M. (2003) X-ray structure of a Maquette scaffold, *Journal of Molecular Biology* 326, 1219-1225.
3. Arai, R., Kobayashi, N., Kimura, A., Sato, T., Matsuo, K., Wang, A. F., Platt, J. M., Bradley, L. H., and Hecht, M. H. (2012) Domain-swapped dimeric structure of a stable and functional *de novo* four-helix bundle protein, WA20, *J Phys Chem B* 116, 6789-6797.
4. Patel, S. C., Bradley, L. H., Jinadasa, S. P., and Hecht, M. H. (2009) Cofactor binding and enzymatic activity in an unevolved superfamily of *de novo* designed 4-helix bundle proteins, *Protein Sci* 18, 1388-1400.
5. Koder, R. L., Anderson, J. L., Solomon, L. A., Reddy, K. S., Moser, C. C., and Dutton, P. L. (2009) Design and engineering of an O(2) transport protein, *Nature* 458, 305-309.
6. Farid, T. A., Kodali, G., Solomon, L. A., Lichtenstein, B. R., Sheehan, M. M., Fry, B. A., Bialas, C., Ennist, N. M., Siedlecki, J. A., Zhao, Z., Stetz, M. A., Valentine, K. G., Anderson,

- J. L., Wand, A. J., Discher, B. M., Moser, C. C., and Dutton, P. L. (2013) Elementary tetrahelical protein design for diverse oxidoreductase functions, *Nat Chem Biol* 9, 826-833.
7. Gibney, B. R., Mulholland, S. E., Rabanal, F., and Dutton, P. L. (1996) Ferredoxin and ferredoxin-heme maquettes, *Proc Natl Acad Sci U S A* 93, 15041-15046.
 8. Fry, B. A., Solomon, L. A., Dutton, P. L., and Moser, C. C. (2016) Design and engineering of a man-made diffusive electron-transport protein, *Biochim Biophys Acta* 1857, 513-521.
 9. Crick, F. H. C. (1953) The Packing of Alpha-Helices - Simple Coiled-Coils, *Acta Crystallogr* 6, 689-697.
 10. Shifman, J. M., Moser, C. C., Kalsbeck, W. A., Bocian, D. F., and Dutton, P. L. (1998) Functionalized de novo designed proteins: mechanism of proton coupling to oxidation/reduction in heme protein maquettes, *Biochemistry* 37, 16815-16827.
 11. Falzone, C. J., Mayer, M. R., Whiteman, E. L., Moore, C. D., and Lecomte, J. T. (1996) Design challenges for hemoproteins: the solution structure of apocytochrome b5, *Biochemistry* 35, 6519-6526.
 12. Landfried, D. A., Vuletich, D. A., Pond, M. P., and Lecomte, J. T. (2007) Structural and thermodynamic consequences of b heme binding for monomeric apoglobins and other apoproteins, *Gene* 398, 12-28.
 13. Smith, L. J., Kahraman, A., and Thornton, J. M. (2010) Heme proteins-Diversity in structural characteristics, function, and folding, *Proteins-Structure Function and Bioinformatics* 78, 2349-2368.
 14. Torres Martin de Rosales, R., Faiella, M., Farquhar, E., Que, L., Jr., Andreozzi, C., Pavone, V., Maglio, O., Natri, F., and Lombardi, A. (2010) Spectroscopic and metal-binding properties of DF3: an artificial protein able to accommodate different metal ions, *J Biol Inorg Chem* 15, 717-728.
 15. Faiella, M., Andreozzi, C., de Rosales, R. T., Pavone, V., Maglio, O., Natri, F., DeGrado, W. F., and Lombardi, A. (2009) An artificial di-iron oxo-protein with phenol oxidase activity, *Nat Chem Biol* 5, 882-884.
 16. Lahr, S. J., Engel, D. E., Stayrook, S. E., Maglio, O., North, B., Geremia, S., Lombardi, A., and DeGrado, W. F. (2005) Analysis and design of turns in alpha-helical hairpins, *J Mol Biol* 346, 1441-1454.
 17. Allen, J. P., Olson, T. L., Oyala, P., Lee, W. J., Tufts, A. A., and Williams, J. C. (2012) Light-driven oxygen production from superoxide by Mn-binding bacterial reaction centers, *Proc Natl Acad Sci U S A* 109, 2314-2318.
 18. Kalman, L., LoBrutto, R., Allen, J. P., and Williams, J. C. (1999) Modified reaction centres oxidize tyrosine in reactions that mirror photosystem II, *Nature* 402, 696-699.
 19. Kalman, L., Williams, J. C., and Allen, J. P. (2011) Energetics for oxidation of a bound manganese cofactor in modified bacterial reaction centers, *Biochemistry* 50, 3310-3320.
 20. Thielges, M., Uyeda, G., Camara-Artigas, A., Kalman, L., Williams, J. C., and Allen, J. P. (2005) Design of a redox-linked active metal site: manganese bound to bacterial reaction centers at a site resembling that of photosystem II, *Biochemistry* 44, 7389-7394.
 21. Hingorani, K., Conlan, B., Hillier, W., and Wydrzynski, T. (2009) Elucidating Photochemical Pathways of Tyrosine Oxidation in an Engineered Bacterioferritin 'Reaction Centre', *Aust J Chem* 62, 1351-1354.

22. Hingorani, K., Pace, R., Whitney, S., Murray, J. W., Smith, P., Cheah, M. H., Wydrzynski, T., and Hillier, W. (2014) Photo-oxidation of tyrosine in a bio-engineered bacterioferritin 'reaction centre'-a protein model for artificial photosynthesis, *Biochim Biophys Acta* 1837, 1821-1834.
23. Megiatto, J. D., Jr., Antoniuk-Pablant, A., Sherman, B. D., Kodis, G., Gervaldo, M., Moore, T. A., Moore, A. L., and Gust, D. (2012) Mimicking the electron transfer chain in photosystem II with a molecular triad thermodynamically capable of water oxidation, *Proc Natl Acad Sci U S A* 109, 15578-15583.
24. Imahori, H., Tamaki, K., Guldi, D. M., Luo, C., Fujitsuka, M., Ito, O., Sakata, Y., and Fukuzumi, S. (2001) Modulating charge separation and charge recombination dynamics in porphyrin-fullerene linked dyads and triads: Marcus-normal versus inverted region, *J Am Chem Soc* 123, 2607-2617.
25. Zhang, L., Andersen, E. M., Khajo, A., Magliozzo, R. S., and Koder, R. L. (2013) Dynamic factors affecting gaseous ligand binding in an artificial oxygen transport protein, *Biochemistry* 52, 447-455.
26. Komatsu, T., Ohmichi, N., Zunszain, P. A., Curry, S., and Tsuchida, E. (2004) Dioxygenation of human serum albumin having a prosthetic heme group in a tailor-made heme pocket, *J Am Chem Soc* 126, 14304-14305.
27. Phillips, S. E., and Schoenborn, B. P. (1981) Neutron diffraction reveals oxygen-histidine hydrogen bond in oxymyoglobin, *Nature* 292, 81-82.

Chapter 7: Appendix

7.1 Protein expression and purification

A gene encoding MZH3 including an N-terminal His₆-tag and TEV protease cleavage sequence was purchased from DNA2.0 in a pJexpress414 vector with codons optimized for expression in *E. coli*. After finding that TEV cleavage was slow due to the proximity of a proline to the TEV cleavage site, Gly22 in the sequence below was inserted using site-directed mutagenesis. The TEV protease cleavage site is between Q21 and G22; G22 becomes G1 in the protein used for experimental studies in this thesis. Primers for mutagenesis were purchased from Invitrogen, and mutant plasmids were PCR amplified using AccuPrime™ Pfx SuperMix (Invitrogen). Other mutations including Y168L, L71H, L31D, E34A, and H124M were prepared similarly. The final amino acid sequence of the protein expressed for experimental studies was:

MKGGGHHHHHGGDGENLYFQGSPQLRQEHQQLAQEFQQLLQEIQQLGRELLKGELQGIKQLREASEKAR
NPEKKSVLQKILEDEEKHIELLETLQQTGQEAQQLLQELQQTGQELWQLGGSGGPELRQKHQQLAQKIQQLL
QKHQQLGAKILEDEEKHIELLETILGGSGGDELRELLKGELQGIKQYRELQQLGQKAQQLVQKLQQTGQKLW
QLG

The plasmids were transformed into BL21-(DE3) competent cells (New England Biolabs), and bacteria were grown to 0.6 OD at 600 nm. Expression was induced with between 40 μM and 1 mM IPTG for 4 hours at 37°C. The cells were pelleted by centrifugation, resuspended in 20 mM sodium phosphate buffer at pH 7.4 with 500 mM NaCl, 40 mM imidazole, 1% w/v

octylthioglucoside, ~0.1 mg/mL DNase, and lysed by homogenization or sonication. The lysate was centrifuged at 25,000 g for 30 minutes, and the supernatant was applied to a 5 mL Ni-NTA HisTrap FF preppacked column (GE Healthcare Life Sciences) on an Akta FPLC. The protein was treated with TEV protease and incubated at 4°C for up to 2 weeks, applied to an Ni-NTA column again, and finally purified by size exclusion chromatography (SEC) using an XK 16/70 column (GE Healthcare Life Sciences) packed with 110 mL of Superdex 75 prep grade gel filtration medium (GE Healthcare Life Sciences). Where noted, an additional purification step by high performance liquid chromatography (HPLC) was done with a Waters reverse-phase HPLC system using a C4 or C18 HPLC column (Grace Davison Discovery Sciences). HPLC-pure samples were lyophilized and resuspended in >6.5 M GdnHCl, refolded by dilution, and the monomeric MZH3 protein was isolated by SEC. Sample purity and molecular weight estimations were made using denaturing sodium dodecyl sulfate polyacrylamide gel electrophoresis (SDS-PAGE).

7.2 Ultraviolet/visible spectroscopy

Ultraviolet/visible spectroscopy (UV/vis) was performed using a Varian Cary-50 spectrophotometer at room temperature. Cofactor binding titrations were performed by preparing a 1 mL protein sample near 1 μ M in a quartz cuvette, unless otherwise noted. Concentrations were determined using an extinction coefficient of $\epsilon_{280\text{nm}}=12490 \text{ M}^{-1}\text{cm}^{-1}$ for MZH3, based on the predicted absorbance of the two tryptophan and one tyrosine amino acids. A stock solution of cofactor was titrated into the protein solution until at least three equivalents of cofactor per protein had been added. Cofactor was typically added in steps of 0.1 equivalents of cofactor per protein until after the binding capacity of the protein appeared to have been reached, at which point 0.2 equivalents of cofactor per protein were added for each step. At

least 10 minutes were allowed for equilibration before adding the next aliquot. Heme B stock concentrations were measured by hemochrome assay (1). Stock concentrations of other tetrapyrrole cofactors and $\text{Co}(\text{NO}_3)_2$ were estimated by mass measurements. Soluble cofactor stocks were prepared in water, and insoluble tetrapyrrole stocks were prepared in dimethyl sulfoxide. Tetrapyrrole stock solutions were 100-200 μM and the $\text{Co}(\text{NO}_3)_2$ stock was 17 mM in water.

Estimates of the amounts of heme B incorporated into MZH3 during overexpression were made by UV/vis measurements. The heme concentration was determined from the absorbance at 415 nm using an extinction coefficient of $115,000 \text{ M}^{-1}\text{cm}^{-1}$, and the protein concentration was estimated by the difference in the absorbance between 280 nm (where apo-MZH3 absorbs with an extinction coefficient of $12490 \text{ M}^{-1}\text{cm}^{-1}$) and 317 nm. The low absorbance of heme B at 317 nm serves as a baseline for the protein peak at 280 nm, because heme B absorbance is similar at 280 and 317 nm.

7.3 Circular dichroism

Circular dichroism measurements were made using an Aviv Model 410 instrument. Far UV CD spectra were measured from 190 to 260 nm and were performed in a 0.1 cm path length quartz cuvette. Thermal denaturation was measured at 222 nm for 5 seconds with a 2 nm bandwidth, and data were collected every 2°C with a heating rate of $10^\circ\text{C}/\text{min}$ followed by a 4 minute incubation time. The mean molar ellipticity per residue, θ_{MMR} , was calculated by dividing the measured ellipticity by 196 residues. Measurements of exciton coupling in the Soret region of the spectrum were made at 25°C from 370 nm to 470 nm in either a 1 cm or 0.1 cm path length cuvette, as noted. Spectra were collected with a 1 nm bandwidth every 1 nm for 5

seconds per data point, and each reported spectrum was the average of three spectra that were measured consecutively.

7.4 Redox titration

A redox titration was performed as described previously (2). A sample of 7 mL of ~40 μM MZH3 with heme B was prepared in 15 mM NaCl and 10 mM sodium phosphate, pH 7 in a cuvette modified for this technique. The sample was kept anaerobic by continuously flushing with argon scrubbed with an acid vanadyl sulfate/granular zinc bubble train, as described previously (3). Changes in the absorption of the Q-bands of heme B were monitored as a function of solution potential, which was measured by a calomel electrode (Radiometer Analytical). The solution potential was lowered by addition of 1 μL aliquots of dithionite (reducing direction) or 5 μL of ferricyanide (oxidizing direction). The Nernst curves in both directions were compared to look for hysteresis. Redox mediators are needed to bring the measuring electrodes into equilibrium with the redox state of the cofactor, because biological redox centers usually cannot transfer electrons to and from the electrode because the protein shields the cofactor (2). The following redox mediators were used: duroquinone (25 μM), pyocyanine (10 μM), indigo-trisulfonate (10 μM), 2-hydroxy-1,4-naphthoquinone (10 μM), phenazine (10 μM), anthroquinone-2-sulfonate (20 μM), and benzyl viologen (10 μM).

7.5 Crystallography methods and crystal structure statistics

Protein samples for crystallography were purified as described in section 7.1. Protein samples for crystal structures CS-F and CS-G were purified by HPLC using a C4 column, followed

by lyophilization, denaturation by GdnHCl, refolding, and SEC. No other samples were purified by HPLC, lyophilized, or denatured. All crystals of MZH3 were grown in hanging drops at 4°C. MZH3 stock solutions contained 20-40 mM NaCl and 10-20 mM piperazine-N,N'-bis(2-ethanesulfonic acid) (PIPES) buffer at pH 6.5, and were stored at 4°C.

Addition of heme B was done after the final SEC purification step. In order to prevent aggregation and precipitation of heme B, the MZH3 sample was diluted to ≤ 100 μM and was kept stirring at room temperature. Heme B was added dropwise from a stock solution of ≤ 1 mM heme in dimethyl sulfoxide (DMSO) up to 0.9 equivalents of heme per protein. At this point, a more dilute heme B stock solution, typically ≤ 200 μM , heme B was titrated into the MZH3 solution until 1.0 equivalents heme B per protein had been added. Full occupancy of heme B was verified by diluting the sample to ~ 2 μM and adding ~ 0.1 equivalent of heme B per protein. If the difference spectrum showed signs of additional heme binding, more heme was added to the MZH3 stock until binding stopped. A similar method was used for the addition of ZnPCP. Sample buffers were exchanged to the low salt PIPES buffer using 5 kDa MWCO Vivaspin Turbo 15 concentrators (Sartorius AG) by centrifuging to concentrate the sample and diluting with the new buffer several times. Table 7.1 gives the MZH3 stock concentrations, cofactors bound to MZH3 in the stock solution, well solutions for the hanging drop experiments at 4°C, drop volumes, and cryoprotectant for each crystal structure. Crystal structures CS-B and CS-C were grown from crystal seeds starting from crystals that lacked ZnPCP using a Seed Bead kit (Hamilton). Crystal structure CS-H used streak seeding with a cat whisker.

Crystal Structure	MZH3 stock (μM)	Cofactors	Well solution	Drop volumes (well solution: protein stock)	Cryoprotectant
CS-A (Tray 7, D5)	550	Heme B, ZnPCP, 1.5 mM ZnCl ₂	3.6 M NaCl, 100 mM NaAc pH 4.5	1 μL :1 μL	30% glycerol, 3.5 M NaCl, 100 mM NaAc pH 4.4
CS-B (Tray 54, A2)	600	Heme B, ZnPCP, ~35 mM MnCl ₂	3.0 M NaCl, 100 mM NaAc pH 4.9	1.2 μL :2.5 μL and 0.5 μL seed stock ^a	30% glycerol, 3.5 M NaCl, 100 mM NaAc pH 4.4
CS-C (Tray 52, D5)	600	Heme B, ZnPCP, 2 mM MnCl ₂	3.0 M NaCl, 100 mM NaAc pH 4.8	1.2 μL :2.5 μL and 0.5 μL seed stock ^b	30% glycerol, 3.5 M NaCl, 100 mM NaAc pH 4.4
CS-D (Tray 1, B2)	630	Heme B, 1.5 mM ZnCl ₂	2.7 M NaCl, 100 mM NaAc pH 4.5	1 μL :1 μL	30% glycerol, 3.5 M NaCl, 100 mM NaAc pH 4.4
CS-E (Tray 53, B4)	540	Heme B, 1 mM MnCl ₂	1.2 M Li ₂ SO ₄ , 0.5 M (NH ₄) ₂ SO ₄ , 150 mM Na citrate, pH 5.9	1 μL :1 μL	28% glycerol, 1.25 M Li ₂ SO ₄ , 0.5 M (NH ₄) ₂ SO ₄ , 100 mM Na citrate, pH 5.85
CS-F (Tray 32, B6)	500	Heme B, ZnPCP, 1.5 mM ZnCl ₂	19.5% w/v PEG 8000, 100 mM CdCl ₂ , 100 mM NaAc pH 4.2	1 μL :1 μL	40% v/v glycerol, 100 mM CdCl ₂ , 100 mM NaAc pH 4.2
CS-G (Tray 21, D4)	560	Heme B, 1.5 mM ZnCl ₂	24% w/v PEG 1500, 100 mM CdCl ₂ , 100 mM NaAc pH 4.8	1 μL :1 μL	2-methyl-2,4-pentanediol
CS-H (Tray 73, A5)	630 (L71H mutant)	Heme B	24% w/v PEG 1500, 70 mM CdCl ₂ , 100 mM NaAc pH 4.6	5 μL : 1 μL , seeds ^c	40% v/v glycerol, 70 mM CdCl ₂ , 100 mM NaAc pH 4.6

Table 7.1: Crystallization conditions used to obtain MZH3 crystal structures

Crystals were quickly dipped in the indicated cryoprotectant for no more than 30 seconds immediately prior to flash freezing in liquid nitrogen or a nitrogen gas stream at 100 K. PEG 8000 and PEG 1500 stand for polyethylene glycol with an average molecular weight of 8000 and 1500 g/mol, respectively. NaAc stands for sodium acetate.

^a Seed stock was prepared from similar crystals grown with heme, ZnPCP, and 2 mM MnCl₂ over 3.0 M NaCl, 100 mM NaAc, pH 4.8, which in turn were grown from the seed stock used for CS-C (see note ^b)

^b Seed stock was prepared from crystals grown with heme and 1 mM MnCl₂ over 2.8 M NaCl, 100 mM NaAc, pH 4.7 that did not contain ZnPCP

^c Streak seeded with cat whisker from crystals grown with the same protein stock solution hanging over 25% PEG 1500, 80 mM CdCl₂, pH 4.6

All X-ray crystallographic data sets were collected from single crystals at 100 K. X-ray diffraction data for crystal structures CS-A and CS-D were collected at the National Synchrotron

Light Source, beamline X6A using an ADSC Q270 CCD x-ray area detector. X-ray diffraction data for crystal structures CS-B, CS-C, CS-E, CS-F, CS-G, and CS-H were collected using a Rigaku Micromax-007 HF rotating copper anode X-ray generator and VariMax HF optics with a Rigaku Saturn 944 HG CCD detector.

Multiwavelength anomalous dispersion (MAD) data was collected to solve crystal structure CS-A. Data were integrated with XDS (4) and initial phases were calculated using SOLVE (5). All other crystals used the CS-A crystal structure as a model for molecular replacement using Phaser (6). Software packages CCP4i (7) and PHENIX (8) were used throughout the structure solution and refinement process. Intensities were scaled using SCALA (9). Refinement was done using REFMAC5 (10), phenix.refine (11), and PDB_REDO (12). Real space refinement was done by manually fitting models into electron density maps in Coot (13). Model bias removal was done using prime-and-switch phasing (14) and density modification was done with RESOLVE (15).

Statistics for the three data sets collected for MAD to solve crystal structure CS-A are given in Table 7.2.

Measurement	Zn K edge	Zn K inflection point	Remote energy
Wavelength	1.2824 Å	1.2831 Å	1.0781 Å
Space group	P4 ₁ 2 ₁ 2	P4 ₁ 2 ₁ 2	P4 ₁ 2 ₁ 2
Resolution	2.1 Å	2.1 Å	2.0 Å
Completeness	99.1%	99.1%	99.4%
I/σ	18.15	19.53	16.8
R _{merge}	6.6%	6.3%	8.5%
R _{merge} (outer shell)	49.9%	53%	97%
Table 7.2: Multiwavelength anomalous dispersion (MAD) statistics for crystal structure CS-A			

Data collection and refinement statistics for all eight crystal structures reported in this thesis are given in Table 7.3.

Crystal	CS-A	CS-B	CS-C	CS-D	CS-E	CS-F	CS-G	CS-H
Resolution, high (Å)	2.0	2.02	2.10	1.45	1.90	2.01	1.78	2.02
Resolution, low (Å)	61.43	61.17	38.90	61.38	59.64	19.58	18.36	71.54
Wavelength (Å)	1.0781	1.54178	1.54178	1.0781	1.54178	1.54178	1.54178	1.54178
X-ray Source	NSLS	Cu K α	Cu K α	NSLS	Cu K α	Cu K α	Cu K α	Cu K α
Space group	P4 $_1$ 2 $_1$ 2	C2	C2	P2 $_1$				
Cell dimensions:								
a (Å)	43.749	44.14	44.243	43.747	44.968	91.777	89.692	44.467
b (Å)	43.749	44.14	44.243	43.747	44.968	25.206	23.693	25.872
c (Å)	245.74	244.7	244.95	245.52	238.29	73.165	72.756	73.623
α (°)	90	90	90	90	90	90	90	90
β (°)	90	90	90	90	90	102.12	99.93	103.67
γ (°)	90	90	90	90	90	90	90	90
Total reflections	130,054	205,441	198,057	382,473	253,427	71,446	47,861	72,034
Unique reflections	17,105	16,830	15,112	43,568	20,059	10,978	14,127	10,744
Redundancy:								
All data:	7.6	12.2	13.1	8.8	12.6	6.5	3.4	6.7
Outer shell:	7.4	4.3	10.8	5.2	5.2	2.3	1.7	3.3
Completeness (%):								
All data:	99.4	99.2	99.7	99.7	98.4	96.5	95.1	97.3
Outer shell:	98.8	89.1	96.1	96.1	86.6	61.8	68.9	71.0
I/ σ (I):								
All data:	16.80	18.32	22.65	15.30	22.22	15.47	17.12	25.98
Outer shell:	2.52	1.58	4.63	1.26	1.66	3.40	3.79	9.46
R $_$ merge (%):								
All data:	8.5	10.4	8.6	9.9	8.9	7.9	4.7	5.1
Outer shell:	97.0	97.2	54.6	133.7	105.3	22.8	17.5	10.1
Final refinement:								
R $_$ work (%)	22.5	22.4	22.6	20.4	22.4	23.9	19.8	20.7
R $_$ free (%)	27.2	27.1	28.0	23.7	25.5	30.0	23.3	25.5
R $_$ work (last shell) (%)	35.5	37.1	26.9	35.2	38.4	30.6	21.6	20.7
R $_$ free (last shell) (%)	40.7	43.7	30.3	39.0	35.9	49.9	21.0	29.7

Table 7.3: Data collection and refinement statistics

7.6 Transient absorption

Transient absorption experiments were performed at 20°C with a 10 Hz Q-switched frequency-doubled Nd:YAG laser (532 nm, DCR-11 Spectra Physics). The laser pulse duration was 2 ns long. A Xe flash lamp emitted probe beams of white light into split fiber optic cables at times t after the laser flash to measure the change in absorbance spectra as a function of time after the laser flash. The gate width of the Xe flash was either 600 ns or 1 μ s, with the exposure

beginning at time t . The split fiber optic cables were used to direct one probe beam through the laser-pumped (experimental) region and the other probe beam through the dark (reference) region of the sample in the cuvette. Each probe beam was collected by a fiber optic bundle and flattened into a line of fibers at the entrance slit of an Acton SP-2156 spectrograph. The images from the exit slit of the monochromator were focused onto a Princeton Instruments PiMax-3 ICCD camera. Delay times t were set by a Stanford Research System DG 535 digital delay generator. A ThorLabs beam shutter allowed the 10-Hz laser repetition rate to be lowered to seconds for measurements at times t longer than 100 ms.

7.7 Singular value decomposition (SVD)

Absorbance spectra were collected at varying times or potentials, depending on the experiment, and the raw absorbance data were compiled into a matrix A . Matrix A contained one spectrum per column so that each column had λ absorbance values and there were t columns, where t is the number of spectra collected. Singular value decomposition was performed using the built-in “SingularValueDecomposition” function in Mathematica 10.3. Calling the function with matrix A as the input variable returned three output matrices U , S , and V , such that $A = USV^T$. Matrix U had dimensions λ by λ , V had dimension t by t , and S was a diagonal matrix with dimensions λ by t .

The V matrix was used to fit a kinetics model in which ordinary differential equations are used to describe the development of the electron transfer system with time. In the monad case, where a pigment (P) is alone in the maquette, the model includes the rate of decay of the excited state (P^*) to the ground state. In this case, the P^* minus ground state difference spectrum is the only spectrum of interest, and model fitting gives this spectrum and its rate

constant. In the dyad case, rates of electron transfer from P^* to the electron acceptor (A) and from A^- to P^+ are included in the model. (It is assumed that P^+ goes back to the ground state when it accepts the electron from A^- , because the return to the P^* state is negligible). The dyad model therefore includes two difference spectra: P^* minus the ground state and P^+/A^- minus the ground state. In the triad case, when an electron donor (D) is included, the model includes electron transfer from D to P^+ and from P to D^+ . If the rate of electron transfer from D to P^+ is significantly faster than from P to A, then the population of the $D/P^+/A^-$ state will not be observable and the D to P^+ rate constant will not be resolved.

Model fitting followed a variation of the methods of Henry and Hofrichter (16). The model described above was used to calculate an expected population matrix P with maximum dimensions t by t . A square transformation matrix C with maximum dimensions t by t was applied to P , and the mean square difference between V and the CP product was minimized using the "FindMinimum" function in Mathematica 10.3. Electron transfer rates and the elements of matrix C were allowed to vary during minimization. The minimization followed a quasi-newton procedure starting with various initial estimates of the rates and C matrix elements. The best initial estimates were identified by comparing the residuals of the minimization procedures. The final values of the rates and the C matrix elements were used to reconstruct the elemental spectra from the raw data and the electron transfer kinetics that best explain the absorbance measurements.

7.8 Spectroelectrochemistry

Midpoint potential measurements of heme B in MZH3 variants were made using a spectroelectrochemical setup. A CH Instruments Electrochemical Analyzer was used to set

electrode potentials in a honeycomb spectroelectrochemical cell (Pine Research Instrumentation). The sample was placed in the 0.18 cm path length cuvette with a fine gold honeycomb working electrode modified with cystamine to prevent protein adsorption to the electrode. The reference electrode was Ag/AgCl (3 M NaCl), which has a potential of 209 mV with respect to the standard hydrogen electrode (SHE). Ultraviolet/visible absorbance spectra were collected using an Ocean Optics DH-2000 Deuterium-Halogen Light Source that emitted light through a fiber optic cable through the honeycomb working electrode and through another fiber optic cable to an Ocean Optics spectrometer. To speed redox equilibration, redox mediators were added to the sample including 1,2-naphthoquinone (25 μ M), 2,3,5,6-tetramethylphenylenediamine (25 μ M), phenazine methosulfate (20 μ M), phenazine ethosulfate (20 μ M), duroquinone (50 μ M), phenazine (20 μ M), pyocyanine (10 μ M), 2-hydroxy-1,4-naphthoquinone (25 μ M), anthraquinone-2-sulfonate (20 μ M), indigo trisulfonate (6 μ M), and benzyl viologen (20 μ M) (2).

7.9 References

1. Berry, E. A., and Trumpower, B. L. (1987) Simultaneous Determination of Hemes-a, Hemes-B, and Hemes-C from Pyridine Hemochrome Spectra, *Analytical Biochemistry* 161, 1-15.
2. Dutton, P. L. (1978) Redox potentiometry: determination of midpoint potentials of oxidation-reduction components of biological electron-transfer systems, *Methods Enzymol* 54, 411-435.
3. Englander, S. W., Calhoun, D. B., and Englander, J. J. (1987) Biochemistry without Oxygen, *Analytical Biochemistry* 161, 300-306.
4. Kabsch, W. (2010) Xds, *Acta Crystallogr D Biol Crystallogr* 66, 125-132.
5. Terwilliger, T. C., and Berendzen, J. (1999) Automated MAD and MIR structure solution, *Acta Crystallogr D Biol Crystallogr* 55, 849-861.
6. McCoy, A. J., Grosse-Kunstleve, R. W., Adams, P. D., Winn, M. D., Storoni, L. C., and Read, R. J. (2007) Phaser crystallographic software, *J Appl Crystallogr* 40, 658-674.
7. Winn, M. D., Ballard, C. C., Cowtan, K. D., Dodson, E. J., Emsley, P., Evans, P. R., Keegan, R. M., Krissinel, E. B., Leslie, A. G., McCoy, A., McNicholas, S. J., Murshudov, G. N.,

- Pannu, N. S., Potterton, E. A., Powell, H. R., Read, R. J., Vagin, A., and Wilson, K. S. (2011) Overview of the CCP4 suite and current developments, *Acta Crystallogr D Biol Crystallogr* 67, 235-242.
8. Adams, P. D., Afonine, P. V., Bunkoczi, G., Chen, V. B., Davis, I. W., Echols, N., Headd, J. J., Hung, L. W., Kapral, G. J., Grosse-Kunstleve, R. W., McCoy, A. J., Moriarty, N. W., Oeffner, R., Read, R. J., Richardson, D. C., Richardson, J. S., Terwilliger, T. C., and Zwart, P. H. (2010) PHENIX: a comprehensive Python-based system for macromolecular structure solution, *Acta Crystallogr D Biol Crystallogr* 66, 213-221.
 9. Evans, P. (2006) Scaling and assessment of data quality, *Acta Crystallogr D Biol Crystallogr* 62, 72-82.
 10. Vagin, A. A., Steiner, R. A., Lebedev, A. A., Potterton, L., McNicholas, S., Long, F., and Murshudov, G. N. (2004) REFMAC5 dictionary: organization of prior chemical knowledge and guidelines for its use, *Acta Crystallogr D Biol Crystallogr* 60, 2184-2195.
 11. Afonine, P. V., Grosse-Kunstleve, R. W., Echols, N., Headd, J. J., Moriarty, N. W., Mustyakimov, M., Terwilliger, T. C., Urzhumtsev, A., Zwart, P. H., and Adams, P. D. (2012) Towards automated crystallographic structure refinement with phenix.refine, *Acta Crystallogr D Biol Crystallogr* 68, 352-367.
 12. Joosten, R. P., Long, F., Murshudov, G. N., and Perrakis, A. (2014) The PDB_REDO server for macromolecular structure model optimization, *IUCrJ* 1, 213-220.
 13. Emsley, P., Lohkamp, B., Scott, W. G., and Cowtan, K. (2010) Features and development of Coot, *Acta Crystallogr D Biol Crystallogr* 66, 486-501.
 14. Terwilliger, T. C. (2004) Using prime-and-switch phasing to reduce model bias in molecular replacement, *Acta Crystallogr D* 60, 2144-2149.
 15. Terwilliger, T. C. (2000) Maximum-likelihood density modification, *Acta Crystallogr D Biol Crystallogr* 56, 965-972.
 16. Henry, E. R., and Hofrichter, J. (1992) Singular Value Decomposition - Application to Analysis of Experimental-Data, *Method Enzymol* 210, 129-192.